

# Research in Physics

## 2008-2013

Theoretical Physics.....	1
Condensed Matter, Materials and Soft Matter Physics.....	38
Nanoscale Physics Cluster.....	38
Magnetic Resonance Cluster .....	96
Materials Physics Cluster .....	121
Astronomy and Astrophysics (A&A).....	172
Elementary Particle Physics (EPP).....	204
Centre for Fusion Space and Astrophysics (CFSA) .....	247

# Condensed Matter, Materials and Soft Matter Physics

The physics of materials has been a major research strength of the Dept. since its inception, and has continued along-side more recent diversification, culminating in large strategic investments in equipment and construction in 2010 of a £24 M Materials & Analytical Sciences building. In 2011, the Knight review of CMP specifically noted the excellent facilities for materials physics research, both within the Dept. and via extensive use of world-class Central Facilities, including those for materials modelling, preparation through epitaxy and single crystal growth, analysis of surfaces and bulk materials, and atomic resolution microscopy.

## Nanoscale Physics Cluster

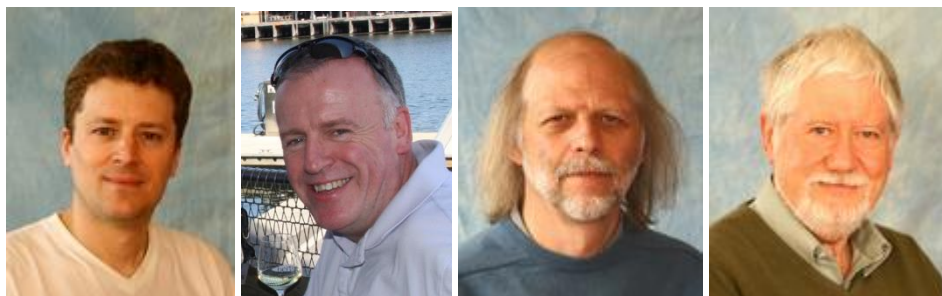
❖ *15 Staff; 11 PDRAs; 28 PhDs;*

❖ *287 articles; 2349 citations; £7.8 M grant awards; ~£2 M in-kind; 24 PhDs awarded*

Multi-functional materials with material dimensions on the nanoscale, e.g. Si structures, binary and complex oxides, magnetic semiconductors, and graphene, are fabricated and characterised with a range of epitaxial growth facilities, microscopies and spectroscopies. Close collaboration exists with the Theory Group on materials modelling and demonstration devices are made with facilities across UoW. Major investments have been made in high resolution electron microscopy and the field/vibration-free, temperature-controlled environment required to optimise their performance.



A *Microscopy* group (**Beanland, Sanchez, Sloan, Wilson**) has been established that aims to understand new materials and develop new techniques (often concurrently), with interests from graphene and CNT encapsulated ions, to crystal growth, quantum dots and phase transformations. The group is now involved with the majority of CMP projects and collaborates with Theory Group, researchers across UoW and nationally through SuperSTEM.



The *Surfaces, Interfaces & Thin Films* group (**Bell, McConville, Robinson, Woodruff**) has long been recognised for interface formation and surface structure determination, esp. with synchrotron radiation techniques, and for studying epitaxy of III-nitrides and transparent conducting oxides (TCO). A new facility for pulsed laser deposition (PLD) of oxides has been established, which is substantially enhanced by Alexe bringing his expertise, a further 2 PLD chambers, AFM capability and oxide device processing capabilities from MPI Halle. New research is being initiated in spintronic materials (ferromagnet/semiconductor epitaxy and half-metallic ferromagnets) with a dedicated MBE-STM system and collaboration from TP (Staunton) and industry (Toshiba).

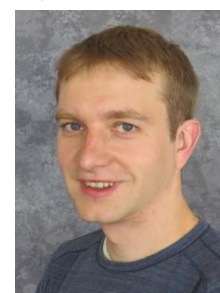


The *Nano-Silicon* group (**Leadley, Myronov, Parker, Whall**) has the UK's only academic wafer scale epitaxy facility for Group IV semiconductors and investigates Si, Ge, Sn heterostructures for applications in electronics, photonics and beyond. A new SiC epitaxy capability is being created via the BIS *Underpinning Power Electronics* initiative - again unique in the UK.



*Analytical Science Projects* (**Dowsett**) is devoted to the invention of novel instrumentation, evolution of techniques, and data processing methods for semiconductor analysis, synchrotron research and now applying materials science expertise to challenges in cultural artefact and art preservation.

An experimental *Biological Physics* group was created, in 2013, with **Kantsler** and **Polin** focussing around the dynamics of biological assemblies, from cilia to whole cells and more. It is co-located with Microscopy, anticipates strong research collaboration with Theory Group, and has research synergy with Warwick Medical School and Engineering's micro-fluidics research.

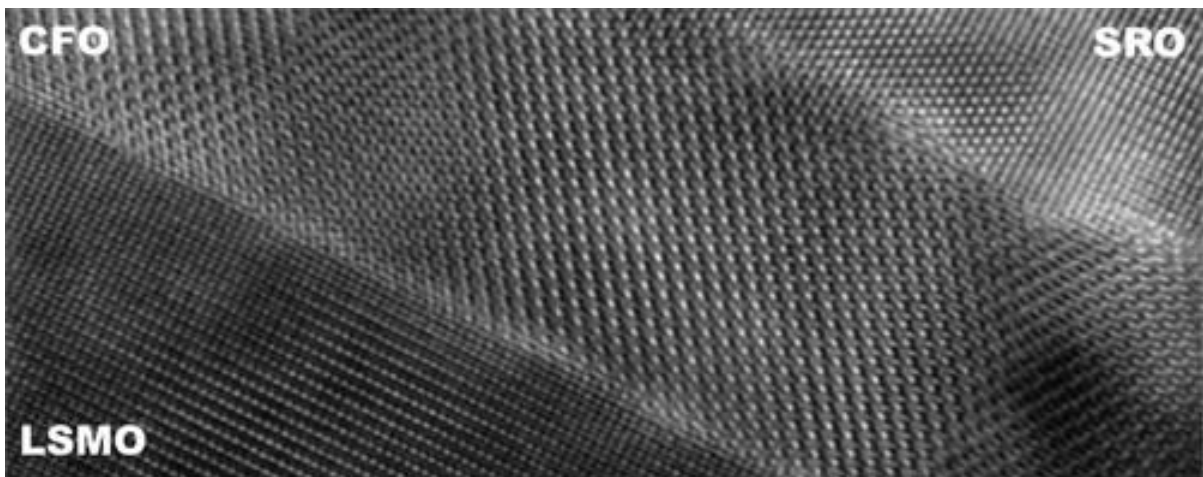


## **Towards all-oxide magnetic tunnel junctions – Epitaxial growth of SrRuO<sub>3</sub>/CoFe<sub>2</sub>O<sub>4</sub>/La<sub>2/3</sub>Sr<sub>1/3</sub>MnO<sub>3</sub> trilayers**

*Crystal Growth & Design* 12, 954-959 (2012)    [10.1021/cg201418q](https://doi.org/10.1021/cg201418q)

A.M. Sanchez, L. Äkäslompolo, Q.H. Qin and S. van Dijken

Epitaxial growth of SrRuO<sub>3</sub>/CoFe<sub>2</sub>O<sub>4</sub>/La<sub>2/3</sub>Sr<sub>1/3</sub>MnO<sub>3</sub> trilayers on SrTiO<sub>3</sub> (001) substrates has been successfully achieved using pulsed laser deposition. This trilayer configuration, which consists of two conducting ferromagnetic oxides separated by a thin insulating ferrite film, is a promising candidate for all-oxide magnetic tunnel junctions. Structural analyses carried out using transmission electron microscopy and X-ray diffraction demonstrate a remarkable continuation of the in-plane and out-plane crystallographic relations across the entire structure. Magnetic measurements on SrRuO<sub>3</sub>/CoFe<sub>2</sub>O<sub>4</sub>/La<sub>2/3</sub>Sr<sub>1/3</sub>MnO<sub>3</sub> trilayers indicate independent magnetic switching in an external magnetic field, which is one of the prerequisites for large tunneling magnetoresistance effects.

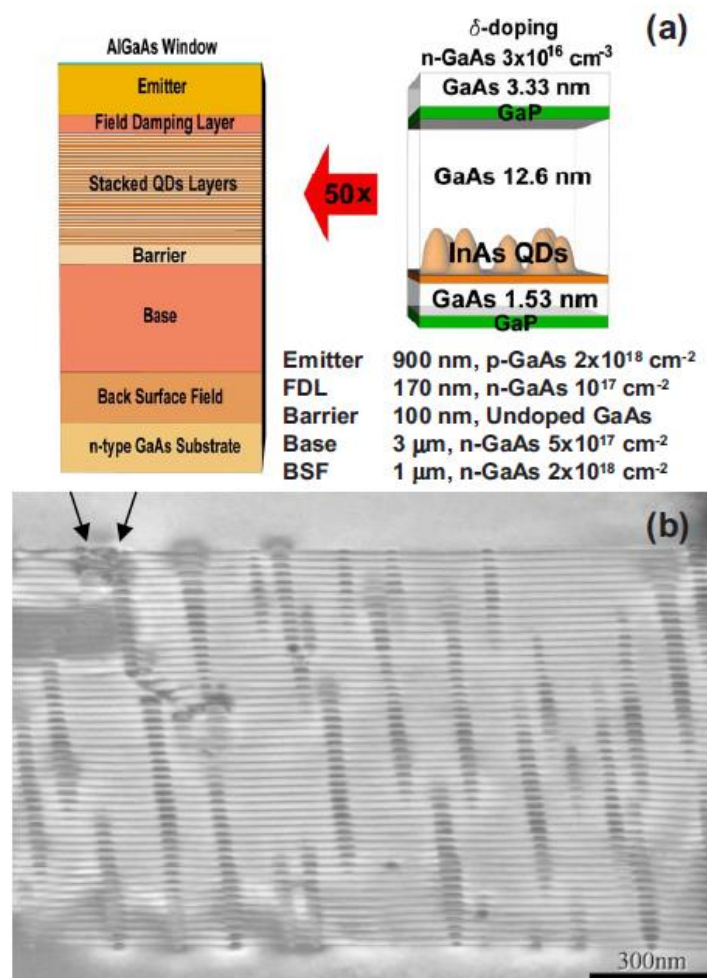


## Carrier recombination effects in strain compensated quantum dot stacks embedded in solar cells

*Applied Physics Letters* 93, 123114 (2008) [10.1063/1.2978243](https://doi.org/10.1063/1.2978243)

D. Alonso-Alvarez, A.G. Taboada, J.M. Ripalda, B. Alen, Y. Gonzalez, L. Gonzalez, J.M. Garcia, F. Briones, A. Marti, A. Luque, A.M. Sanchez and S.I. Molina

In this work we report the stacking of 50 InAs/GaAs quantum dot layers with a GaAs spacer thickness of 18 nm using GaP monolayers for strain compensation. We find a good structural and optical quality of the fabricated samples including a planar growth front across the whole structure, a reduction in the quantum dot size inhomogeneity, and an enhanced thermal stability of the emission. The optimized quantum dot stack has been embedded in a solar cell structure and we discuss the benefits and disadvantages of this approach for high efficiency photovoltaic applications.



(a) Structure of the 50 stacked QD solar cell with SC layers. Each GaP layer has a nominal thickness of 1 ML=0.273 nm. (b) Cross-sectional TEM image of the 50 stacked QD layers. The arrows indicate the defects observable in the image.

## A simple approach to characterising block copolymer assemblies: graphene oxide supports for high contrast multi-technique imaging

*Soft Matter* 8 (12) , pp. 3322-3328 (2012) [10.1039/C2SM07040E](https://doi.org/10.1039/C2SM07040E)

J.P. Patterson, A.M. Sanchez, N. Petzetakis, T.P. Smart, T.H. Epps, I. Portman, N. Wilson, R.K. O'Reilly

Block copolymers are well-known to self-assemble into a range of 3-dimensional morphologies. However, due to their nanoscale dimensions, resolving their exact structure can be a challenge. Transmission electron microscopy (TEM) is a powerful technique for achieving this, but for polymeric assemblies chemical fixing/staining techniques are usually required to increase image contrast and protect specimens from electron beam damage. Graphene oxide (GO) is a robust, water-dispersible, and nearly electron transparent membrane: an ideal support for TEM. We show that when using GO supports no stains are required to acquire high contrast TEM images and that the specimens remain stable under the electron beam for long periods, allowing sample analysis by a range of electron microscopy techniques. GO supports are also used for further characterization of assemblies by atomic force microscopy. The simplicity of sample preparation and analysis, as well as the potential for significantly increased contrast background, make GO supports an attractive alternative for the analysis of block copolymer assemblies.

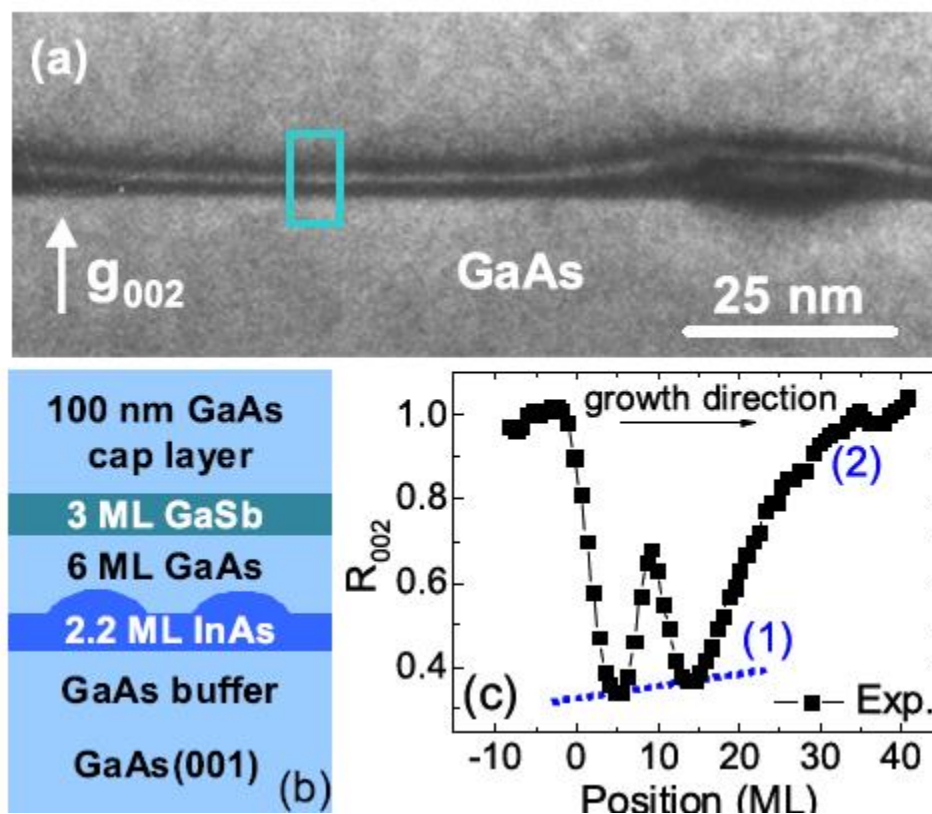


## Quantitative study of the interfacial intermixing and segregation effects across the wetting layer of Ga(As,Sb)-capped InAs quantum dots

*Applied Physics Letters* 101, 011601 (2012) [10.1063/1.4731790](https://doi.org/10.1063/1.4731790)

Luna, E., Beltrán, A.M., Sánchez, A.M., Molina, S.I.

Quantitative chemical information from semiconductor nanostructures is of primary importance, in particular at interfaces. Using a combination of analytical transmission electron microscopy techniques, we are able to quantify the interfacial intermixing and surface segregation across the intricate non-common-atom wetting layer (WL) of Ga(As,Sb)-capped InAs quantum dots. We find: (i) the WL-on-GaAs(buffer) interface is abrupt and perfectly defined by sigmoidal functions, in analogy with two-dimensional epitaxial layers, suggesting that the interface formation process is similar in both cases; (ii) indium segregation is the prevailing mechanism (e.g., over antimony segregation), which eventually determines the composition profile across the GaAs(cap)-on-WL interface.



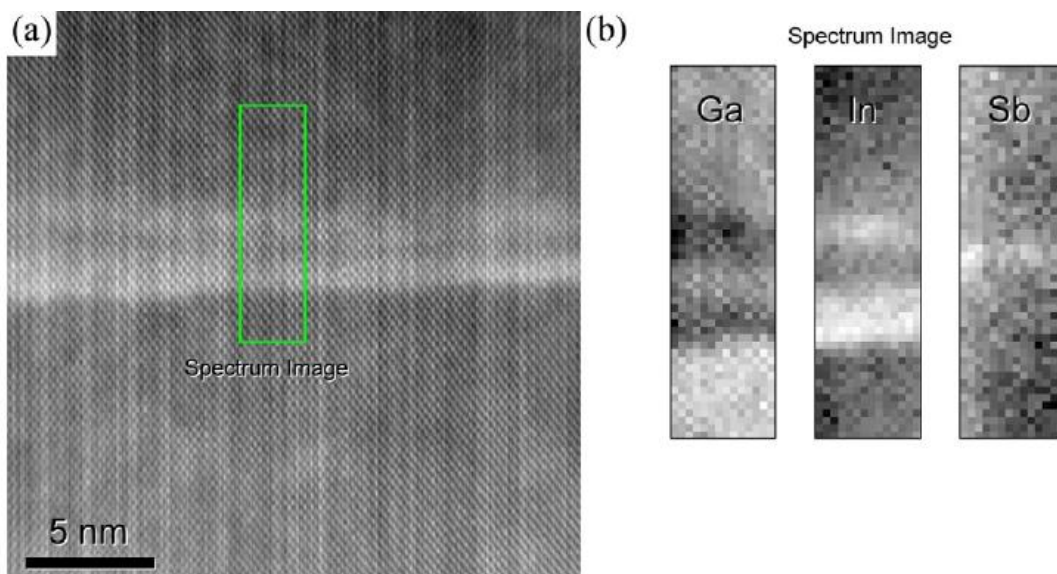
(a)  $g_{002}$  DFTEM micrograph (sensitive to composition) of the QD structure (b) (not scaled). Also displayed is the area across the WL from where the intensity profile ( $R_{002}$ ) is extracted (c). The labels (1) and (2) in (c) refer to the baseline and to the trail edge at the GaAs(cap)-on-WL interface, respectively.

## Blocking of indium incorporation by antimony in III-V-Sb nanostructures

*Nanotechnology* 21, 145606 (2010) [10.1088/0957-4484/21/14/145606](https://doi.org/10.1088/0957-4484/21/14/145606)

Sanchez, A.M, Beltran, A.M., Beanland, R., Ben, T., Gass, M.H., De La Pëa, F., Walls, M., Taboada, A.G., Ripalda, J.M., Molina, S.I.

The addition of antimony to III–V nanostructures is expected to give greater freedom in bandgap engineering for device applications. One of the main challenges to overcome is the effect of indium and antimony surface segregation. Using several very high resolution analysis techniques we clearly demonstrate blocking of indium incorporation by antimony. Furthermore, indium incorporation resumes when the antimony concentration drops below a critical level. This leads to major differences between nominal and actual structures.



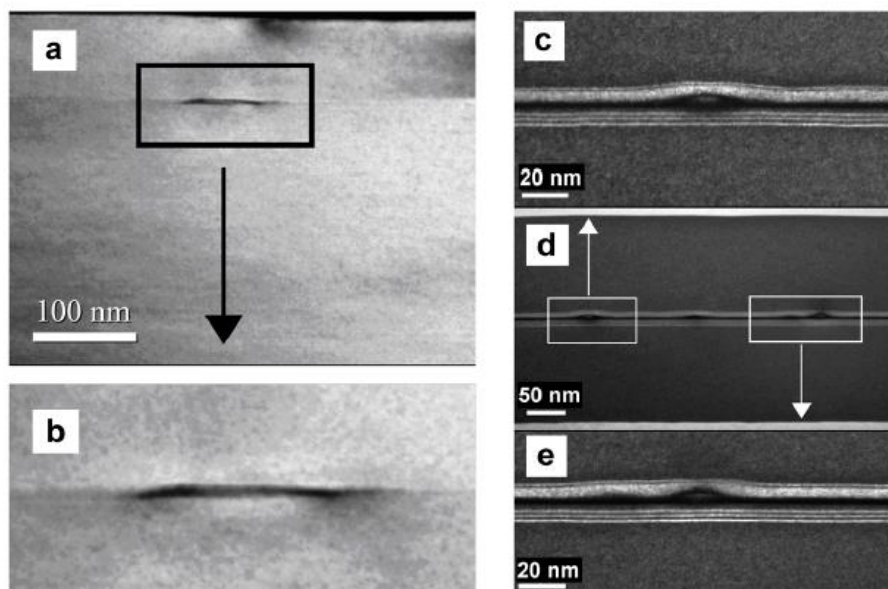
(a) HAADF image of an area between QDs in sample C6 viewed along [110]. The region used for EELS analysis is marked by the rectangle. (b) EELS-ICA analysis images of Ga, In and Sb distribution in the marked area.

## Structural analysis of strained quantum dots using nuclear magnetic resonance

*Nature Nanotechnology* 7, 646–650 (2012) [10.1038/nnano.2012.142](https://doi.org/10.1038/nnano.2012.142)

E. A. Chekhovich, K. V. Kavokin, J. Puebla, A. B. Krysa, M. Hopkinson, A. D. Andreev, A. M. Sanchez, R. Beanland, M. S. Skolnick & A. I. Tartakovskii

Strained semiconductor nanostructures can be used to make single-photon sources, detectors and photovoltaic devices, and could potentially be used to create quantum logic devices. The development of such applications requires techniques capable of nanoscale structural analysis, but the microscopy methods typically used to analyse these materials are destructive. NMR techniques can provide non-invasive structural analysis, but have been restricted to strain-free semiconductor nanostructures because of the significant strain-induced quadrupole broadening of the NMR spectra. Here, we show that optically detected NMR spectroscopy can be used to analyse individual strained quantum dots. Our approach uses continuous-wave broadband radiofrequency excitation with a specially designed spectral pattern and can probe individual strained nanostructures containing only  $1 \times 10^5$  quadrupole nuclear spins. With this technique, we are able to measure the strain distribution and chemical composition of quantum dots in the volume occupied by the single confined electron. The approach could also be used to address problems in quantum information processing such as the precise control of nuclear spins in the presence of strong quadrupole effects.



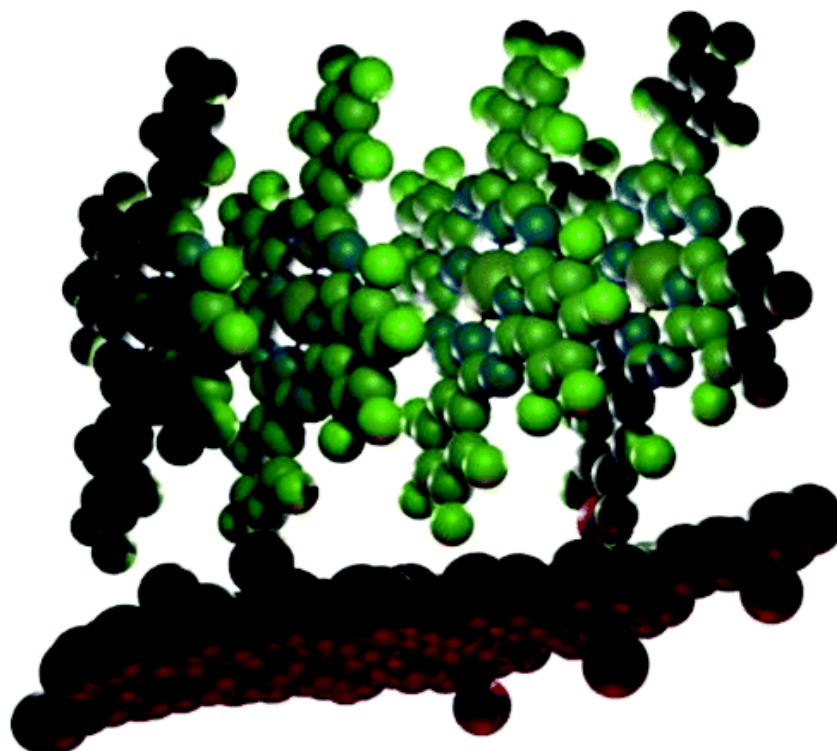
Transmission electron microscope (TEM) images. a, b, TEM images of InP/GaInP quantum dots. c, d, e, Images of InGaAs/GaAs dots. b shows zoomed part of the image in a, while c and e are zoomed parts of d.

## Resolving the Nanoscale Morphology and Crystallographic Structure of Molecular Thin Films: F<sub>16</sub>CuPc on Graphene Oxide

*Chemistry of Materials*, 24, 1365–1370 (2012) [10.1021/cm300073v](https://doi.org/10.1021/cm300073v)

Priyanka A. Pandey, Luke A. Rochford, Dean S. Keeble, Jonathan P. Rourke, Tim S. Jones, Richard Beanland, and Neil R. Wilson

Electron microscopy and diffraction are used to examine the nanoscale structure and molecular orientation in molecular films down to nominally monolayer thickness. The films studied consist of the planar n-type molecular semiconductor copper hexadecafluorophthalocyanine (F<sub>16</sub>CuPc) directly deposited onto graphene oxide (GO) membranes by organic molecular beam deposition. The graphene oxide support crucially provides the strength and low background required to analyze the crystal structure and morphology of even nominally monolayer thick films and is of relevance for molecular electronic applications. The crystal structure of the F<sub>16</sub>CuPc polymorph is solved by X-ray diffraction of single crystals and used to analyze the electron diffraction patterns from the thin-films, revealing that the F<sub>16</sub>CuPc molecules assemble with their molecular plane oriented perpendicular to the GO. There is no evidence for changes in the unit cell with film thickness, although the thinnest films show the greatest disorder in molecular packing. Direct deposition of molecular materials on low contrast and relevant substrates combined with electron and scanning probe microscopy is thus shown to be a powerful technique for elucidating structure in nanostructured organic thin films.



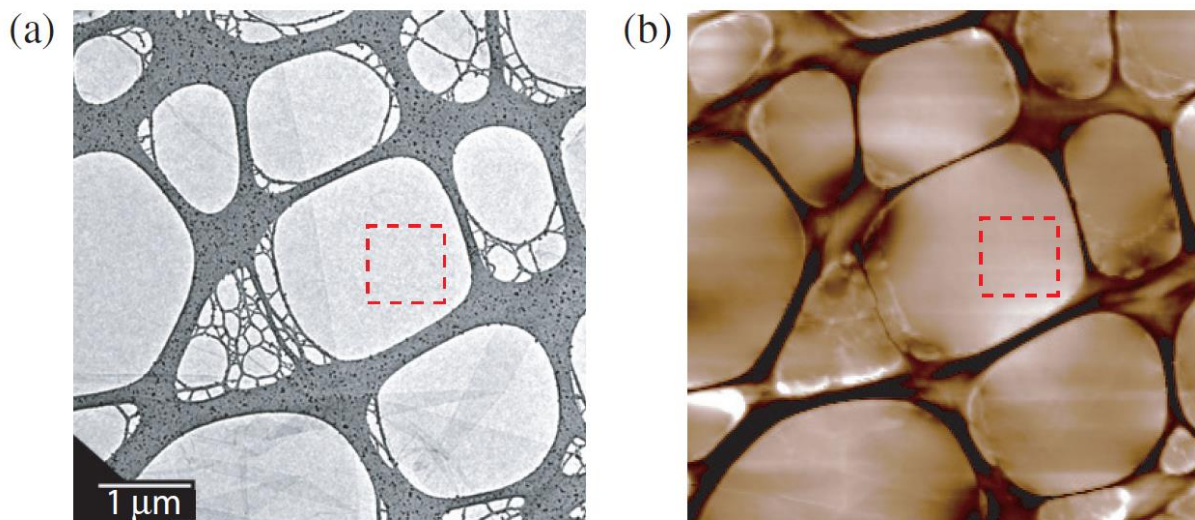
## On the structure and topography of free-standing chemically modified graphene

*New Journal of Physics* **12** 125010 (2010)

[10.1088/1367-2630/12/12/125010](https://doi.org/10.1088/1367-2630/12/12/125010)

N R Wilson, P A Pandey, R Beanland, J P Rourke, U Lupo, G Rowlands and R A Römer

The mechanical, electrical and chemical properties of chemically modified graphene (CMG) are intrinsically linked to its structure. Here, we report on our study of the topographic structure of free-standing CMG using atomic force microscopy (AFM) and electron diffraction. We find that, unlike graphene, suspended sheets of CMG are corrugated and distorted on nanometre length scales. AFM reveals not only long-range (100 nm) distortions induced by the support, as previously observed for graphene, but also short-range corrugations with length scales down to the resolution limit of 10 nm. These corrugations are static not dynamic, and are significantly diminished on CMG supported on atomically smooth substrates. Evidence for even shorter-range distortions, down to a few nanometres or less, is found by electron diffraction of suspended CMG. Comparison of the experimental data with simulations reveals that the mean atomic displacement from the nominal lattice position is of order 10% of the carbon-carbon bond length. Taken together, these results suggest a complex structure for CMG where heterogeneous functionalization creates local strain and distortion.



(a) Bright-field TEM image of GO on a lacy carbon support. (b) A 5 μm square AFM height image of the same region. The full height-scale is 35 nm.

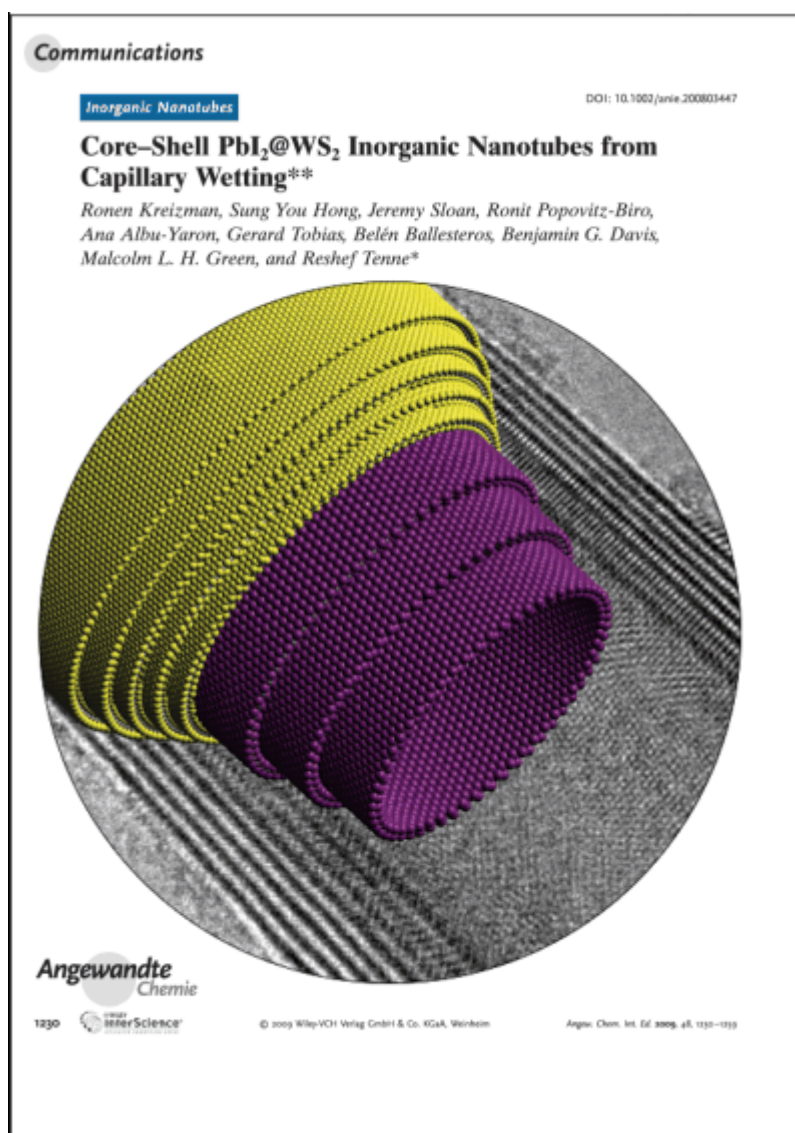
## Core-Shell $\text{PbI}_2@WS_2$ Inorganic Nanotubes from Capillary Wetting

*Angewandte Chemie International Edition* 48, 1230–1233, (2009)

[10.1002/anie.200803447](https://doi.org/10.1002/anie.200803447)

R. Kreizman, S. You Hong, J. Sloan, R. Popovitz-Biro, A. Albu-Yaron, G. Tobias, B. Ballesteros, B.G. Davis, M.L.H. Green and R. Tenne

**Multiwall  $WS_2$  nanotube templates** were used as hosts to prepare core-shell  $\text{PbI}_2@WS_2$  nanotubes by a capillary-wetting method. Conformal growth of  $\text{PbI}_2$  layers on the inner wall of the relatively wide  $WS_2$  nanotubes (i.d. ca. 10 nm) leads to nanotubular structures which were not previously observed in narrow carbon nanotube templates. Image simulation after structural modeling showed good agreement with the experimental HRTEM image.

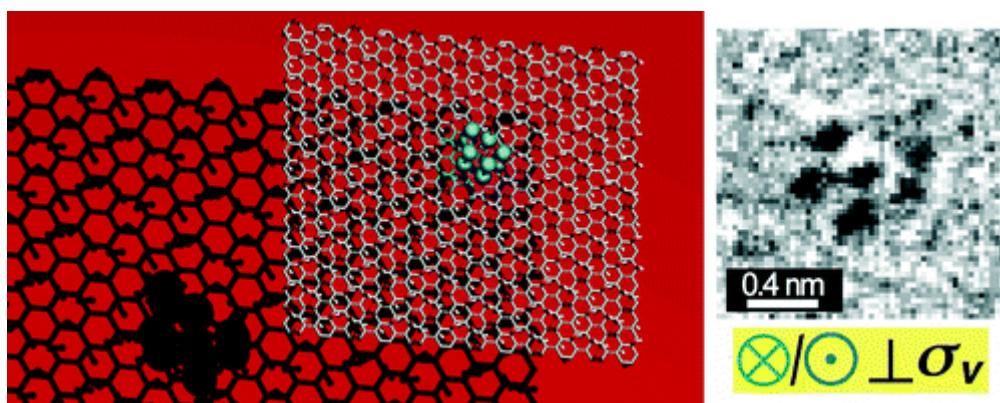


## Imaging the Structure, Symmetry, and Surface-Inhibited Rotation of Polyoxometalate Ions on Graphene Oxide

*Nano Letters*, 10, 4600–4606 (2010) [10.1021/nl1026452](https://doi.org/10.1021/nl1026452)

J. Sloan, Z. Liu, K. Suenaga, N.R. Wilson, P.A. Pandey, L.M. Perkins, J.P. Rourke, and I.J. Shannon

Atomic-resolution imaging of discrete  $[\gamma\text{-SiW}_{10}\text{O}_{36}]^{8-}$  lacunary Keggin ions dispersed onto monolayer graphene oxide (GO) films by low voltage aberration corrected transmission electron microscopy is described. Under low electron beam dose, individual anions remain stationary for long enough that a variety of projections can be observed and structural information extracted with ca.  $\pm 0.03$  nm precision. Unambiguous assignment of the orientation of individual ions with respect to the point symmetry elements can be determined. The  $C_{2v}$  symmetry  $[\gamma\text{-SiW}_{10}\text{O}_{36}]^{8-}$  ion was imaged along its 2-fold  $C_2$  axis or orthogonally with respect to one of two nonequivalent mirror planes (i.e.,  $\sigma_v$ ). Continued electron beam exposure of a second ion imaged orthogonal to  $\sigma_v$  causes it to translate and/or rotate in an inhibited fashion so that the ion can be viewed in different relative orientations. The inhibited surface motion of the anion, which is in response to H-bonding-type interactions, reveals an important new property for GO in that it demonstrably behaves as a chemically modified (i.e., rather than chemically neutral) surface in electron microscopy. This behavior indicates that GO has more in common with substrates used in imaging techniques such as atomic force microscopy and scanning tunneling microscopy, and this clearly sets it apart from other support films used in transmission electron microscopy.

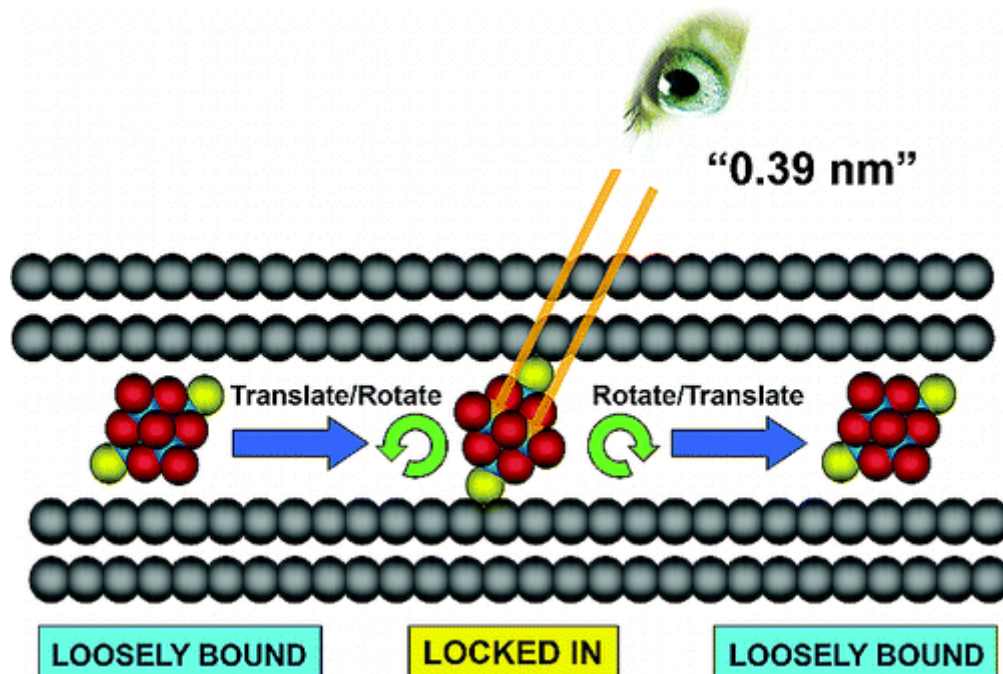


## Direct Imaging of the Structure, Relaxation, and Sterically Constrained Motion of Encapsulated Tungsten Polyoxometalate Lindqvist Ions within Carbon Nanotubes

ACS Nano, 2, 966–976 (2008) [10.1021/nn7002508](https://doi.org/10.1021/nn7002508)

J. Sloan, G. Matthewman, C. Dyer-Smith, A-Young Sung, Z. Liu, K. Suenaga, A.I. Kirkland, E. Flahaut

The imaging properties and observation of the sterically regulated translational motion of discrete tungsten polyoxometalate Lindqvist ions (*i.e.*,  $[W_6O_{19}]^{2-}$ ) within carbon nanotubes of specific internal diameter are reported. The translational motion of the nonspheroidal anion within the nanotube capillary is found to be impeded by its near-perfect accommodation to the internal van der Waals surface of the nanotube wall. Rotational motion of the anion about one remaining degree of freedom permits translational motion of the anion along the nanotube followed by locking in at sterically favorable positions in a mechanism similar to a molecular ratchet. This steric locking permits the successful direct imaging of the constituent octahedral cation template of individual  $[W_6O_{19}]^{2-}$  anions by high resolution transmission electron microscopy thereby permitting metrological measurements to be performed directly on the anion. Direct imaging of pairs of equatorial  $W_2$  atoms within the anion reveal steric relaxation of the anion contained within the nanotube capillary relative to the bulk anion structure.

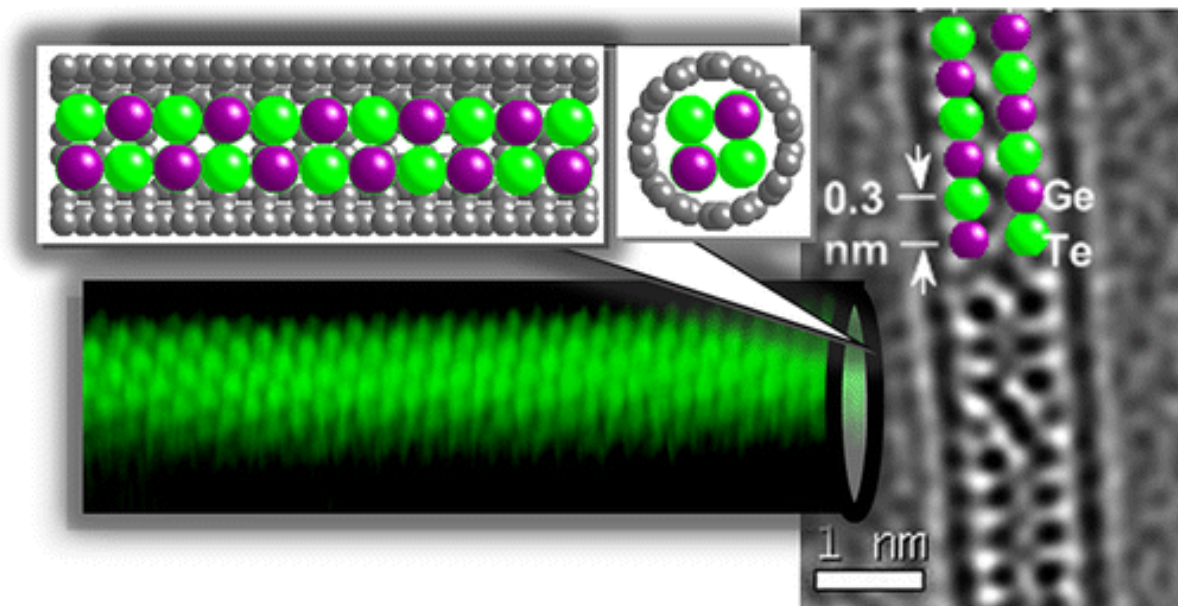


## Confined Crystals of the Smallest Phase-Change Material

*Nano Letters*, 13, 4020–4027 (2013) [10.1021/nl4010354](https://doi.org/10.1021/nl4010354)

C.E. Giusca, V. Stolojan, J. Sloan, F. Börrnert, H. Shiozawa, K. Sader, M.H. Rummeli, B. Büchner, and S. Ravi P. Silva

The demand for high-density memory in tandem with limitations imposed by the minimum feature size of current storage devices has created a need for new materials that can store information in smaller volumes than currently possible. Successfully employed in commercial optical data storage products, phase-change materials, that can reversibly and rapidly change from an amorphous phase to a crystalline phase when subject to heating or cooling have been identified for the development of the next generation electronic memories. There are limitations to the miniaturization of these devices due to current synthesis and theoretical considerations that place a lower limit of 2 nm on the minimum bit size, below which the material does not transform in the structural phase. We show here that by using carbon nanotubes of less than 2 nm diameter as templates phase-change nanowires confined to their smallest conceivable scale are obtained. Contrary to previous experimental evidence and theoretical expectations, the nanowires are found to crystallize at this scale and display amorphous-to-crystalline phase changes, fulfilling an important prerequisite of a memory element. We show evidence for the smallest phase-change material, extending thus the size limit to explore phase-change memory devices at extreme scales.



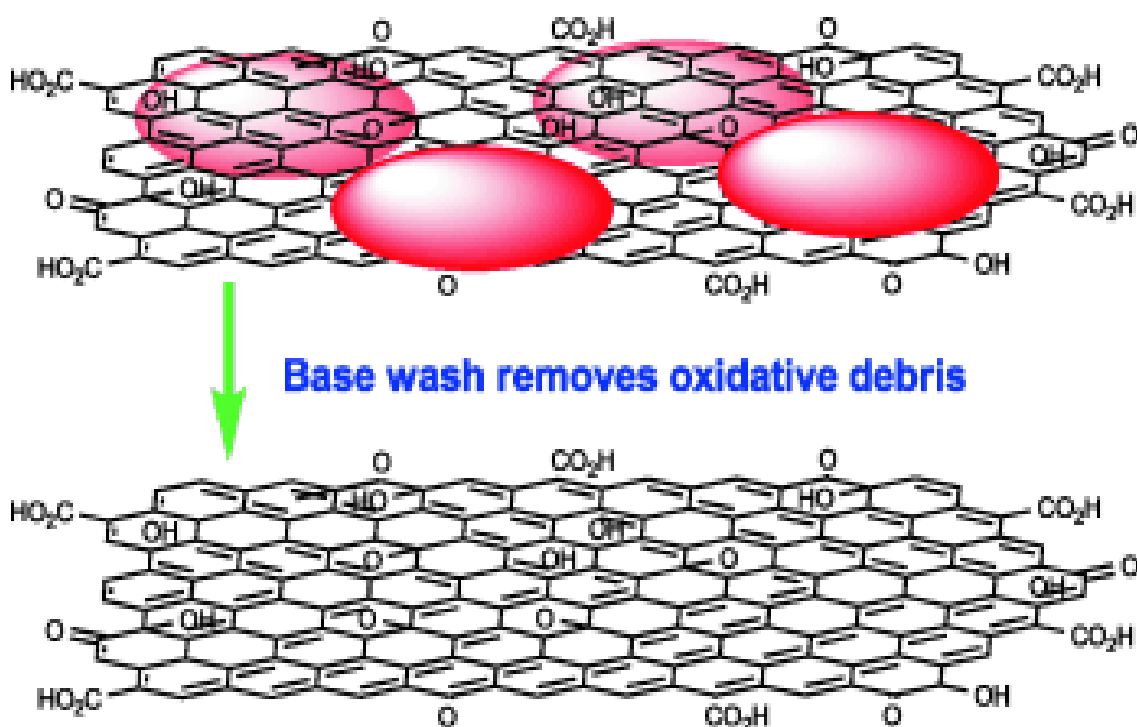
## The Real Graphene Oxide Revealed: Stripping the Oxidative Debris from the Graphene-like Sheets

*Angewandte Chemie International Edition* 50, 3173, (2011)

[10.1002/anie.20100752](https://doi.org/10.1002/anie.20100752)

J.P. Rourke, P.A. Pandey, J.J. Moore, M. Bates, I.A. Kinloch, R.J. Young and N.R. Wilson

It'll come out in the wash! Graphene oxide has been shown to be a stable complex of oxidative debris (red ellipses in the picture) strongly adhered to functionalized graphene-like sheets. Under basic conditions the oxidative debris is stripped from the graphene-like sheets, and the resulting graphene oxide is conducting and cannot easily be resuspended in water.

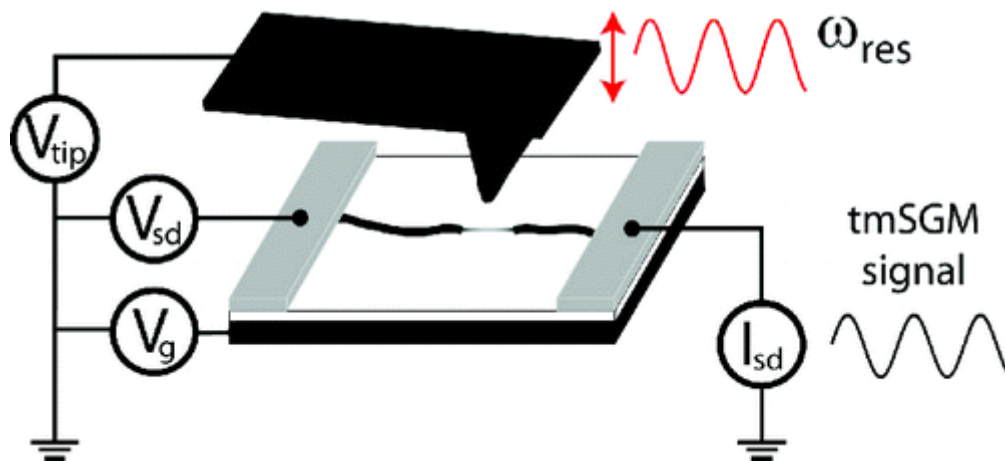


## Tip-Modulation Scanned Gate Microscopy

*Nano Letters*, 8, 2161–2165 (2008) [10.1021/nl080488i](https://doi.org/10.1021/nl080488i)

Neil R. Wilson and David H. Cobden

We introduce a technique that improves the sensitivity and resolution and eliminates the nonlocal background of scanned gate microscopy (SGM). In conventional SGM, a voltage bias is applied to the atomic force microscope tip and the sample conductance is measured as the tip is scanned. In the new technique, which we call tip-modulation SGM (tmSGM), the biased tip is oscillated and the induced oscillation of the sample conductance is measured. Applied to single-walled carbon nanotube network devices, tmSGM gives sharp, low-noise and background-free images.



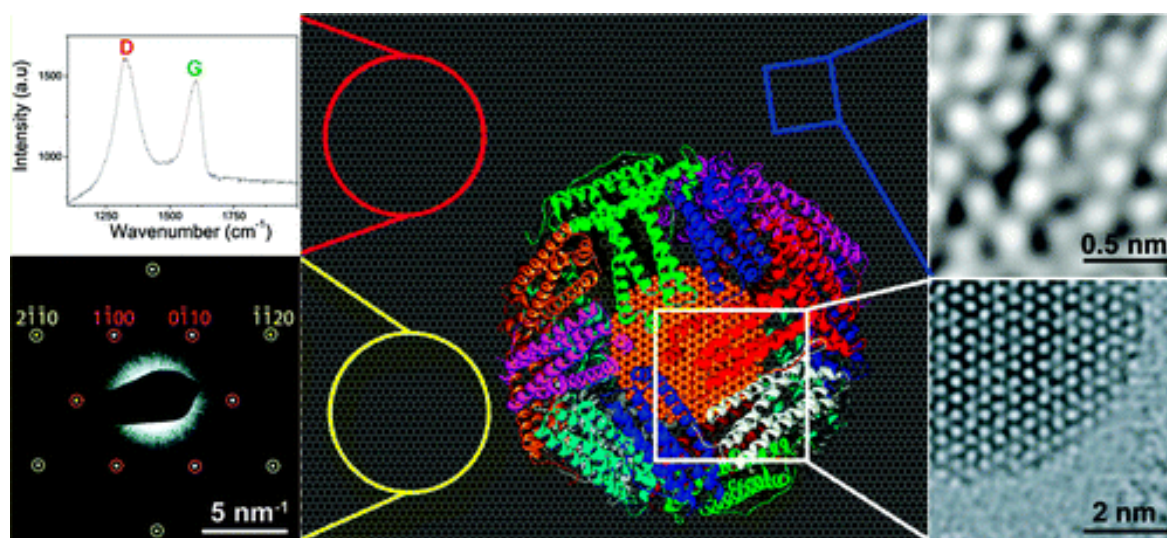
## Graphene Oxide: Structural Analysis and Application as a Highly Transparent Support for Electron Microscopy

ACS Nano, 3, 2547–2556 (2009)

[10.1021/nn900694t](https://doi.org/10.1021/nn900694t)

Neil R. Wilson, Priyanka A. Pandey, Richard Beanland, Robert J. Young, Ian A. Kinloch, Lei Gong, Zheng Liu, Kazu Suenaga, Jonathan P. Rourke, Stephen J. York and Jeremy Sloan

We report on the structural analysis of graphene oxide (GO) by transmission electron microscopy (TEM). Electron diffraction shows that on average the underlying carbon lattice maintains the order and lattice-spacings of graphene; a structure that is clearly resolved in 80 kV aberration-corrected atomic resolution TEM images. These results also reveal that single GO sheets are highly electron transparent and stable in the electron beam, and hence ideal support films for the study of nanoparticles and macromolecules by TEM. We demonstrate this through the structural analysis of physiological ferritin, an iron-storage protein.

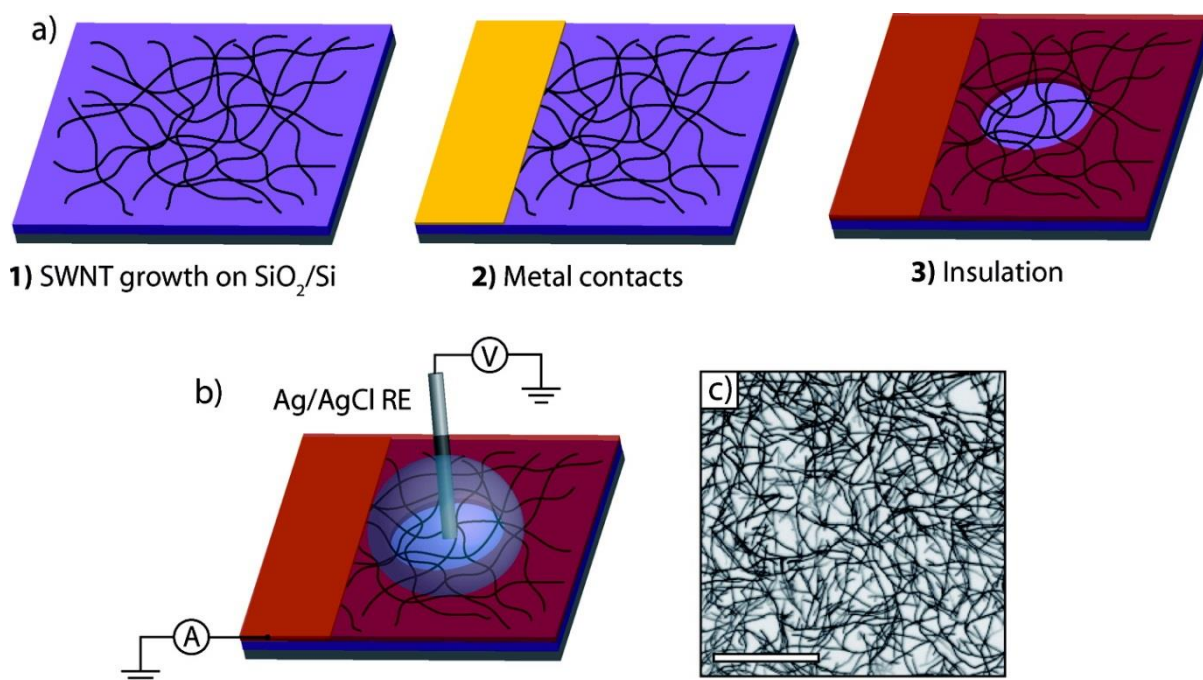


## Single-Walled Carbon Nanotube Network Ultramicroelectrodes

*Analytical Chemistry*, 80, 3598–3605 (2008) [10.1021/ac702518g](https://doi.org/10.1021/ac702518g)

Ioana Dumitrescu, Patrick R. Unwin, Neil R. Wilson and Julie V. Macpherson

Ultramicroelectrodes (UMEs) fabricated from networks of chemical vapor deposited single-walled carbon nanotubes (SWNTs) on insulating silicon oxide surfaces are shown to offer superior qualities over solid UMEs of the same size and dimensions. Disk shaped UMEs, comprising two-dimensional “metallic” networks of SWNTs, have been fabricated lithographically, with a surface coverage of <1% of the underlying insulating surface. The electrodes are long lasting and give highly reproducible responses (either for repeat runs with the same electrode or when comparing several electrodes with the same size). For redox concentrations  $\leq 1$  mM the steady-state behavior of SWNT network UMEs is as expected for conventional solid metal UMEs (e.g., Pt, Au), due to diffusional overlap between neighboring SWNTs. Importantly, the low intrinsic capacitance of the SWNTs and much reduced surface area lead to much faster response times and lower background currents. The well-defined geometry of the SWNT network electrode is also useful for studying electron transfer (ET) kinetics at SWNTs. Given the intrinsically high mass transport rates to SWNTs within a network electrode, the reversible nature of the CVs recorded for  $\text{Ru}(\text{NH}_3)_6^{3+/2+}$  and  $\text{FcTMA}^{+/2+}$  suggests that ET driven solely by defects on the sidewalls of the SWNTs is highly unlikely.



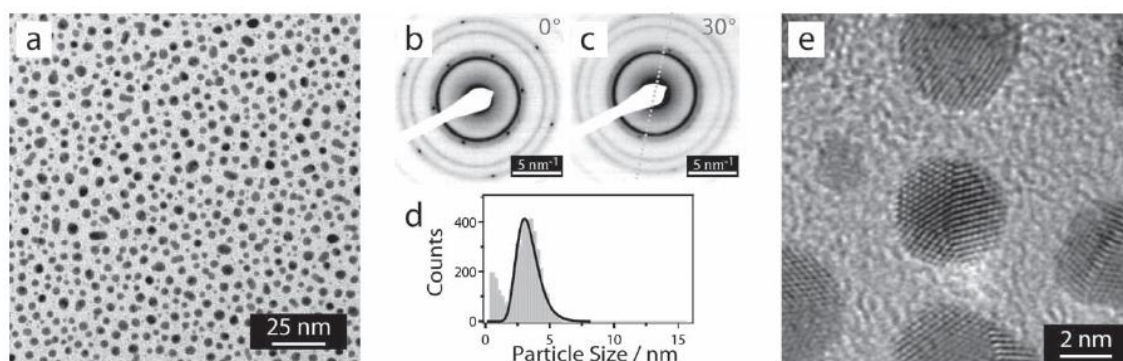
(a) Schematic of the lithographic procedure for fabricating SWNT disk UMEs. (b) Schematic of the experimental droplet cell setup used for electrochemical measurements. (c) FE-SEM image of a typical SWNT network sample, with a density of  $4 \mu\text{m}_{\text{SWNT}} \mu\text{m}^{-2}$ . Scale bar is  $5 \mu\text{m}$ .

## Physical Vapor Deposition of Metal Nanoparticles on Chemically Modified Graphene: Observations on Metal–Graphene Interactions

*Small* 7, 3202 (2011) [10.1002/sml.201101430](https://doi.org/10.1002/sml.201101430)

Priyanka A. Pandey, Gavin R. Bell, Jonathan P. Rourke, Ana M. Sanchez, Mark D. Elkin, Bryan J. Hickey and Neil R. Wilson

The growth of metallic nanoparticles formed on chemically modified graphene (CMG) by physical vapor deposition is investigated. Fine control over the size (down to  $\sim 1.5$  nm for Au) and coverage (up to  $5 \times 10^4 \mu\text{m}^{-2}$  for Au) of nanoparticles can be achieved. Analysis of the particle size distributions gives evidence for Au nanocluster diffusion at room temperature, while particle size statistics differ clearly between metal deposited on single- and multilayer regions. The morphology of the nanoparticles varies markedly for different metals (Ag, Au, Fe, Pd, Pt, Ti), from a uniform thin film for Ti to a droplet-like growth for Ag. A simple model explains these morphologies, based only on consideration of 1) the different energy barriers to surface diffusion of metal adatoms on graphene, and 2) the ratio of the bulk cohesive energy of the metal to the metal–graphene binding energy. Understanding these interactions is important for controlling nanoparticle and thin-film growth on graphene, and for understanding the resultant charge transfer between metal and graphene.



a) Bright-field TEM image of Au deposited at 0.75 nm thickness on single-layer GO. Selected area electron diffraction patterns of Au on single-layer graphene with the sample tilted at b)  $0^\circ$  and c)  $30^\circ$  to the electron beam (contrast inverted). On (c), the approximate direction of the tilt axis is marked by the dashed line. d) Histogram of the Au nanoparticle sizes,  $d$ , measured from a typical image. e) HR-TEM image of  $<1$  nm Au deposition on single-sheet GO.

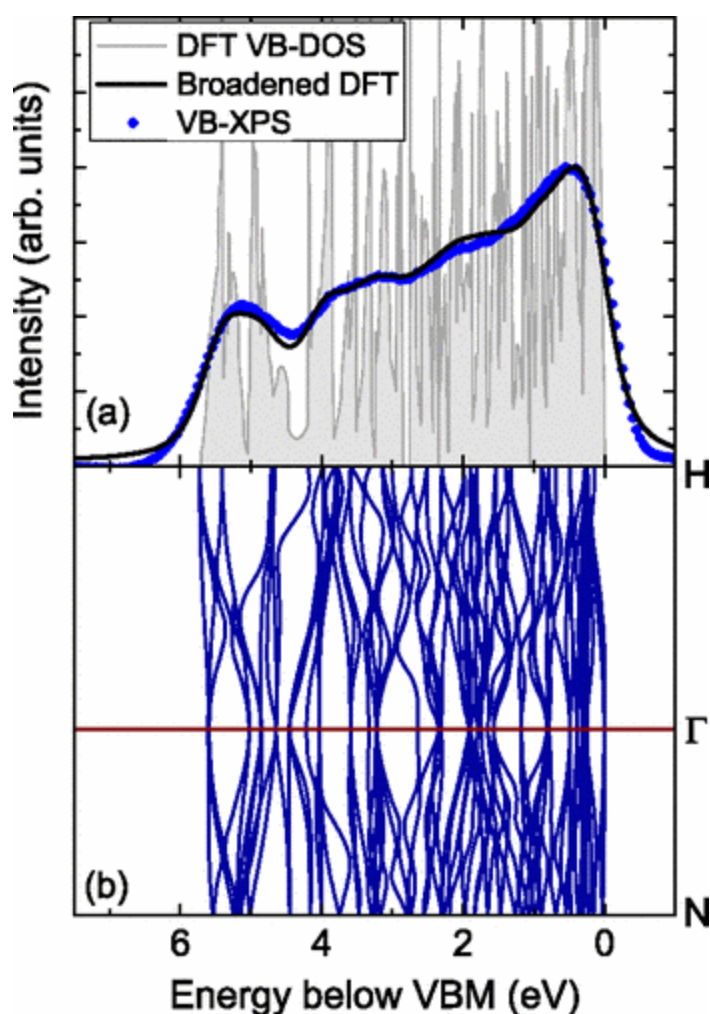
## Band gap, electronic structure, and surface electron accumulation of cubic and rhombohedral $\text{In}_2\text{O}_3$

*Phys. Rev. B* 79, 205211 (2009)

[10.1103/PhysRevB.79.205211](https://doi.org/10.1103/PhysRevB.79.205211)

P. D. C. King, T. D. Veal, F. Fuchs, Ch. Y. Wang, D. J. Payne, A. Bourlange, H. Zhang, G. R. Bell, V. Cimalla, O. Ambacher, R. G. Egdell, F. Bechstedt, and C. F. McConville

The bulk and surface electronic structure of  $\text{In}_2\text{O}_3$  has proved controversial, prompting the current combined experimental and theoretical investigation. The band gap of single-crystalline  $\text{In}_2\text{O}_3$  is determined as  $2.93 \pm 0.15$  and  $3.02 \pm 0.15$  eV for the cubic bixbyite and rhombohedral polymorphs, respectively. The valence-band density of states is investigated from x-ray photoemission spectroscopy measurements and density-functional theory calculations. These show excellent agreement, supporting the absence of any significant indirect nature of the  $\text{In}_2\text{O}_3$  band gap. Clear experimental evidence for an  $s$ - $d$  coupling between In  $4d$  and O  $2s$  derived states is also observed. Electron accumulation, recently reported at the (001) surface of bixbyite material, is also shown to be present at the bixbyite (111) surface and the (0001) surface of rhombohedral  $\text{In}_2\text{O}_3$ .



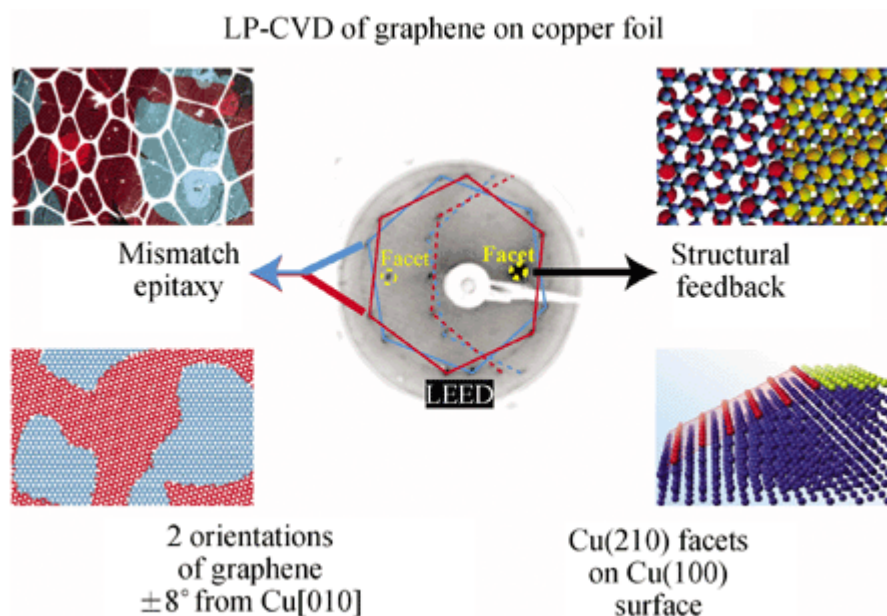
(a) Shirley-background-subtracted valence-band photoemission spectrum and DFT VB-DOS calculations shown without (shaded) and with lifetime and instrumental broadening for bcc- $\text{In}_2\text{O}_3$  (111). The measured valence-band photoemission is rigidly shifted to lower energies by 3.4 eV to align the VBM at 0 eV binding energy as for the calculations. The XPS and DFT spectra are normalized to the same maximum peak intensity. The corresponding DFT valence-band-structure calculations for bcc- $\text{In}_2\text{O}_3$  are shown in (b)

## Weak mismatch epitaxy and structural Feedback in graphene growth on copper foil

*Nano Research* 6, 99 (2013) [10.1007/s12274-013-0285-y](https://doi.org/10.1007/s12274-013-0285-y)

Neil R. Wilson, Alexander J. Marsden, Mohammed Saghir, Catherine J. Bromley, Renald Schaub, Giovanni Costantini, Thomas W. White, Cerianne Partridge, Alexei Barinov, Pavel Dudin, Ana M. Sanchez, James J. Mudd, Marc Walker, Gavin R. Bell

Graphene growth by low-pressure chemical vapor deposition on low cost copper foils shows great promise for large scale applications. It is known that the local crystallography of the foil influences the graphene growth rate. Here we find an epitaxial relationship between graphene and copper foil. Interfacial restructuring between graphene and copper drives the formation of  $(n10)$  facets on what is otherwise a mostly Cu(100) surface, and the facets in turn influence the graphene orientations from the onset of growth. Angle resolved photoemission shows that the electronic structure of the graphene is decoupled from the copper indicating a weak interaction between them. Despite this, two preferred orientations of graphene are found,  $\pm 8^\circ$  from the Cu[010] direction, creating a non-uniform distribution of graphene grain boundary misorientation angles. Comparison with the model system of graphene growth on single crystal Cu(110) indicates that this orientational alignment is due to mismatch epitaxy. Despite the differences in symmetry the orientation of the graphene is defined by that of the copper. We expect these observations to not only have importance for controlling and understanding the growth process for graphene on copper, but also to have wider implications for the growth of two-dimensional materials on low cost metal substrates.

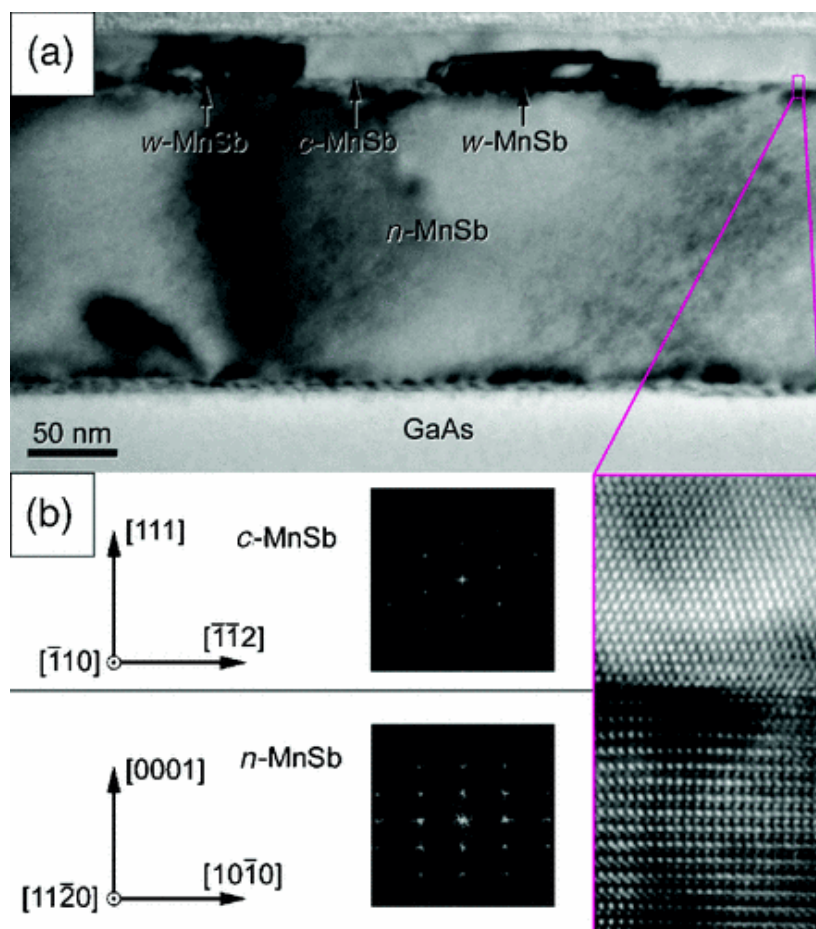


## Cubic MnSb: Epitaxial growth of a predicted room temperature half-metal

*Phys. Rev. B* 85, 060403(R) (2012) [10.1103/PhysRevB.85.060403](https://doi.org/10.1103/PhysRevB.85.060403)

James D. Aldous, Christopher W. Burrows, Ana M. Sánchez, Richard Beanland, Ian Maskery, Matthew K. Bradley, Manuel dos Santos Dias, Julie B. Staunton, and Gavin R. Bell

Epitaxial films including bulk-like cubic and wurtzite polymorphs of MnSb have been grown by molecular beam epitaxy on GaAs via careful control of the  $Sb_4/Mn$  flux ratio. Nonzero-temperature density functional theory was used to predict *ab initio* the half-metallicity of the cubic polymorph and compare its spin polarization as a function of reduced magnetization with that of the well-known half-metal NiMnSb. In both cases, half-metallicity is lost at a threshold magnetization reduction, corresponding to a temperature  $T^* < T_C$ . This threshold is far higher for cubic MnSb compared to NiMnSb and corresponds to  $T^* > 350$  K, making epitaxial cubic MnSb a promising candidate for efficient room temperature spin injection into semiconductors.



TEM data for polymorphic MnSb films on GaAs(111).

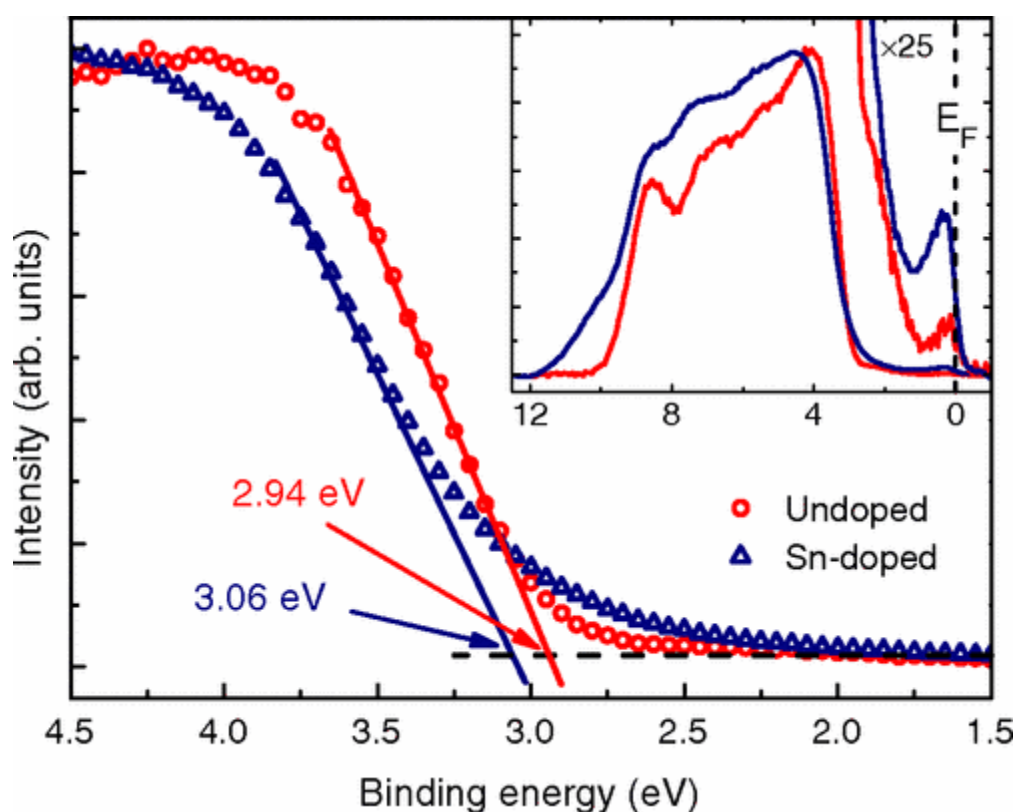
A typical bright-field image (a) and Fourier transforms from individual regions (b) are labeled with constituent phases, while a high resolution micrograph of the c-MnSb/n-MnSb boundary shows a sharp epitaxial interface.

## Surface Electron Accumulation and the Charge Neutrality Level in $\text{In}_2\text{O}_3$

*Phys. Rev. Lett.* 101, 116808 (2008) [10.1103/PhysRevLett.101.116808](https://doi.org/10.1103/PhysRevLett.101.116808)

P. D. C. King, T. D. Veal, D. J. Payne, A. Bourlange, R. G. Egdell, and C. F. McConville

High-resolution x-ray photoemission spectroscopy, infrared reflectivity and Hall effect measurements, combined with surface space-charge calculations, are used to show that electron accumulation occurs at the surface of undoped single-crystalline  $\text{In}_2\text{O}_3$ . From a combination of measurements performed on undoped and heavily Sn-doped samples, the charge neutrality level is shown to lie  $\sim 0.4$  eV above the conduction band minimum in  $\text{In}_2\text{O}_3$ , explaining the electron accumulation at the surface of undoped material, the propensity for *n*-type conductivity, and the ease of *n*-type doping in  $\text{In}_2\text{O}_3$ , and hence its use as a transparent conducting oxide material.



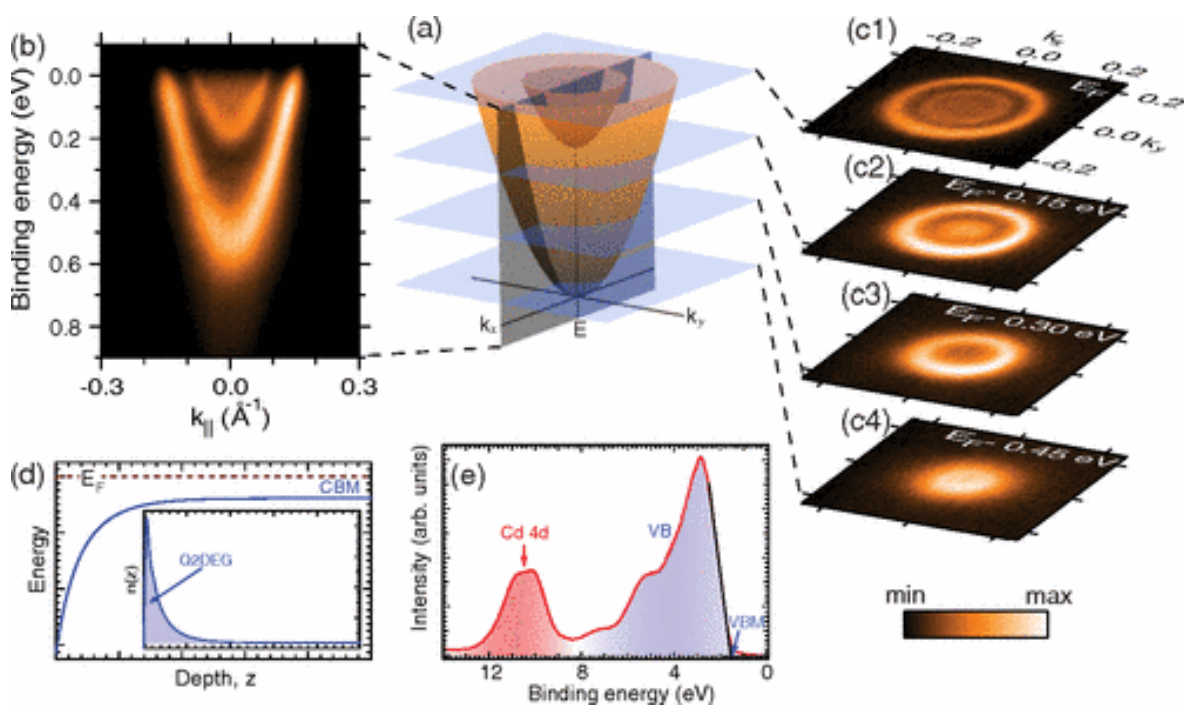
Leading edge of the valence band photoemission of undoped and Sn-doped  $\text{In}_2\text{O}_3$ , and the linear extrapolations used to determine the VBM to surface Fermi level separation. The Shirley-background subtracted valence band photoemission spectra are shown over an extended binding energy range inset, with the conduction band emission also magnified  $\times 25$ .

## Surface Band-Gap Narrowing in Quantized Electron Accumulation Layers

*Phys. Rev. Lett.* 104, 256803 (2010) [10.1103/PhysRevLett.104.256803](https://doi.org/10.1103/PhysRevLett.104.256803)

P. D. C. King, T. D. Veal, C. F. McConville, J. Zúñiga-Pérez, V. Muñoz-Sanjosé, M. Hopkinson, E. D. L. Rienks, M. Fuglsang Jensen, and Ph. Hofmann

An energy gap between the valence and the conduction band is the defining property of a semiconductor, and the gap size plays a crucial role in the design of semiconductor devices. We show that the presence of a two-dimensional electron gas near to the surface of a semiconductor can significantly alter the size of its band gap through many-body effects caused by its high electron density, resulting in a surface band gap that is much smaller than that in the bulk. Apart from reconciling a number of disparate previous experimental findings, the results suggest an entirely new route to spatially inhomogeneous band-gap engineering.



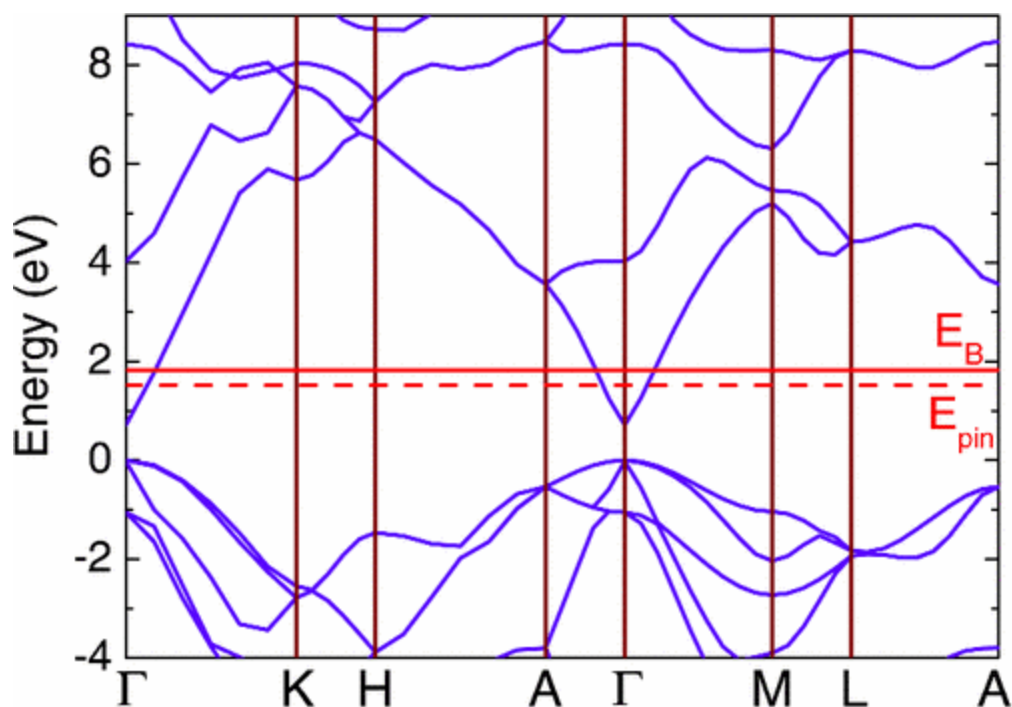
(a) Quantized conduction-band subbands of a surface Q2DEG. (b)  $E$  vs  $k_{\parallel}$  and (c) constant energy cuts through the subband dispersions measured by ARPES, shown here for a CdO(001) surface recorded with a photon energy of  $h\nu=30$  eV at room temperature. The constant energy cuts are integrated over  $\pm 3$  meV about (c1) the Fermi level and (c2) 0.15, (c3) 0.30, and (c4) 0.45 eV below the Fermi level, respectively. (d) Schematic of downward bending of the conduction band and (inset) corresponding increase in free-carrier density within the semiconductor surface electron accumulation layer (Q2DEG). (e) AIPES measurements of the valence bands and Cd 4d core levels in CdO, recorded at a photon energy of  $h\nu=120$  eV.

## Determination of the branch-point energy of InN: Chemical trends in common-cation and common-anion semiconductors

*Phys. Rev. B* 77, 045316 (2008) [10.1103/PhysRevB.77.045316](https://doi.org/10.1103/PhysRevB.77.045316)

P. D. C. King, T. D. Veal, P. H. Jefferson, S. A. Hatfield, L. F. J. Piper, C. F. McConville, F. Fuchs, J. Furthmüller, F. Bechstedt, Hai Lu, and W. J. Schaff

Bulk and surface electronic properties of Si-doped InN are investigated using high-resolution x-ray photoemission spectroscopy, optical absorption spectroscopy, and quasiparticle corrected density functional theory calculations. The branch point energy in InN is experimentally determined to lie  $1.83 \pm 0.10$  eV above the valence-band maximum. This high position relative to the band edges is used to explain the extreme fundamental electronic properties of the material. Far from being anomalous, these properties are reconciled within chemical trends of common-cation and common-anion semiconductors.



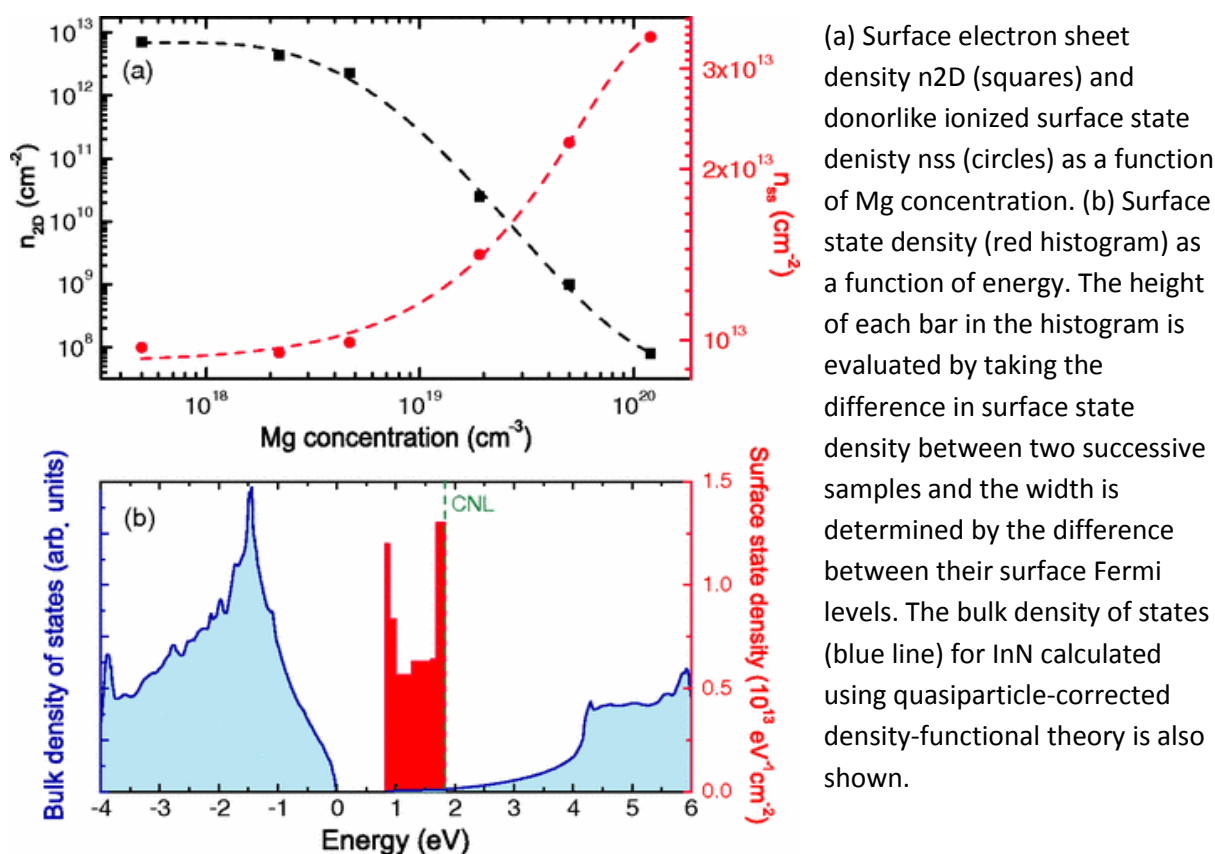
QPC-DFT band structure across the Brillouin zone with the determined branch point  $E_B$  and surface Fermi level pinning  $E_{pin}$  positions.

## Giant Reduction of InN Surface Electron Accumulation: Compensation of Surface Donors by Mg Dopants

*Phys. Rev. Lett.* 109, 247605 (2012) [10.1103/PhysRevLett.109.247605](https://doi.org/10.1103/PhysRevLett.109.247605)

W. M. Linhart, J. Chai, R. J. H. Morris, M. G. Dowsett, C. F. McConville, S. M. Durbin, and T. D. Veal

Extreme electron accumulation with sheet density greater than  $10^{13} \text{ cm}^{-2}$  is almost universally present at the surface of indium nitride (InN). Here, x-ray photoemission spectroscopy and secondary ion mass spectrometry are used to show that the surface Fermi level decreases as the Mg concentration increases, with the sheet electron density falling to below  $10^8 \text{ cm}^{-2}$ . Surface space-charge calculations indicate that the lowering of the surface Fermi level increases the density of unoccupied donor-type surface states and that these are largely compensated by Mg acceptors in the near-surface hole depletion region rather than by accumulated electrons. This is a significant step towards the realization of InN-based optoelectronic devices.

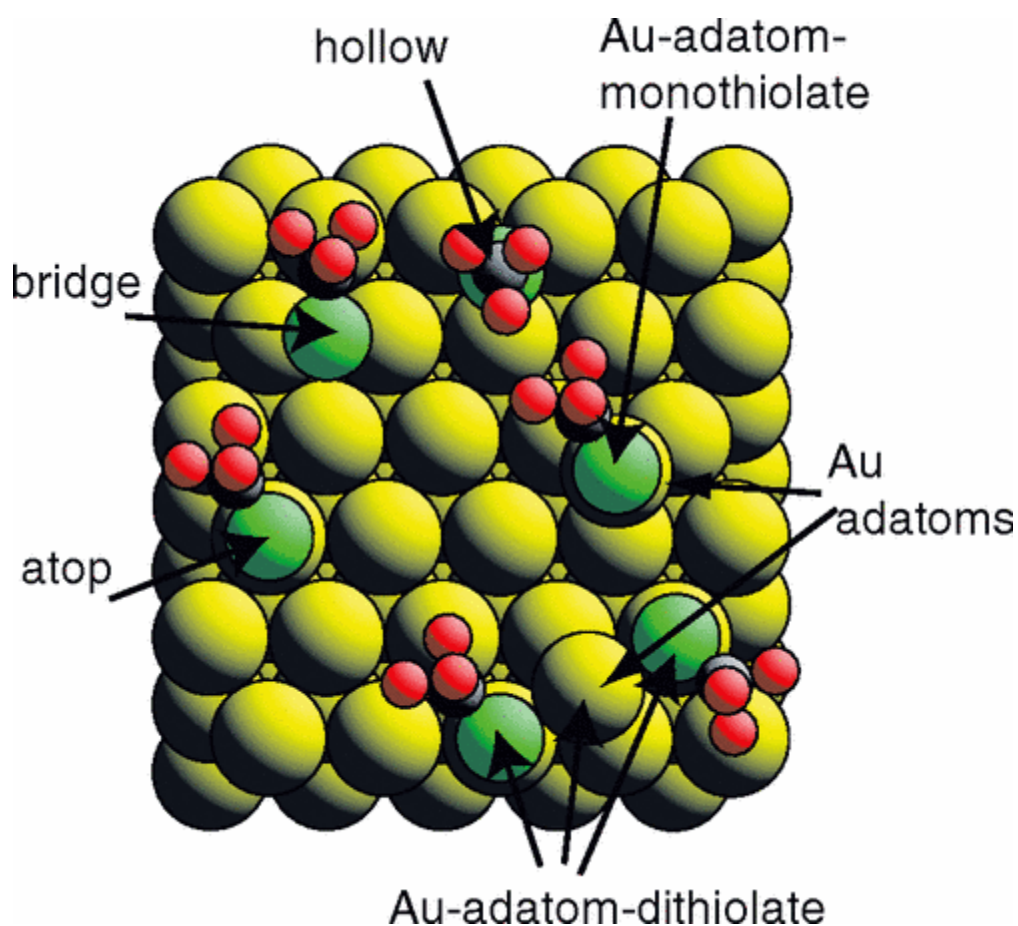


## Local Methylthiolate Adsorption Geometry on Au(111) from Photoemission Core-Level Shifts

*Phys. Rev. Lett.* 102, 126101 (2009) [10.1103/PhysRevLett.102.126101](https://doi.org/10.1103/PhysRevLett.102.126101)

A. Chaudhuri, T. J. Leroholi, D. C. Jackson, D. P. Woodruff, and V. Dhanak

The local adsorption structure of methylthiolate in the ordered Au(111)-(3 $\sqrt{3}\times 3\sqrt{3}$ )R30° phase has been investigated using core-level-shift measurements of the surface and bulk components of the Au 4 $f_{7/2}$  photoelectron binding energy. The amplitude ratio of the core-level-shift components associated with surface Au atoms that are, and are not, bonded to the thiolate is found to be compatible only with the previously proposed Au-adatom-monothiolate moiety in which the thiolate is bonded atop Au adatoms in hollow sites, and not on an unreconstructed surface, or in Au-adatom-dithiolate species.



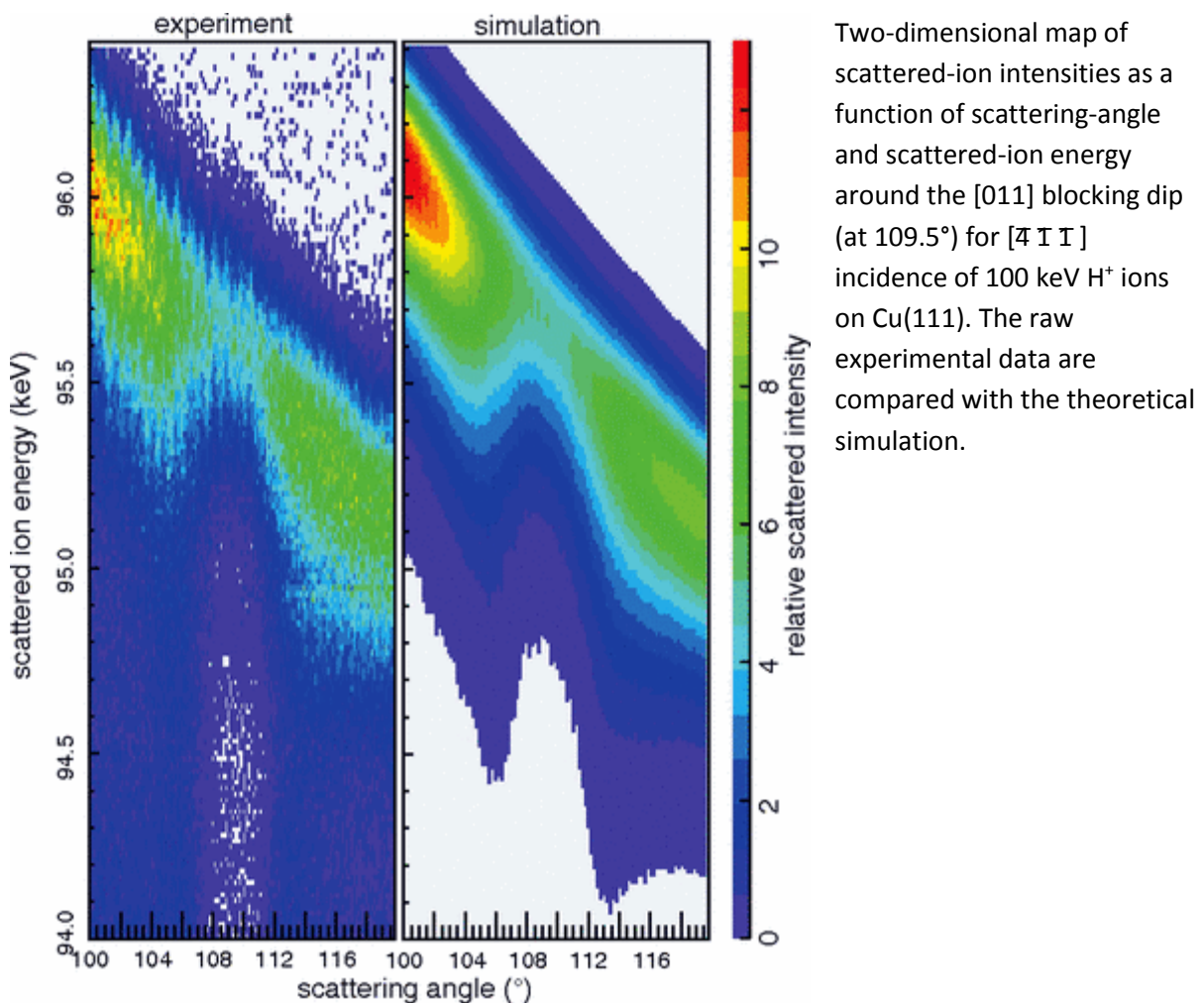
Schematic plan view of the Au(111) surface showing the five different local adsorption structure models for methylthiolate

## Direct Observation and Theory of Trajectory-Dependent Electronic Energy Losses in Medium-Energy Ion Scattering

*Phys. Rev. Lett.* 102, 096103 (2009) [10.1103/PhysRevLett.102.096103](https://doi.org/10.1103/PhysRevLett.102.096103)

A. Hentz, G. S. Parkinson, P. D. Quinn, M. A. Muñoz-Márquez, D. P. Woodruff, P. L. Grande, G. Schiwietz, P. Bailey, and T. C. Q. Noakes

The energy spectrum associated with scattering of 100 keV H<sup>+</sup> ions from the outermost few atomic layers of Cu(111) in different scattering geometries provides direct evidence of trajectory-dependent electronic energy loss. Theoretical simulations, combining standard Monte Carlo calculations of the elastic scattering trajectories with coupled-channel calculations to describe inner-shell ionization and excitation as a function of impact parameter, reproduce the effects well and provide a means for far more complete analysis of medium-energy ion scattering data.

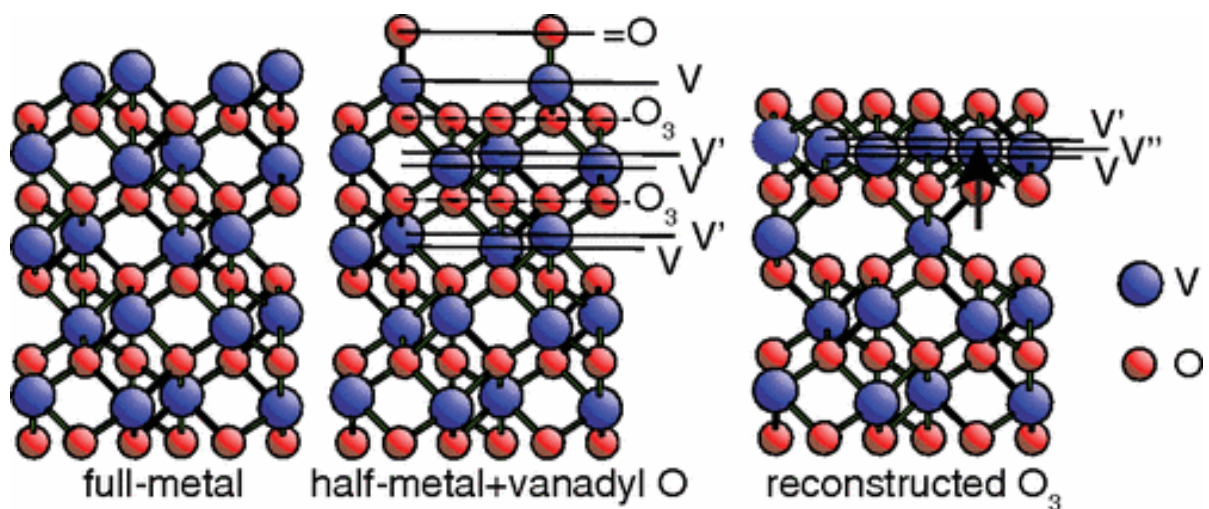


## $V_2O_3(0001)$ Surface Termination: Phase Equilibrium

*Phys. Rev. Lett.* 107, 016105 (2011) [10.1103/PhysRevLett.107.016105](https://doi.org/10.1103/PhysRevLett.107.016105)

A. J. Window, A. Hentz, D. C. Sheppard, G. S. Parkinson, H. Niehus, D. Ahlbehrendt, T. C. Q. Noakes, P. Bailey, and D. P. Woodruff

Complementary but independent medium-energy and low-energy ion scattering studies of the (0001) surfaces of  $V_2O_3$  films grown on Pd(111), Au(111) and  $Cu_3Au(100)$  reveal a reconstructed full  $O_3$ -layer termination creating a  $VO_2$  surface trilayer. This structure is fully consistent with previous calculations based on thermodynamic equilibrium at the surface during growth, but contrasts with previous suggestions that the surface termination comprises a complete monolayer of vanadyl ( $V=O$ ) species.



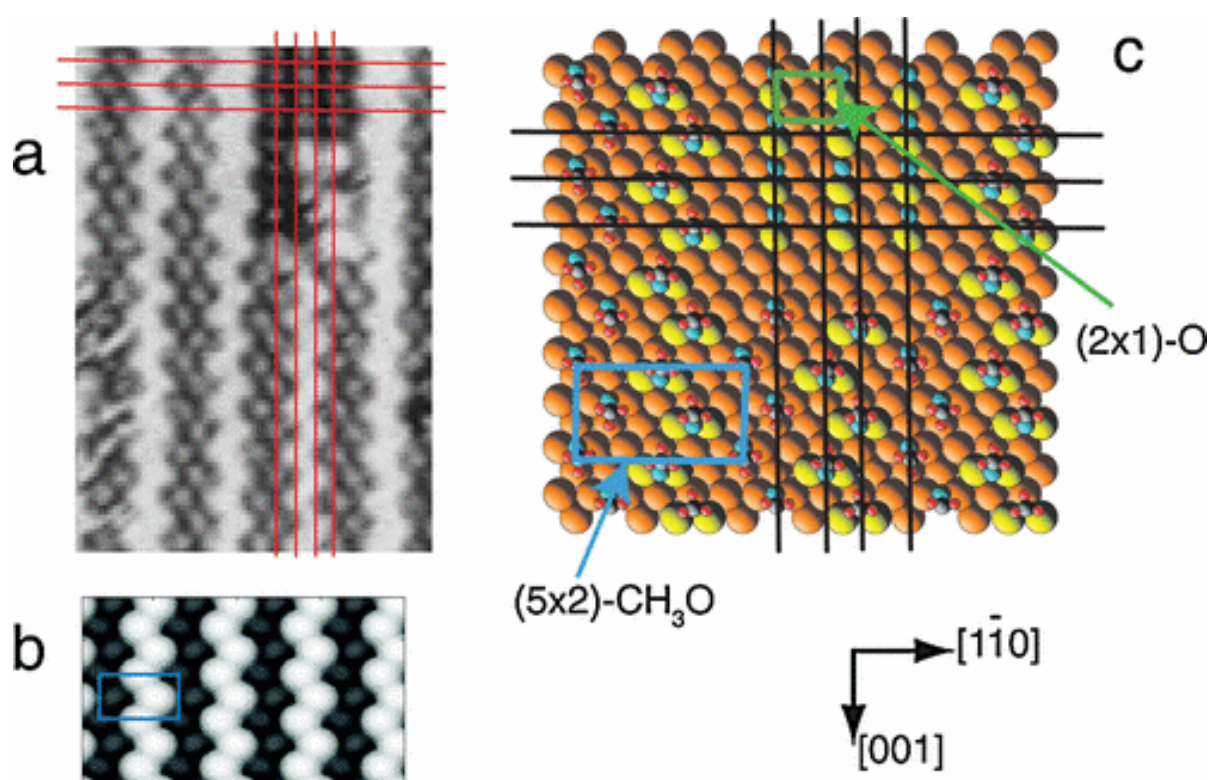
Side views (viewed along  $[21\bar{1}0]$ ) of  $V_2O_3(0001)$ , showing three possible surface terminations. In the reconstructed  $O_3$  termination second-layer  $V'$  atoms move up to become  $V''$  atoms in the outermost metal layer (see arrow).

## Methoxy Species on Cu(110): Understanding the Local Structure of a Key Catalytic Reaction Intermediate

*Phys. Rev. Lett.* 105, 086101 (2010) [10.1103/PhysRevLett.105.086101](https://doi.org/10.1103/PhysRevLett.105.086101)

M. K. Bradley, D. Kreikemeyer Lorenzo, W. Unterberger, D. A. Duncan, T. J. Lerotholi, J. Robinson, and D. P. Woodruff

Partial oxidation of methanol to formaldehyde over Cu(110) is one of the most studied catalytic reactions in surface science, yet the local site of the reaction intermediate, methoxy, remains unknown. Using a combination of experimental scanned-energy mode photoelectron diffraction, and density functional theory, a consistent structural solution is presented in which all methoxy species occupy twofold coordinated “short-bridge” adsorption sites. The results are consistent with previously-published scanning tunnelling microscopy images and theoretical calculations of the reaction mechanism.



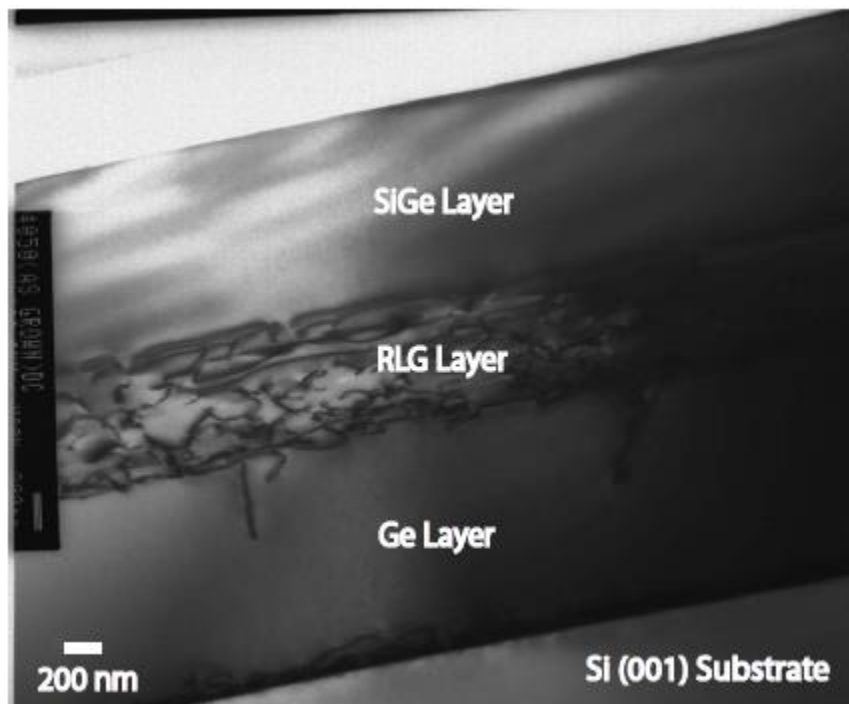
Comparison of (a) an experimental STM image (reprinted with permission from Fig. 2c of Ref. 9; copyright (1994) by the American Physical Society) showing coexistent (2×1)-O and (5×2)-methoxy regions with (c) a model of a similar region of the surface, and (b) a simulated STM image of the (5×2)-methoxy region. The simulated image is based on the structure shown in (c) that is the result of the DFT and PhD calculations

## Reverse graded relaxed buffers for high Ge content SiGe virtual substrates

*Applied Physics Letters* 93, 192103 (2008) [10.1063/1.3023068](https://doi.org/10.1063/1.3023068)

V. A. Shah, A. Dobbie, M. Myronov, D. R. Leadley, D. J. F. Fulgoni, L. J. Nash

An innovative approach is proposed for epitaxial growth of high Ge content, relaxed  $\text{Si}_{1-x}\text{Ge}_x$  buffer layers on a  $\text{Si}(001)$  substrate. The advantages of the technique are demonstrated by growing such structures via chemical vapor deposition and their characterization. Relaxed Ge is first grown on the substrate followed by the reverse grading approach to reach a final buffer composition of 0.78. The optimized buffer structure is only  $2.8\mu\text{m}$  thick and demonstrates a low surface threading dislocation density of  $4\times 10^6\text{cm}^{-2}$ , with a surface roughness of 2.6nm. The buffers demonstrate a relaxation of up to 107%.



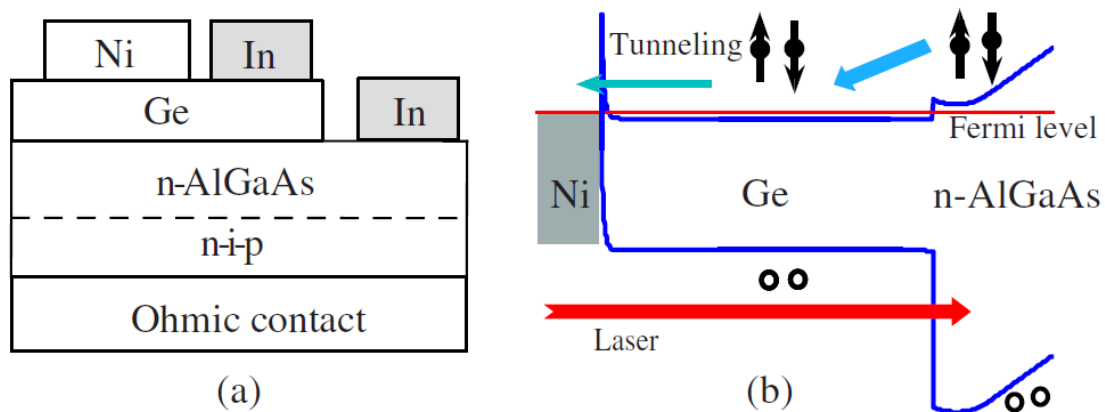
A cross-sectional TEM image in the (220) diffraction condition. Shown are dislocations confined to the RLG region but not penetrating upwards.

## Spin transport in germanium at room temperature

*Applied Physics Letters* 97, 162104 (2010) [10.1063/1.3505337](https://doi.org/10.1063/1.3505337)

C. Shen, T. Trypiniotis, K.Y. Lee, S.N. Holmes, R. Mansell, M. Husain, V. Shah, X.V. Li, H. Kurebayashi, I. Farrer, C.H. de Groot, D.R. Leadley, G. Bell, E.H.C. Parker, T. Whall, D.A. Ritchie, and C.H.W. Barnes

Spin-dependent transport is investigated in a Ni/Ge/AlGaAs junction with an electrodeposited Ni contact. Spin-polarized electrons are excited by optical spin orientation and are subsequently used to measure the spin dependent conductance at the Ni/Ge Schottky interface. We demonstrate electron spin transport and electrical extraction from the Ge layer at room temperature.



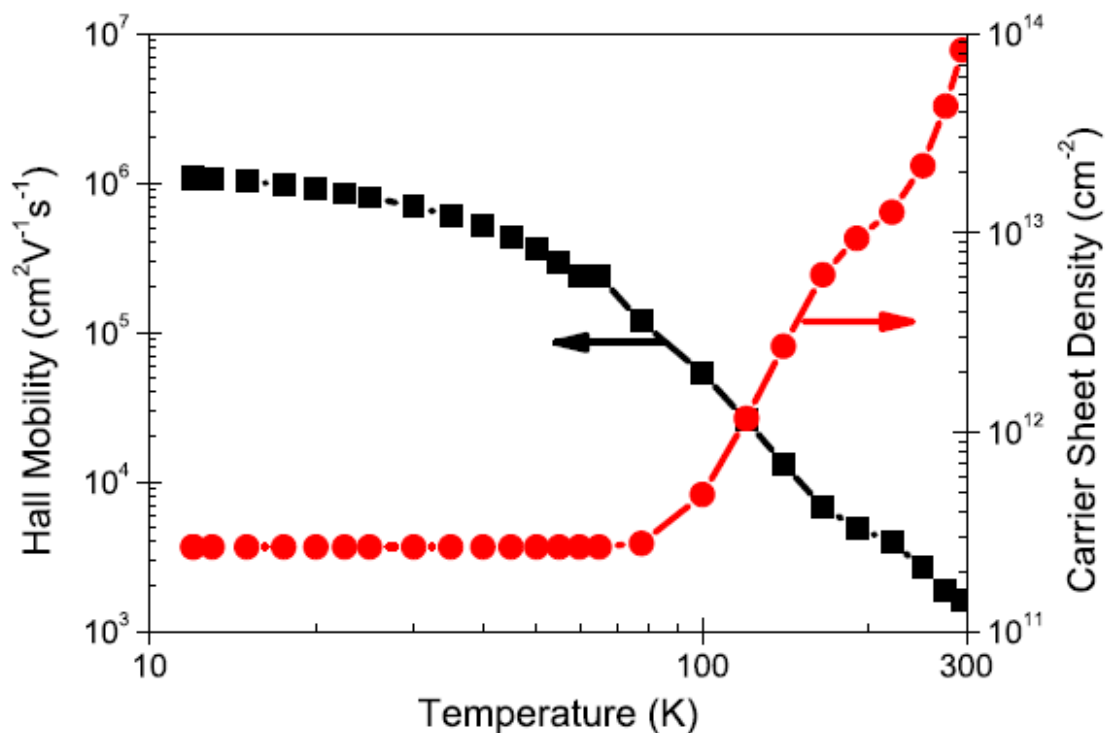
A schematic cross section of the heterostructure used and simulated band diagram of the Ni/Ge/AlGaAs junction.

## Ultra-High Hall Mobility of One Million in a Two-Dimensional Hole Gas in a Strained Germanium Quantum Well

*Applied Physics Letters*, 101, 172108 (2012) [10.1063/1.4763476](https://doi.org/10.1063/1.4763476)

A. Dobbie, M. Myronov, R.J.H. Morris, A.H.A. Hassan, M.J. Prest, V.A. Shah, E.H.C. Parker, T.E. Whall, and D.R. Leadley

In this paper, we report a Hall mobility of one million in a germanium two-dimensional hole gas. The extremely high hole mobility of  $1.1 \times 10^6 \text{ cm}^2 \text{ V}^{-1} \text{ s}^{-1}$  at a carrier sheet density of  $3 \times 10^{11} \text{ cm}^{-2}$  was observed at 12 K. This mobility is nearly an order of magnitude higher than any previously reported. From the structural analysis of the material and mobility modeling based on the relaxation time approximation, we attribute this result to the combination of a high purity Ge channel and a very low background impurity level that is achieved from the reduced-pressure chemical vapor deposition growth method.

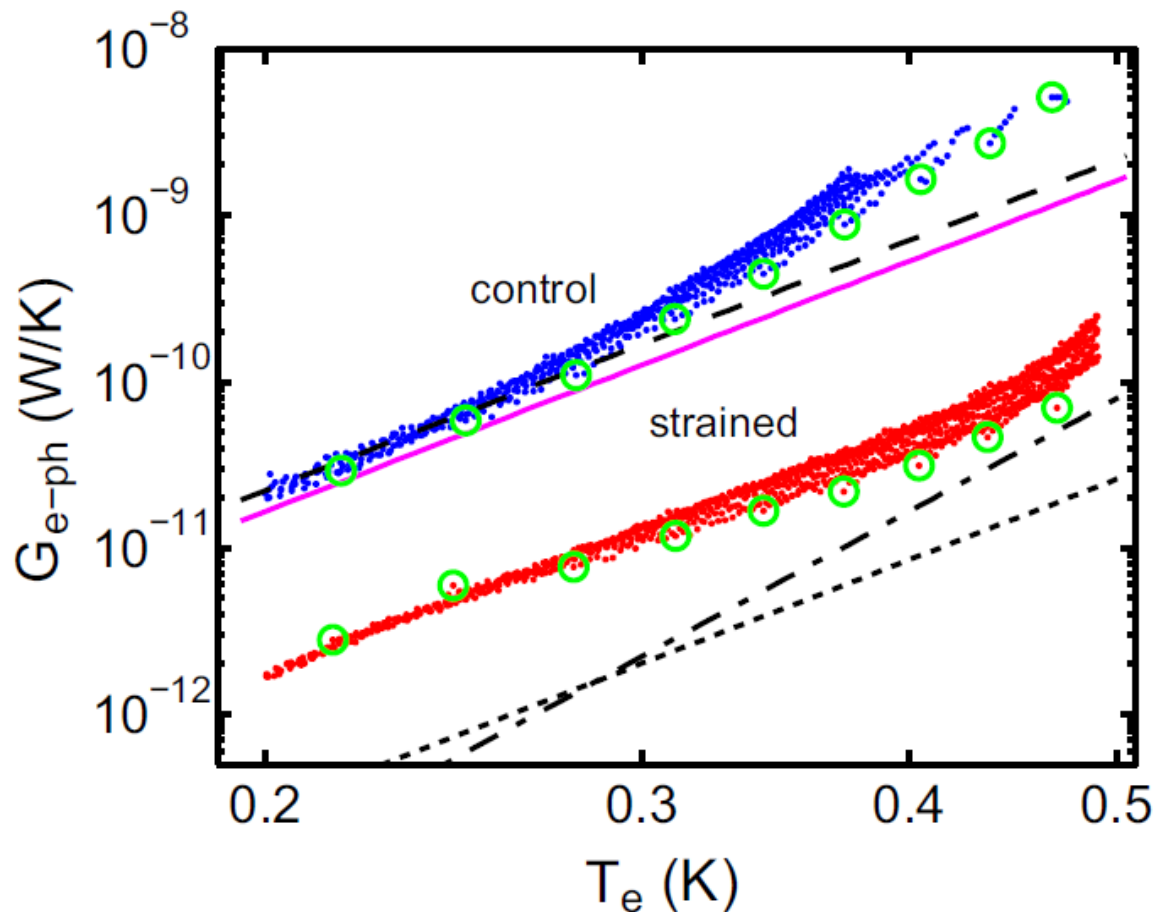


## Strain dependence of electron-phonon energy loss rate in many-valley semiconductors

*Applied Physics Letters* 98, 182103 (2011) [10.1063/1.3579524](https://doi.org/10.1063/1.3579524)

J. T. Muhonen, M. J. Prest, M. Prunnila, D. Gunnarsson, V. A. Shah, A. Dobbie, M. Myronov, R. J. H. Morris, T. E. Whall, E. H. C. Parker and D. R. Leadley

We demonstrate significant modification of the electron-phonon energy loss rate in a many-valley semiconductor system due to lattice mismatch induced strain. We show that the thermal conductance from the electron system to the phonon bath in strained n<sup>+</sup>Si, at phonon temperatures between 200 and 480 mK, is more than an order of magnitude lower than that for a similar unstrained sample.



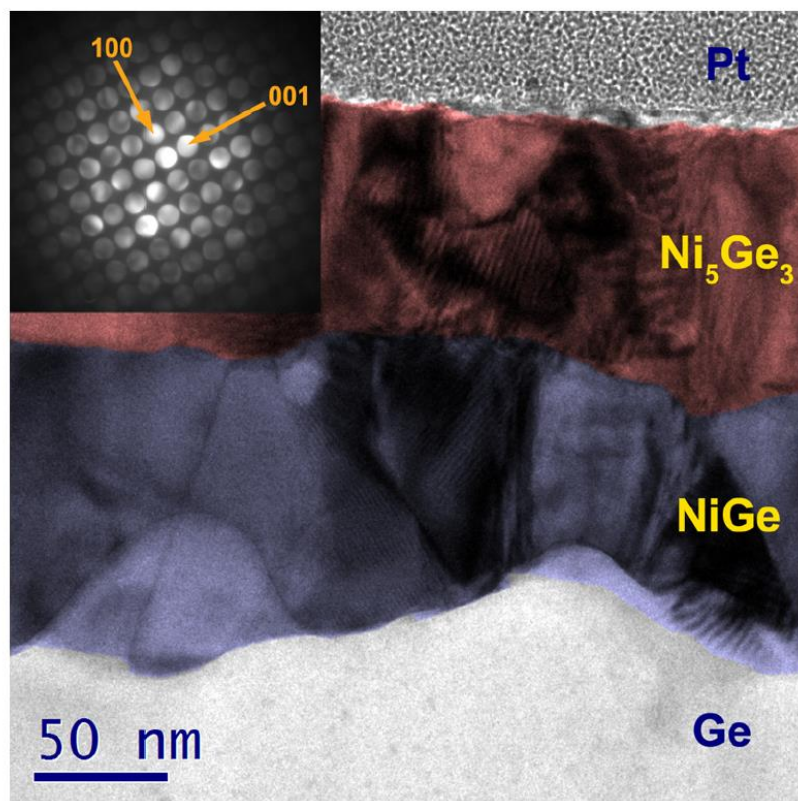
The  $e$ - $ph$  thermal conductance  $G_{e-ph}$ . Circles showing the lowest heating power data points, *ie*, points where  $T_e$  is very close to  $T_{ph}$ .

## Ohmic contacts to n-type germanium with low specific contact resistivity

*Applied Physics Letters* 100 (2) , art. no. 022113 (2012) [10.1063/1.3676667](https://doi.org/10.1063/1.3676667)

Gallacher, K., Velha, P., Paul, D.J., MaLaren, I., Myronov, M., Leadley, D.R.

A low temperature nickel process has been developed that produces Ohmic contacts to n-type germanium with specific contact resistivities down to  $(2.3 \pm 1.8) \times 10^{-7} \Omega\text{-cm}^2$  for anneal temperatures of 340 °C. The low contact resistivity is attributed to the low resistivity NiGe phase which was identified using electron diffraction in a transmission electron microscope. Electrical results indicate that the linear Ohmic behaviour of the contact is attributed to quantum mechanical tunnelling through the Schottky barrier formed between the NiGe alloy and the heavily doped n-Ge.



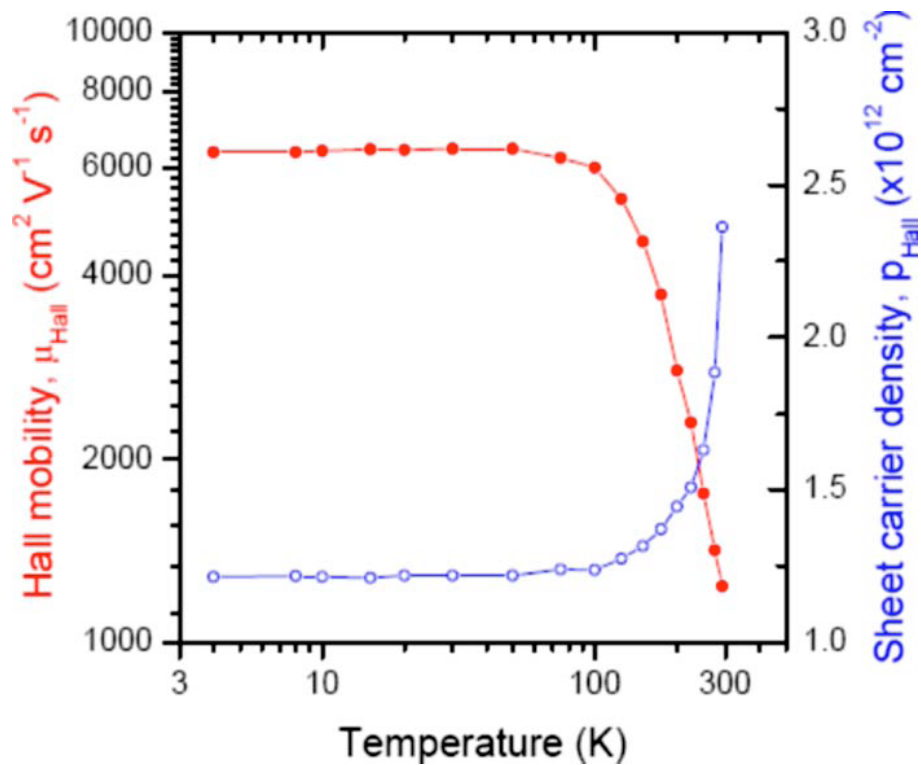
A TEM bright field image of a Ni-Ge contact annealed at 340 °C showing the 2 layers of the contact on the Ge substrate. False colour shading was used to highlight the 2 layers of the alloy contact. The amorphous Pt on top protects the sample prior to preparation by a focused ion beam lift-out process. The insert is a convergent beam diffraction pattern from 1 grain of the lower layer consistent with the [010] zone axis of NiGe in the orthorhombic (Pnma) structure.

## High mobility holes in a strained Ge quantum well grown on a thin and relaxed Si<sub>0.4</sub>Ge<sub>0.6</sub>/LT-Si<sub>0.4</sub>Ge<sub>0.6</sub>/Si(001) virtual substrate

*Applied Physics Letters* 94, 092108 (2009) : [10.1063/1.3090034](https://doi.org/10.1063/1.3090034)

M. Myronov, D.R. Leadley and Y. Shiraki

Epitaxial growth of a compressively strained Ge quantum well (QW) on an ultrathin, 345 nm thick, Si<sub>0.4</sub>Ge<sub>0.6</sub>/LT-Si<sub>0.4</sub>Ge<sub>0.6</sub>/Si(001) virtual substrate (VS) has been demonstrated. The VS, grown with a low temperature Si<sub>0.4</sub>Ge<sub>0.6</sub> seed layer on a Si(001) substrate, is found to be fully relaxed and the Ge QW is fully strained. The temperature dependence of Hall mobility and carrier density clearly indicates a two-dimensional hole gas in the Ge QW. At room temperature, which is more relevant for electronic devices applications, the samples show a very high Hall mobility of 1235 cm<sup>2</sup> V<sup>-1</sup> s<sup>-1</sup> at a carrier density of 2.36×10<sup>12</sup> cm<sup>-2</sup>.

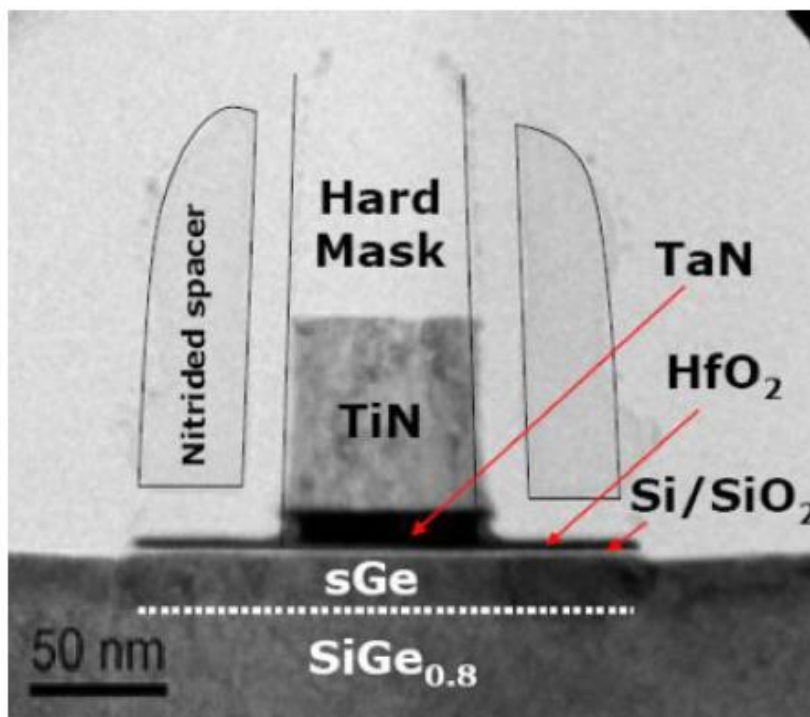


## High Hole Mobility in 65 nm Strained Ge p-Channel Field Effect Transistors with HfO<sub>2</sub> Gate Dielectric

*Japanese Journal of Applied Physics* 50, 04DC17 (2011) [10.1143/JJAP.50.04DC17](https://doi.org/10.1143/JJAP.50.04DC17)

J. Mitard, B. De Jaeger, G. Eneman, A. Dobbie, M. Myronov, M. Kobayashi, J. Geypen, H. Bender, B. Vincent, R. Krom, J. Franco, G. Winderickx, E. Vrancken, W. Vanherle, W.-E. Wang, J. Tseng, R. Loo, K. De Meyer, M. Caymax, L. Pantisano, D. R. Leadley, M. Meuris, P. P. Absil, S. Biesemans and T. Hoffmann

Biaxially-strained Ge p-channel field effect transistors (pFETs) have been fabricated for the first time in a 65 nm technology. The devices are designed to have a reduced effective oxide thickness (EOT) while maintaining minimized short channel effects. Low and high field transport has been studied by in-depth electrical characterization, showing a high hole-mobility that is enhanced by up to 70% in the strained devices. The important role of pocket implants in degrading the drive current is highlighted. Using a judicious implantation scheme, we demonstrate a significant gain in on-current (up to 35%) for nanoscaled strained Ge pFETs. Simultaneous optimization of the gate metal and dielectric, together with the corresponding uniaxial stress engineering, is identified as a promising path for further performance enhancement.



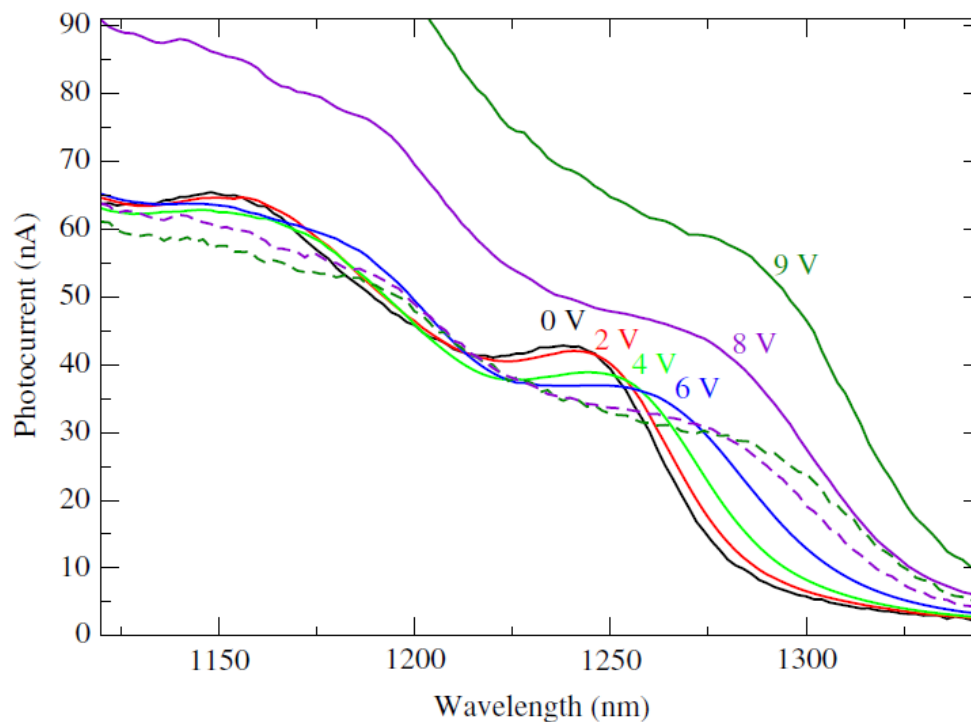
TEM image of a 65 nm strained Ge pFETs using a 200mm Si compatible process flow

## Modulation of the absorption coefficient at 1.3 $\mu\text{m}$ in Ge/SiGe multiple quantum well heterostructures on silicon

*Optics Letters*, 36, 4158-4160 (2011) [10.1364/OL.36.004158](https://doi.org/10.1364/OL.36.004158)

L. Lever, Y. Hu, M. Myronov, X. Liu, N. Owens, F.Y. Gardes, I.P. Marko, S.J. Sweeney, Z. Ikoni, D.R. Leadley, G.T. Reed, and R.W. Kelsall

We report modulation of the absorption coefficient at 1.3  $\mu\text{m}$  in Ge/SiGe multiple quantum well heterostructures on silicon via the quantum-confined Stark effect. Strain engineering was exploited to increase the direct optical bandgap in the Ge quantum wells. We grew 9 nm-thick Ge quantum wells on a relaxed  $\text{Si}_{0.22}\text{Ge}_{0.78}$  buffer and a contrast in the absorption coefficient of a factor of greater than 3.2 was achieved in the spectral range 1290–1315 nm .



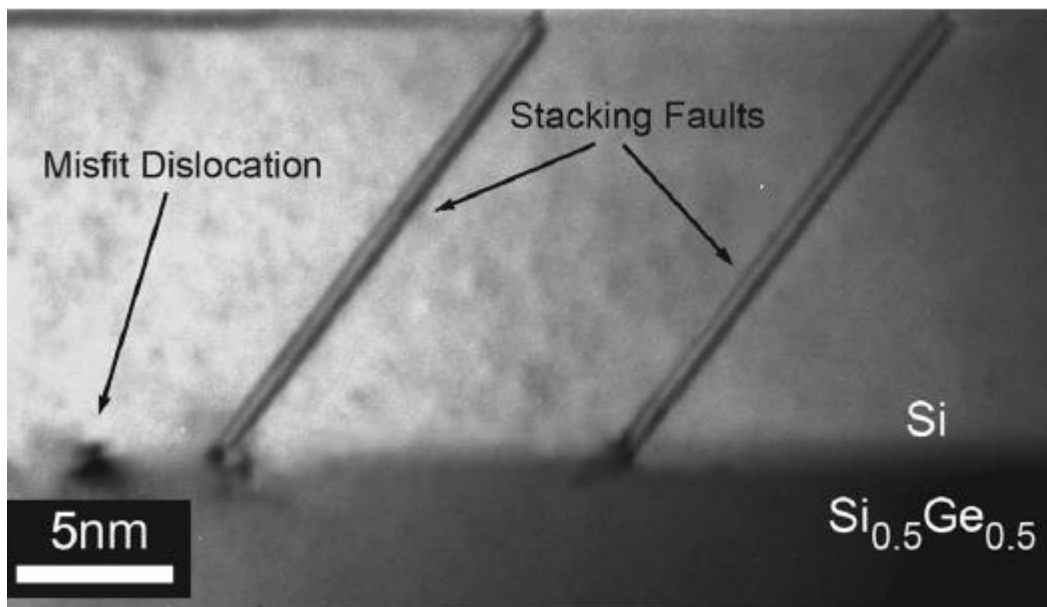
Measured photocurrent data for the Ge/Si<sub>0.4</sub>Ge<sub>0.6</sub> MQW stack at a range of biases applied across the p-i-n diode. The light-hole exciton can be seen at approximately 1150nm in the zero-field curve. This large light-hole/heavy-hole splitting is evidence of the large strain due to the high Si fraction of the virtual substrate. The curves at 8 V and 9 V appear larger than the lower-bias curves, which is attributed to avalanche gain within the device. The dashed curves show these data rescaled according to the simulated ratios of the absorption at the electron/heavy-hole exciton peak.

## Relaxation of strained silicon on $\text{Si}_{0.5}\text{Ge}_{0.5}$ virtual substrates

*Applied Physics Letters* 93 072108 (2008). [10.1063/1.2975188](https://doi.org/10.1063/1.2975188)

J. Parsons, R. J. H. Morris, D. R. Leadley, E. H. C. Parker, D. J. F. Fulgoni and L. J. Nash

Strain relaxation has been studied in tensile strained silicon layers grown on  $\text{Si}_{0.5}\text{Ge}_{0.5}$  virtual substrates, for layers many times the critical thickness, using high resolution x-ray diffraction. Layers up to 30 nm thick were found to relax less than 2% by the glide of pre-existing  $60^\circ$  dislocations. Relaxation is limited because many of these dislocations dissociate into extended stacking faults that impede the dislocation glide. For thicker layers, nucleated microtwins were observed, which significantly increased relaxation to 14%. All these tensile strained layers are found to be much more stable than layers with comparable compressive strain.



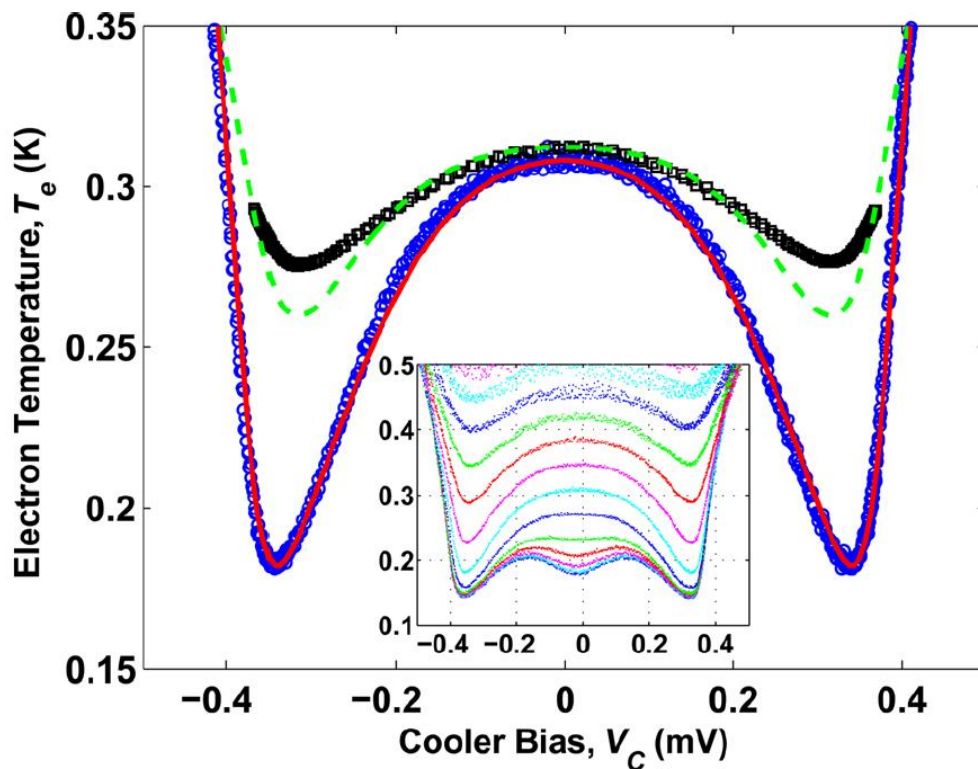
XTEM image of a 15 nm strained silicon layer showing two stacking faults and a misfit dislocation.

## Strain Enhanced Electron Cooling in a Degenerately Doped Semiconductor

*Applied Physics Letters*, 99, 251908 (2011) [10.1063/1.3670330](https://doi.org/10.1063/1.3670330)

M. J. Prest, J.T. Muhonen, M. Prunnila, D. Gunnarsson, V.A. Shah, J.S. Richardson-Bullock, A. Dobbie, M. Myronov, R.J.H. Morris, T.E. Whall, E.H.C. Parker and D.R. Leadley

Enhanced electron cooling is demonstrated in a strained-silicon/superconductor tunnel junction refrigerator of volume  $40 \mu\text{m}^3$ . The electron temperature is reduced from 300 mK to 174 mK, with the enhancement over an unstrained silicon control (300 mK–258 mK) being attributed to the smaller electron-phonon coupling in the strained case. Modeling and the resulting predictions of silicon-based cooler performance are presented. Further reductions in the minimum temperature are expected if the junction sub-gap leakage and tunnel resistance can be reduced. However, if only tunnel resistance is reduced, Joule heating is predicted to dominate.



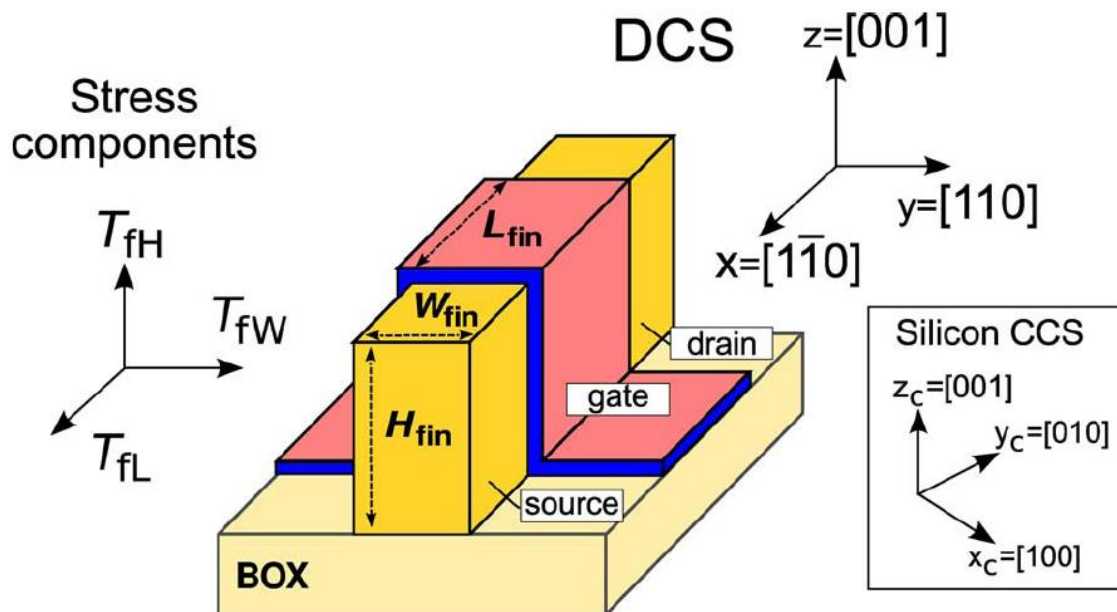
Electron temperature  $T_e$  vs. cooler bias  $V_c$ . The green broken curve is a fit to the experimental data (black squares) from the unstrained control. Blue circles are data for the strained sample and the red curve is a fit to the model. The inset shows  $T_e$  versus  $V_c$  at different bath temperatures  $T_b$  for the strained sample. Note that  $T_b = T_e$  when  $V_c = 0$ .

## Investigation of strain engineering in FinFETs comprising experimental analysis and numerical simulations

*IEEE Transactions on Electron Devices* 58, 1583 (2011) [10.1109/TED.2011.2119320](https://doi.org/10.1109/TED.2011.2119320)

F. Conzatti, N. Serra, D. Esseni, M. De Michielis, P. Palestri, L. Selmi, S.M. Thomas, T.E. Whall, D.R. Leadley, E.H.C. Parker, L. Witters, M.J. Hÿtch, E. Snoeck, T.J. Wang, W.C. Lee, G. Doornbos, G. Vellianitis, M.J.H. van Dal, and R.J.P. Lander

This study combines direct measurements of strain, electrical mobility measurements, and a rigorous modeling approach to provide insights about strain-induced mobility enhancement in FinFETs and guidelines for device optimization. Good agreement between simulated and measured mobility is obtained using strain components measured directly at device level by a novel holographic technique. A large vertical compressive strain is observed in metal gate FinFETs, and the simulations show that this helps recover the electron mobility disadvantage of the (110) FinFET lateral interfaces with respect to (100) interfaces, with no degradation of the hole mobility. The model is then used to systematically explore the impact of stress components in the fin width, height, and length directions on the mobility of both n- and p-type FinFETs and to identify optimal stress configurations. Finally, self-consistent Monte Carlo simulations are used to investigate how the most favorable stress configurations can improve the on current of nanoscale MOSFETs.



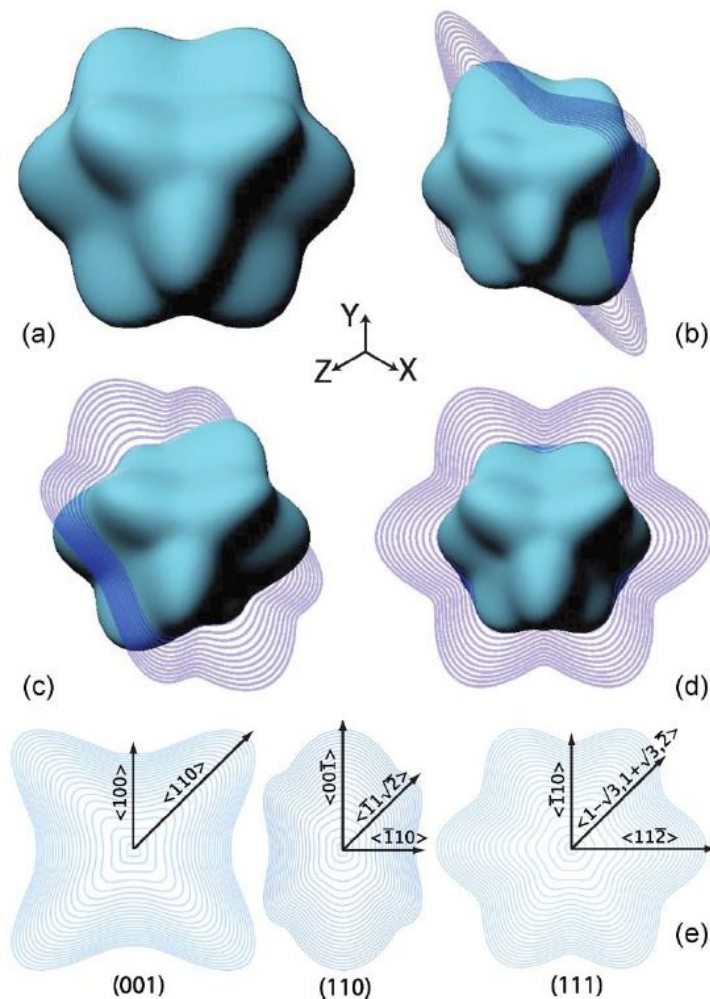
Schematic of a (110)/(110) FinFET obtained with a standard Manhattan layout in a (100) wafer. The figure illustrates the stress components in the fin height  $T_{fH}$ , width  $T_{fW}$ , and length  $T_{fL}$  direction in the device coordinate system.

## Hole mobility in germanium as a function of substrate and channel orientation, strain, doping, and temperature

*IEEE Transactions on Electron Devices* 59, 1878 (2012) [10.1109/TED.2012.2194498](https://doi.org/10.1109/TED.2012.2194498)

Riddet, C., Watling, J.R., Chan, K.-H., Parker, E.H.C., Whall, T.E., Leadley, D.R., Asenov, A.

We present a comprehensive study of hole transport in germanium layers on “virtual” substrates using a full band Monte Carlo simulation approach, considering alternate “virtual” substrate and channel orientations and including the impact of the corresponding biaxial strain, doping, and lattice temperature. The superior mobility in strained germanium channels with orientation on a (110) “virtual” substrate is confirmed, and the factors leading to this enhancement are evaluated. The significant decrease in strain-and-orientation-induced mobility enhancement due to impurity scattering in doped material and at increasing lattice temperature is also demonstrated. Both factors determine how efficiently the mobility enhancement translates into transistor performance enhancement. Additionally, we shine light on the question of which factor has stronger impact in mediating the increase in mobility due to strain—the breaking of degeneracy for the heavy- and light-hole bands at the point or the reduction in the density of states.



Energy isosurfaces for the HH band at 1 eV calculated using six-band  $k \cdot p$ , all viewed from the [111] direction. Shown here are the (a) relaxed case and strained cases ( $x = 40\%$ ) on the three substrates considered here, i.e., (b) (001), (c) (110), and (d) (111), with energy contours shown out to 2 eV.

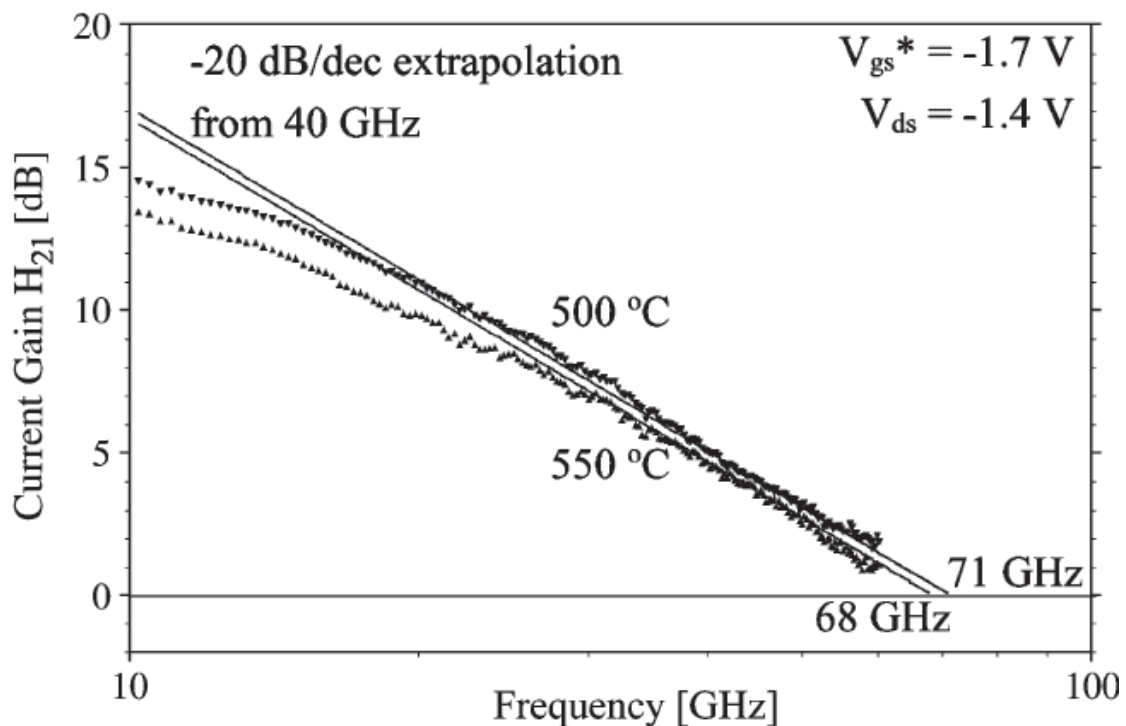
The channel orientations for each surface are given in (e).

## High-frequency performance of Schottky Source/Drain Silicon pMOS devices

*IEEE Electronic Device Letters* 29, 396 (2008) [10.1109/LED.2008.918250](https://doi.org/10.1109/LED.2008.918250)

J.-P. Raskin, D. J. Pearman, G. Pailloncy, J. M. Larson, J. Snyder, D.R. Leadley and T. E. Whall

A radio-frequency performance of 85-nm gate-length p-type Schottky barrier (SB) with PtSi source/drain materials is investigated. The impact of silicidation annealing temperature on the high-frequency behavior of SB MOSFETs is analyzed using an extrinsic small-signal equivalent circuit. It is demonstrated that the current drive and the gate transconductance strongly depend on the silicidation anneal temperature, whereas the unity-gain cutoff frequency of the measured devices remains nearly unchanged.



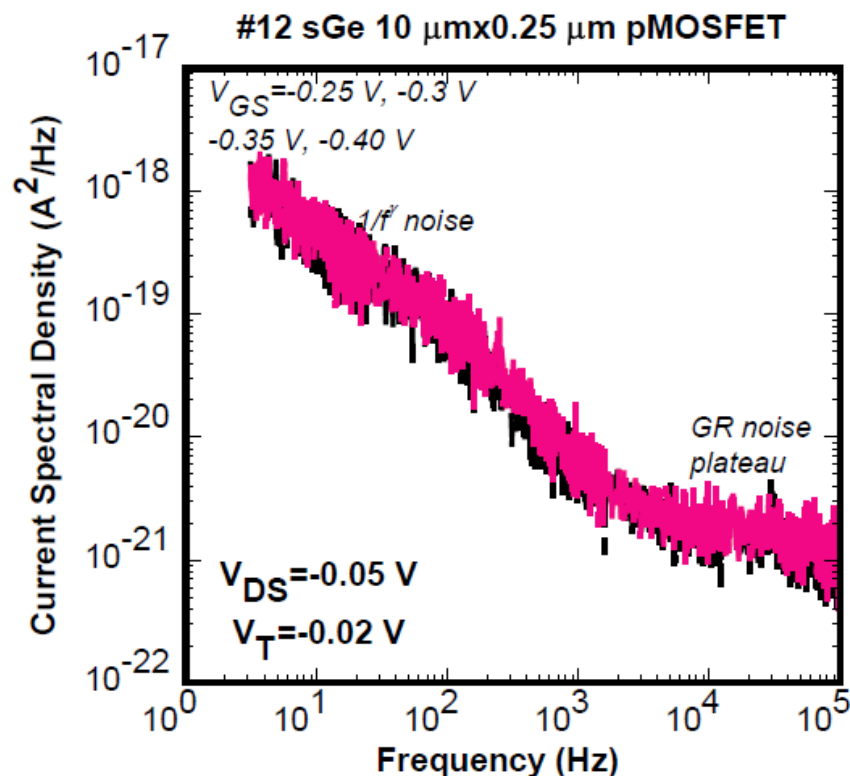
Current gain versus frequency for wafers annealed at 500°C and 550°C.

## Low-frequency Noise Characterisation of Strained Germanium pMOSFETs

*IEEE Transactions on Electronic Devices* 58, 3132 (2011) [10.1109/TED.2011.2160679](https://doi.org/10.1109/TED.2011.2160679)

E. Simoen, J. Mitard, B. De Jaeger, G. Eneman, A. Dobbie, M. Myronov, T.E. Whall, D.R. Leadley, M. Meuris, T. Hoffmann and C. Claeys

The low-frequency (LF) noise in strained Ge epitaxial layers, grown on reverse-graded relaxed SiGe buffer layers, has been evaluated for different front-end processing conditions. It has been shown that the  $1/f$  noise in strong inversion is governed by trapping in the gate oxide (number fluctuations) and not affected by the presence of compressive strain in the channel. However, some impact has been found from the type of halo implantation used, whereby the lowest noise spectral density and highest hole mobility is obtained by replacing the standard As halo by a P implantation. At the same time, the omission of the junction anneal results in poor device characteristics, which can be understood by considering the presence of a high density of non-annealed implantation damage in the channel and the gate stack near source and drain.



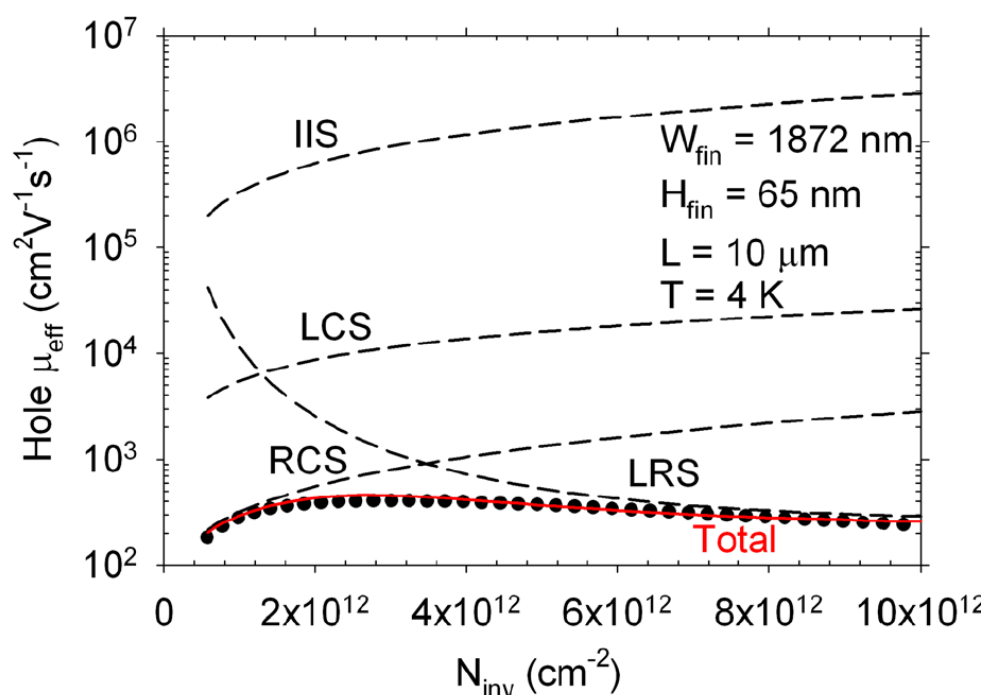
Low-frequency noise spectra for a 10  $\mu\text{m} \times 0.25 \mu\text{m}$  sGe pMOSFET, fabricated without junction anneal, corresponding with different gate voltages.

## On the role of Coulomb scattering in hafnium-silicate gated silicon n and p-channel metal-oxide-semiconductor-field-effect-transistors

*Journal of Applied Physics* 110, 124503 (2011) [10.1063/1.3669490](https://doi.org/10.1063/1.3669490)

S.M.Thomas, M.J.Prest, T.E.Whall, D.R.Leadley, E.H.C.Parker, F. Conzattib, N. Serra, D. Esseni, M. De Michielis, A. Paussa, P. Palestri, L. Selmi, L. Donetti, F. Gámiz, R.J.P. Lander, G. Vellianitis, P.-E. Hellström, G. Malm, M. Östling

In this work, the impact of the local and remote Coulomb scattering mechanisms on electron and hole mobility are investigated. The effective mobilities in quasi-planar finFETs with TiN/Hf<sub>0.4</sub>Si<sub>0.6</sub>O/SiO<sub>2</sub> gate stacks have been measured at 300 K and 4 K. At 300 K, electron mobility is degraded below that of bulk MOSFETs in the literature, whereas hole mobility is comparable. The 4 K electron and hole mobilities have been modeled in terms of ionized impurity, local Coulomb, remote Coulomb and local roughness scattering. An existing model for remote Coulomb scattering from a polycrystalline silicon gate has been adapted to model remote Coulomb scattering from a high- $\kappa$ /SiO<sub>2</sub> gate stack. Subsequently, remote charge densities of  $8 \times 10^{12} \text{ cm}^{-2}$  at the Hf<sub>0.4</sub>Si<sub>0.6</sub>O/SiO<sub>2</sub> interface were extracted and shown to be the dominant Coulomb scattering mechanism for both electron and hole mobilities at 4 K. Finally, a Monte Carlo simulation showed remote Coulomb scattering was responsible for the degraded 300 K electron mobility.



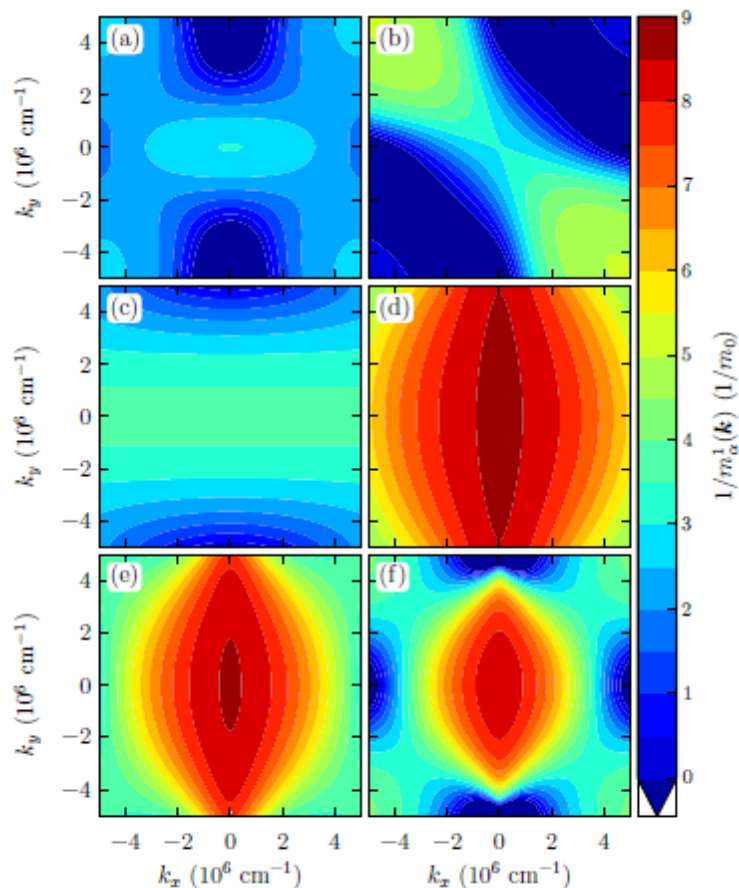
4 K effective hole mobility of the high-k device (circles), the individual modeled ionised impurity scattering IIS, local Coulomb scattering from interface charge LCS, remote Coulomb scattering RCS, and local roughness scattering LRS limited mobilities (dashed lines) and the total modeled mobility (continuous line).

## Hole effective mass in silicon inversion layers with different substrate orientations and channel directions.

*Journal of Applied Physics* 107, 064304 (2010) [10.1063/1.3639281](https://doi.org/10.1063/1.3639281)

L. Donetti, F. Gámiz, S.M. Thomas, T.E. Whall, D.R. Leadley, P.E. Hellström, G. Malm, M. Östling

We explore the possibility to define an effective mass parameter to describe hole transport in inversion layers in bulk MOSFETs and silicon-on-insulator devices. To do so, we employ an accurate and computationally efficient self-consistent simulator based on the six-band k-p model. The valence band structure is computed for different substrate orientations and silicon layer thicknesses and is then characterized through the calculation of different effective masses taking account of the channel direction. The effective masses for quantization and density of states are extracted from the computed energy levels and subband populations, respectively. For the transport mass, a weighted averaging procedure is introduced and justified by comparing the results with hole mobility from experiments and simulations.



Transport mass  $m_{\alpha}^1$  as a function of  $k$  for the following SOI devices:  $t_{\text{Si}} = 2$  nm with (100) surface orientation and  $k_{\alpha}$  parallel to  
 (a)  $\langle 100 \rangle$ ,  
 (b)  $(100)/\langle 110 \rangle$ ,  
 (c)  $(110)/\langle 100 \rangle$ ,  
 (d)  $(110)/\langle 110 \rangle$ ;  
 (e) and (f) are the same as (d) but with  $t_{\text{Si}} = 3$  nm and 5 nm, respectively.

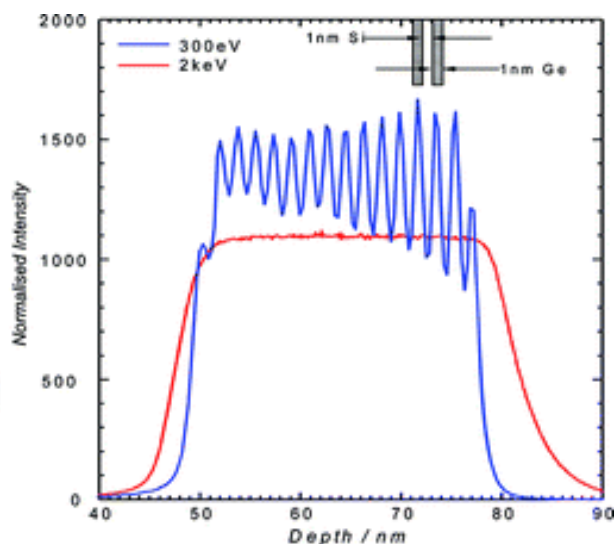
For (100) orientation  $k_x$  and  $k_y$  are directed along  $[010]$  and  $[001]$  while for (110) orientation they are directed along  $[001]$  and  $[1-10]$

## Overcoming low Ge ionization and erosion rate variation for quantitative ultralow energy secondary ion mass spectrometry depth profiles of $\text{Si}_{1-x}\text{Ge}_x/\text{Ge}$ quantum well structures

*Analytical Chemistry* 84 (5), pp. 2292-2298 (2012) : [10.1021/ac202929x](https://doi.org/10.1021/ac202929x)

Morris, R.J.H., Dowsett, M.G., Beanland, R., Dobbie, A., Myronov, M., Leadley, D.R.

We specify the  $\text{O}_2^+$  probe conditions and subsequent data analysis required to obtain high depth resolution secondary ion mass spectrometry profiles from multiple  $\text{Ge}/\text{Si}_{1-x}\text{Ge}_x$  quantum well structures ( $0.6 \leq x \leq 1$ ). Using an  $\text{O}_2^+$  beam at normal incidence and with energies  $>500$  eV, we show that the measured Ge signal is not monotonic with concentration, the net result being an unrepresentative and unquantifiable depth profile. This behavior is attributed to a reduced Ge ionization rate as  $x$  approaches 1. At lower beam energies the signal behaves monotonically with Ge fraction, indicating that the Ge atoms are now ionizing more readily for the whole range of  $x$ , enabling quantitative profiles to be obtained. To establish the depth scale a point-by-point approach based on previously determined erosion rates as a function of  $x$  is shown to produce quantum well thicknesses in excellent agreement with those obtained using transmission electron microscopy. The findings presented here demonstrate that to obtain reliable quantitative depth profiles from Ge containing samples requires  $\text{O}_2^+$  ions below 500 eV and correct account to be taken of the erosion rate variation that exists between layers of different matrix composition.

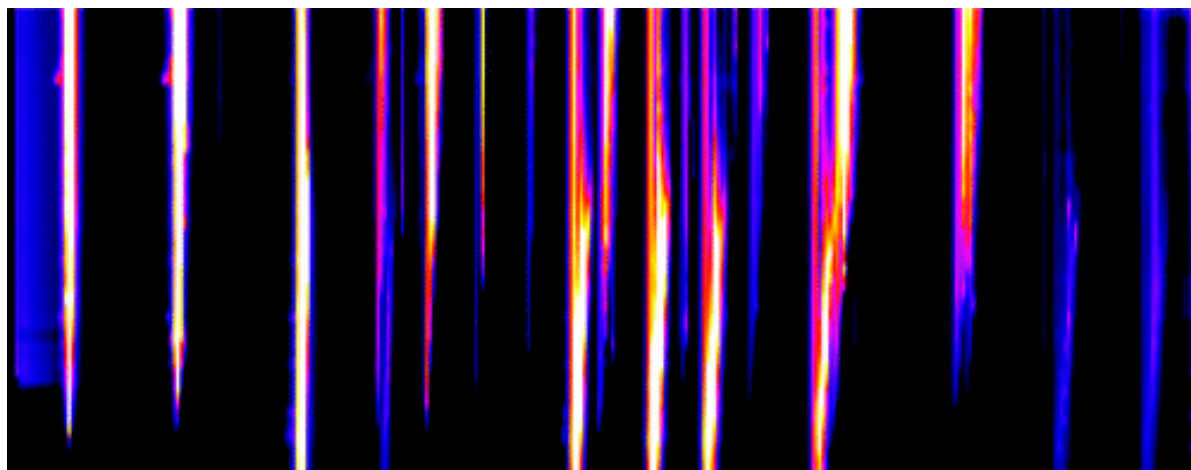


## The use of synchrotron X-rays to observe copper corrosion in real time

*Analytical Chemistry* 84 (11) , pp. 4866-4872 (2012) : [10.1021/ac300457e](https://doi.org/10.1021/ac300457e)

Dowsett, M., Adriaens, A., Martin, C., Bouchenoire, L.

We have developed and tested two complementary methods for making time-lapse synchrotron X-ray diffraction (XRD) measurements of the growth of synthetic corrosion layers using a protocol for producing copper(I) chloride (nantokite), on copper as a test. In the first method, a copper coupon was spin-coated with saturated copper(II) chloride solution in air while the surface was characterized in real time using XRD with a fast one-dimensional (1-D) detector. In the second, a droplet of the same reagent was suspended from an X-ray-transparent window in a hermetically sealed cell and the coupon was brought into contact with this while XRD diffractograms were acquired with a charge-coupled device (CCD) camera. The protocol is completed by a deionized water rinse, which was also studied. The XRD shows nantokite precipitation in solution as well as growth on the surface, but the end products were variable proportions of nantokite, cuprite ( $\text{Cu}_2\text{O}$ ), and paratacamite ( $\text{Cu}_2(\text{OH})_3\text{Cl}$ ). The latter two were observed forming in a reaction between the nantokite and the rinsing water. Comparisons between samples analyzed in the synchrotron and at lower power densities show that the effects of any radiolysis or slight heating of the sample are insignificant in this case. It would be simple to extend these methods to other corrosion or surface reaction systems.

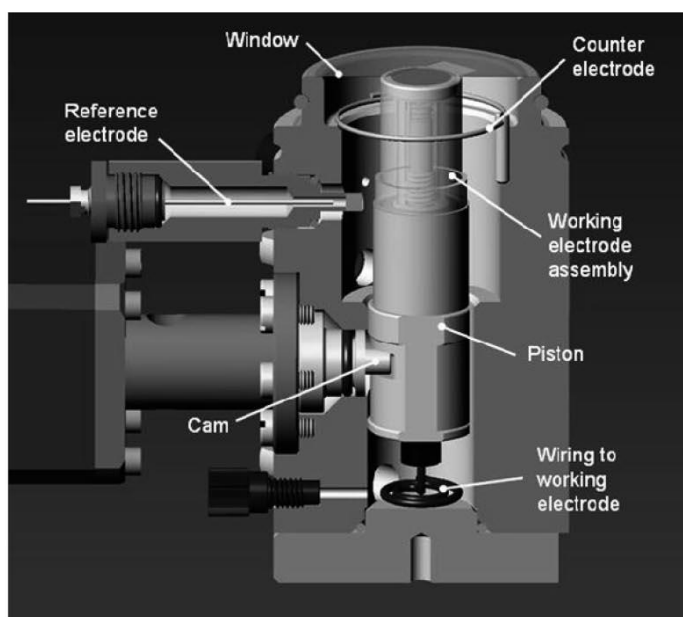


## Optically Detected X-ray Absorption Spectroscopy Measurements as a Means of Monitoring Corrosion Layers on Copper

*Analytical Chemistry* 80 (22) , pp. 8717-8724 (2008) [10.1021/ac800895n](https://doi.org/10.1021/ac800895n)

Dowsett, MG; Adriaens, A; Jones, GKC; Poolton, N; Fiddy, S; Nikitenko, S

XANES and EXAFS information is conventionally measured in transmission through the energy-dependent absorption of X-rays or by observing X-ray fluorescence, but secondary fluorescence processes, such as the emission of electrons and optical photons (e.g., 200-1000 nm), can also be used as a carrier of the XAS signatures, providing complementary information such as improved surface specificity. Where the near-visible photons have a shorter range in a material, the data will be more surface specific. Moreover, optical radiation may escape more readily than X-rays through liquid in an environmental cell. Here, we describe a first test of optically detected X-ray absorption spectroscopy (ODXAS) for monitoring electrochemical treatments on copper-based alloys, for example, heritage metals. Artificially made corrosion products deposited on a copper substrate were analyzed in air and in a 1% (w/v) sodium sesquicarbonate solution to simulate typical conservation methods for copper-based objects recovered from marine environments. The measurements were made on stations 7.1 and 9.2 MF (SRS Daresbury, UK) using the mobile luminescence end station (MoLES), supplemented by XAS measurements taken on DUBBLE (BM26 A) at the ESRF. The ODXAS spectra usually contain fine structure similar to that of XAS spectra measured in X-ray fluorescence. Importantly, for the compounds examined, the ODXAS is significantly more surface specific, and > 98% characteristic of thin surface layers of 0.5-1.5- $\mu$ m thickness in cases where X-ray measurements are dominated by the substrate. However, EXAFS and XANES from broadband optical measurements are superimposed on a high background due to other optical emission modes. This produces statistical fluctuations up to double what would be expected from normal counting statistics because the data retain the absolute statistical fluctuation in the original raw count, while losing up to 70% of their magnitude when background is removed. The problem may be solved in future through optical filtering to isolate the information-containing band, combined with the use of higher input X-ray fluxes available on third-generation light sources.

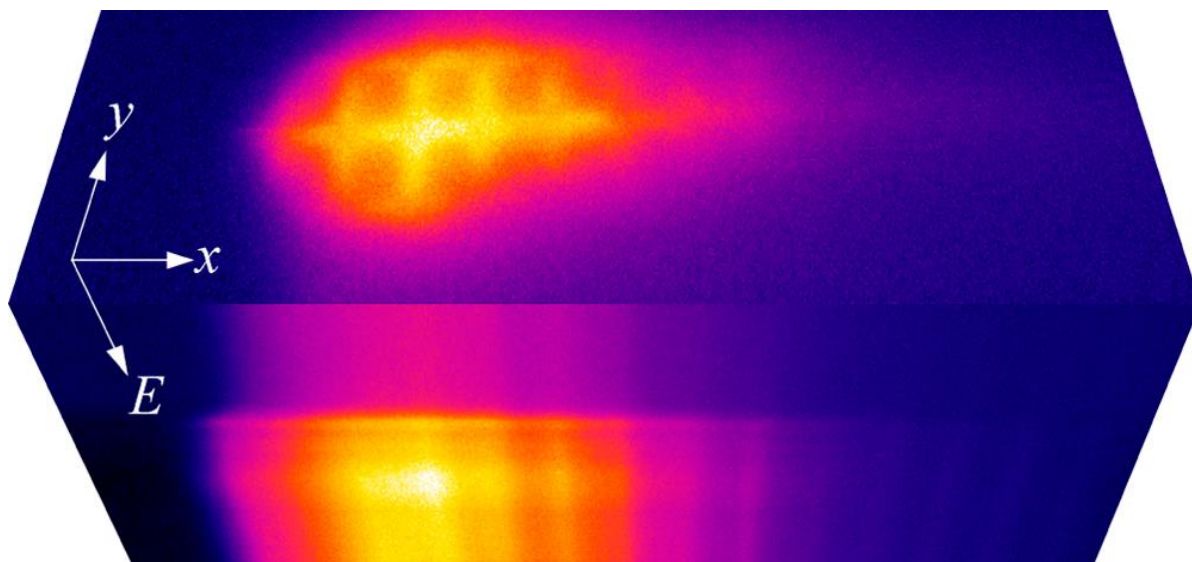


## Real Time Observation of X-ray-Induced Surface Modification Using Simultaneous XANES and XEOL-XANES

*Analytical Chemistry*, 85, pp9556-9563 (2013)

Annemie Adriaens, Paul Quinn, Sergey Nikitenko, and Mark G. Dowsett

In experiments preliminary to the design of an X-ray-excited optical luminescence (XEOL)-based chemical mapping tool we have used X-ray micro ( $4.5 \times 5.2 \mu\text{m}$ ) and macro ( $1 \times 6 \text{ mm}$ ) beams with similar total fluxes to assess the effects of a high flux density beam of X-rays at energies close to an absorption edge on inorganic surfaces in air. The near surface composition of corroded cupreous alloys was analyzed using parallel X-ray and optical photoemission channels to collect X-ray absorption near-edge structure (XANES) data at the Cu K edge. The X-ray fluorescence channel is characteristic of the composition averages over several micrometers into the surface, whereas the optical channel is surface specific to about 200 nm. While the X-ray fluorescence data were mostly insensitive to the X-ray dose, the XEOL-XANES data from the microbeam showed significant dose-dependent changes to the superficial region, including surface cleaning, changes in the oxidation state of the copper, and destruction of surface compounds responsible for pre-edge fluorescence or phosphorescence in the visible. In one case, there was evidence that the lead phase in a bronze had melted. Conversely, data from the macrobeam were stable over several hours. Apart from localized heating effects, the microbeam damage is probably associated with the O<sub>3</sub> loading of the surface and increased reaction rate with atmospheric water vapor.

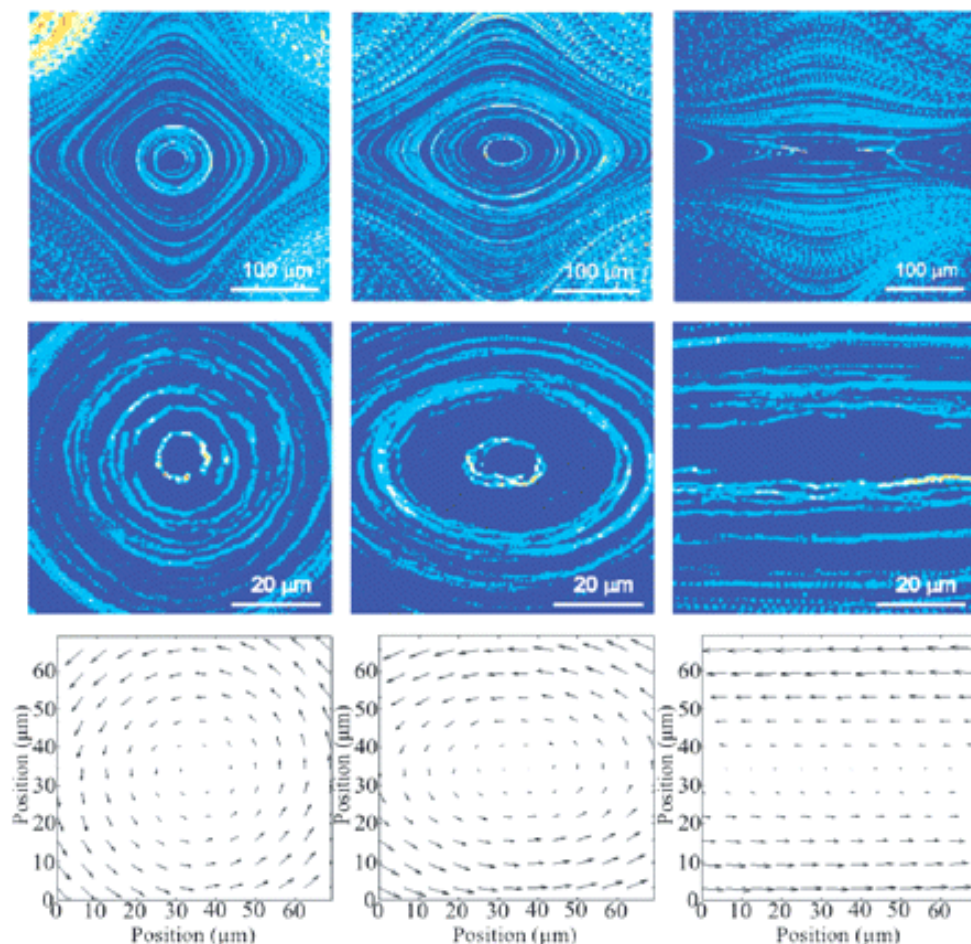


## Dynamics of a vesicle in general flow

*Proceedings of the National Academy of Sciences* 106, 11444 (2009) [10.1073/pnas.0902657106](https://doi.org/10.1073/pnas.0902657106)

J. Deschamps, V. Kantsler, E. Segre and V. Steinberg

An approach to quantitatively study vesicle dynamics as well as biologically-related micro-objects in a fluid flow, which is based on the combination of a dynamical trap and a control parameter, the ratio of the vorticity to the strain rate, is suggested. The flow is continuously varied between rotational, shearing, and elongational in a microfluidic 4-roll mill device, the dynamical trap, that allows scanning of the entire phase diagram of motions, i.e., tank-treading (TT), tumbling (TU), and trembling (TR), using a single vesicle even at  $\lambda = \eta_{in}/\eta_{out} = 1$ , where  $\eta_{in}$  and  $\eta_{out}$  are the viscosities of the inner and outer fluids. This cannot be achieved in pure shear flow, where the transition between TT and either TU or TR is attained only at  $\lambda > 1$ . As a result, it is found that the vesicle dynamical states in a general are presented by the phase diagram in a space of only 2 dimensionless control parameters. The findings are in semiquantitative accord with the recent theory made for a quasi-spherical vesicle, although vesicles with large deviations from spherical shape were studied experimentally. The physics of TR is also uncovered.



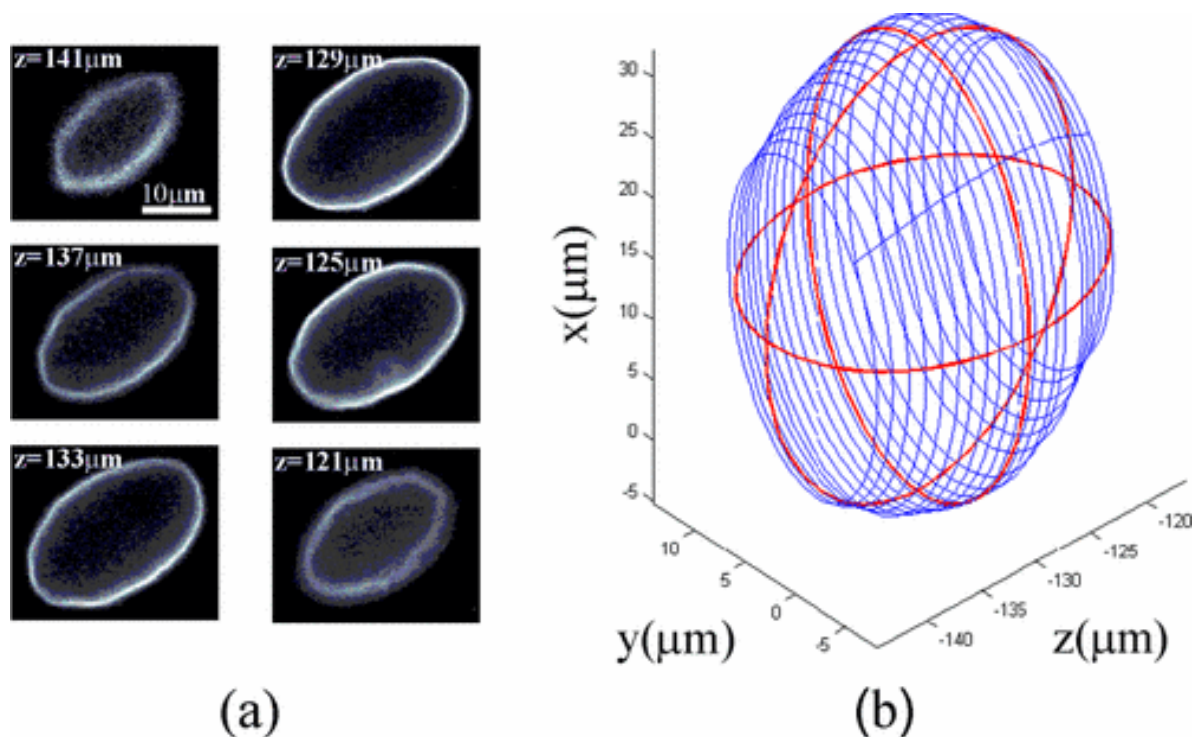
(A) Experimental streamlines images of the velocity fields for pure rotational (first column,  $\omega/s = 43$ ), mixed (second column,  $\omega/s = 2.6$ ) and pure shear (third,  $\omega/s = 1$ ) flows; (B) Zoom of the same experimental flows; (C) velocity vector field representation of the same flows (PTV).

## Phase Diagram of Single Vesicle Dynamical States in Shear Flow

*Phys. Rev. Lett.* 102, 118105 (2009) [10.1103/PhysRevLett.102.118105](https://doi.org/10.1103/PhysRevLett.102.118105)

J. Deschamps, V. Kantsler, and V. Steinberg

We report the first experimental phase diagram of vesicle dynamical states in a shear flow presented in a space of two dimensionless parameters suggested recently by V. Lebedev *et al.* To reduce errors in the control parameters, 3D geometrical reconstruction and determination of the viscosity contrast of a vesicle *in situ* in a plane Couette flow device prior to the experiment are developed. Our results are in accord with the theory predicting three distinctly separating regions of vesicle dynamical states in the plane of just two self-similar parameters.



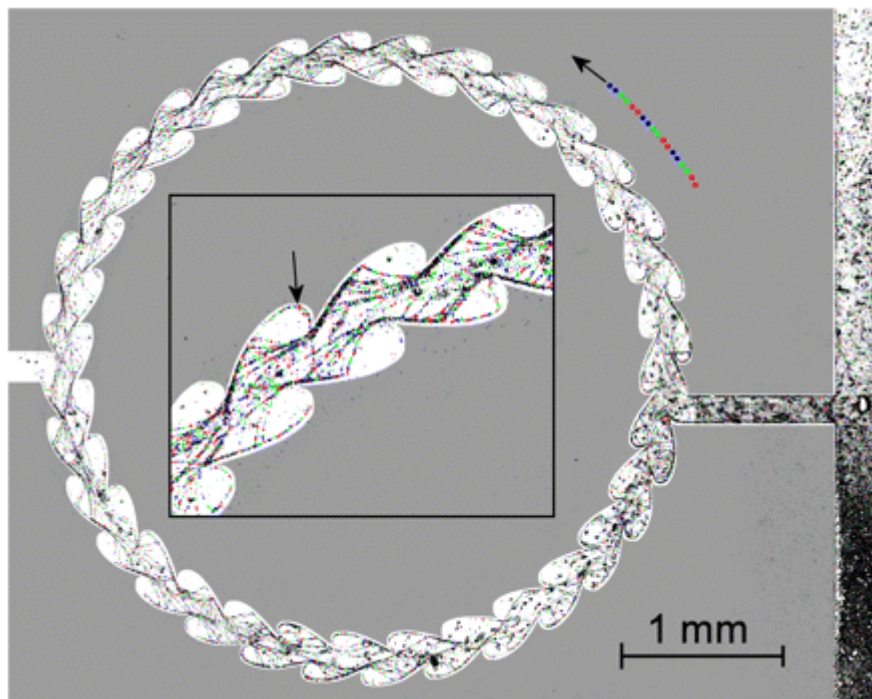
Reconstruction of vesicle ellipsoidal shape. (a) several slices captured at different  $z$ . (b) elliptical approximation of each slice and their stacking in 3D space. Ellipsoidal approximation of 3D vesicle shape provides its three main axis. Here  $R=14.56\pm 0.31 \mu\text{m}$  and  $\Delta=0.49\pm 0.04$ .

## Human spermatozoa migration in microchannels reveals boundary-following navigation

*Proceedings of the National Academy of Sciences* 109, 8007 (2012) [10.1073/pnas.1202934109](https://doi.org/10.1073/pnas.1202934109)

Petr Denissenko, Vasily Kantsler, David J. Smith and Jackson Kirkman-Brown

The migratory abilities of motile human spermatozoa in vivo are essential for natural fertility, but it remains a mystery what properties distinguish the tens of cells which find an egg from the millions of cells ejaculated. To reach the site of fertilization, sperm must traverse narrow and convoluted channels, filled with viscous fluids. To elucidate individual and group behaviors that may occur in the complex three-dimensional female tract environment, we examine the behavior of migrating sperm in assorted microchannel geometries. Cells rarely swim in the central part of the channel cross-section, instead traveling along the intersection of the channel walls (“channel corners”). When the channel turns sharply, cells leave the corner, continuing ahead until hitting the opposite wall of the channel, with a distribution of departure angles, the latter being modulated by fluid viscosity. If the channel bend is smooth, cells depart from the inner wall when the curvature radius is less than a threshold value close to  $150\ \mu\text{m}$ . Specific wall shapes are able to preferentially direct motile cells. As a consequence of swimming along the corners, the domain occupied by cells becomes essentially one-dimensional, leading to frequent collisions, and needs to be accounted for when modeling the behavior of populations of migratory cells and considering how sperm populate and navigate the female tract. The combined effect of viscosity and three-dimensional architecture should be accounted for in future in vitro studies of sperm chemoattraction.



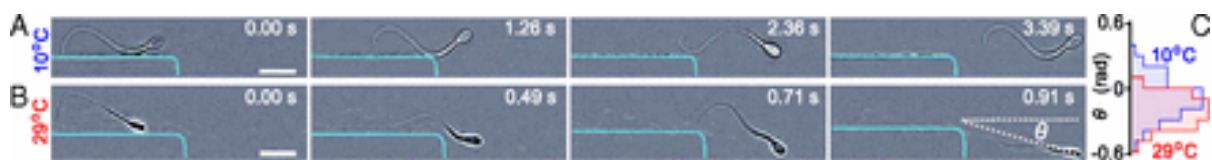
Spermatozoa in the “one way running track” microchannel geometry. The space outside the microchannel is shaded gray to indicate position of the walls. Edges of gray shading are spaced from channel walls by approximately  $10\text{--}20\ \mu\text{m}$  so that they do not interfere with tracks of the cells. The long arrow shows the preferred (counterclockwise) direction of cell migration. The arrow in the zoomed insert of the channel segment points at a track of a cell swimming in the direction opposite to that dictated by features of channel walls. Follow the track to see this cell departing from the inside of the ratchet and traversing the channel, being redirected counterclockwise, as the other cells travel.

## Ciliary contact interactions dominate surface scattering of swimming eukaryotes

*Proceedings of the National Academy of Sciences* 110, 1187 (2013) [10.1073/pnas.1210548110](https://doi.org/10.1073/pnas.1210548110)

Vasily Kantsler, Jörn Dunkel, Marco Polin, and Raymond E. Goldstein

Interactions between swimming cells and surfaces are essential to many microbiological processes, from bacterial biofilm formation to human fertilization. However, despite their fundamental importance, relatively little is known about the physical mechanisms that govern the scattering of flagellated or ciliated cells from solid surfaces. A more detailed understanding of these interactions promises not only new biological insights into structure and dynamics of flagella and cilia but may also lead to new microfluidic techniques for controlling cell motility and microbial locomotion, with potential applications ranging from diagnostic tools to therapeutic protein synthesis and photosynthetic biofuel production. Due to fundamental differences in physiology and swimming strategies, it is an open question of whether microfluidic transport and rectification schemes that have recently been demonstrated for pusher-type microswimmers such as bacteria and sperm cells, can be transferred to puller-type algae and other motile eukaryotes, because it is not known whether long-range hydrodynamic or short-range mechanical forces dominate the surface interactions of these microorganisms. Here, using high-speed microscopic imaging, we present direct experimental evidence that the surface scattering of both mammalian sperm cells and unicellular green algae is primarily governed by direct ciliary contact interactions. Building on this insight, we predict and experimentally verify the existence of optimal microfluidic ratchets that maximize rectification of initially uniform *Chlamydomonas reinhardtii* suspensions. Because mechano-elastic properties of cilia are conserved across eukaryotic species, we expect that our results apply to a wide range of swimming microorganisms.



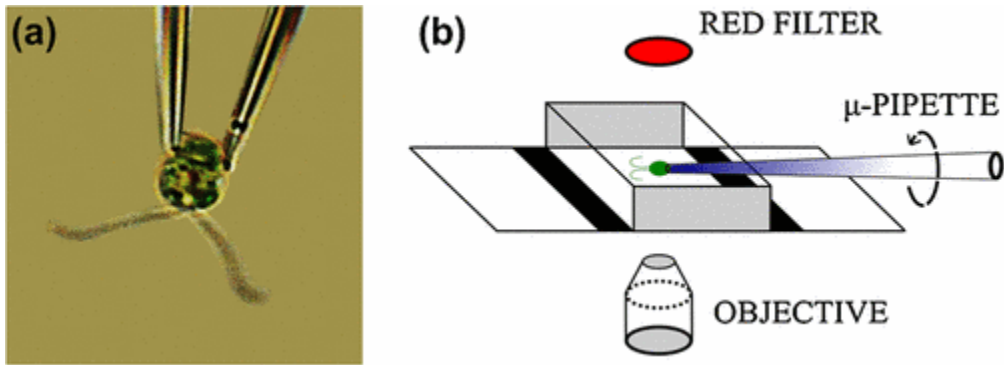
Surface scattering of bull spermatozoa is governed by ciliary contact interactions, as evident from the scattering sequences of individual cells at two temperature values: (A)  $T = 10^\circ\text{C}$  and (B)  $T = 29^\circ\text{C}$ . The background has been subtracted from the micrographs to enhance the visibility of the cilia. The cyan-colored line indicates the corner-shaped boundary of the microfluidic channels. The horizontal dotted line in the last image in B defines  $\vartheta = 0$ . (Scale bars:  $20\ \mu\text{m}$ .) (C) The probability distributions of scattering angles  $\vartheta$  from the corner peak at negative angles, due to the fact that the beat amplitude of the cilia exceeds the size of the cell body (sample size:  $n = 116$  for  $T = 10^\circ\text{C}$  and  $n = 115$  for  $T = 29^\circ\text{C}$ ). At higher temperatures, the cilia exhibit a larger oscillation amplitude and beat frequency (29), resulting in a larger swimming speed and shifting the typical scattering angles to larger absolute values.

## Noise and Synchronization in Pairs of Beating Eukaryotic Flagella

*Phys. Rev. Lett.* 103, 168103 (2009) [10.1103/PhysRevLett.103.168103](https://doi.org/10.1103/PhysRevLett.103.168103)

Raymond E. Goldstein, Marco Polin, and Idan Tuval

It has long been conjectured that hydrodynamic interactions between beating eukaryotic flagella underlie their ubiquitous forms of synchronization; yet there has been no experimental test of this connection. The biflagellate alga *Chlamydomonas* is a simple model for such studies, as its two flagella are representative of those most commonly found in eukaryotes. Using micromanipulation and high-speed imaging, we show that the flagella of a *C. reinhardtii* cell present periods of synchronization interrupted by phase slips. The dynamics of slips and the statistics of phase-locked intervals are consistent with a low-dimensional stochastic model of hydrodynamically coupled oscillators, with a noise amplitude set by the intrinsic fluctuations of single flagellar beats.



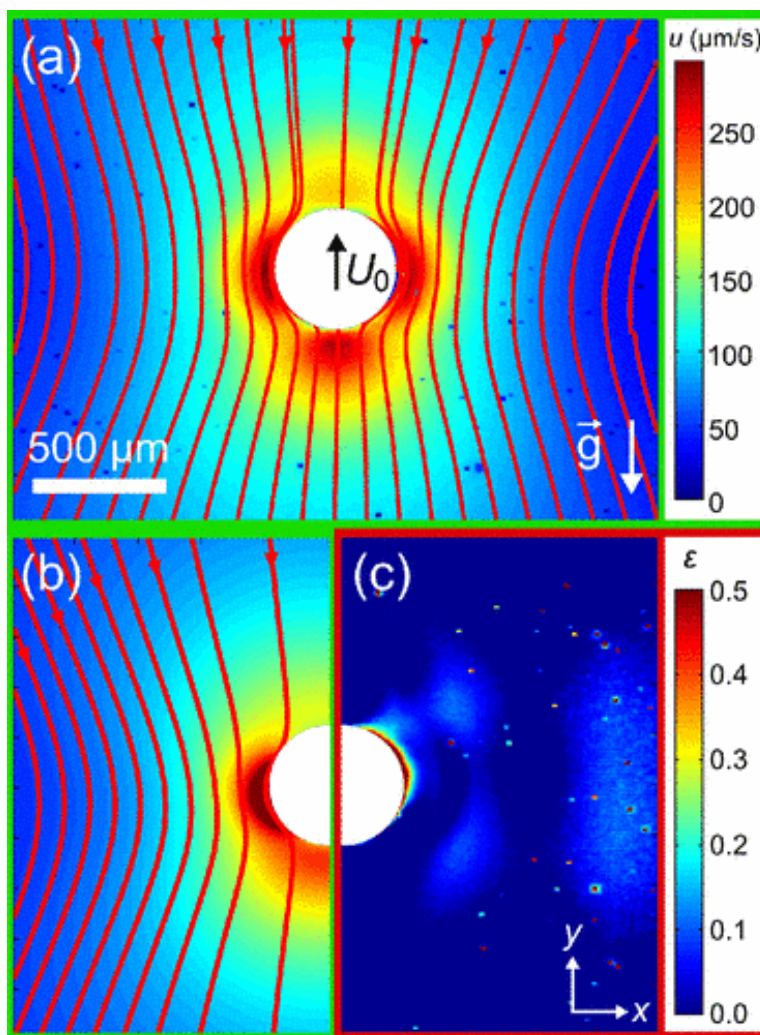
Experimental system. (a) A single cell of *Chlamydomonas reinhardtii* held on a micropipette. (b) Schematic of apparatus for visualization and micromanipulation of cells.

## Direct Measurement of the Flow Field around Swimming Microorganisms

*Phys. Rev. Lett.* 105, 168101 (2010) [10.1103/PhysRevLett.105.168101](https://doi.org/10.1103/PhysRevLett.105.168101)

Knut Drescher, Raymond E. Goldstein, Nicolas Michel, Marco Polin, and Idan Tuval

Swimming microorganisms create flows that influence their mutual interactions and modify the rheology of their suspensions. While extensively studied theoretically, these flows have not been measured in detail around any freely-swimming microorganism. We report such measurements for the microphytes *Volvox carteri* and *Chlamydomonas reinhardtii*. The minute ( $\sim 0.3\%$ ) density excess of *V. carteri* over water leads to a strongly dominant Stokeslet contribution, with the widely-assumed stresslet flow only a correction to the subleading source dipole term. This implies that suspensions of *V. carteri* have features similar to suspensions of sedimenting particles. The flow in the region around *C. reinhardtii* where significant hydrodynamic interaction is likely to occur differs qualitatively from a puller stresslet, and can be described by a simple three-Stokeslet model.

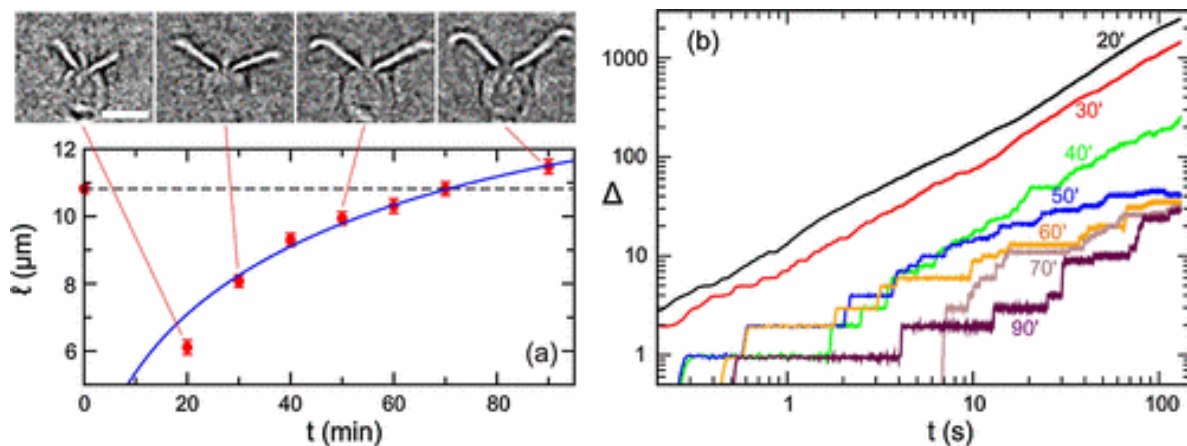


## Emergence of Synchronized Beating during the Regrowth of Eukaryotic Flagella

*Phys. Rev. Lett.* 107, 148103 (2011) [10.1103/PhysRevLett.107.148103](https://doi.org/10.1103/PhysRevLett.107.148103)

Raymond E. Goldstein, Marco Polin, and Idan Tuval

A fundamental issue in the biology of eukaryotic flagella is the origin of synchronized beating observed in tissues and organisms containing multiple flagella. Recent studies of the biflagellate unicellular alga *Chlamydomonas reinhardtii* provided the first evidence that the interflagellar coupling responsible for synchronization is of hydrodynamic origin. To investigate this mechanism in detail, we study here synchronization in *Chlamydomonas* as its flagella slowly regrow after mechanically induced self-scission. The duration of synchronized intervals is found to be strongly dependent on flagellar length. Analysis within a stochastic model of coupled phase oscillators is used to extract the length dependence of the interflagellar coupling and the intrinsic beat frequencies of the two flagella. Physical and biological considerations that may explain these results are proposed.



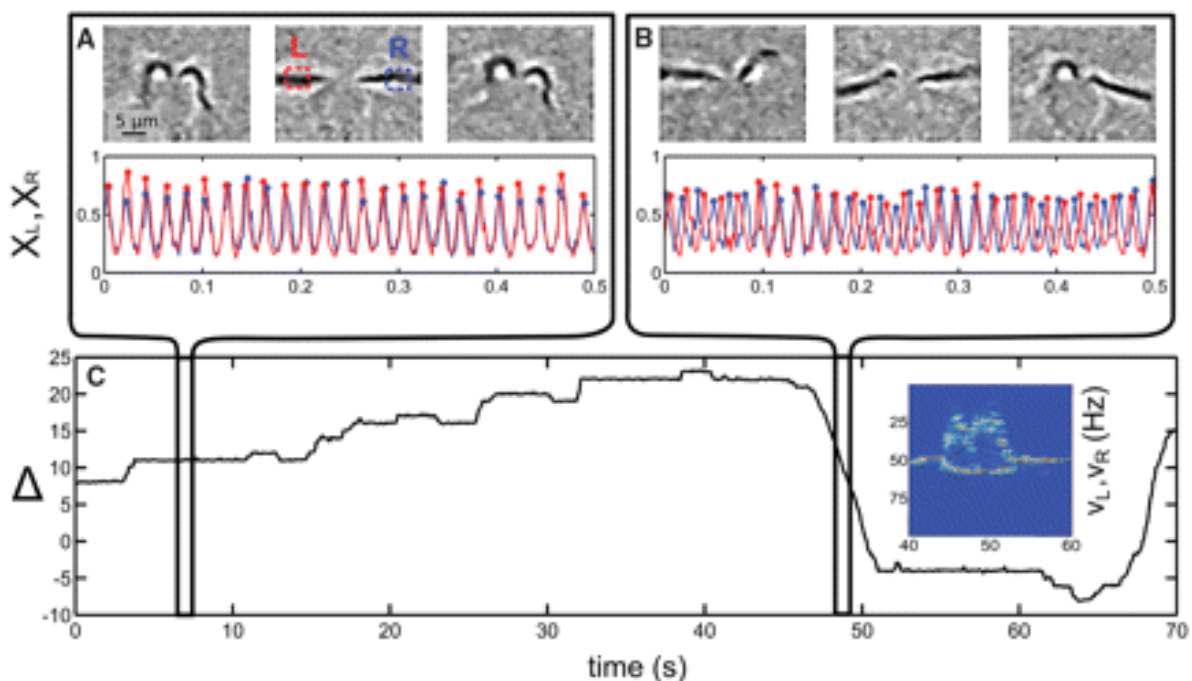
Flagellar regrowth and the emergence of synchrony. (a) Regrowth dynamics of flagella after autotomy, and image processed movie frames at the indicated times after deflagellation. The scale bar is  $10 \mu\text{m}$ . The blue line indicates a fit to the balance-point model of regrowth. (b) Phase difference  $\Delta$  as a function of time for a single cell during short experiments at various times (in minutes) after deflagellation, as indicated. Plateaus in  $\Delta$ , corresponding to periods of synchronous beating, become progressively longer as flagella regrow.

## *Chlamydomonas* Swims with Two “Gears” in a Eukaryotic Version of Run-and-Tumble Locomotion

*Science* 325, 487 (2009) [10.1126/science.1172667](https://doi.org/10.1126/science.1172667)

Marco Polin, Idan Tuval, Knut Drescher, J. P. Gollub, Raymond E. Goldstein

The coordination of eukaryotic flagella is essential for many of the most basic processes of life (motility, sensing, and development), yet its emergence and regulation and its connection to locomotion are poorly understood. Previous studies show that the unicellular alga *Chlamydomonas*, widely regarded as an ideal system in which to study flagellar biology, swims forward by the synchronous action of its two flagella. Using high-speed imaging over long intervals, we found a richer behavior: A cell swimming in the dark stochastically switches between synchronous and asynchronous flagellar beating. Three-dimensional tracking shows that these regimes lead, respectively, to nearly straight swimming and to abrupt large reorientations, which yield a eukaryotic version of the "run-and-tumble" motion of peritrichously flagellated bacteria.



A single *C. reinhardtii* cell moves back and forth between synchronous (A) and asynchronous (B) states. Movie frames showing a few cycles and the oscillatory intensity signals  $X_{L,R}(t) = \Gamma_{L,R}(t)\sin[2\pi\theta_{L,R}(t)]$  ( $X$ , signal; L, left; R, right;  $\Gamma$ , amplitude;  $t$ , time;  $\theta$ , phase), obtained by local sampling of the video light intensity near the two flagella, are shown for both cases. (C) A long (70-s) time series of the phase difference  $\Delta(t) = \theta_L(t) - \theta_R(t)$  contains periods of synchrony interrupted by drifts of either sign. A windowed Fourier transform of the beating signals during the transition from synchronization to drifting and then back again to synchrony (inset) shows a large frequency difference in the asynchronous state. This behavior was characteristic of all 24 observed cells.

## Magnetic Resonance Cluster

❖ 7 Staff; 9 PDRAs; 15 PhDs;



❖ 193 articles; 1730 citations; £3.1 M grant awards; 24 PhDs awarded

Millburn House Magnetic Resonance Centre was set up between 2007 and 2009, with an £8.5 M investment, as a multi-user laboratory to develop advanced MR spectroscopic techniques and instrumentation, and to use these to solve a diverse range of challenging problems in Physics, Chemistry and Life Sciences. Cross-disciplinary fertilisation of ideas is promoted through Physics staff (**Brown, Dupree, Hanna, Iuga, Morley, Newton, Wedge**) working alongside 3 Chemistry-based members.

Since 2010, the Centre has provided the UK 850 MHz Solid State Nuclear Magnetic Resonance (SS-NMR) Facility and leads multi-university CDTs in *Integrated Magnetic Resonance* (iMR-CDT) and in *Diamond Science and Technology*.

The forward strategy is to be at the leading edge of MR technique development and be central to UK provision of high field SS-NMR. MR academics have established a strong international reputation in the following areas, which are supported by many collaborations with leading scientists and companies:

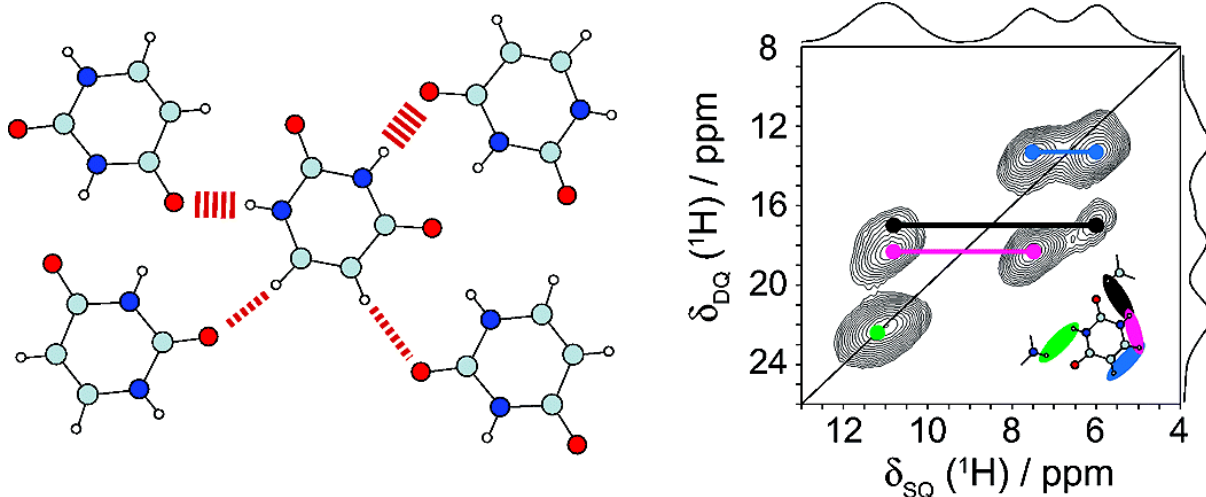
- Application of SS-NMR to problems in materials science, catalysis, supramolecular chemistry, pharmaceuticals, and structure, dynamics and activity of biomolecular systems.
- Development of SS-NMR methodology, incl. new probe technologies, new pulse sequences, and associated computational approaches (involving Quigley from TP).
- Application of EPR and optical techniques to study colour centres in diamond and related materials; development of sensors that exploit diamond's unique combination of properties.
- Novel MR technique development, incl. pulsed EPR at high magnetic fields, high pressure EPR, Dynamic Nuclear Polarization, electrically & optically detected MR.
- Quantum information processing, with coupled electron-nuclear spins in Si and diamond.

## Quantifying Weak Hydrogen Bonding in Uracil and 4-Cyano-4'-ethynylbiphenyl: A Combined Computational and Experimental Investigation of NMR Chemical Shifts in the Solid State

*J. Am. Chem. Soc.*, 2008, 130 (3), pp 945–954 [10.1021/ja075892i](https://doi.org/10.1021/ja075892i)

A. Uldry, J.M. Griffin, J.R. Yates, M. Pérez-Torralba, M.D. Santa María, A.L. Webber, M.L.L. Beaumont, A. Samoson, R.M. Claramunt, C.J. Pickard, and S.P. Brown

Weak hydrogen bonding in uracil and 4-cyano-4'-ethynylbiphenyl, for which single-crystal diffraction structures reveal close  $\text{CH}\cdots\text{O}=\text{C}$  and  $\text{C}\equiv\text{CH}\cdots\text{N}\equiv\text{C}$  distances, is investigated in a study that combines the experimental determination of  $^1\text{H}$ ,  $^{13}\text{C}$ , and  $^{15}\text{N}$  chemical shifts by magic-angle spinning (MAS) solid-state NMR with first-principles calculations using plane-wave basis sets. An optimized synthetic route, including the isolation and characterization of intermediates, to 4-cyano-4'-ethynylbiphenyl at natural abundance and with  $^{13}\text{C}\equiv^{13}\text{CH}$  and  $^{15}\text{N}\equiv\text{C}$  labeling is described. The difference in chemical shifts calculated, on the one hand, for the full crystal structure and, on the other hand, for an isolated molecule depends on both intermolecular hydrogen bonding interactions and aromatic ring current effects. In this study, the two effects are separated computationally by, first, determining the difference in chemical shift between that calculated for a plane (uracil) or an isolated chain (4-cyano-4'-ethynylbiphenyl) and that calculated for an isolated molecule and by, second, calculating intraplane or intrachain nucleus-independent chemical shifts that quantify the ring current effects caused by neighboring molecules. For uracil, isolated molecule to plane changes in the  $^1\text{H}$  chemical shift of 2.0 and 2.2 ppm are determined for the CH protons involved in  $\text{CH}\cdots\text{O}$  weak hydrogen bonding; this compares to changes of 5.1 and 5.4 ppm for the NH protons involved in conventional  $\text{NH}\cdots\text{O}$  hydrogen bonding. A comparison of CH bond lengths for geometrically relaxed uracil molecules in the crystal structure and for geometrically relaxed isolated molecules reveals differences of no more than 0.002 Å, which corresponds to changes in the calculated  $^1\text{H}$  chemical shifts of at most 0.1 ppm. For the  $\text{C}\equiv\text{CH}\cdots\text{N}\equiv\text{C}$  weak hydrogen bonds in 4-cyano-4'-ethynylbiphenyl, the calculated molecule to chain changes are of similar magnitude but opposite sign for the donor  $^{13}\text{C}$  and acceptor  $^{15}\text{N}$  nuclei. In uracil and 4-cyano-4'-ethynylbiphenyl, the CH hydrogen-bonding donors are  $sp^2$  and  $sp$  hybridized, respectively; a comparison of the calculated changes in  $^1\text{H}$  chemical shift with those for the  $sp^3$  hybridized CH donors in maltose reveals no marked dependence on hybridization for weak hydrogen-bonding strength.

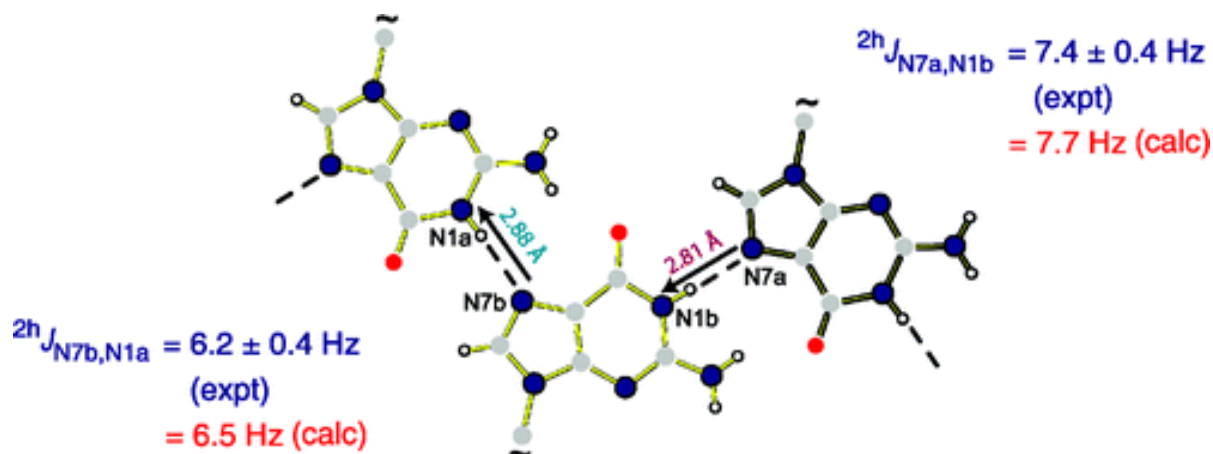


## Density Functional Theory Calculations of Hydrogen-Bond-Mediated NMR $J$ Coupling in the Solid State

*J. Am. Chem. Soc.*, 2008, 130 (38), pp 12663–12670 [10.1021/ja800419m](https://doi.org/10.1021/ja800419m)

S.A. Joyce, J.R. Yates, C.J. Pickard and S.P. Brown

A recently developed method for calculating NMR  $J$  coupling in solid-state systems is applied to calculate hydrogen-bond-mediated  ${}^2\text{h}J_{\text{NN}}$  couplings across intra- or intermolecular N–H $\cdots$ N hydrogen bonds in two 6-aminofulvene-1-alimine derivatives and the ribbon structure formed by a deoxyguanosine derivative. Excellent quantitative agreement is observed between the calculated solid-state  $J$  couplings and those previously determined experimentally in two recent spin-echo magic-angle-spinning NMR studies (Brown, S. P.; et al. *Chem. Commun.* **2002**, 1852–1853 and Pham, T. N.; et al. *Phys. Chem. Chem. Phys.* **2007**, 9, 3416–3423). For the 6-aminofulvene-1-aldimines, the differences in  ${}^2\text{h}J_{\text{NN}}$  couplings in pyrrole and triazole derivatives are reproduced, while for the guanosine ribbons, an increase in  ${}^2\text{h}J_{\text{NN}}$  is correlated with a decrease in the N–H $\cdots$ N hydrogen-bond distance.  $J$  couplings are additionally calculated for isolated molecules of the 6-aminofulvene-1-aldimines extracted from the crystal with and without further geometry optimization. Importantly, it is shown that experimentally observed differences between  $J$  couplings determined by solution- and solid-state NMR are not solely due to differences in geometry; long-range electrostatic effects of the crystal lattice are shown to be significant also.  $J$  couplings that are yet to be experimentally measured are calculated. Notably,  ${}^2\text{h}J_{\text{NO}}$  couplings across N–H $\cdots$ O hydrogen bonds are found to be of a similar magnitude to  ${}^2\text{h}J_{\text{NN}}$  couplings, suggesting that their utilization and quantitative determination should be experimentally feasible.

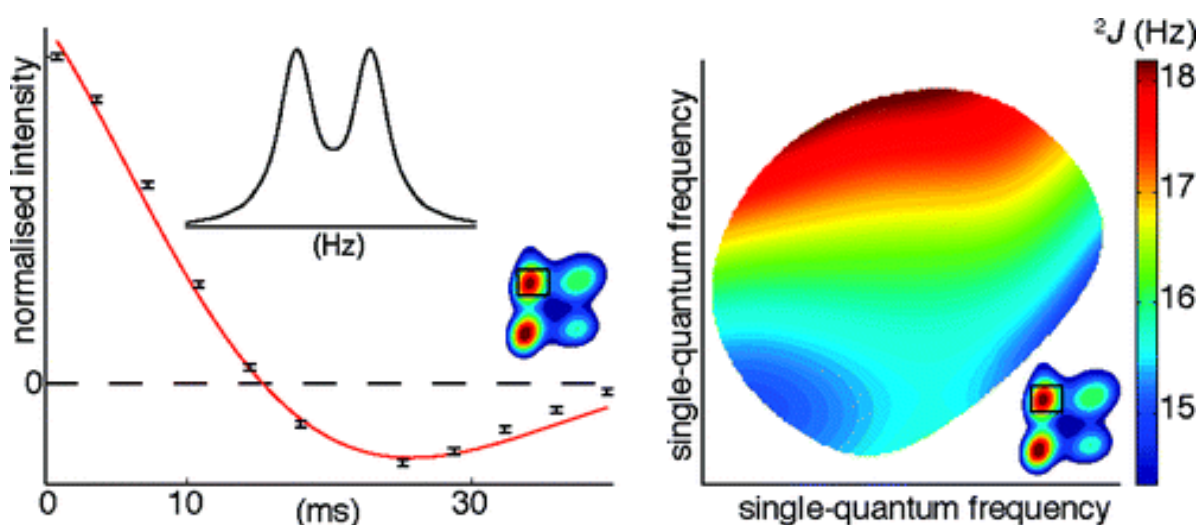


### **<sup>31</sup>P MAS Refocused INADEQUATE Spin–Echo (REINE) NMR Spectroscopy: Revealing *J* Coupling and Chemical Shift Two-Dimensional Correlations in Disordered Solids**

*J. Am. Chem. Soc.*, 2009, 131 (33), pp 11861–11874 [10.1021/ja902238s](https://doi.org/10.1021/ja902238s)

P. Guerry, M.E. Smith and S.P. Brown

Two-dimensional (2D) variations in  ${}^2J_{P_1,P_1}$ ,  ${}^2J_{P_1,P_2}$ , and  ${}^2J_{P_2,P_2}$  are obtained—using the REINE (*RE*focused *INA*DEQUATE spin–*E*cho) pulse sequence presented by Cadars et al. (*Phys. Chem. Chem. Phys.* **2007**, 9, 92–103)—from pixel-by-pixel fittings of the spin–echo modulation for the 2D correlation peaks due to linked phosphate tetrahedra ( $P_1$ – $P_1$ ,  $P_1$ – $P_2$ ,  $P_2$ – $P_1$ , and  $P_2$ – $P_2$ ) in a  ${}^{31}\text{P}$  refocused INADEQUATE solid-state MAS NMR spectrum of a cadmium phosphate glass,  $0.575\text{CdO}$ – $0.425\text{P}_2\text{O}_5$ . In particular, separate variations for each 2D  ${}^{31}\text{P}$  REINE peak are obtained which reveal correlations between the *J* couplings and the  ${}^{31}\text{P}$  chemical shifts of the coupled nuclei that are much clearer than those evident in previously presented 2D z-filtered  ${}^{31}\text{P}$  spin–echo spectra. Notably, such correlations between the *J* couplings and the  ${}^{31}\text{P}$  chemical shifts are observed even though the conditional probability distributions extracted using the protocol of Cadars et al. (*J. Am. Chem. Soc.* **2005**, 127, 4466–4476) indicate that there is no marked correlation between the  ${}^{31}\text{P}$  chemical shifts of neighboring phosphate tetrahedra. For 2D peaks at the  $P_2$   ${}^{31}\text{P}$  chemical shift in the direct dimension, there can be contributions from chains of three units ( $P_1$ – $P_2$ – $P_1$ ), chains of four units ( $P_1$ – $P_2$ – $P_2$ – $P_1$ ), or longer chains or rings ( $-P_2$ – $P_2$ – $P_2-$ ): for the representative glass considered here, best fits are obtained assuming a glass comprised predominantly of chains of four units. The following variations are found:  ${}^2J_{P_1,P_1} = 13.4 \pm 0.3$  to  $14.8 \pm 0.5$  Hz,  ${}^2J_{P_1,P_2} = 15.0 \pm 0.3$  to  $18.2 \pm 0.3$  Hz, and  ${}^2J_{P_2,P_2} = 5.9 \pm 0.6$  to  $9.1 \pm 0.9$  Hz from the fits to the  $P_1$ – $P_1$ ,  $P_1$ – $P_2$ , and  $P_2$ – $P_2$  peaks, respectively. The correlation of a particular *J* coupling with the  ${}^{31}\text{P}$  chemical shifts of the considered nucleus and the coupled nucleus is quantified by the coefficients  $C_{F_2}$  and  $C_{F_1}$  that correspond to the average pixel-by-pixel change in the *J* coupling with respect to the chemical shift of the observed ( $F_2$ ) and neighboring ( $F_1$ )  ${}^{31}\text{P}$  nuclei, respectively.

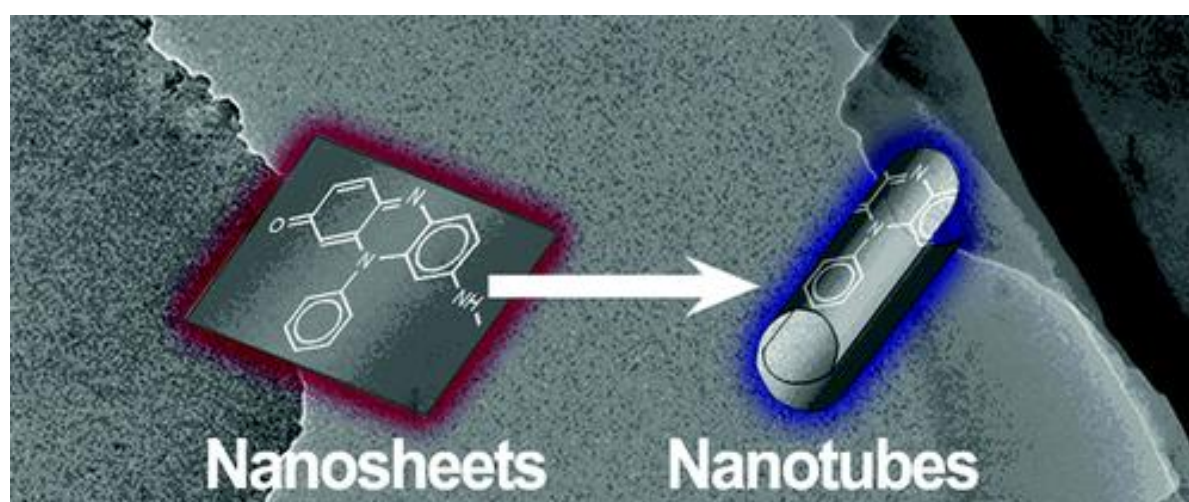


## Role of Aniline Oligomeric Nanosheets in the Formation of Polyaniline Nanotubes

*Macromolecules*, 2010, 43 (2), pp 662–670 [10.1021/ma902109r](https://doi.org/10.1021/ma902109r)

Z.D. Zujovic, C. Laslau, G.A. Bowmaker, P.A. Kilmartin, A.L. Webber, S.P. Brown and J. Travas-Sejdic

We report the phenomenon of nanosheet rolling during typical aqueous polymerization and study its implications for the self-assembly of polyaniline nanotubes. Specifically, this is done through a detailed morphological and structural characterization of products obtained after 20 min, 1 h in falling pH experiments, and after 20 h at constant pH 2.5 during the oxidative polymerization of aniline with ammonium persulfate in the presence of alanine. The chemical structure has been investigated by FTIR, UV-vis, solid-state  $^{13}\text{C}$  and  $^{15}\text{N}$  NMR, liquid NMR, and XRD, whereas the morphology was imaged using scanning electron microscopy (SEM) and transmission electron microscopy (TEM). The presence of self-assembled nanoflakes with different thicknesses ranging from tens to hundreds of nanometers is confirmed through SEM. TEM revealed the presence of very thin layers: nanosheets with sharp and well-defined edges. The presence of hydrogen bonds is confirmed by FTIR and is consistent with XRD results. The stacking of nanosheets and the formation of thicker flakes based on  $\pi$ - $\pi$  electron interactions have been proposed on the basis of XRD experiments, where self-assembled layers made of cross-linked oxidized aniline structures stack on each other and are stabilized by hydrogen bonds and  $\pi$ - $\pi$  interactions. In this way, hydrophobic cross-linked oligomers (formed at the beginning of the synthesis at higher pH) minimize their surface energy, self-assembling into well-ordered macromolecular structures. On the basis of the SEM and TEM images and the information obtained from other analytical techniques applied here, the presence of PANI nanotubes formed in the reaction carried out at constant pH of 2.5 is confirmed. The role of the nanosheets in the formation of nanotubes is proposed.

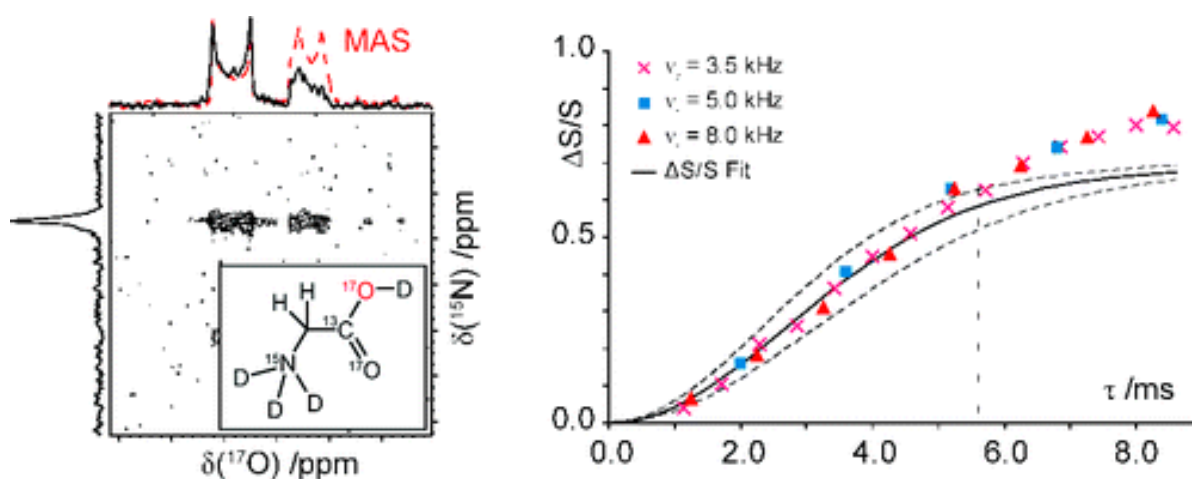


## Probing Heteronuclear $^{15}\text{N}$ – $^{17}\text{O}$ and $^{13}\text{C}$ – $^{17}\text{O}$ Connectivities and Proximities by Solid-State NMR Spectroscopy

*J. Am. Chem. Soc.*, 2009, 131 (5), pp 1820–1834 [10.1021/ja805898d](https://doi.org/10.1021/ja805898d)

I.Hung, A-C. Uldry, J. Becker-Baldus, A.L. Webber, A. Wong, M.E. Smith, S.A. Joyce, J.R. Yates, C.J. Pickard, R. Dupree and S.P. Brown

Heteronuclear solid-state magic-angle spinning (MAS) NMR experiments for probing  $^{15}\text{N}$ – $^{17}\text{O}$  dipolar and  $J$  couplings are presented for  $[\text{}^2\text{H}(\text{NH}_3), \text{}^1\text{-}^{13}\text{C}, \text{}^{15}\text{N}, \text{}^{17}\text{O}_2]\text{glycine}\cdot\text{}^2\text{HCl}$  and  $[\text{}^{15}\text{N}_2, \text{}^{17}\text{O}_2]\text{uracil}$ . Two-dimensional  $^{15}\text{N}$ – $^{17}\text{O}$  correlation spectra are obtained using the  $\text{R}^3\text{-HMQC}$  experiment; for glycine $\cdot\text{}^2\text{HCl}$ , the intensity of the resolved peaks for the C=O and C–O $^2\text{H}$   $^{17}\text{O}$  resonances corresponds to the relative magnitude of the respective  $^{15}\text{N}$ – $^{17}\text{O}$  dipolar couplings.  $^{17}\text{O}$ – $^{15}\text{N}$  REDOR curves are presented for glycine $\cdot\text{}^2\text{HCl}$ ; fits of the initial buildup ( $\Delta S/S < 0.2$ ) yield effective dipolar couplings in agreement with ( $\pm 20\%$ ) the root-sum-squared dipolar couplings determined from the crystal structure. Experimental  $^{15}\text{N}$ – $^{17}\text{O}$  REAPDOR curves for the  $^{15}\text{N}$  resonances in glycine $\cdot\text{}^2\text{HCl}$  and uracil fit well to the universal curve presented by Goldbourt et al. (*J. Am. Chem. Soc.* **2003**, 125, 11194). Heteronuclear  $^{13}\text{C}$ – $^{17}\text{O}$  and  $^{15}\text{N}$ – $^{17}\text{O}$   $J$  couplings were experimentally determined from fits of the quotient of the integrated intensity obtained in a heteronuclear and a homonuclear spin-echo experiment,  $S_Q(\tau) = S_{\text{HET}}(\tau)/S_{\text{HOM}}(\tau)$ . For glycine $\cdot\text{}^2\text{HCl}$ ,  $^1J_{\text{CO}}$  was determined as  $24.7 \pm 0.2$  and  $25.3 \pm 0.3$  Hz for the C=O and C–O $^2\text{H}$  resonances, respectively, while for uracil, the average of the two NH $\cdots\text{O}$  hydrogen-bond-mediated  $J$  couplings was determined as  $5.1 \pm 0.6$  Hz. In addition, two-bond intramolecular  $J$  couplings,  $^2J_{\text{OO}} = 8.8 \pm 0.9$  Hz and  $^2J_{\text{N}_1, \text{N}_3} = 2.7 \pm 0.1$  Hz, were determined for glycine $\cdot\text{}^2\text{HCl}$  and uracil, respectively. Excellent agreement was found with  $J$  couplings calculated using the CASTEP code using geometrically optimized crystal structures for glycine $\cdot\text{HCl}$  [ $^1J_{\text{CO}}(\text{C=O}) = 24.9$  Hz,  $^1J_{\text{CO}}(\text{C–OH}) = 27.5$  Hz,  $^2J_{\text{OO}} = 7.9$  Hz] and uracil [ $^2J_{\text{N}_1, \text{O}_4} = 6.1$  Hz,  $^2J_{\text{N}_3, \text{O}_4} = 4.6$  Hz,  $^2J_{\text{N}_1, \text{N}_3} = 2.7$  Hz].



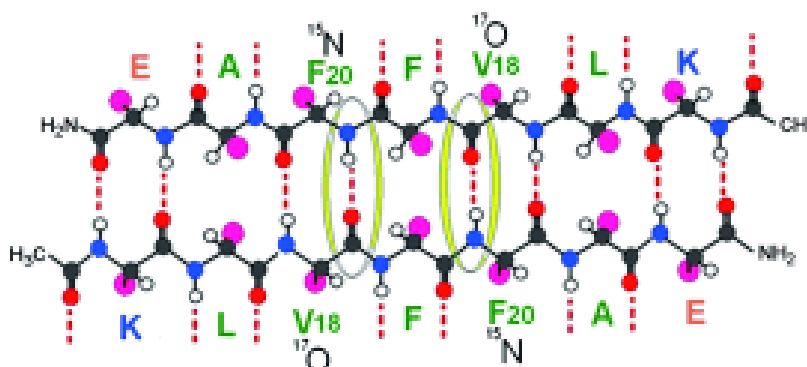
## Hydrogen Bonding in Alzheimer's Amyloid- $\beta$ Fibrils Probed by $^{15}\text{N}\{^{17}\text{O}\}$ REAPDOR Solid-State NMR Spectroscopy

*Angewandte Chemie International Edition* 51 10289-10292 (2012)

[10.1002/anie.201203595](https://doi.org/10.1002/anie.201203595)

O. N. Antzutkin, D. Iuga, A.V. Filippov, R. T. Kelly, J. Becker-Baldus, S. P. Brown, and R. Dupree

An exclusive label:  $^{15}\text{N}\{^{17}\text{O}\}$  REAPDOR NMR was used to validate intermolecular  $\text{C}=\text{}^{17}\text{O}\cdots\text{H}-^{15}\text{N}$  hydrogen bonding in  $\text{Ac-A}\beta_{(16-22)}\text{-NH}_2$  (see scheme) and  $\text{A}\beta_{(11-25)}$  amyloid fibrils, which are associated with Alzheimer's disease, by selectively labeling them with  $^{17}\text{O}$  and  $^{15}\text{N}$ . This method was effective for confirming the structure of these fibrils, and could be useful for a number of other biological samples.

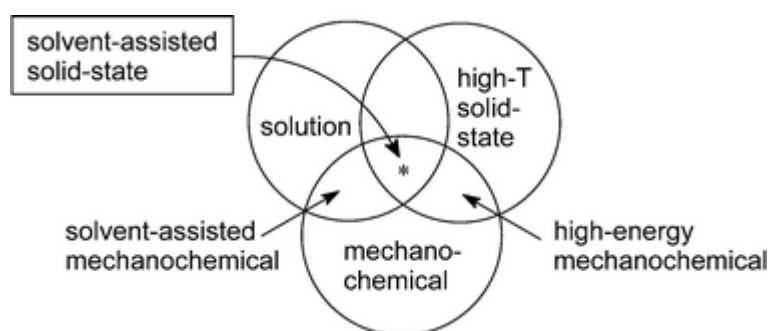


## Solvent-assisted solid-state synthesis: Separating the chemical from the mechanical in mechanochemical synthesis

*Chemical Communications* (16), pp. 2168-2170 (2009) [10.1039/b822370j](https://doi.org/10.1039/b822370j)

Bowmaker, G.A., Hanna, J.V., Skelton, B.W., White, A.H.

High-yielding syntheses involving reactions in the diffusion zone between solid reactants are demonstrated in studies of complex formation between copper(I) thiocyanate and ethylenethiourea.



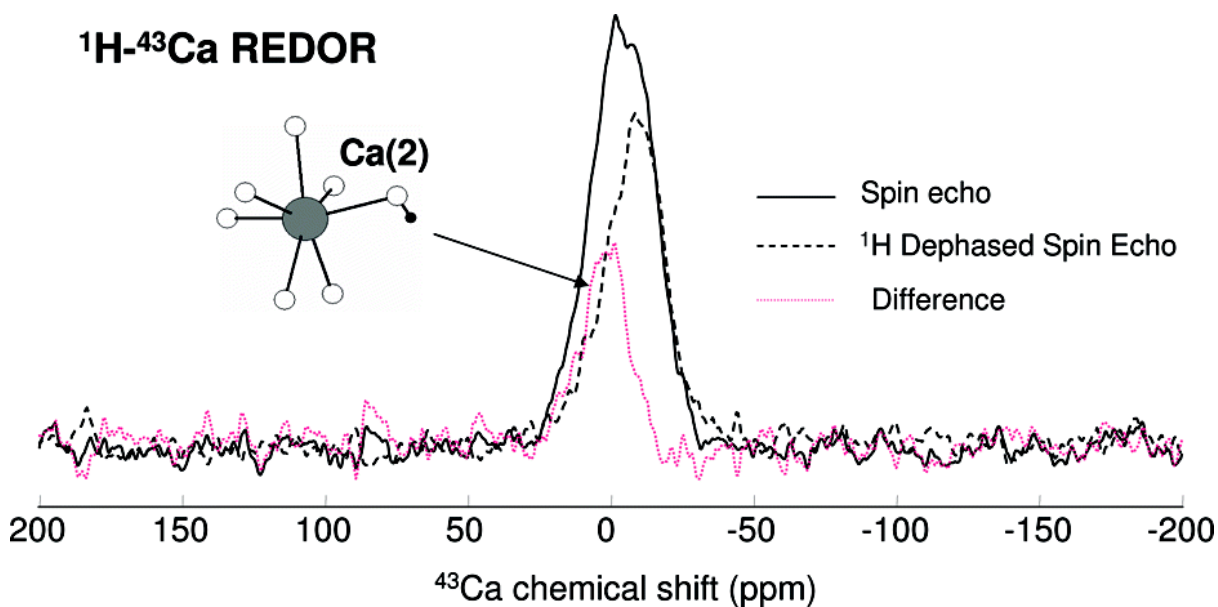
## A High-Resolution $^{43}\text{Ca}$ Solid-State NMR Study of the Calcium Sites of Hydroxyapatite

*J. Am. Chem. Soc.*, 2008, 130 (8), pp 2412–2413

[10.1021/ja710557t](https://doi.org/10.1021/ja710557t)

Laurencin, D; Wong, A; Hanna, JV; Dupree, R; Smith, ME

High resolution  $^{43}\text{Ca}$  solid-state NMR studies of hydroxyapatite ( $\text{Ca}_{10}(\text{PO}_4)_6(\text{OH})_2$ ) were performed at 14.1 T. The two crystallographically distinct calcium sites were unequivocally resolved by a triple-quantum magic angle spinning experiment, and the unambiguous assignment of the signals was possible using  $^1\text{H}$ - $^{43}\text{Ca}$  rotational echo double resonance and  $^1\text{H}$ - $^{43}\text{Ca}$  cross polarization magic angle spinning experiments.

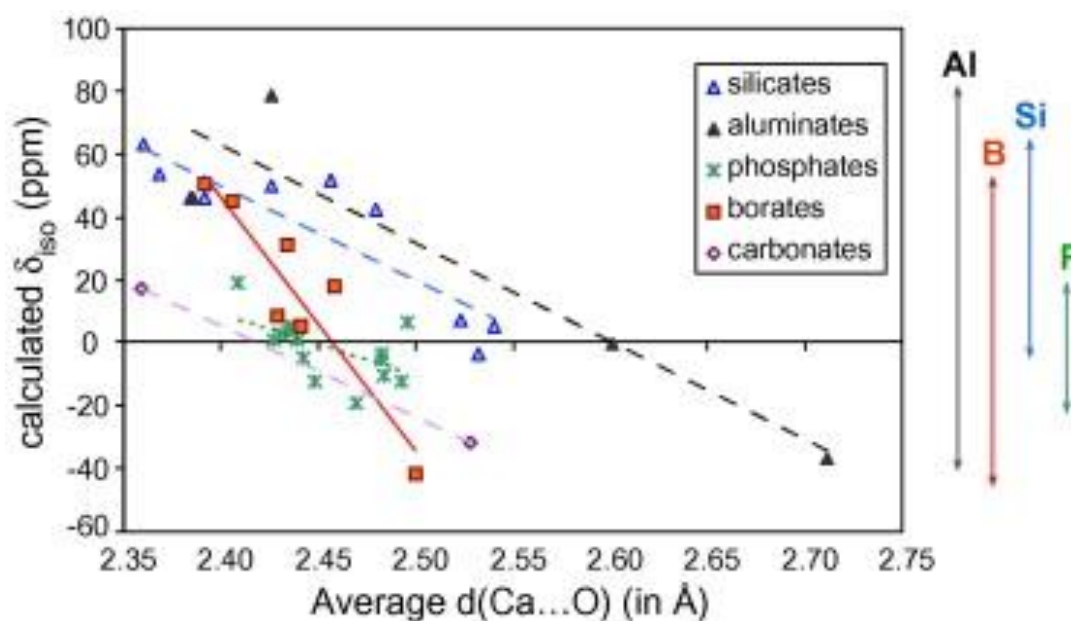


## New perspectives on calcium environments in inorganic materials containing calcium–oxygen bonds: A combined computational–experimental $^{43}\text{Ca}$ NMR approach

*Chemical Physics Letters* 464, 42–48 (2008) [10.1016/j.cplett.2008.09.004](https://doi.org/10.1016/j.cplett.2008.09.004)

C. Gervais, D. Laurencin, A. Wong, F. Pourpoint, J. Labram, B. Woodward, A. P. Howes, K. J. Pike, R. Dupree, F. Mauri, C. Bonhomme & M. E. Smith

The potential of a combined experimental–computational  $^{43}\text{Ca}$  solid state NMR approach for the structural analysis of different families of inorganic compounds (calcium phosphates, silicates, aluminates and borates) has been investigated. Natural-abundance  $^{43}\text{Ca}$  NMR data of six crystalline calcium phosphates is reported. DFT periodic calculations of  $^{43}\text{Ca}$  NMR parameters of an extensive number of Ca–O inorganic species have been performed, showing that the isotropic chemical shift of calcium can accurately be predicted. A strong dependence of the isotropic chemical shift on the average Ca···O bond distance and on the nature of the associated oxoanion is found.



Correlation between the computed  $^{43}\text{Ca}$  isotropic chemical shifts and the mean Ca···O bond distance in a series of calcium-inorganic species. The double arrows to the right indicate the range of variation of  $\delta_{\text{iso}}$  for each one of the families considered. The slopes correspond to the linear fits for the different families, the values found being  $-300 \text{ ppm } \text{\AA}^{-1}$  for silicates,  $-190 \text{ ppm } \text{\AA}^{-1}$  for phosphates,  $-310 \text{ ppm } \text{\AA}^{-1}$  for aluminates, and  $-810 \text{ ppm } \text{\AA}^{-1}$  for borates.

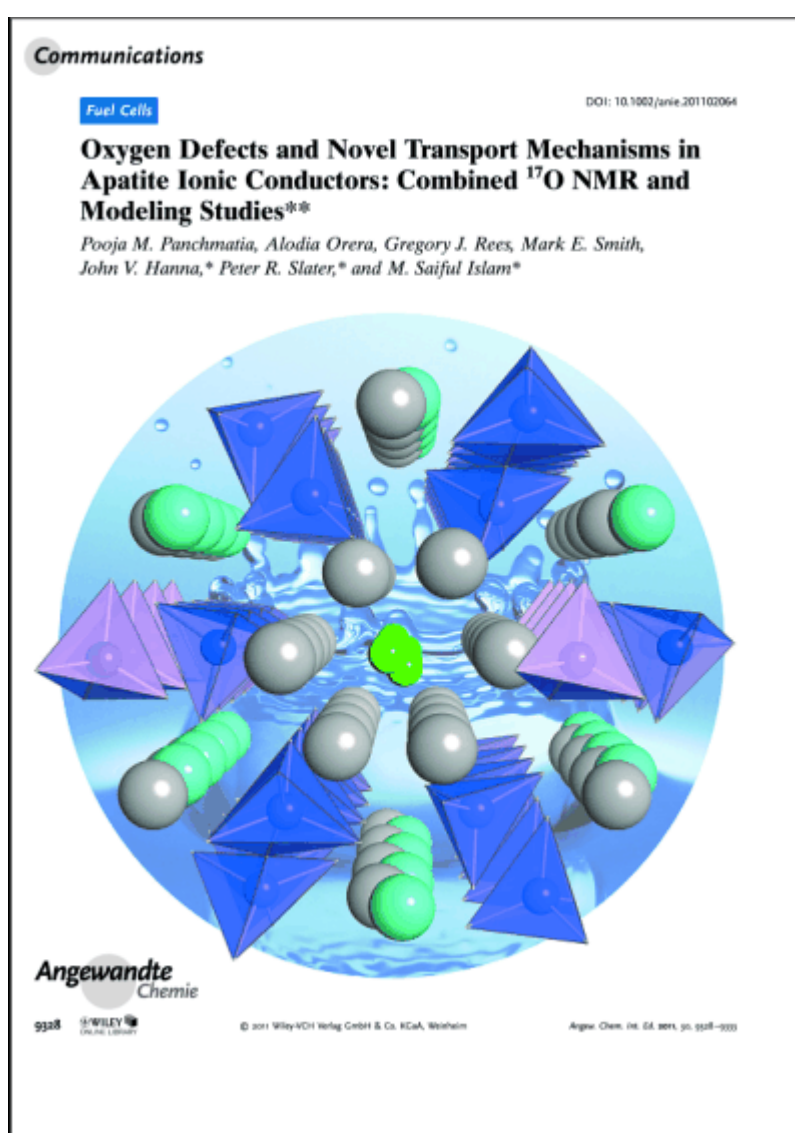
## Oxygen Defects and Novel Transport Mechanisms in Apatite Ionic Conductors: Combined $^{17}\text{O}$ NMR and Modeling Studies

Angewandte Chemie International Edition 50 , 932 (2011)

[10.1002/anie.201102064](https://doi.org/10.1002/anie.201102064)

Panchmatia, PM; Orera, A; Rees, GJ; Smith, ME; Hanna, JV; Slater, PR; Islam, MS

**Germanium-based apatite** compounds are fast oxide-ion conductors for potential use in fuel cells. A combination of solid-state  $^{17}\text{O}$  NMR spectroscopy, atomistic modeling, and DFT techniques help to elucidate oxygen defect sites and novel cooperative mechanisms of ion conduction. The picture shows oxygen diffusion in the studied apatite compound from molecular dynamics simulations.

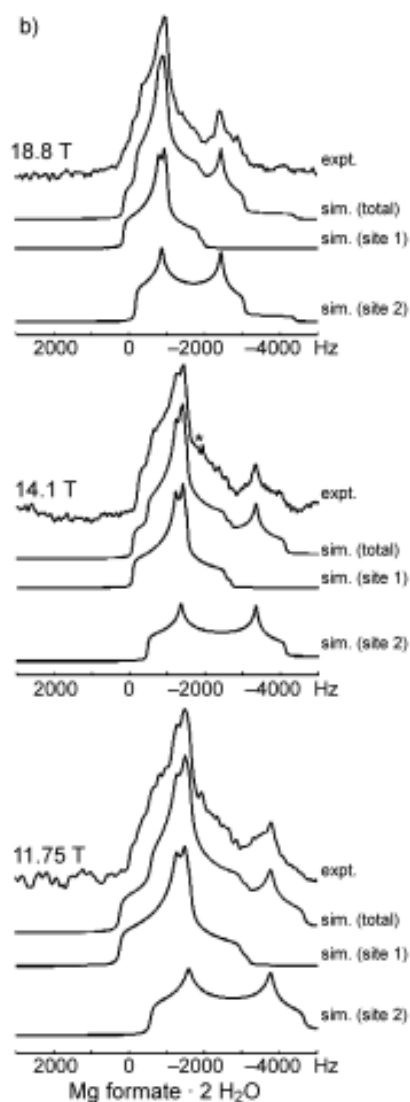


## Natural Abundance $^{25}\text{Mg}$ Solid-State NMR of Mg Oxyanion Systems: A Combined Experimental and Computational Study

*Chemistry - A European Journal* 15 (38), pp. 9785-9798 (2009) [10.1002/chem.200900346](https://doi.org/10.1002/chem.200900346)

Cahill, LS; Hanna, JV; Wong, A; Freitas, JCC; Yates, JR; Harris, RK; Smith, ME

Solid-state  $^{25}\text{Mg}$  magic angle spinning nuclear magnetic resonance (MAS NMR) data are reported from a range of organic and inorganic magnesium–oxyanion compounds at natural abundance. To constrain the determination of the NMR interaction parameters ( $\delta_{\text{iso}}$ ,  $\chi_{\text{Q}}$ ,  $\eta_{\text{Q}}$ ) data have been collected at three external magnetic fields (11.7, 14.1 and 18.8T). Corresponding NMR parameters have also been calculated by using density functional theory (DFT) methods using the GIPAW approach, with good correlations being established between experimental and calculated values of both  $\chi_{\text{Q}}$  and  $\delta_{\text{iso}}$ . These correlations demonstrate that the  $^{25}\text{Mg}$  NMR parameters are very sensitive to the structure, with small changes in the local  $\text{Mg}^{2+}$  environment and the overall hydration state profoundly affecting the observed spectra. The observations suggest that  $^{25}\text{Mg}$  NMR spectroscopy is a potentially potent probe for addressing some key problems in inorganic materials and of metal centres in biologically relevant molecules.



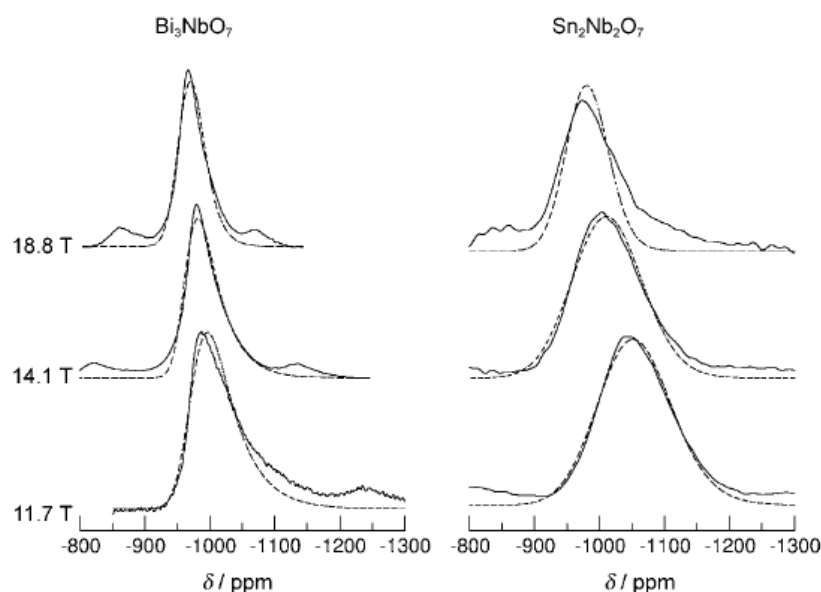
Experimental and simulated natural abundance  $^{25}\text{Mg}$  MAS NMR spectra with increasing magnetic field for Mg formate dihydrate. The experimental spectra, shown in the upper trace of each part, were acquired under ambient bearing gas temperature, with MAS at 3–10 kHz.

## A $^{93}\text{Nb}$ Solid-State NMR and Density Functional Theory Study of Four- and Six-Coordinate Niobate Systems

*Chemistry - A European Journal* 16 (10), pp. 3222-3239 (2010) [10.1002/chem.200901581](https://doi.org/10.1002/chem.200901581)

Hanna, JV; Pike, KJ ; Charpentier, T ; Kemp, TF ; Smith, ME ; Lucier, BEG; Schurko, RW ; Cahill, LS

A variable  $B_0$  field static (broadline) NMR study of a large suite of niobate materials has enabled the elucidation of high-precision measurement of  $^{93}\text{Nb}$  NMR interaction parameters such as the isotropic chemical shift ( $\delta_{\text{iso}}$ ), quadrupole coupling constant and asymmetry parameter ( $C_Q$  and  $\eta_Q$ ), chemical shift span/anisotropy and skew/asymmetry ( $\Omega/\Delta\delta$  and  $\kappa/\eta_\delta$ ) and Euler angles ( $\alpha, \beta, \gamma$ ) describing the relative orientation of the quadrupolar and chemical shift tensorial frames. These measurements have been augmented with ab initio DFT calculations by using WIEN2k and NMR-CASTEP codes, which corroborate these reported values. Unlike previous assertions made about the inability to detect CSA (chemical shift anisotropy) contributions from  $\text{Nb}^{\text{V}}$  in most oxo environments, this study emphasises that a thorough variable  $B_0$  approach coupled with the VOCS (variable offset cumulative spectroscopy) technique for the acquisition of undistorted broad ( $-1/2 \leftrightarrow +1/2$ ) central transition resonances facilitates the unambiguous observation of both quadrupolar and CSA contributions within these  $^{93}\text{Nb}$  broadline data. These measurements reveal that the  $^{93}\text{Nb}$  electric field gradient tensor is a particularly sensitive measure of the immediate and extended environments of the  $\text{Nb}^{\text{V}}$  positions, with  $C_Q$  values in the 0 to >80 MHz range being measured; similarly, the  $\delta_{\text{iso}}$  (covering an approximately 250 ppm range) and  $\Omega$  values (covering a 0 to approximately 800 ppm range) characteristic of these niobate systems are also sensitive to structural disposition. However, their systematic rationalisation in terms of the Nb—O bond angles and distances defining the immediate  $\text{Nb}^{\text{V}}$  oxo environment is complicated by longer-range influences that usually involve other heavy elements comprising the structure. It has also been established in this study that the best computational method(s) of analysis for the  $^{93}\text{Nb}$  NMR interaction parameters generated here are the all-electron WIEN2k and the gauge included projector augmented wave (GIPAW) NMR-CASTEP DFT approaches, which account for the short- and long-range symmetries, periodicities and interaction-potential characteristics for all elements (and particularly the heavy elements) in comparison with Gaussian 03 methods, which focus on terminated portions of the total structure.

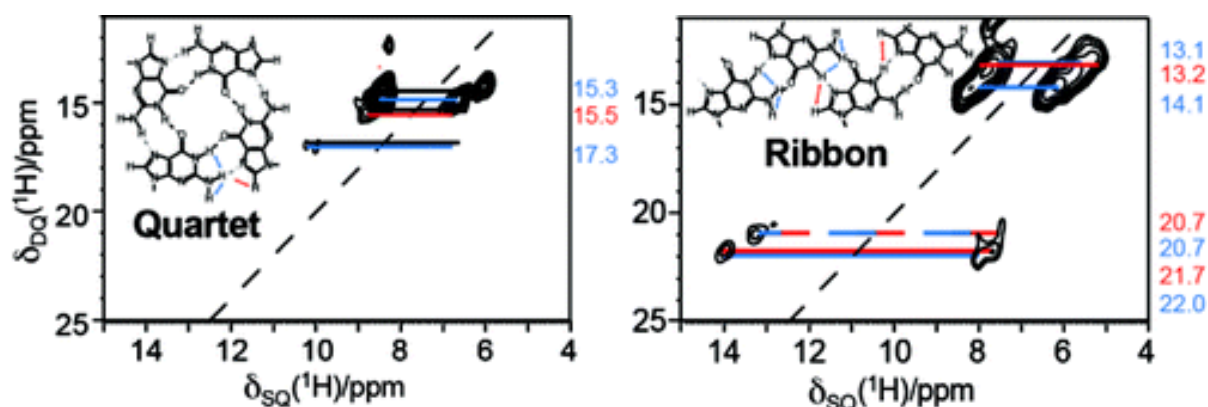


## Identifying Guanosine Self Assembly at Natural Isotopic Abundance by High-Resolution $^1\text{H}$ and $^{13}\text{C}$ Solid-State NMR Spectroscopy

*J. Am. Chem. Soc.* 133 (49), pp. 19777-19795 (2011) [10.1021/ja206516u](https://doi.org/10.1021/ja206516u)

Webber, A.L., Masiero, S, Pieraccini, S., Burley, J.C., Tatton, A.S., Iuga, D., Pham, T.N., Spada, G.P., Brown, S.P.

By means of the  $^1\text{H}$  chemical shifts and the proton–proton proximities as identified in  $^1\text{H}$  double-quantum (DQ) combined rotation and multiple-pulse spectroscopy (CRAMPS) solid-state NMR correlation spectra, ribbon-like and quartet-like self-assembly can be identified for guanosine derivatives without isotopic labeling for which it was not possible to obtain single crystals suitable for diffraction. Specifically, characteristic spectral fingerprints are observed for dG(C10) $_2$  and dG(C3) $_2$  derivatives, for which quartet-like and ribbon-like self-assembly has been unambiguously identified by  $^{15}\text{N}$  refocused INADEQUATE spectra in a previous study of  $^{15}\text{N}$ -labeled derivatives (Pham, T. N.; et al. *J. Am. Chem. Soc.* **2005**, *127*, 16018). The NH  $^1\text{H}$  chemical shift is observed to be higher (13–15 ppm) for ribbon-like self-assembly as compared to 10–11 ppm for a quartet-like arrangement, corresponding to a change from NH $\cdots$ N to NH $\cdots$ O intermolecular hydrogen bonding. The order of the two NH $_2$  $^1\text{H}$  chemical shifts is also inverted, with the NH $_2$  proton closest in space to the NH proton having a higher or lower  $^1\text{H}$  chemical shift than that of the other NH $_2$  proton for ribbon-like as opposed to quartet-like self-assembly. For the dG(C3) $_2$  derivative for which a single-crystal diffraction structure is available, the distinct resonances and DQ peaks are assigned by means of gauge-including projector-augmented wave (GIPAW) chemical shift calculations. In addition,  $^{14}\text{N}$ – $^1\text{H}$  correlation spectra obtained at 850 MHz under fast (60 kHz) magic-angle spinning (MAS) confirm the assignment of the NH and NH $_2$  chemical shifts for the dG(C3) $_2$  derivative and allow longer range through-space N $\cdots$ H proximities to be identified, notably to the N7 nitrogens on the opposite hydrogen-bonding face.

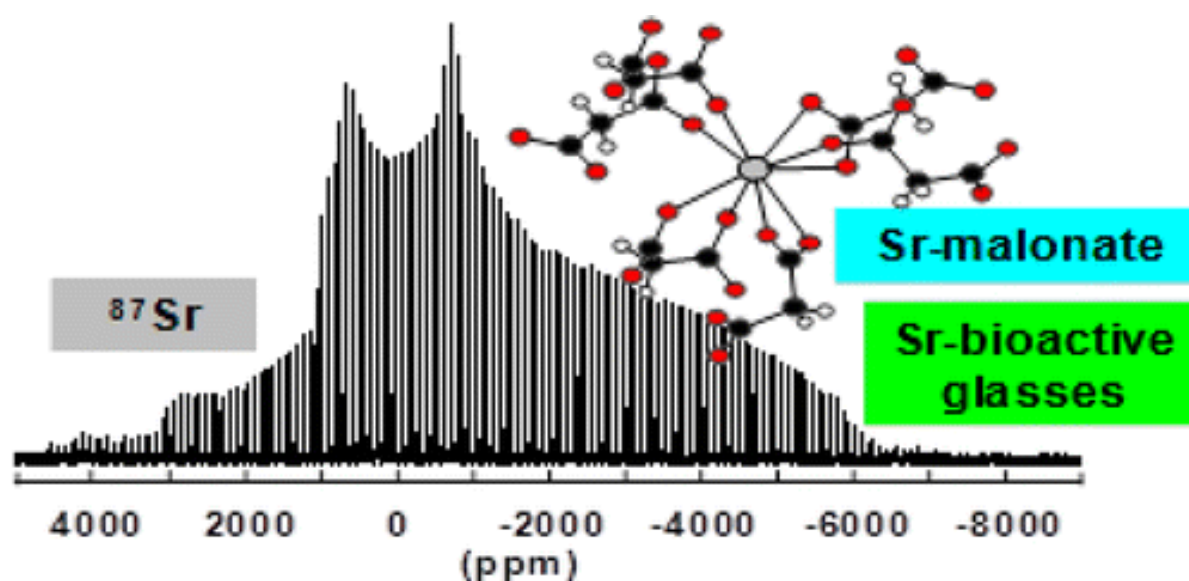


## **<sup>87</sup>Sr solid-state NMR as a structurally sensitive tool for the investigation of materials: Antiosteoporotic pharmaceuticals and bioactive glasses**

*J. Am. Chem. Soc.* 134 (30) , pp. 12611-12628 (2012) [10.1021/ja303505g](https://doi.org/10.1021/ja303505g)

Bonhomme, C. , Gervais, C, Folliet, N., Pourpoint, F., Coelho Diogo, C., Lao, J., Jallot, E., Lacroix, J, Nedelec, J.-M.d, Iuga, D., Hanna, J.V., Smith, M.E., Xiang, Y., Du, J., Laurencin, D.

Strontium is an element of fundamental importance in biomedical science. Indeed, it has been demonstrated that Sr<sup>2+</sup> ions can promote bone growth and inhibit bone resorption. Thus, the oral administration of Sr-containing medications has been used clinically to prevent osteoporosis, and Sr-containing biomaterials have been developed for implant and tissue engineering applications. The bioavailability of strontium metal cations in the body and their kinetics of release from materials will depend on their local environment. It is thus crucial to be able to characterize, in detail, strontium environments in disordered phases such as bioactive glasses, to understand their structure and rationalize their properties. In this paper, we demonstrate that <sup>87</sup>Sr NMR spectroscopy can serve as a valuable tool of investigation. First, the implementation of high-sensitivity <sup>87</sup>Sr solid-state NMR experiments is presented using <sup>87</sup>Sr-labeled strontium malonate (with DFS (double field sweep), QCPMG (quadrupolar Carr–Purcell–Meiboom–Gill), and WURST (wideband, uniform rate, and smooth truncation) excitation). Then, it is shown that GIPAW DFT (gauge including projector augmented wave density functional theory) calculations can accurately compute <sup>87</sup>Sr NMR parameters. Last and most importantly, <sup>87</sup>Sr NMR is used for the study of a (Ca,Sr)-silicate bioactive glass of limited Sr content (only ~9 wt %). The spectrum is interpreted using structural models of the glass, which are generated through molecular dynamics (MD) simulations and relaxed by DFT, before performing GIPAW calculations of <sup>87</sup>Sr NMR parameters. Finally, changes in the <sup>87</sup>Sr NMR spectrum after immersion of the glass in simulated body fluid (SBF) are reported and discussed.

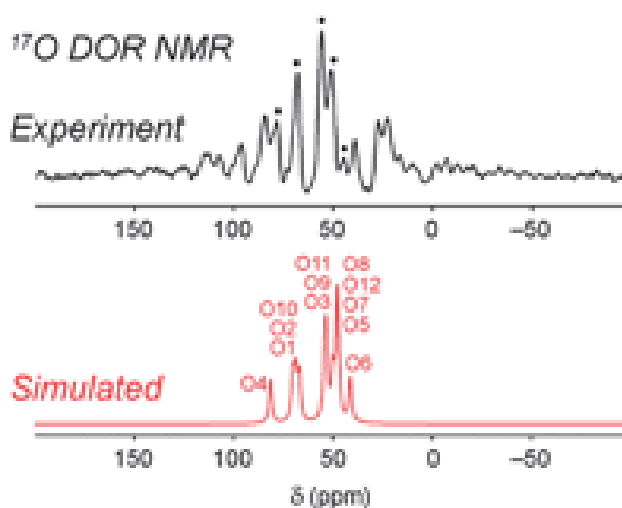
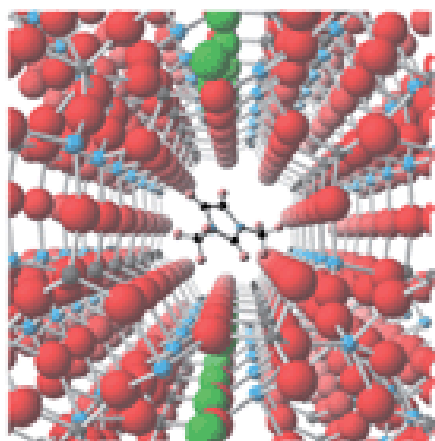


## Ionothermal $^{17}\text{O}$ enrichment of oxides using microlitre quantities of labelled water

*Chemical Science* 3 (7), pp. 2293-2300 (2012) [10.1039/c2sc20155k](https://doi.org/10.1039/c2sc20155k)

Griffin, J.M., Clark, L., Seymour, V.R., Aldous, D.W., Dawson, D.M., Iuga, D., Morris, R.E., Ashbrook, S.E.

We present an ionothermal-based method for the simple and low-cost enrichment in  $^{17}\text{O}$  of oxide materials. This is demonstrated for the case of SIZ-4, an ionothermally-prepared aluminophosphate framework with the CHA topology. A preliminary study of unenriched samples of SIZ-4 highlights the importance of the careful choice of template in order to obtain an ordered structure. We then show how an ionothermal synthesis procedure incorporating microlitre quantities of  $^{17}\text{O}$ -enriched  $\text{H}_2\text{O}$  enables as-prepared and calcined samples of SIZ-4 to be obtained with  $^{17}\text{O}$  enrichment levels that are sufficient to enable the recording of high-quality  $^{17}\text{O}$  solid-state NMR spectra. While second-order quadrupolar-broadened resonances are unresolved in  $^{17}\text{O}$  MAS NMR spectra,  $^{17}\text{O}$  double-rotation (DOR) and multiple-quantum (MQ)MAS NMR spectra reveal distinct resonances that are partially assigned by comparison with NMR parameters derived using first-principles calculations. The calculations also enable an investigation of the dependence of  $^{17}\text{O}$  NMR parameters on the local structural environment. We find that both the  $^{17}\text{O}$  isotropic chemical shift and quadrupolar coupling constant show clear dependencies on Al–O–P bond lengths, and angles and will therefore provide a sensitive probe of structure and geometry in aluminophosphate frameworks in future studies.

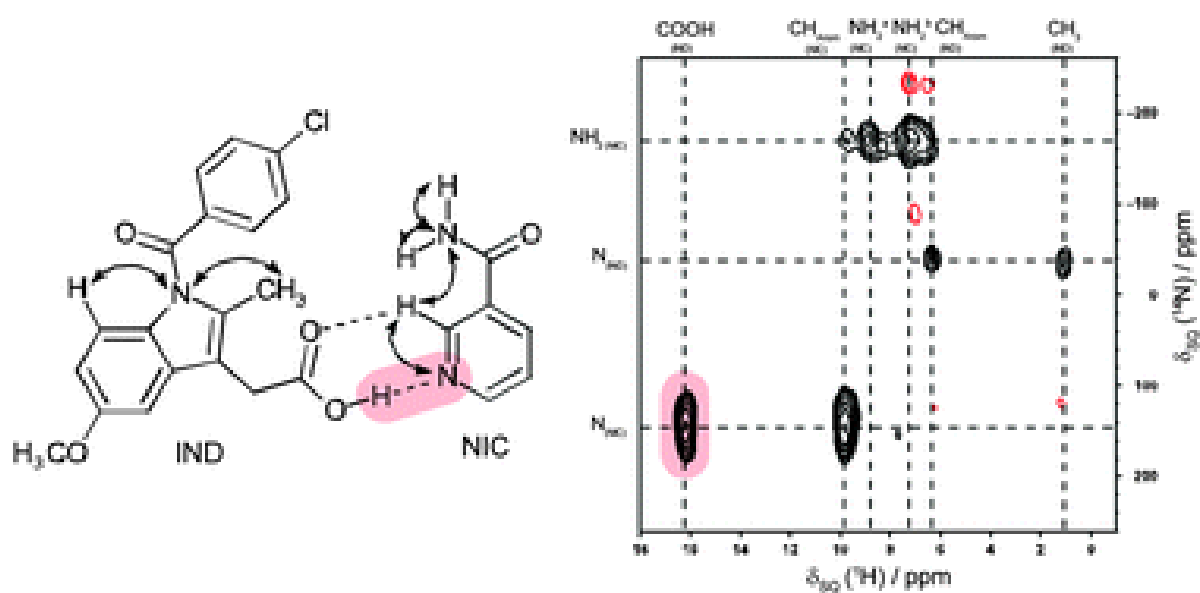


## Identifying the Intermolecular Hydrogen-Bonding Supramolecular Synthons in an Indomethacin-Nicotinamide Cocrystal by Solid-State NMR

*Chemical Communications* 48, 10844-6 (2012) [10.1039/C2CC36094B](https://doi.org/10.1039/C2CC36094B)

K. Maruyoshi, D. Iuga, O.N. Antzutkin, A. Alhalaweh, S.P. Velaga, S.P. Brown

Two-dimensional  $^1\text{H}$  double-quantum and  $^{14}\text{N}$ - $^1\text{H}$  &  $^1\text{H}$ - $^{13}\text{C}$  heteronuclear magic-angle spinning (MAS) NMR spectra recorded at natural isotopic abundance identify specific intermolecular  $\text{COOH}\cdots\text{N}_{\text{arom}}$  and  $\text{CH}_{\text{arom}}\cdots\text{O}=\text{C}$  hydrogen-bonding interactions in the solid-state structure of an indomethacin–nicotinamide cocrystal, thus additionally proving cocrystal formation.

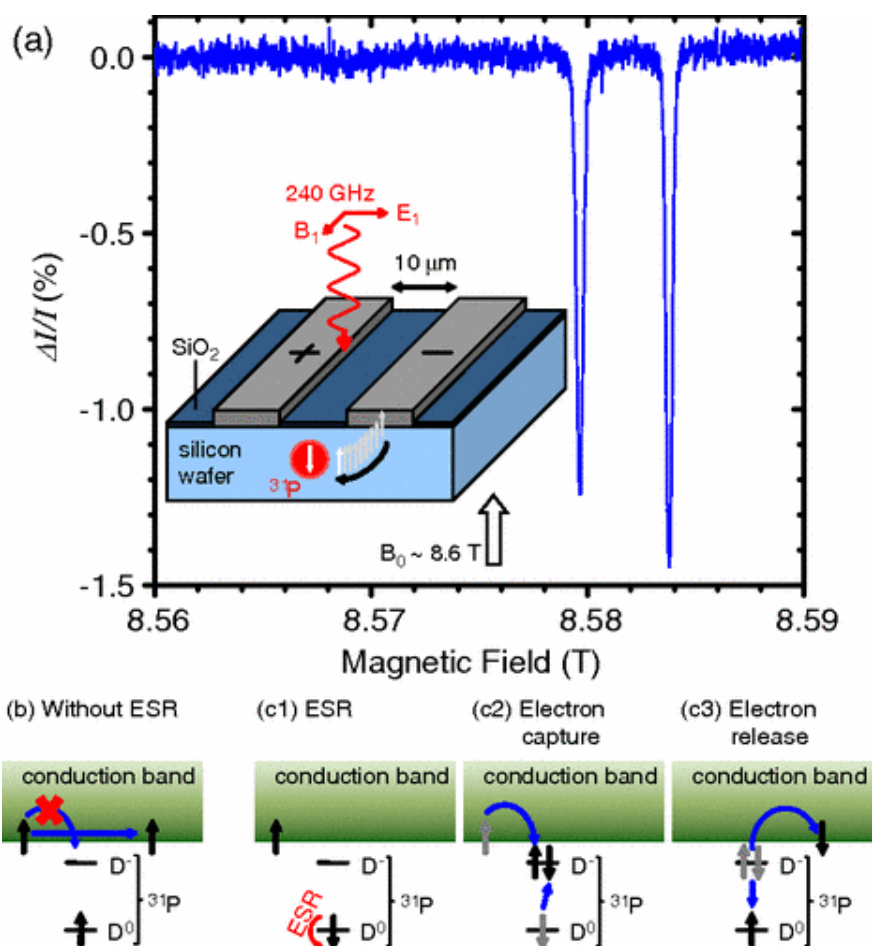


## Long-Lived Spin Coherence in Silicon with an Electrical Spin Trap Readout

*Phys. Rev. Lett.* 101, 207602 (2008) [10.1103/PhysRevLett.101.207602](https://doi.org/10.1103/PhysRevLett.101.207602)

G. W. Morley, D. R. McCamey, H. A. Seipel, L.-C. Brunel, J. van Tol, and C. Boehme

Pulsed electrically detected magnetic resonance of phosphorous ( $P_{31}$ ) in bulk crystalline silicon at very high magnetic fields ( $B_0 > 8.5$  T) and low temperatures ( $T = 2.8$  K) is presented. We find that the spin-dependent capture and reemission of highly polarized ( $>95\%$ ) conduction electrons by equally highly polarized  $P_{31}$  donor electrons introduces less decoherence than other mechanisms for spin-to-charge conversion. This allows the electrical detection of spin coherence times in excess of  $100 \mu\text{s}$ , 50 times longer than the previous maximum for electrically detected spin readout experiments.



(a) 240 GHz electrically detected magnetic resonance spectrum of phosphorus donors in crystalline silicon. The two large resonances are separated by 4.2 mT, a signature of the hyperfine interaction with a phosphorus nuclear spin. The inset is a schematic of our experiment, shown in more detail in Fig. 1 of Ref. 17. (b) The spin of an excess electron in the conduction band is initially aligned with the applied field so the Pauli exclusion principle means it avoids the coaligned phosphorus spin. (c1) ESR flips the phosphorus spin. (c2) The conduction electron is trapped, reducing the current. (c3) An electron is reemitted, leaving the electron that remains in the opposite spin state.

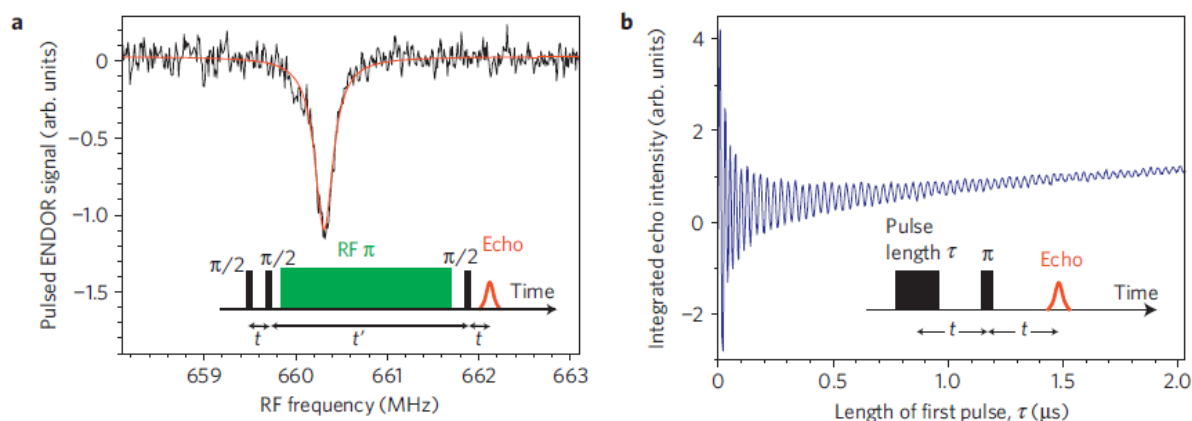
## The initialization and manipulation of quantum information stored in silicon by bismuth dopants

*Nature Materials* 9, 725 (2010)

[10.1038/nmat2828](https://doi.org/10.1038/nmat2828)

G W Morley, M Warner, A M Stoneham, P T Greenland, J van Tol, C W M Kay & G Aeppli

A prerequisite for exploiting spins for quantum data storage and processing is long spin coherence times. Phosphorus dopants in silicon (Si:P) have been favoured as hosts for such spins because of measured electron spin coherence times ( $T_2$ ) longer than any other electron spin in the solid state: 14 ms at 7 K with isotopically purified silicon. Heavier impurities such as bismuth in silicon (Si:Bi) could be used in conjunction with Si:P for quantum information proposals that require two separately addressable spin species. However, the question of whether the incorporation of the much less soluble Bi into Si leads to defect species that destroy coherence has not been addressed. Here we show that schemes involving Si:Bi are indeed feasible as the electron spin coherence time  $T_2$  is at least as long as for Si:P with non-isotopically purified silicon. We polarized the Si:Bi electrons and hyperpolarized the  $I=9/2$  nuclear spin of  $^{209}\text{Bi}$ , manipulating both with pulsed magnetic resonance. The larger nuclear spin means that a Si:Bi dopant provides a 20-dimensional Hilbert space rather than the four-dimensional Hilbert space of an  $I=1/2$  Si:P dopant.



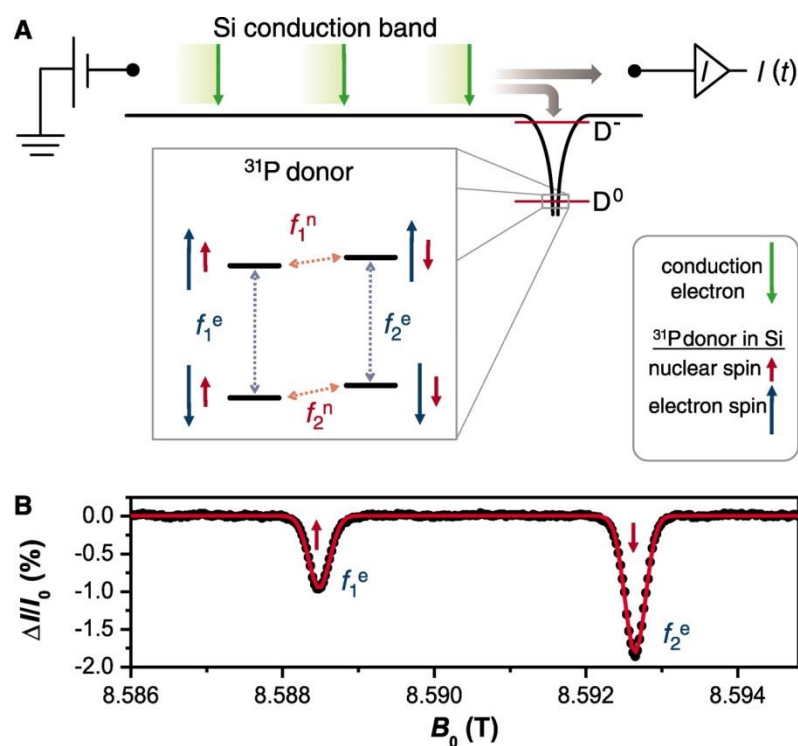
Qubit manipulation. **a**, Pulsed ENDOR manipulates the Bi nuclear spin as well as the electron spin. A microwave frequency of 240 GHz (black rectangles in inset that control the electron spin) was used at a temperature of 3 K and the length of the radiofrequency (RF) pulse (green rectangle that controls the nuclear spin) was 150  $\mu\text{s}$ . **b**, Rabi oscillations of the electron spin at 25 K with 9.7 GHz radiation. The spin is flipped using a pulse of  $\tau = 13$  ns duration.

## Electronic Spin Storage in an Electrically Readable Nuclear Spin Memory with a Lifetime >100 Seconds

Science 330, 1652-1656 (2010) [10.1126/science.1197931](https://doi.org/10.1126/science.1197931)

D.R. McCamey, J. van Tol, G.W. Morley & C. Boehme

Electron spins are strong candidates with which to implement spintronics because they are both mobile and able to be manipulated. The relatively short lifetimes of electron spins, however, present a problem for the long-term storage of spin information. We demonstrated an ensemble nuclear spin memory in phosphorous-doped silicon, which can be read out electrically and has a lifetime exceeding 100 seconds. The electronic spin information can be mapped onto and stored in the nuclear spin of the phosphorus donors, and the nuclear spins can then be repetitively read out electrically for time periods that exceed the electron spin lifetime. We discuss how this memory can be used in conjunction with other silicon spintronic devices.



The Si:P system used for implementing spin storage. (A) The singly occupied ( $D^0$ ) state of the phosphorus donor in silicon may capture a conduction electron and form a doubly occupied ( $D^-$ ) state only if they have opposite spin. Modifying the capture rate by manipulating the donor electron spin leads to a change in current through the silicon crystal. (B) Electron spin resonance reveals two resonances in the device current, due to the different donor nuclear-spin orientations, which couple to the electron spins through a contact hyperfine interaction.

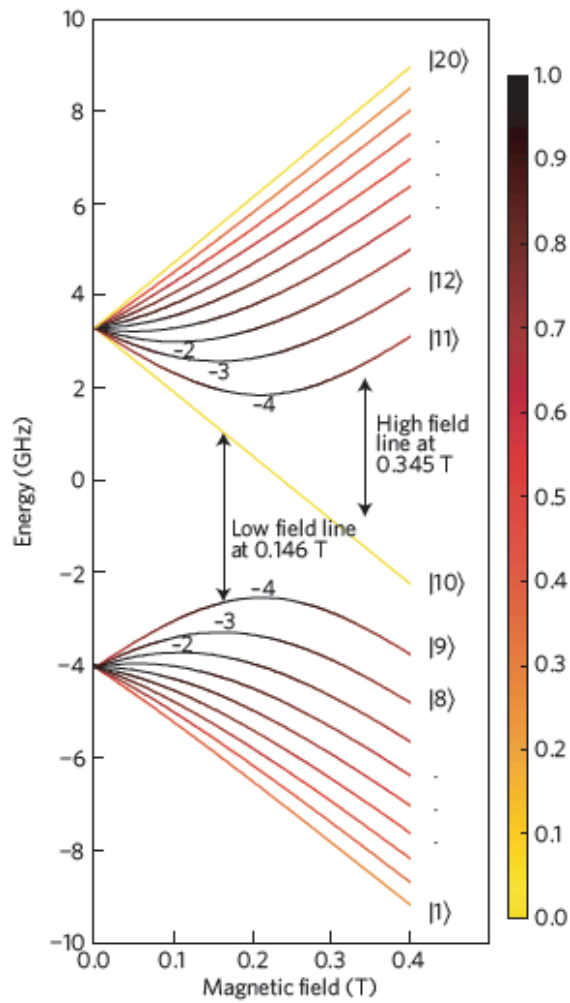
## Quantum control of hybrid nuclear–electronic qubits

*Nature Materials* 12, 103 (2013)

[10.1038/nmat3499](https://doi.org/10.1038/nmat3499)

G.W. Morley, P. Lueders, M. Hamed Mohammady, S.J. Balian, G. Aeppli, C.W.M. Kay, W.M. Witzel, G. Jeschke & T.S. Monteiro

Pulsed magnetic resonance allows the quantum state of electronic and nuclear spins to be controlled on the timescale of nanoseconds and microseconds respectively. The time required to flip dilute spins is orders of magnitude shorter than their coherence times leading to several schemes for quantum information processing with spin qubits. Instead, we investigate ‘hybrid nuclear–electronic’ qubits consisting of near 50:50 superpositions of the electronic and nuclear spin states. Using bismuth-doped silicon, we demonstrate quantum control over these states in 32 ns, which is orders of magnitude faster than previous experiments using pure nuclear states. The coherence times of up to 4 ms are five orders of magnitude longer than the manipulation times, and are limited only by naturally occurring  $^{29}\text{Si}$  nuclear spin impurities. We find a quantitative agreement between our experiments and an analytical theory for the resonance positions, as well as their relative intensities and Rabi oscillation frequencies. These results bring spins in a solid material a step closer to research on ion-trap qubits.



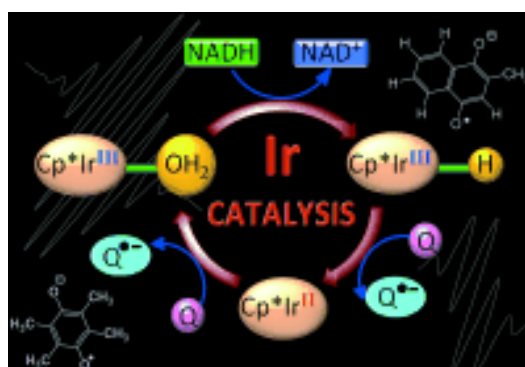
Spectroscopy of hybrid nuclear–electronic qubits. Analytical simulation of the 20 Si:Bi energy levels. The electron–nuclear hybridization is shown as a colour scale using concurrence $D_0$  (separable states, yellow) to 1 (fully hybridized, black). The two transitions that exist for 4 GHz excitation are shown with vertical arrows, and they link state 10 (which is always unhybridized) to states with large concurrences of 0.92 (state 9) and 0.76 (state 11). Magnetic field jumps could be used to move from a regime where the electronic and nuclear spins are not good quantum numbers to a regime where they are.

## Reduction of Quinones by NADH Catalyzed by Organoiridium Complexes

*Angewandte Chemie International Edition* 52 , 4194 (2013) [10.1002/anie.201300747](https://doi.org/10.1002/anie.201300747)

Liu, Z; Deeth, R. J; Butler, J. S; Habtemariam, A.; Newton, M.E; Sadler, P.J.

**One electron at a time:** Half-sandwich organometallic cyclopentadienyl-Ir<sup>III</sup> complexes containing N,N-chelated ligands can catalyze the reduction of quinones (Q), such as vitamin K<sub>3</sub>, to semiquinones (Q<sup>-</sup>) by coenzyme NADH (see picture). DFT calculations suggest that the mechanism involves hydride transfer followed by two one-electron transfers and the unusual Ir<sup>II</sup> oxidation state as a key transient intermediate.

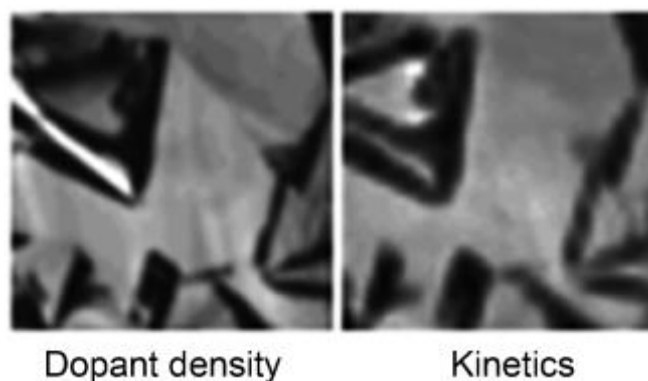


## Electrochemical mapping reveals direct correlation between heterogeneous electron-transfer kinetics and local density of states in diamond electrodes

*Angewandte Chemie International Edition* 51, 7002 (2012) [10.1002/anie.201203057](https://doi.org/10.1002/anie.201203057)

Patten, H.V., Meadows, K.E., Hutton, L.A., Iacobini, J.G., Battistel, D, McKelvey, K., Colburn, A.W., Newton, M.E., MacPherson, J.V. , Unwin, P.R

Conducting carbon materials: A multi-microscopy approach shows that local heterogeneous electron-transfer rates at conducting diamond electrodes correlate with the local density of electronic states. This model of electroactivity is of considerable value for the rational design of conducting diamond electrochemical technologies, and also provides key general insights on electrode structure controls in electrochemical kinetics (see picture).



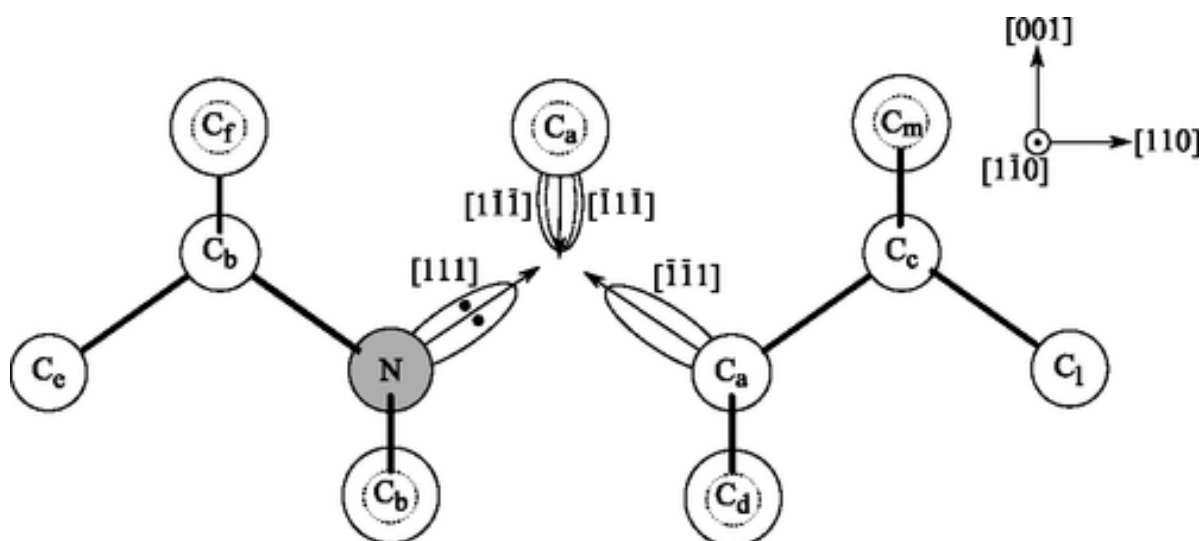
## Hyperfine interaction in the ground state of the negatively charged nitrogen vacancy center in diamond

*Physical Review B* 79 (7) , art. no. 075203 (2009)

[10.1103/PhysRevB.79.075203](https://doi.org/10.1103/PhysRevB.79.075203)

Felton, S; Edmonds, AM; Newton, ME; Martineau, PM; Fisher, D; Twitchen, DJ; Baker, JM

The N14, N15, and C13 hyperfine interactions in the ground state of the negatively charged nitrogen vacancy (NV<sup>-</sup>) center have been investigated using electron-paramagnetic-resonance spectroscopy. The previously published parameters for the N14 hyperfine interaction do not produce a satisfactory fit to the experimental NV<sup>-</sup> electron-paramagnetic-resonance data. The small anisotropic component of the NV<sup>-</sup> hyperfine interaction can be explained from dipolar interaction between the nitrogen nucleus and the unpaired-electron probability density localized on the three carbon atoms neighboring the vacancy. Optical spin polarization of the NV<sup>-</sup> ground state was used to enhance the electron-paramagnetic-resonance sensitivity enabling detailed study of the hyperfine interaction with C13 neighbors. The data confirmed the identification of three equivalent carbon nearest neighbors but indicated the next largest C13 interaction is with six, rather than as previously assumed three, equivalent neighboring carbon atoms.



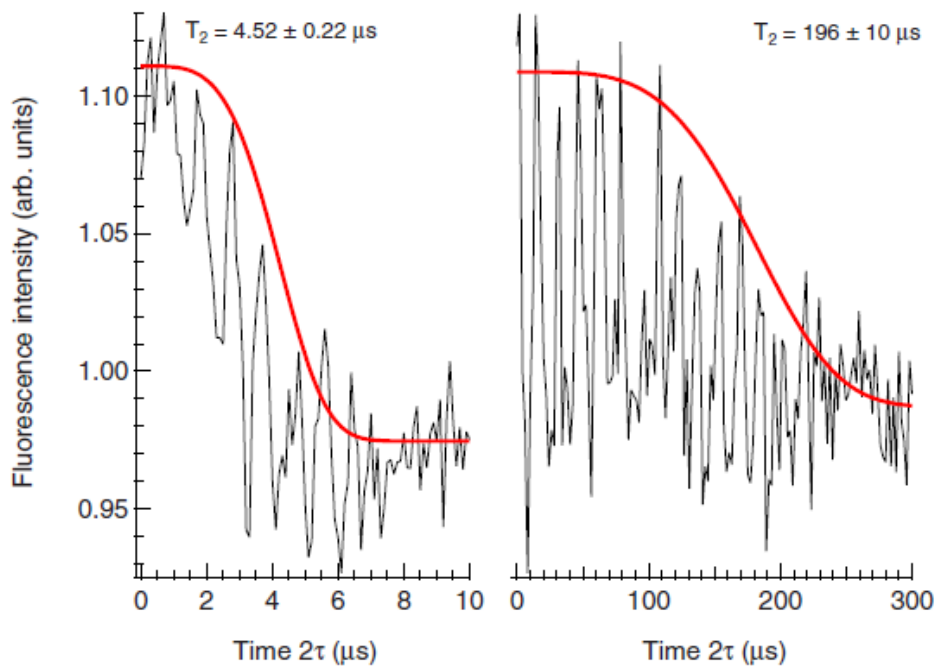
Projection of the nitrogen vacancy center in diamond on the (110) plane. The grey disc represents a nitrogen atom and the other circles represent carbon atoms. The larger circles represent carbon atoms located above the plane of the paper and the smaller dashed circles represent carbon atoms below the plane of the paper. The labels on the carbon atoms denote sets of equivalent neighbors.

## Increasing the coherence time of single electron spins in diamond by high temperature annealing

*Applied Physics Letters*, 97, 242511 (2010) [10.1063/1.3527975](https://doi.org/10.1063/1.3527975)

Naydenov, B; Reinhard, F; Lammler, A; Richter, V; Kalish, R; D'Haenens-Johansson, UFS; Newton, M;

Negatively charged nitrogen-vacancy (NV<sup>-</sup>) centers in diamond produced by ion implantation often show properties different from NVs created during the crystal growth. We observe that NVs created from nitrogen ion implantation at 30–300 keV show much shorter electron spin coherence time  $T_2$  as compared to the “natural” NVs and about 20% of them show switching from NV<sup>-</sup> to NV<sup>0</sup>. We show that annealing the diamond at  $T=1200$  °C substantially increases  $T_2$  and at the same time the fraction of NVs converting from NV<sup>-</sup> to NV<sup>0</sup> is greatly reduced.



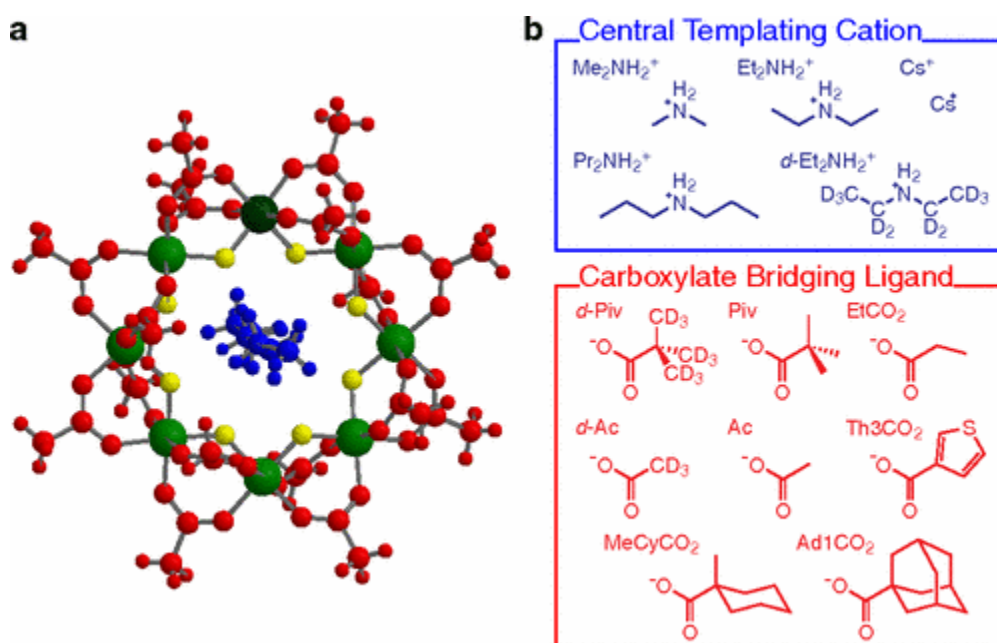
Hahn echo decays of single NV centers produced by implanting nitrogen ions with  $E=300$  keV showing two types of  $T_2$ : short (left) and long (right). The oscillations are induced by coupling to the  $^{15}\text{N}$  nitrogen nucleus (left) and  $^{13}\text{C}$  spin bath (right).

## Chemical Engineering of Molecular Qubits

*Physical Review Letters* 108, 107204 (2012) [10.1103/PhysRevLett.108.107204](https://doi.org/10.1103/PhysRevLett.108.107204)

C.J. Wedge, G.A. Timco, E.T. Spielberg, R.E. George, F. Tuna, S. Rigby, E.J.L. McInnes, R.E.P. Winpenny, S.J. Blundell, and A. Ardavan

We show that the electron spin phase memory time, the most important property of a molecular nanomagnet from the perspective of quantum information processing, can be improved dramatically by chemically engineering the molecular structure to optimize the environment of the spin. We vary systematically each structural component of the class of antiferromagnetic Cr<sub>7</sub>Ni rings to identify the sources of decoherence. The optimal structure exhibits a phase memory time exceeding 15 μs.



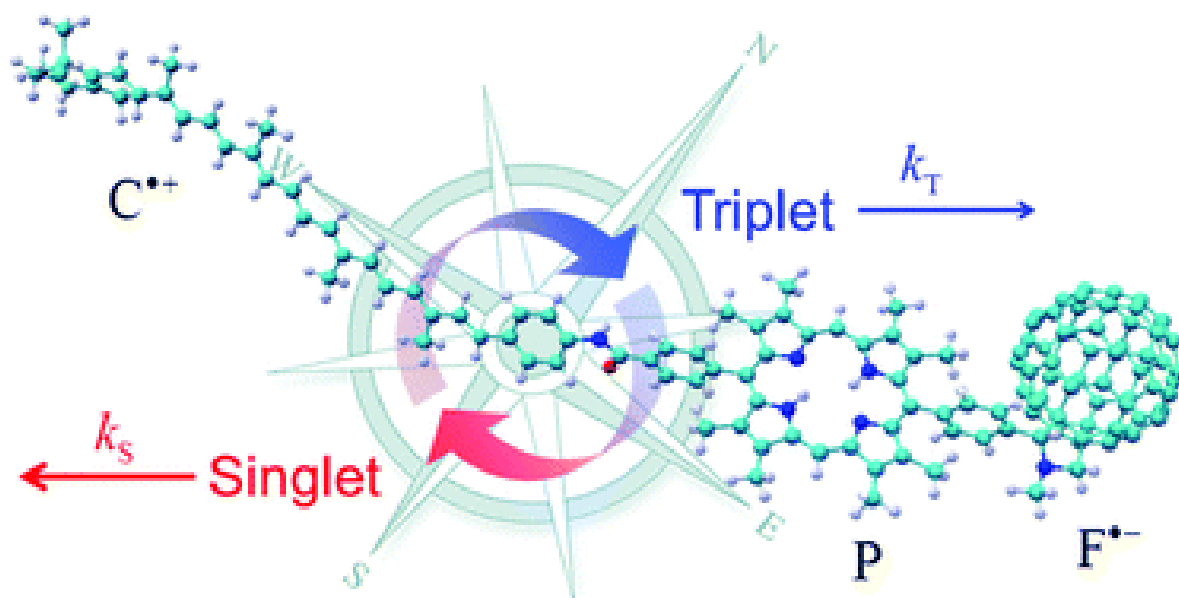
Structures of the Cr<sub>7</sub>Ni molecules. (a) Crystal structure of [Pr<sub>2</sub>NH<sub>2</sub>][Cr<sub>7</sub>NiF<sub>8</sub>Ac<sub>16</sub>]. The colored balls represent either different atom types: Cr (light green), Ni (dark green), F (yellow), or different interchangeable substituents: central templating cation (blue), carboxylate bridging ligand (red). (b) Appropriately color coded chemical structures of some possible variants with abbreviated names.

## Spin-selective recombination kinetics of a model chemical magnetoreceptor

*Chemical Communications* 47, 6563 (2011) [10.1039/C1CC11625H](https://doi.org/10.1039/C1CC11625H)

Maeda, K., Wedge, C.J., Storey, J.G., Henbest, K.B., Liddell, P.A., Kodis, G., Gust, D., Hore, P.J., Timmel, C.R.

We determine the spin-selective kinetics of a carotenoid–porphyrin–fullerene triad that has previously been used to establish the principle that a photochemical reaction could form the basis of the magnetic compass sensor of migratory birds and show that its magnetic sensitivity can be understood without invoking quantum Zeno effects.



## Materials Physics Cluster

❖ 12 Staff; 11 PDRA's; 21 PhDs;

❖ 449 articles; 4377 citations; £7.1 M grant awards; ~£9 M in-kind; 22 PhDs awarded

This cluster measures material properties on the atomic to mm length scales, with comprehensive facilities for X-ray studies, ultrafast THz spectroscopy, transport, magnetic, and non-contact ultrasound, with many at low-temperatures, in magnetic fields, and under pressure. It is a leading centre for single crystal growth, esp. using infra-red image furnaces. Interdisciplinary projects with Engineering & Chemistry are flourishing, as are collaborations with > 100 research groups world-wide and industrial partnerships. Cluster members are recognised as scientifically leading users of Central Facilities for neutron scattering, muon spectroscopy, X-ray studies, and high magnetic field measurements, with facility time valued in excess of £2 M p.a awarded at APS, BESSY, Diamond, ESRF, ILL, ISIS, NHFML, NSLS, PSI and Spring8. Warwick co-leads XMaS, which is the UK's flagship X-ray beamline for materials research at the ESRF and an EPSRC Mid-Range Facility.



In *strongly correlated electron systems* (**Balakrishnan, Duffy, Hase, Lees, Paul, Petrenko**), interesting and topical materials have been identified that can be grown and studied with these techniques e.g. muon spectroscopy & Fermi surface studies of exotic iron-based superconductors; pioneering investigations of the mixed state by small angle neutron scattering; frustrated magnetism in rare-earth and transition metal oxides; bulk and surface properties of topological insulators.



Research on the *structural physics of ferroic crystals* (**Thomas**) has become well known for the NBT and KNN families of lead-free piezo-electrics, and for contributions to understanding the archetypal PZT system. Novel X-ray and neutron diffraction techniques, optical birefringence imaging and SHG measurements have elicited the origins of enhanced piezoelectric properties. Research in non-linear optical materials, esp. lithium niobate-tantalate, led to a 2011 patent application. Extensive Central Facility use includes synchrotron radiation for spatially-coherent X-ray imaging of domains, building on Thomas's original method (*Nature* 1998). A significant addition has been attracting **Alexe** to focus on the physics and engineering of complex oxide thin films and nanoscale systems. He will address a large spectrum of research topics: quantum phenomena in ferroelectric/multiferroic tunnel junctions, abnormal photovoltaic effect, domain walls electronics. He is well known for closing the loop of structure-functional properties-device research, so close cooperation with Thomas on structure, McConville on surface analysis and Dixon on thin film piezoelectric devices and MEMS is anticipated. He will use his expertise to setup a nanofabrication lab and a nano-characterisation lab based on low temperature scanning probe microscopy. Two further activities were also initiated in 2013: in low-dimensional magnetism in molecular materials & thin-film heterostructures (**Goddard**); and in *ultrafast THz spectroscopy* as a probe of fundamental excitations in novel functional materials (**Lloyd-Hughes**), e.g. novel spin waves in magnetoelectric multiferroics.



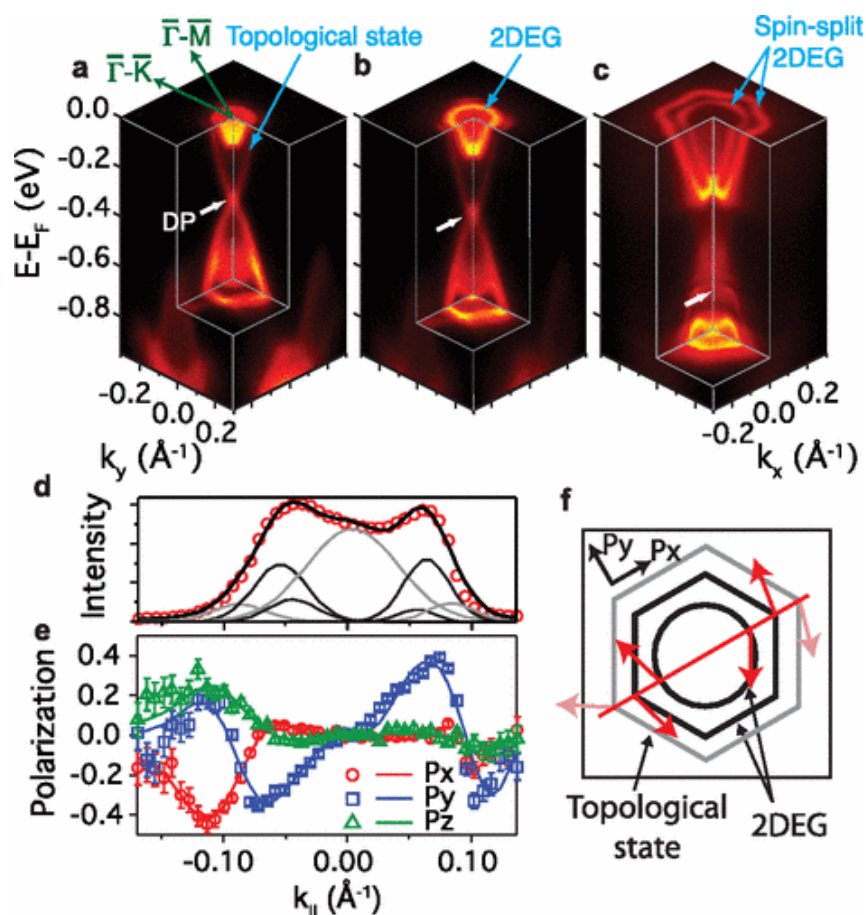
The *Ultrasound* group (**Dixon, Edwards**) focuses on the interaction of ultrasound with defects and on non-contact measurements of single crystals, establishing the UK's only such facility. Materials investigated cover magnetic rare-earths, organic superconductors and magnetocalorics, as well as ferrous metals. The group collaborates with academic institutions through the EPSRC *Research Centre for Non-Destructive Evaluation* and extensively with industry via research projects, a spin-out company (Sonemat Ltd) and by creating the *Centre for Industrial Ultrasonics*.

## Large Tunable Rashba Spin Splitting of a Two-Dimensional Electron Gas in $\text{Bi}_2\text{Se}_3$

*Phys. Rev. Lett.* 107, 096802 (2011) [10.1103/PhysRevLett.107.096802](https://doi.org/10.1103/PhysRevLett.107.096802)

P. D. C. King, R. C. Hatch, M. Bianchi, R. Ovsyannikov, C. Lupulescu, G. Landolt, B. Slomski, J. H. Dil, D. Guan, J. L. Mi, E. D. L. Rienks, J. Fink, A. Lindblad, S. Svensson, S. Bao, G. Balakrishnan, B. B. Iversen, J. Osterwalder, W. Eberhardt, F. Baumberger, and Ph. Hofmann

We report a Rashba spin splitting of a two-dimensional electron gas in the topological insulator  $\text{Bi}_2\text{Se}_3$  from angle-resolved photoemission spectroscopy. We further demonstrate its electrostatic control, and show that spin splittings can be achieved which are at least an order-of-magnitude larger than in other semiconductors. Together these results show promise for the miniaturization of spintronic devices to the nanoscale and their operation at room temperature.



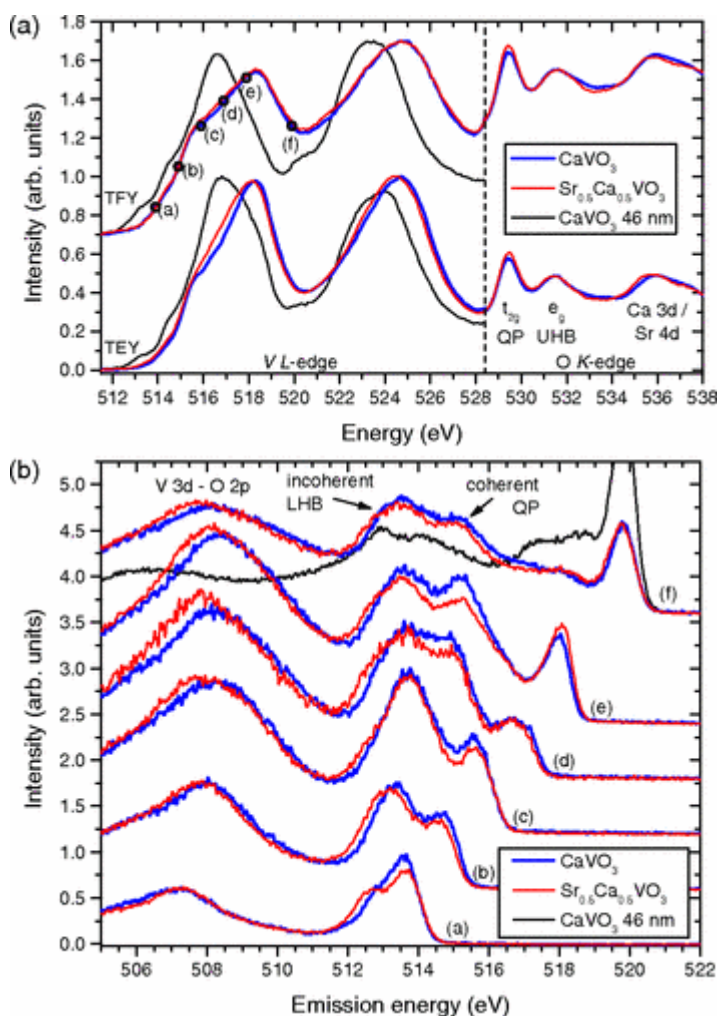
(a)–(c) Electronic structure of  $\text{Bi}_2\text{Se}_3$ , measured using time-of-flight ARPES at increasing times after cleaving the sample [marked in Fig. 4a] ( $h\nu=19.2$  eV,  $T=10$  K). (d) Spin-ARPES total intensity MDC at the Fermi level ( $h\nu=19.5$  eV,  $T=60$  K) along the  $T$ – $\bar{M}$  direction, and (e) the measured (points) and fitted (lines) radial ( $P_x$ ), tangential ( $P_y$ ), and out-of-plane ( $P_z$ ) components of the spin polarization along this cut. (f) Schematic representation of the in-plane component of the Fermi surface spin texture.

## Resonant Soft-X-Ray Emission as a Bulk Probe of Correlated Electron Behavior in Metallic $\text{Sr}_x\text{Ca}_{1-x}\text{VO}_3$

*Phys. Rev. Lett.* 111, 047402 (2013) [10.1103/PhysRevLett.111.047402](https://doi.org/10.1103/PhysRevLett.111.047402)

J. Laverock, B. Chen, K. E. Smith, R. P. Singh, G. Balakrishnan, M. Gu, J. W. Lu, S. A. Wolf, R. M. Qiao, W. Yang, and J. Adell

The evolution of electron correlation in  $\text{Sr}_x\text{Ca}_{1-x}\text{VO}_3$  has been studied using a combination of bulk-sensitive resonant soft x-ray emission spectroscopy, surface-sensitive photoemission spectroscopy, and *ab initio* band structure calculations. We show that the effect of electron correlation is enhanced at the surface. Strong incoherent Hubbard subbands are found to lie  $\sim 20\%$  closer in energy to the coherent quasiparticle features in surface-sensitive photoemission spectroscopy measurements compared with those from bulk-sensitive resonant soft x-ray emission spectroscopy, and a  $\sim 10\%$  narrowing of the overall bandwidth at the surface is also observed.



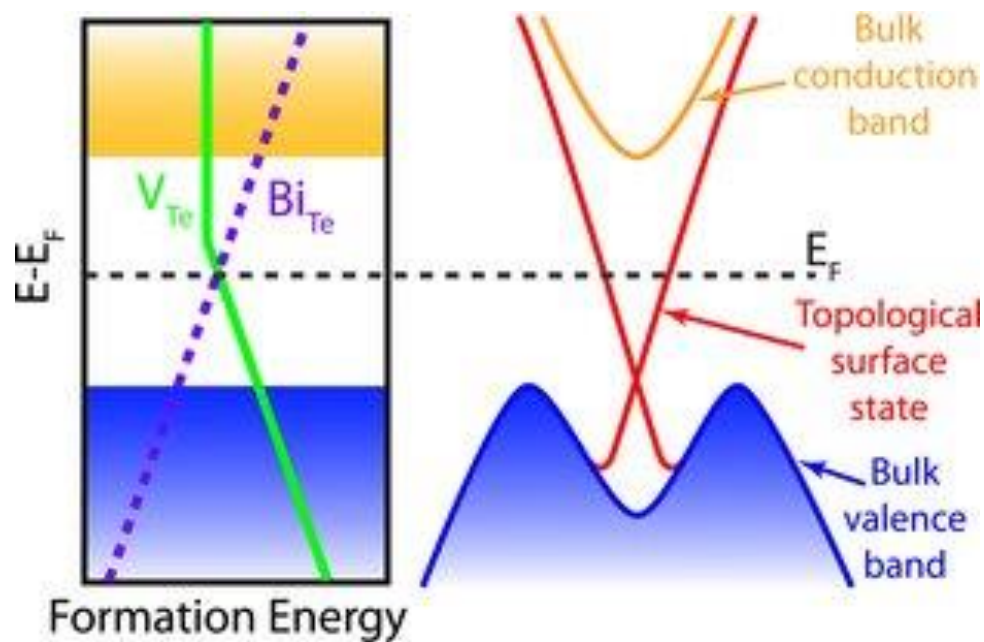
Bulk (a) XAS and (b) RXES measurements of CVO and SCVO. The spectra of a 46 nm thin film of CVO are also shown for comparison. The excitation energies used in the RXES measurements of (b) are shown by the circles in (a). The vertical line in (a) indicates separate V L-edge (left) and O K-edge (right) measurements, which have been separately scaled for clarity.

## Controlling Bulk Conductivity in Topological Insulators: Key Role of Anti-Site Defects

*Advanced Materials* 24, 2154 (2012) [10.1002/adma.201200187](https://doi.org/10.1002/adma.201200187)

Scanlon, D.O., King, P.D.C., Singh, R.P., De La Torre, A., Walker, S.M., Balakrishnan, G., Baumberger, F., Catlow, C.R.A.

Intrinsic topological insulators are realized by alloying  $\text{Bi}_2\text{Te}_3$  with  $\text{Bi}_2\text{Se}_3$ . Angle-resolved photoemission and bulk transport measurements reveal that the Fermi level is readily tuned into the bulk bandgap. First-principles calculations of the native defect landscape highlight the key role of anti-site defects for achieving this, and predict optimal growth conditions to realize maximally resistive topological insulators.

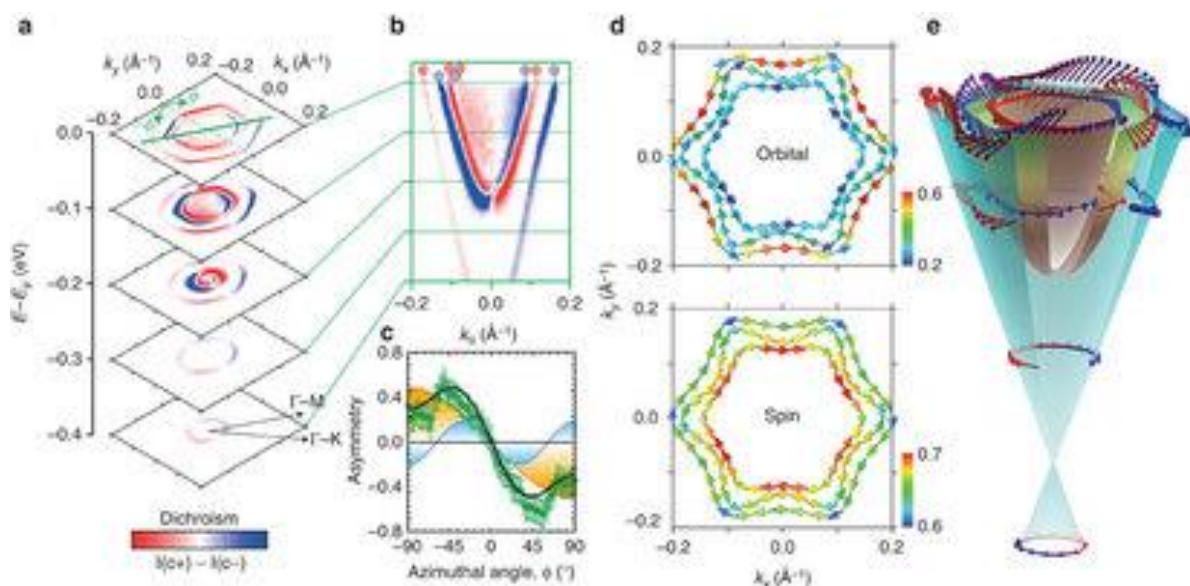


## Emergent quantum confinement at topological insulator surfaces

*Nature Communications* **3**, 1159 (2012) [10.1038/ncomms2162](https://doi.org/10.1038/ncomms2162)

M.S. Bahramy, P.D.C King, A. de la Torre, J. Chang, M. Shi, L. Patthey, G. Balakrishnan, Ph. Hofmann, R. Arita, N. Nagaosa & F. Baumberger

Bismuth-chalcogenides are model examples of three-dimensional topological insulators. Their ideal bulk-truncated surface hosts a single spin-helical surface state, which is the simplest possible surface electronic structure allowed by their non-trivial  $Z_2$  topology. However, real surfaces of such compounds, even if kept in ultra-high vacuum, rapidly develop a much more complex electronic structure whose origin and properties have proved controversial. Here we demonstrate that a conceptually simple model, implementing a semiconductor-like band bending in a parameter-free tight-binding supercell calculation, can quantitatively explain the entire measured hierarchy of electronic states. In combination with circular dichroism in angle-resolved photoemission experiments, we further uncover a rich three-dimensional spin texture of this surface electronic system, resulting from the non-trivial topology of the bulk band structure. Moreover, our study sheds new light on the surface-bulk connectivity in topological insulators, and reveals how this is modified by quantum confinement.



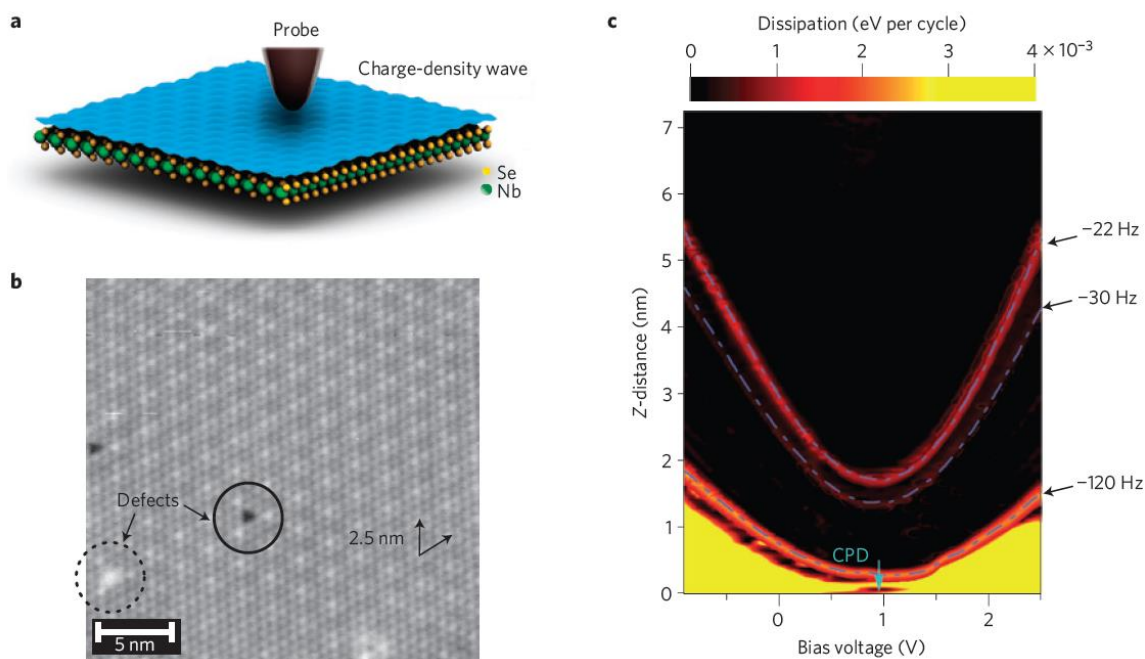
Three-dimensional orbital and spin texture of the topological and 2DEG states.

## Giant frictional dissipation peaks and charge-density-wave slips at the NbSe<sub>2</sub> surface

*Nature Materials* **13**, 173 (2014) [10.1038/nmat3836](https://doi.org/10.1038/nmat3836)

M. Langer, M. Kisiel, R. Pawlak, F. Pellegrini, G.E. Santoro, R. Buzio, A. Gerbi, G. Balakrishnan, A. Baratoff, E. Tosatti and E. Meyer

Understanding nanoscale friction and dissipation is central to nanotechnology. The recent detection of the electronic friction drop caused by the onset of superconductivity in Nb by means of an ultrasensitive non-contact pendulum atomic force microscope (AFM) raised hopes that a wider variety of mechanical-dissipation mechanisms become accessible. Here, we report a multiplet of AFM dissipation peaks arising a few nanometres above the surface of NbSe<sub>2</sub>—a layered compound exhibiting an incommensurate charge-density wave (CDW). Each peak appears at a well-defined tip–surface interaction force of the order of a nano-newton, and persists up to 70 K, where the short-range order of CDWs is known to disappear. Comparison of the measurements with a theoretical model suggests that the peaks are associated with local, tip-induced  $2\pi$  phase slips of the CDW, and that dissipation maxima arise from hysteretic behaviour of the CDW phase as the tip oscillates at specific distances where sharp local slips occur.



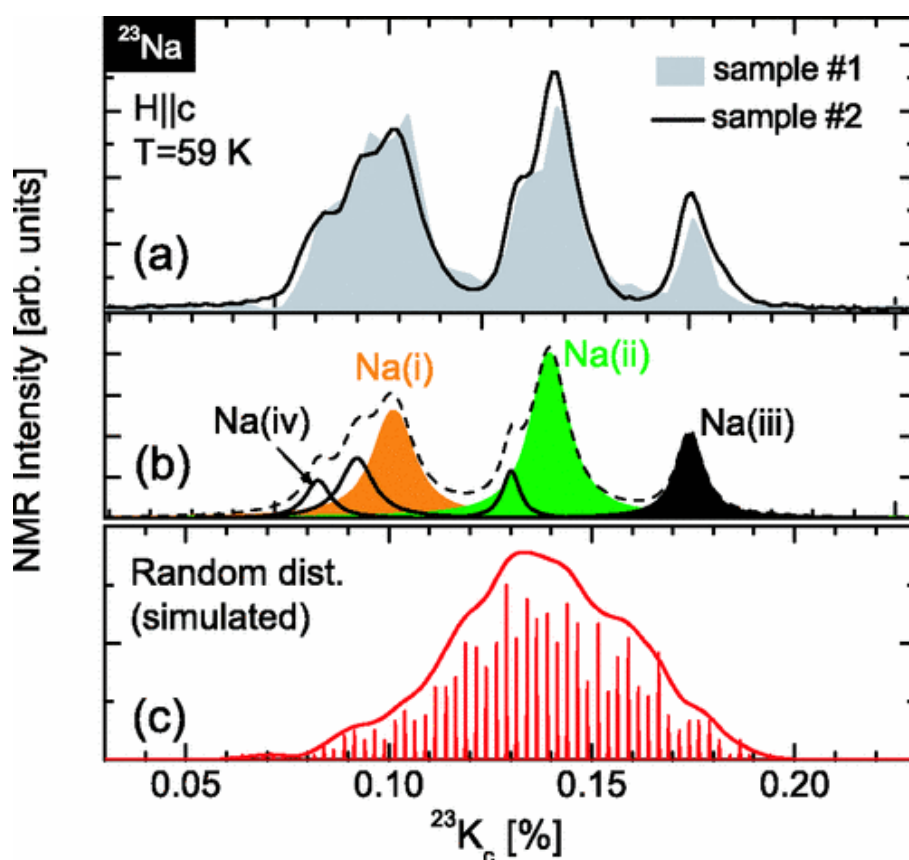
Observation of a charge-density wave on a NbSe<sub>2</sub> surface and accompanied non-contact friction. **a**, An oscillating AFM tip in proximity to the charge-density wave on the NbSe<sub>2</sub> surface. **b**, Constant-current STM image of the NbSe<sub>2</sub> surface showing a hexagonal CDW-induced Moiré pattern as well as two types of surface defect—adsorbed CO molecules (dashed circle) and Se atom vacancies (solid circle). **c**, Energy dissipation between the NbSe<sub>2</sub> surface and the pendulum-AFM tip versus tip–sample distance ( $Z$ ) and bias voltage  $V$ . Bright features on the image represent large non-contact friction.

## Electronic Texture of the Thermoelectric Oxide $\text{Na}_{0.75}\text{CoO}_2$

*Phys. Rev. Lett.* 100, 096405 (2008) [10.1103/PhysRevLett.100.096405](https://doi.org/10.1103/PhysRevLett.100.096405)

M.-H. Julien, C. de Vaulx, H. Mayaffre, C. Berthier, M. Horvatić, V. Simonet, J. Wooldridge, G. Balakrishnan, M. R. Lees, D. P. Chen, C. T. Lin, and P. Lejay

From  $^{59}\text{Co}$  and  $^{23}\text{Na}$  NMR, we demonstrate the impact of the  $\text{Na}^+$  vacancy ordering on the cobalt electronic states in  $\text{Na}_{0.75}\text{CoO}_2$ : at long time scales, there is neither a disproportionation into 75%  $\text{Co}^{3+}$  and 25%  $\text{Co}^{4+}$  states, nor a mixed-valence metal with a uniform  $\text{Co}^{3.25+}$  state. Instead, the system adopts an intermediate configuration in which 30% of the lattice sites form an ordered pattern of localized  $\text{Co}^{3+}$  states. Above 180 K, an anomalous mobility of specific  $\text{Na}^+$  sites is found to coexist with this electronic texture, suggesting that the formation of the latter may contribute to stabilizing the  $\text{Na}^+$  ordering. Control of the ion doping in these materials thus appears to be crucial for fine-tuning of their thermoelectric properties.



(a) Central lines ( $1/2 \leftrightarrow -1/2$  transitions) of the spectrum in two different single crystals at  $T=30$  K. (b) Fit to six lines, having a similar quadrupole frequency  $^{23}\nu_c \approx 1.9$  MHz to within  $\pm 10\%$ . (c) Simulated  $^{23}\text{Na}$  NMR spectrum (line) obtained by a Gaussian broadening of the histogram computed for randomly distributed magnetic and nonmagnetic Co sites. Assuming two different types of magnetic sites further increases the number of lines. Hyperfine couplings to first neighbors  $a$  and to second neighbors  $b=a/2$  were assumed to be identical for the Na(1) and Na(2) sites.

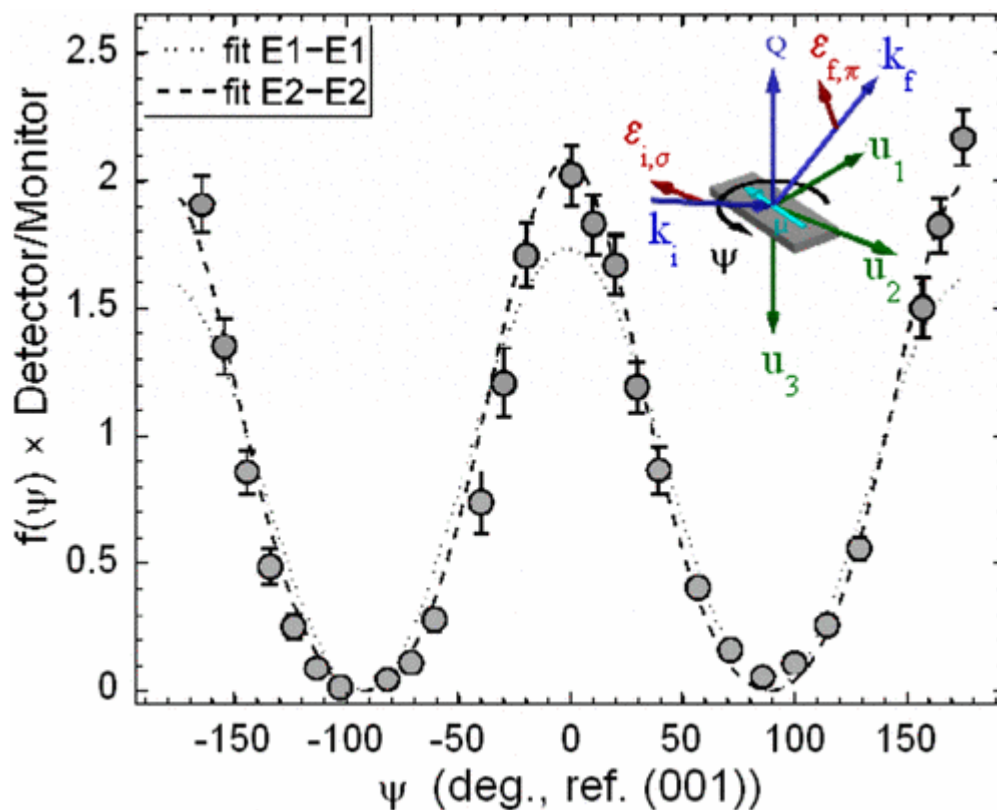
## Incommensurate magnetic ground state revealed by resonant x-ray scattering in the frustrated spin system $\text{Ca}_3\text{Co}_2\text{O}_6$

*Phys. Rev. B* 77, 140403(R) (2008)

[10.1103/PhysRevB.77.140403](https://doi.org/10.1103/PhysRevB.77.140403)

S. Agrestini, C. Mazzoli, A. Bombardi, and M. R. Lees

We have performed a resonant x-ray scattering study at the Co pre-K edge on a single crystal of  $\text{Ca}_3\text{Co}_2\text{O}_6$ . The measurements reveal an abrupt transition to a magnetically ordered state immediately below  $T_N=25\text{K}$ , with a magnetic correlation length in excess of  $5500\text{\AA}$  along the  $c$  axis chains. There is no evidence for modifications to the  $\text{Co}^{3+}$  spin state. A temperature dependent modulation in the magnetic order along the  $c$  axis and an unusual decrease in the magnetic correlation lengths on cooling are observed. The results are compatible with the onset of a partially disordered antiferromagnetic structure in  $\text{Ca}_3\text{Co}_2\text{O}_6$ .



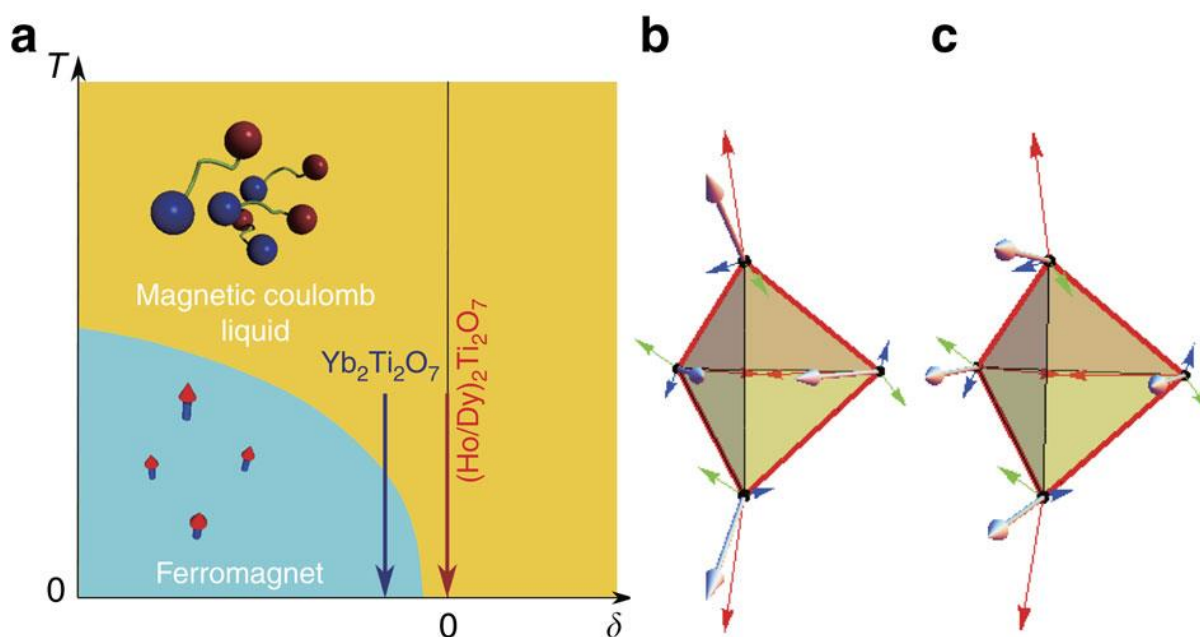
Azimuth scan on the (3 2 0) reflection collected in the  $\sigma$ - $\pi$  channel at  $E=7.707\text{ keV}$  and  $T=4.2\text{ K}$ . Azimuth reference (0 0 1). The dotted line shows a purely  $E1-E1$  fit and the dashed line is a fit including  $E1-E1$  and  $E2-E2$  contributions. The inset shows the geometry of the scattering and the fixed reference system  $u_1, u_2$ , and  $u_3$  used.

## Higgs transition from a magnetic Coulomb liquid to a ferromagnet in $\text{Yb}_2\text{Ti}_2\text{O}_7$

*Nature Communications* 3, 992 (2012) [10.1038/ncomms1989](https://doi.org/10.1038/ncomms1989)

Chang, L.-J., Onoda, S., Su, Y., Kao, Y.-J., Tsuei, K.-D., Yasui, Y., Kakurai, K., Lees, M.R.

In a class of frustrated magnets known as spin ice, magnetic monopoles emerge as classical defects and interact via the magnetic Coulomb law. With quantum-mechanical interactions, these magnetic charges are carried by fractionalized bosonic quasi-particles, spinons, which can undergo Bose–Einstein condensation through a first-order transition via the Higgs mechanism. Here, we report evidence of a Higgs transition from a magnetic Coulomb liquid to a ferromagnet in single-crystal  $\text{Yb}_2\text{Ti}_2\text{O}_7$ . Polarized neutron scattering experiments show that the diffuse [111]-rod scattering and pinch-point features, which develop on cooling are suddenly suppressed below  $T_c \sim 0.21$  K, where magnetic Bragg peaks and a full depolarization of the neutron spins are observed with thermal hysteresis, indicating a first-order ferromagnetic transition. Our results are explained on the basis of a quantum spin-ice model, whose high-temperature phase is effectively described as a magnetic Coulomb liquid, whereas the ground state shows a nearly collinear ferromagnetism with gapped spin excitations.



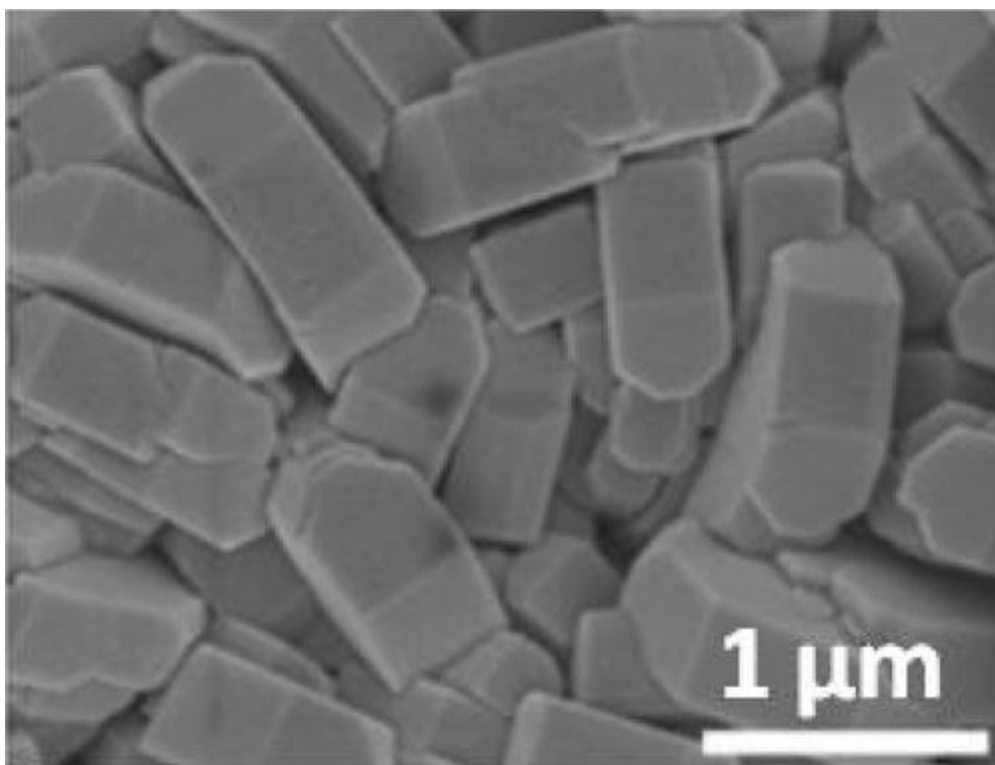
(a) Schematic phase diagram as a function of temperature  $T$  and the relative strength  $\delta$  of the  $U(1)$ -symmetric planar exchange interaction and the Ising exchange. A first-order Higgs transition appears between a Coulomb liquid phase and a Higgs phase of magnetic monopoles. Monopoles (blue balls) and antimonopoles (red balls) are illustrated for both the phases. In the magnetic Coulomb liquid phase (yellow), magnetic monopoles are carried by pseudospin-1/2 fractionalized gapped spinon excitations out of quasi-degenerate spin-ice manifold, obeying a Coulombic law. In the Higgs phase (cyan), monopolar spinons are condensed to form local magnetic dipole moments (arrows) showing ferromagnetic long-range order. (b,c) Hypothetical ferromagnetically ordered structures of the pseudospins (b) and the magnetic moments (c) in the low-temperature Higgs phase.

## Direct Hydrothermal Synthesis and Physical Properties of Rare-Earth and Yttrium Orthochromite Perovskites

*Chemistry of Materials* 23, 48 (2011) [10.1021/cm102925z](https://doi.org/10.1021/cm102925z)

Sardar, K., Lees, M.R., Kashtiban, R.J., Sloan, J., Walton, R.I.

We describe a systematic study of the hydrothermal synthesis of rare-earth orthochromites,  $\text{RCrO}_3$  ( $R = \text{La, Pr, Sm, Gd, Dy, Ho, Yb, and Lu}$ ) and  $\text{YCrO}_3$ . All nine of these materials can be prepared in a single step by hydrothermal treatment of an amorphous mixed-metal hydroxide at temperatures above  $300\text{ }^\circ\text{C}$  upon heating around 24 h, with no post-synthesis annealing needed. The as-made materials are highly crystalline powders with submicrometer particle size. In the case of  $\text{LaCrO}_3$  the addition of solution additives to the hydrothermal synthesis allows some modification of crystallite form of the material, and in the presence of sodium dodecylsulfate nanocrystalline powders are produced. Profile refinement of powder X-ray diffraction (XRD) data show that each of the  $\text{RCrO}_3$  materials adopts an orthorhombic distorted ( $Pbmn$ ) perovskite structure. Detailed, magnetization studies as a function of temperature reveal the high quality of the specimens, with low temperature antiferromagnetic behavior seen by direct current (DC) magnetization, and  $T_N$  values that correlate with the structural distortion. A high temperature structural phase transition ( $\sim 540\text{ K}$  to rhombohedral  $R3c$ ) seen by variable temperature XRD in the hydrothermally prepared  $\text{LaCrO}_3$  is consistent with the reported behavior of the same composition prepared using conventional high temperature synthesis.

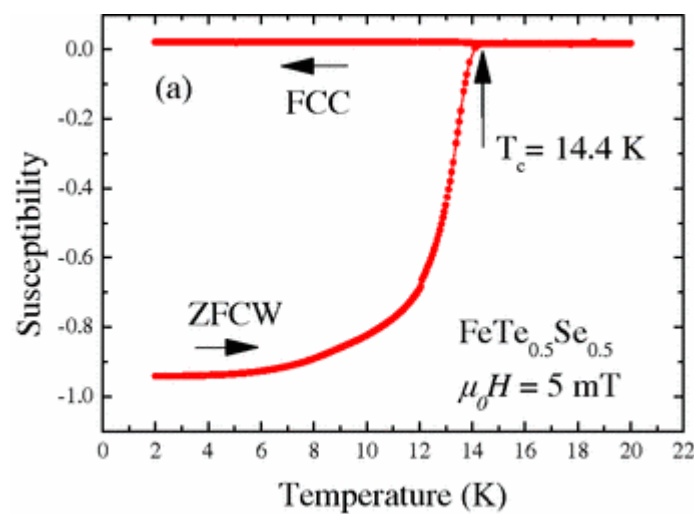


## Muon-spin-spectroscopy study of the penetration depth of $\text{FeTe}_{0.5}\text{Se}_{0.5}$

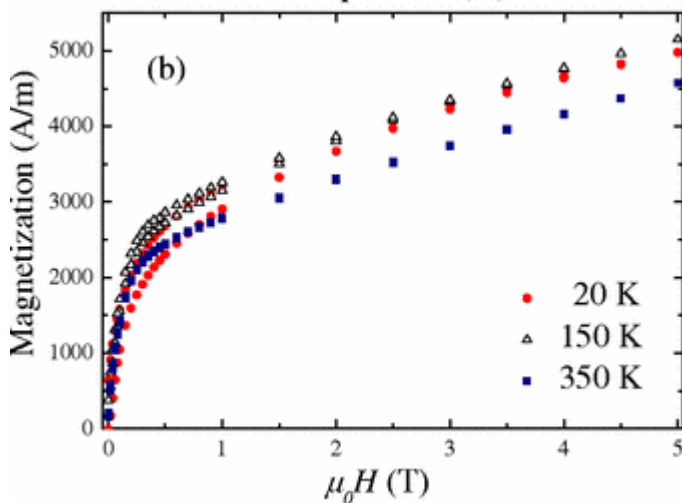
*Phys. Rev. B* 81, 092510 (2010) [10.1103/PhysRevB.81.092510](https://doi.org/10.1103/PhysRevB.81.092510)

P. K. Biswas, G. Balakrishnan, D. M. Paul, C. V. Tomy, M. R. Lees, and A. D. Hillier

Muon-spin-spectroscopy measurements have been used to study the superconducting state of  $\text{FeTe}_{0.5}\text{Se}_{0.5}$ . The temperature dependence of the in-plane magnetic penetration depth,  $\lambda_{ab}(T)$ , is found to be compatible with either a two-gap  $s+s$ -wave or an anisotropic  $s$ -wave model. The value for  $\lambda_{ab}(T)$  at  $T=0$  K is estimated to be  $\lambda_{ab}(0)=534(2)$  nm.



(a) Temperature dependence of the magnetic susceptibility of  $\text{FeTe}_{0.5}\text{Se}_{0.5}$  measured using zero-field-cooled warming and field-cooled cooling protocols. The diamagnetic susceptibility corresponds to complete diamagnetic screening with a  $T_c$  onset of 14.4 K.



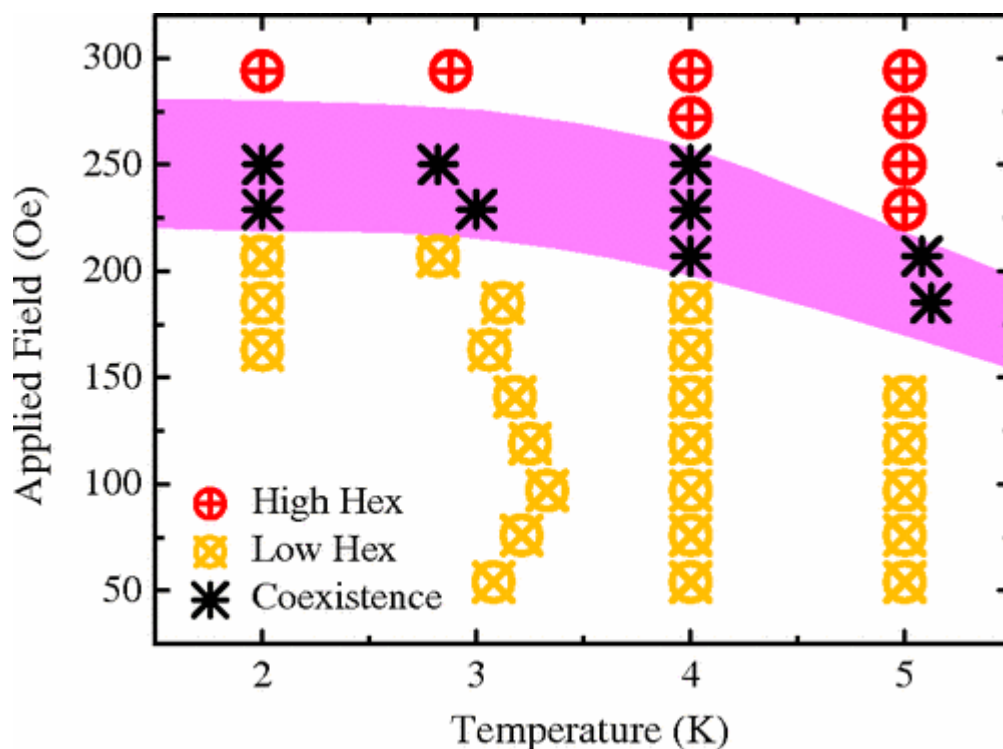
(b) Magnetization versus applied field curves for  $\text{FeTe}_{0.5}\text{Se}_{0.5}$  collected above  $T_c$  at 20, 150, and 350 K.

## First-Order Reorientation Transition of the Flux-Line Lattice in CaAlSi

*Phys. Rev. Lett.* 108, 077001 (2012) [10.1103/PhysRevLett.108.077001](https://doi.org/10.1103/PhysRevLett.108.077001)

P. K. Biswas, M. R. Lees, G. Balakrishnan, D. Q. Liao, D. S. Keeble, J. L. Gavilano, N. Egetenmeyer, C. D. Dewhurst, and D. McK. Paul

The flux-line lattice in CaAlSi has been studied by small-angle neutron scattering. A well-defined hexagonal flux-line lattice is seen just above  $H_{c1}$  in an applied field of only 54 Oe. A  $30^\circ$  reorientation of this vortex lattice has been observed in a very low field of 200 Oe. This reorientation transition appears to be first-order and could be explained by nonlocal effects. The magnetic field dependence of the form factor is well-described by a single penetration depth of  $\lambda=1496(1)$  Å and a single coherence length of  $\xi=307(1)$  Å at 2 K. At 1.5 K, the penetration depth anisotropy is  $\gamma\lambda=2.7(1)$ , with the field applied perpendicular to the  $c$  axis, and agrees with the coherence length anisotropy determined from critical field measurements.



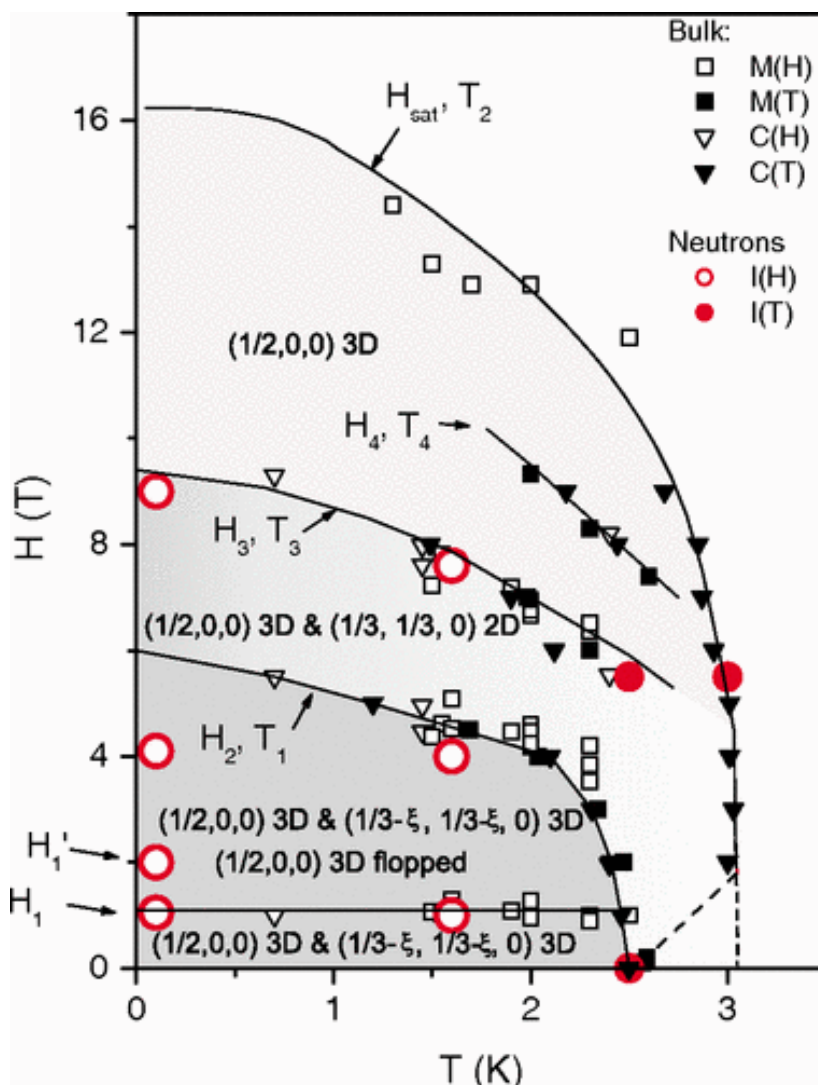
H-T phase diagram of CaAlSi indicating the temperatures and applied fields at which we observe either a High-Hex or a Low-Hex state for the flux line lattice. A shaded region in which the two states coexist is also marked.

### Chiral and Collinear Ordering in a Distorted Triangular Antiferromagnet

*Phys. Rev. Lett.* 102, 037202 (2009) [10.1103/PhysRevLett.102.037202](https://doi.org/10.1103/PhysRevLett.102.037202)

A. I. Smirnov, L. E. Svistov, L. A. Prozorova, A. Zheludev, M. D. Lumsden, E. Ressouche, O. A. Petrenko, K. Nishikawa, S. Kimura, M. Hagiwara, K. Kindo, A. Ya. Shapiro, and L. N. Demianets

Magnetization, specific heat, and neutron diffraction measurements are used to map out the entire magnetic phase diagram of  $\text{KFe}(\text{MoO}_4)_2$ . This stacked triangular antiferromagnet is structurally similar to the famous multiferroic system  $\text{RbFe}(\text{MoO}_4)_2$ . Because of an additional small crystallographic distortion, it contains two sets of inequivalent distorted magnetic triangular lattices. As a result, the spin network breaks down into two intercalated yet almost independent magnetic subsystems. One is a collinear antiferromagnet that shows a simple spin-flop behavior in applied magnetic fields. The other is a helimagnet that instead goes through a series of exotic commensurate-incommensurate phase transformations. In the various phases one observes either true three-dimensional or unconventional quasi-two-dimensional ordering.



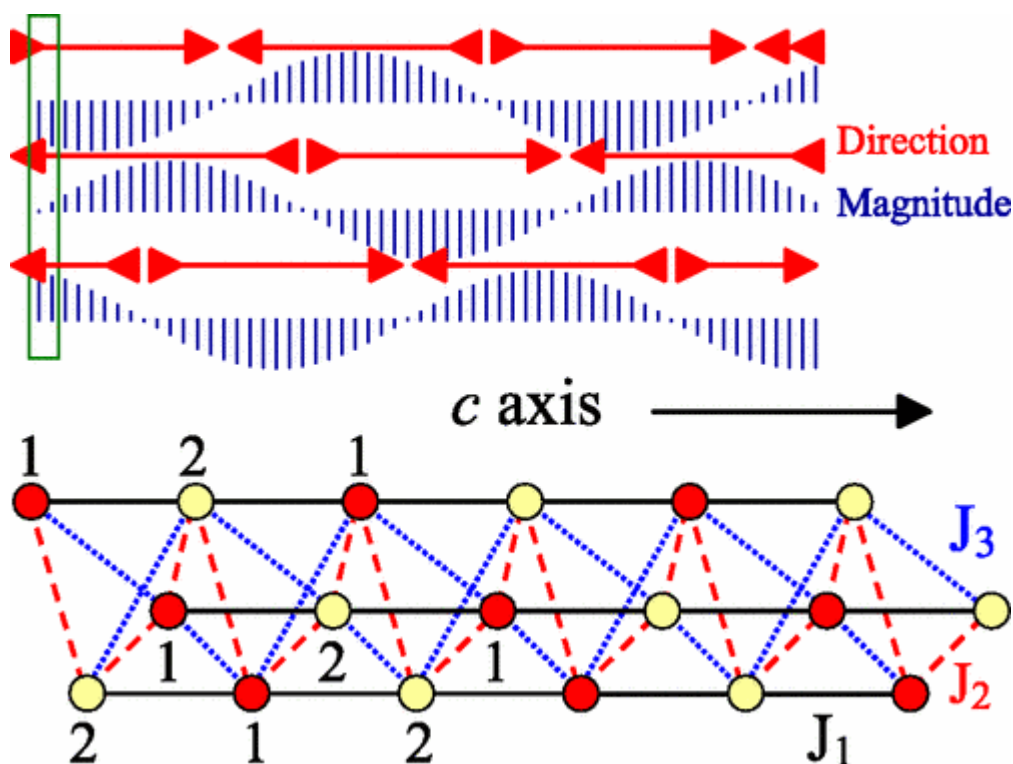
Cumulative magnetic phase diagram of  $\text{KFe}(\text{MoO}_4)_2$  for a magnetic field applied in the (a,b) plane.

## Nature of the Magnetic Order in $\text{Ca}_3\text{Co}_2\text{O}_6$

*Phys. Rev. Lett.* 101, 097207 (2008) [10.1103/PhysRevLett.101.097207](https://doi.org/10.1103/PhysRevLett.101.097207)

S. Agrestini, L. C. Chapon, A. Daoud-Aladine, J. Schefer, A. Gukasov, C. Mazzoli, M. R. Lees, and O. A. Petrenko

We present a detailed powder and single-crystal neutron diffraction study of the spin chain compound  $\text{Ca}_3\text{Co}_2\text{O}_6$ . Below 25 K, the system orders magnetically with a modulated partially disordered antiferromagnetic structure. We give a description of the magnetic interactions in the system which is consistent with this magnetic structure. Our study also reveals that the long-range magnetic order coexists with a shorter-range order with a correlation length scale of  $\sim 180 \text{ \AA}$  in the  $ab$  plane. Remarkably, on cooling, the volume of material exhibiting short-range order increases at the expense of the long-range order.



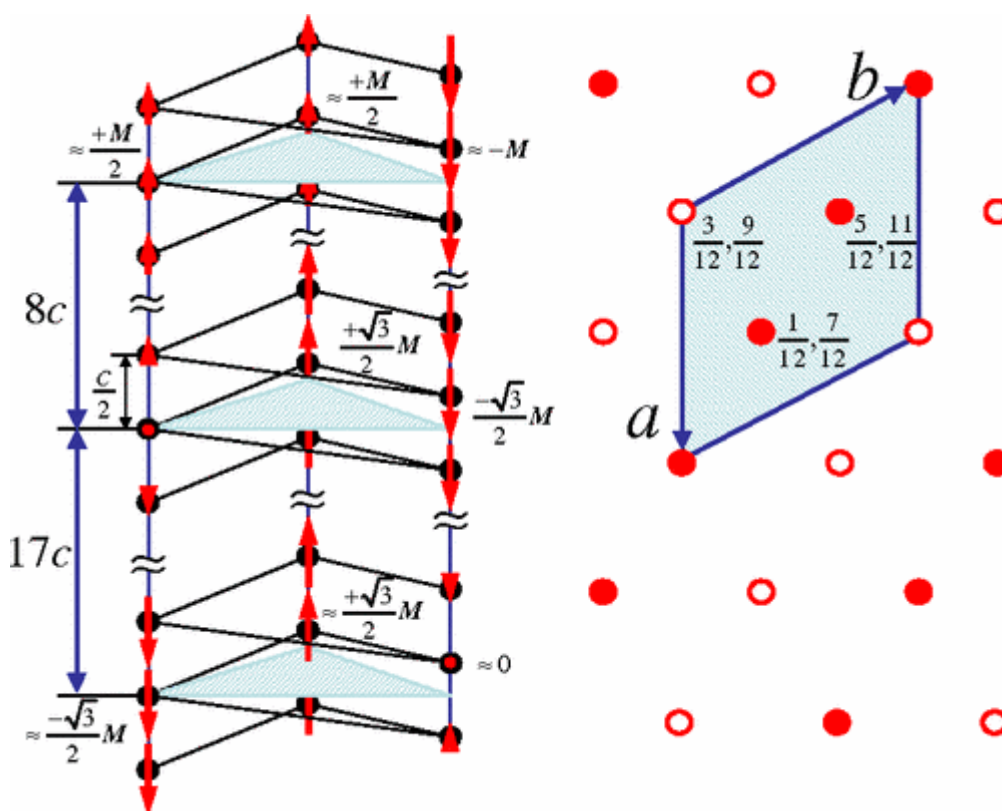
(a) Schematic of the proposed incommensurate magnetic structure for 30 unit cells along the  $c$  axis with  $k_z$  increased to 1.05 to emphasize the modulation of the moments. The magnitude and direction at sites in three adjacent chains are shown. (b) Magnetic exchange interactions in  $\text{Ca}_3\text{Co}_2\text{O}_6$ :  $J_1$  (black lines) FM;  $J_2$  (red dashed lines) AFM;  $J_3$  (blue dotted lines) AFM. Co II sites at  $(0, 0, 1/4)$  and  $(0, 0, 3/4)$  are labeled 1 and 2.

## Slow Magnetic Order-Order Transition in the Spin Chain Antiferromagnet $\text{Ca}_3\text{Co}_2\text{O}_6$

*Phys. Rev. Lett.* 106, 197204 (2011) [10.1103/PhysRevLett.106.197204](https://doi.org/10.1103/PhysRevLett.106.197204)

S. Agrestini, C. L. Fleck, L. C. Chapon, C. Mazzoli, A. Bombardi, M. R. Lees, and O. A. Petrenko

Using powder neutron diffraction, we have discovered an unusual magnetic order-order transition in the Ising spin chain compound  $\text{Ca}_3\text{Co}_2\text{O}_6$ . On lowering the temperature, an antiferromagnetic phase with a propagation vector  $\mathbf{k}=(0.5,-0.5,1)$  emerges from a higher temperature spin density wave structure with  $\mathbf{k}=(0,0,1.01)$ . This transition occurs over an unprecedented time scale of several hours and is never complete.



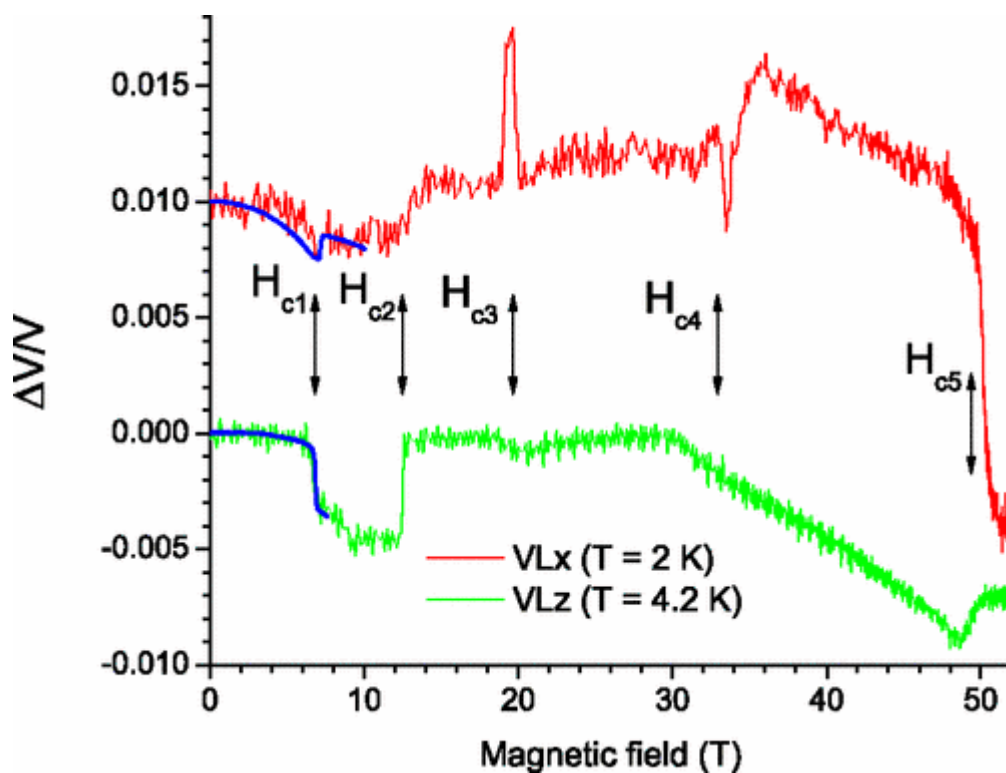
Schematics of the SDW and the CAFM phases. For the SDW phase, three sets of spin chains are shown, along with selected values for the magnetic moments on the trigonal prismatic  $\text{Co}_{II}^{3+}$  sites. The solid line indicates the dominant interchain, AFM supersuperexchange pathway. In the CAFM phase the moments are aligned ferromagnetically along the  $c$  axis. The open and closed circles represent magnetic moments on the  $\text{Co}_{II}^{3+}$  sites pointing up and down the  $c$  axis, respectively, along with the fractional coordinates of these sites along the  $c$  axis within a unit cell

## Magnetic phase diagram of magnetoelectric $\text{CuFeO}_2$ in high magnetic fields

*Phys. Rev. B* 80, 064420 (2009) [10.1103/PhysRevB.80.064420](https://doi.org/10.1103/PhysRevB.80.064420)

G. Quirion, M. L. Plumer, O. A. Petrenko, G. Balakrishnan, and C. Proust

A series of ultrasonic velocity measurements using both high-field pulsed and conventional superconducting magnets were used to determine the magnetic phase diagram of magnetoelectric  $\text{CuFeO}_2$  up to 53 T. The results clearly indicate a previously undetected transition at about 49 T below 10 K. Analysis of Landau-type free energy suggests that this new phase boundary is due to a spin-flop transition.



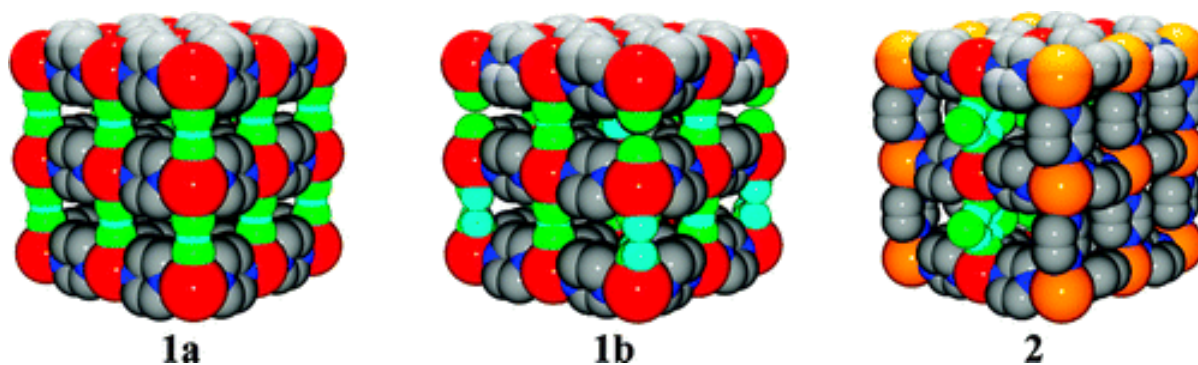
Field dependence of the normalized velocity variation of longitudinal waves propagating along the  $x$  axis ( $V_{Lx}$ ) and  $c$  axis ( $V_{Lz}$ ). The continuous blue curves represent data collected using a quasistatic field produced by a conventional superconducting magnet up to 10 T.

## Strong H...F Hydrogen Bonds as Synthons in Polymeric Quantum Magnets: Structural, Magnetic, and Theoretical Characterization of $[\text{Cu}(\text{HF}_2)(\text{pyrazine})_2]\text{SbF}_6$ , $[\text{Cu}_2\text{F}(\text{HF})(\text{HF}_2)(\text{pyrazine})_4](\text{SbF}_6)_2$ , and $[\text{CuAg}(\text{H}_3\text{F}_4)(\text{pyrazine})_5](\text{SbF}_6)_2$

*Journal of the American Chemical Society*, 131, 6733 (2009) [10.1021/ja808761d](https://doi.org/10.1021/ja808761d)

Manson, J.L., Schlueter, J.A., Funk, K.A., Southerland, H.I., Twamley, B., Lancaster, T., Blundell, S.J., Baker, P.J., Pratt, F.L., Singleton, J., McDonald, R.

Three  $\text{Cu}^{2+}$ -containing coordination polymers were synthesized and characterized by experimental (X-ray diffraction, magnetic susceptibility, pulsed-field magnetization, heat capacity, and muon-spin relaxation) and electronic structure studies (quantum Monte Carlo simulations and density functional theory calculations).  $[\text{Cu}(\text{HF}_2)(\text{pyz})_2]\text{SbF}_6$  (pyz = pyrazine) (**1a**),  $[\text{Cu}_2\text{F}(\text{HF})(\text{HF}_2)(\text{pyz})_4](\text{SbF}_6)_2$  (**1b**), and  $[\text{CuAg}(\text{H}_3\text{F}_4)(\text{pyz})_5](\text{SbF}_6)_2$  (**2**) crystallize in either tetragonal or orthorhombic space groups; their structures consist of 2D square layers of  $[\text{M}(\text{pyz})_2]^{n+}$  that are linked in the third dimension by either  $\text{HF}_2^-$  (**1a** and **1b**) or  $\text{H}_3\text{F}_4^-$  (**2**). The resulting 3D frameworks contain charge-balancing  $\text{SbF}_6^-$  anions in every void. Compound **1b** is a defective polymorph of **1a**, with the difference being that 50% of the  $\text{HF}_2^-$  links are broken in the former, which leads to a cooperative Jahn–Teller distortion and  $d_{x^2-y^2}$  orbital ordering. Magnetic data for **1a** and **1b** reveal broad maxima in  $\chi$  at 12.5 and 2.6 K and long-range magnetic order below 4.3 and 1.7 K, respectively, while **2** displays negligible spin interactions owing to long and disrupted superexchange pathways. The isothermal magnetization,  $M(B)$ , for **1a** and **1b** measured at 0.5 K reveals contrasting behaviors: **1a** exhibits a concave shape as  $B$  increases to a saturation field,  $B_c$ , of 37.6 T, whereas **1b** presents an unusual two-step saturation in which  $M(B)$  is convex until it reaches a step near 10.8 T and then becomes concave until saturation is reached at 15.8 T. The step occurs at two-thirds of  $M_{\text{sat}}$ , suggesting the presence of a ferrimagnetic structure. Compound **2** shows unusual hysteresis in  $M(B)$  at low temperature, although  $\chi$  vs  $T$  does not reveal the presence of a magnetic phase transition. Quantum Monte Carlo simulations based on an anisotropic cubic lattice were applied to the magnetic data of **1a** to afford  $g = 2.14$ ,  $J = -13.4$  K (Cu-pyz-Cu), and  $J_{\perp} = -0.20$  K (Cu-F...H...F-Cu), while  $\chi$  vs  $T$  for **1b** could be well reproduced by a spin-1/2 Heisenberg uniform chain model for  $g = 2.127(1)$ ,  $J_1 = -3.81(1)$ , and  $zJ_2 = -0.48(1)$  K, where  $J_1$  and  $J_2$  are the intra- and interchain exchange couplings, respectively, which considers the number of magnetic nearest-neighbors ( $z$ ). The  $M(B)$  data for **1b** could not be satisfactorily explained by the chain model, suggesting a more complex magnetic structure in the ordered state and the need for additional terms in the spin Hamiltonian. The observed variation in magnetic behaviors is driven by differences in the H...F hydrogen-bonding motifs.

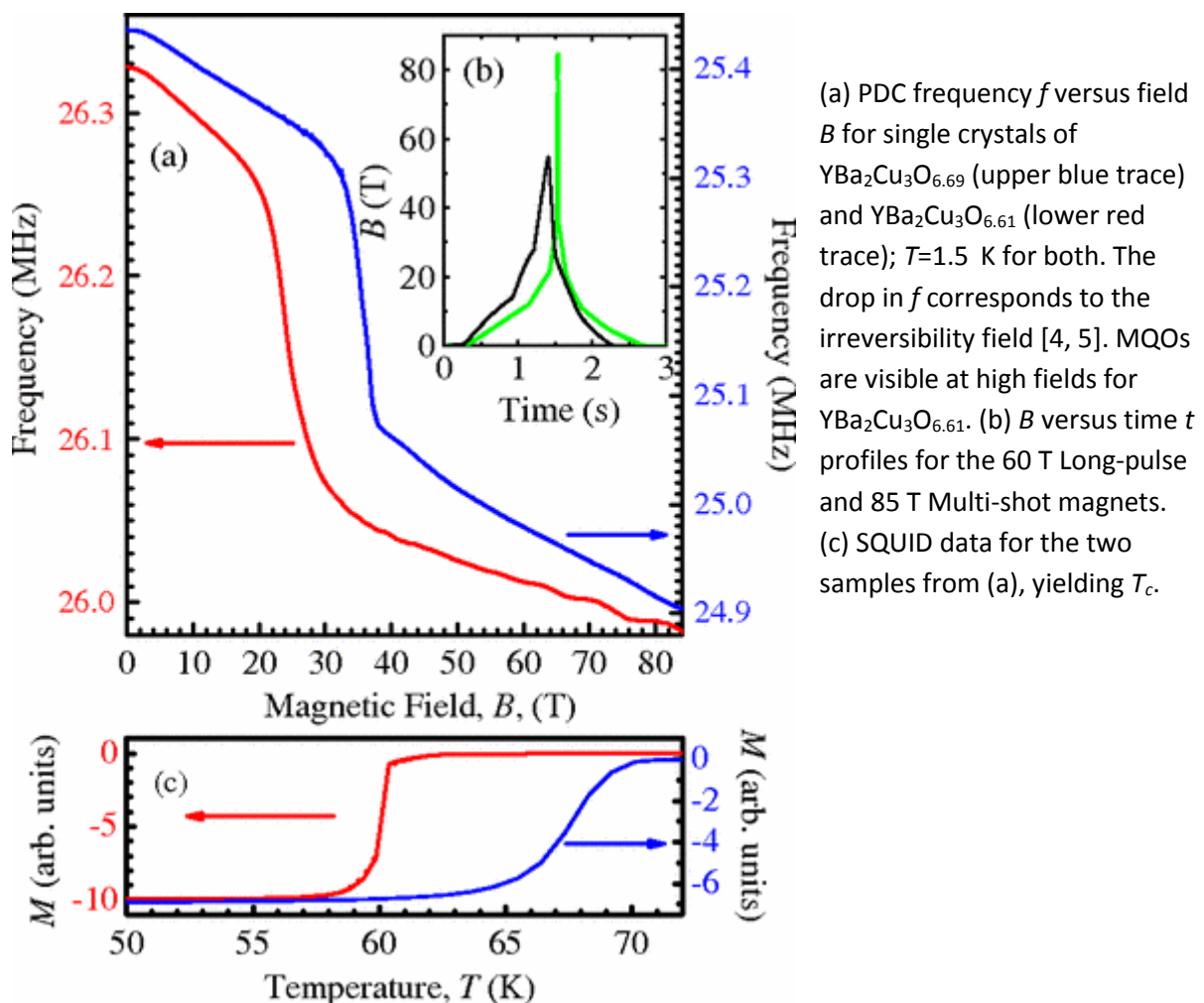


## Magnetic Quantum Oscillations in $\text{YBa}_2\text{Cu}_3\text{O}_{6.61}$ and $\text{YBa}_2\text{Cu}_3\text{O}_{6.69}$ in Fields of up to 85 T: Patching the Hole in the Roof of the Superconducting Dome

*Phys. Rev. Lett.* 104, 086403 (2010) [10.1103/PhysRevLett.104.086403](https://doi.org/10.1103/PhysRevLett.104.086403)

Singleton, J., De La Cruz, C., McDonald, R.D., Li, S., Altarawneh, M., Goddard, P., Franke, I., Rickel, D., Mielke, C.H., Yao, X., Dai, P.

We measure magnetic quantum oscillations in the underdoped cuprates  $\text{YBa}_2\text{Cu}_3\text{O}_{6+x}$  with  $x=0.61, 0.69$ , using fields of up to 85 T. The quantum-oscillation frequencies and effective masses obtained suggest that the Fermi energy in the cuprates has a maximum at hole doping  $p \approx 0.11-0.12$ . On either side, the effective mass may diverge, possibly due to phase transitions associated with the  $T=0$  limit of the metal-insulator crossover (low- $p$  side), and the postulated topological transition from small to large Fermi surface close to optimal doping (high  $p$  side).

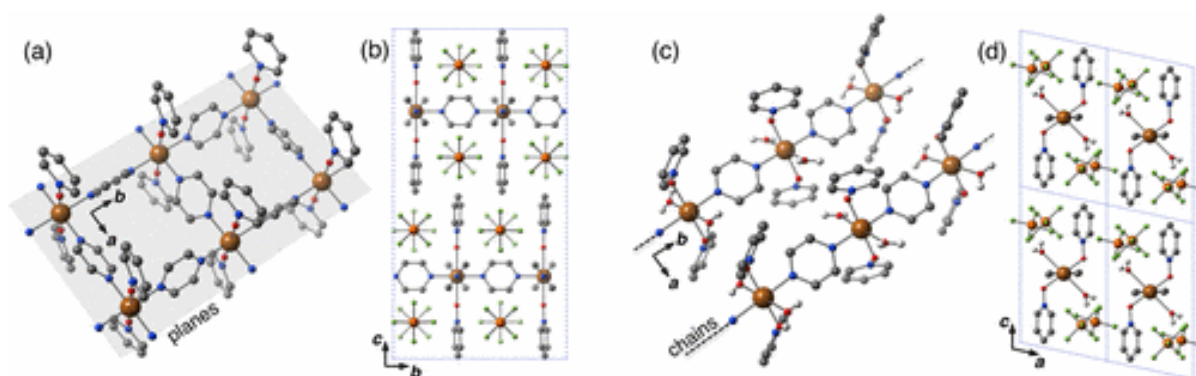


## Dimensionality Selection in a Molecule-Based Magnet

*Phys. Rev. Lett.* 108, 077208 (2012) [10.1103/PhysRevLett.108.077208](https://doi.org/10.1103/PhysRevLett.108.077208)

Goddard, P.A., Manson, J.L., Singleton, J., Franke, I., Lancaster, T., Steele, A.J., Blundell, S.J., Baines, C., Pratt, F.L., McDonald, R.D., Ayala-Valenzuela, O.E., Corbey, J.F., Southerland, H.I., Sengupta, P., Schlueter, J.A.

Gaining control of the building blocks of magnetic materials and thereby achieving particular characteristics will make possible the design and growth of bespoke magnetic devices. While progress in the synthesis of molecular materials, and especially coordination polymers, represents a significant step towards this goal, the ability to tune the magnetic interactions within a particular framework remains in its infancy. Here we demonstrate a chemical method which achieves dimensionality selection via preferential inhibition of the magnetic exchange in an  $S=1/2$  antiferromagnet along one crystal direction, switching the system from being quasi-two- to quasi-one-dimensional while effectively maintaining the nearest-neighbor coupling strength.



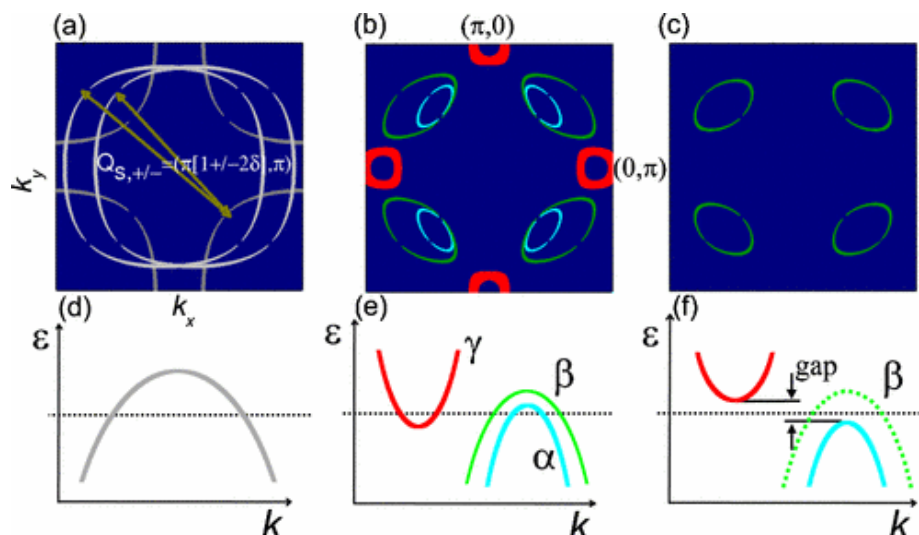
(a) View of the crystal structure of the planar material  $[\text{Cu}(\text{pyz})_2(\text{pyO})_2](\text{PF}_6)_2$  determined using x-ray diffraction showing the 2D Cu—pyrazine network in the  $ab$  plane. (b) A projection of the same structure along the  $a$  axis highlighting the shift between adjacent Cu—pyrazine layers and the arrangement of the  $\text{PF}_6$  counterions. (c) Crystal structure of the chainlike material  $[\text{Cu}(\text{pyz})(\text{pyO})_2(\text{H}_2\text{O})_2](\text{PF}_6)_2$  showing the 1D Cu—pyrazine chains in the  $ab$  plane, and (d) a projection along the chains showing the arrangement of the  $\text{pyO}$  and  $\text{H}_2\text{O}$  ligands and the  $\text{PF}_6$  counterions. The dashed lines in (c) and (d) enclose one unit cell. Cu, brown; C, grey; N, blue; O, red; P, orange; F, green. Print edition: In each diagram, the largest sphere denotes the spin-carrying Cu ion [21]. Hydrogen atoms other than those in the water molecules have been omitted for clarity.

## Compensated electron and hole pockets in an underdoped high- $T_c$ superconductor

*Phys. Rev. B* 81, 214524 (2010) [10.1103/PhysRevB.81.214524](https://doi.org/10.1103/PhysRevB.81.214524)

Sebastian, S.E., Harrison, N., Goddard, P.A., Altarawneh, M.M., Mielke, C.H., Liang, R., Bonn, D.A., Hardy, W.N., Andersen, O.K., Lonzarich, G.G.

We report quantum oscillations in the underdoped high-temperature superconductor  $\text{YBa}_2\text{Cu}_3\text{O}_{6+x}$  over a wide range in magnetic field  $28 \leq \mu_0 H \leq 85$  T corresponding to  $\approx 12$  oscillations, enabling the Fermi surface topology to be mapped to high resolution. As earlier reported by [Sebastian et al.](#), we find a Fermi surface comprising multiple pockets, as revealed by the additional distinct quantum oscillation frequencies and harmonics reported in this work. We find the originally reported broad low-frequency Fourier peak at  $\approx 535$  T to be clearly resolved into three separate peaks at  $\approx 460$ ,  $\approx 532$ , and  $\approx 602$  T, in reasonable agreement with the reported frequencies of [Audouard et al.](#). However, our increased resolution and angle-resolved measurements identify these frequencies to originate from two similarly sized pockets with greatly contrasting degrees of interlayer corrugation. The spectrally dominant frequency originates from a pocket (denoted  $\alpha$ ) that is almost ideally two-dimensional in form (exhibiting negligible interlayer corrugation). In contrast, the newly resolved weaker adjacent spectral features originate from a deeply corrugated pocket (denoted  $\gamma$ ). On comparison with band structure, the  $d$ -wave symmetry of the interlayer dispersion locates the minimally corrugated  $\alpha$  pocket at the “nodal” point  $\mathbf{k}_{\text{nodal}} = (\pi/2, \pi/2)$ , and the significantly corrugated  $\gamma$  pocket at the “antinodal” point  $\mathbf{k}_{\text{antinodal}} = (\pi, 0)$  within the Brillouin zone. The differently corrugated pockets at different locations indicate creation by translational symmetry breaking—a spin-density wave has been suggested from the suppression of Zeeman splitting for the spectrally dominant pocket. In a broken-translational symmetry scenario, symmetry points to the nodal ( $\alpha$ ) pocket corresponding to holes, with the weaker antinodal ( $\gamma$ ) pocket corresponding to electrons—likely responsible for the negative Hall coefficient reported by [LeBoeuf et al.](#). Given the similarity in  $\alpha$  and  $\gamma$  pocket volumes, their opposite carrier type and the previous report of a diverging effective mass in [Sebastian et al.](#), we discuss the possibility of a secondary Fermi surface instability at low dopings of the excitonic insulator type, associated with the metal-insulator quantum critical point. Its potential involvement in the enhancement of superconducting transition temperatures is also discussed.



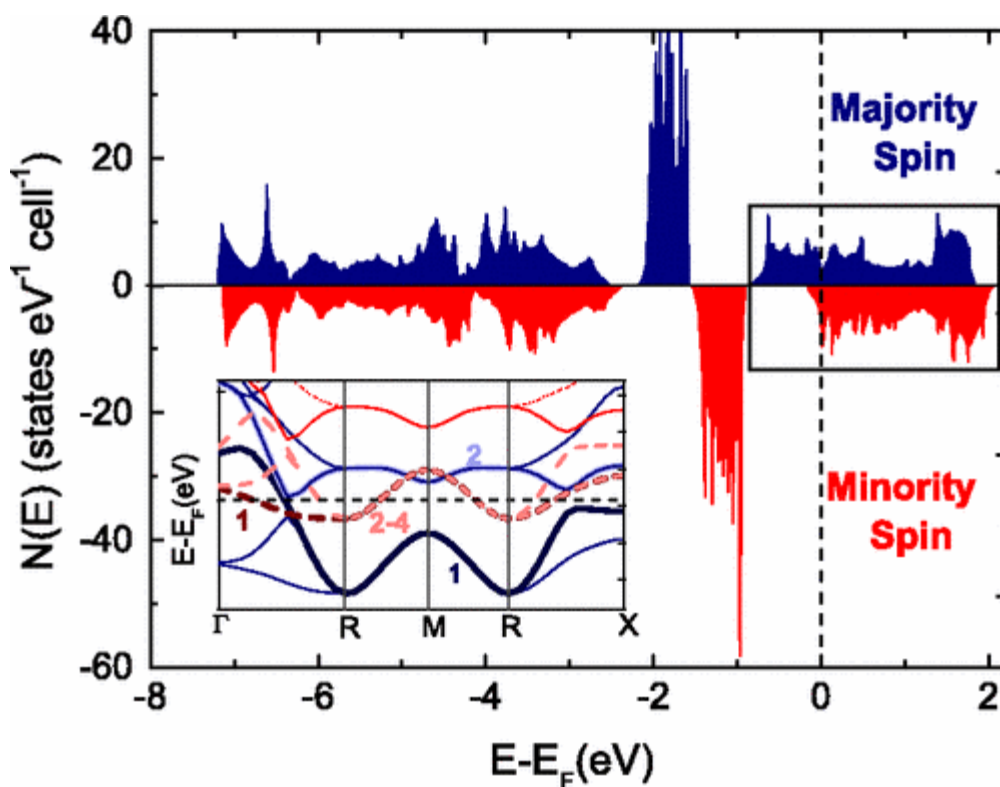
## Bulk Spin Polarization of $\text{Co}_{(1-x)}\text{Fe}_x\text{S}_2$

*Phys. Rev. Lett.* 103, 226403 (2009) [10.1103/PhysRevLett.103.226403](https://doi.org/10.1103/PhysRevLett.103.226403)

C. Utfeld, S. R. Giblin, J. W. Taylor, J. A. Duffy, C. Shenton-Taylor, J. Laverock, S. B. Dugdale, M. Manno, C. Leighton, M. Itou, and Y. Sakurai

We report on a new method to determine the degree of bulk spin polarization in single crystal  $\text{Co}_{(1-x)}\text{Fe}_x\text{S}_2$  by modeling magnetic Compton scattering with *ab initio* calculations. Spin-dependent Compton profiles were measured for  $\text{CoS}_2$  and  $\text{Co}_{0.9}\text{Fe}_{0.1}\text{S}_2$ . The *ab initio* calculations were then refined by rigidly shifting the bands to provide the best fit between the calculated and experimental directional profiles for each sample. The bulk spin polarizations,  $P$ , corresponding to the spin-polarized density of states at the Fermi level, were then extracted from the *refined* calculations. The values were found to be  $P = -72 \pm 6\%$  and  $P = 18 \pm 7\%$  for  $\text{CoS}_2$  and  $\text{Co}_{0.9}\text{Fe}_{0.1}\text{S}_2$ , respectively.

Furthermore, determinations of  $P$  weighted by the Fermi velocity ( $v_F$  or  $v_{2F}$ ) were obtained, permitting a rigorous comparison with other experimental data and highlighting the experimental dependence of  $P$  on  $v_F$ .



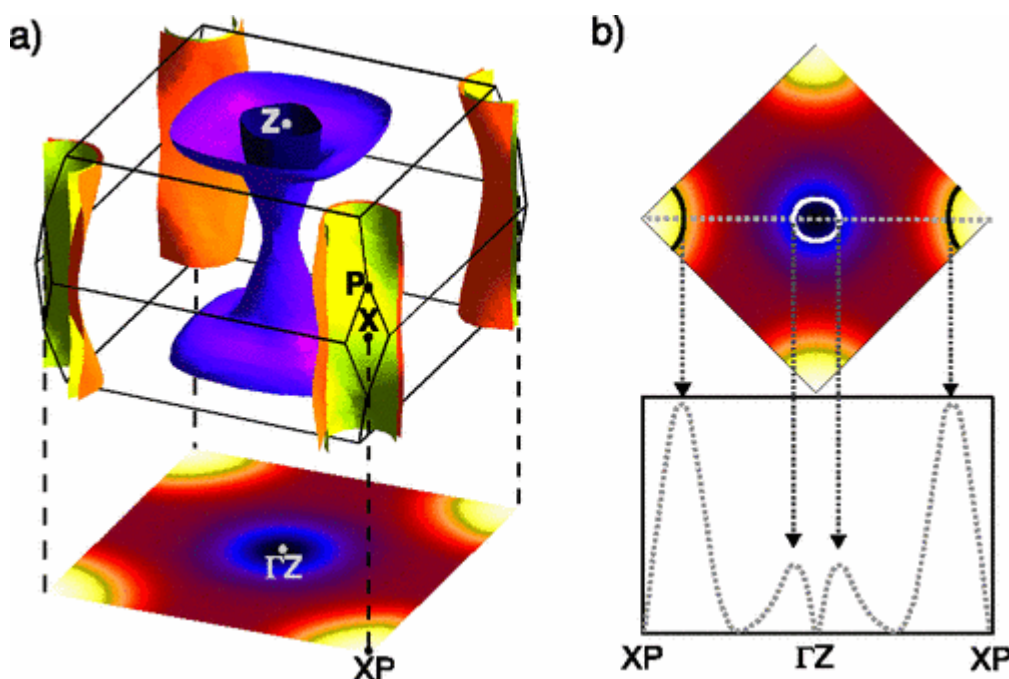
The DOS of  $\text{CoS}_2$ , where the sulfur  $p$  and cobalt  $d$  manifolds are depicted for the majority and minority spin states. The inset shows the band structure of the  $e_g$  manifold around the Fermi level along a high symmetry path in the cubic Brillouin zone. Overall six bands composed of two in the majority (blue solid lines) and four in the minority (red dashed lines) channel cross the Fermi level.

## Bulk electronic structure of optimally doped $\text{Ba}(\text{Fe}_{1-x}\text{Co}_x)_2\text{As}_2$

*Phys. Rev. B* 81, 064509 (2010) [10.1103/PhysRevB.81.064509](https://doi.org/10.1103/PhysRevB.81.064509)

C. Uffeld, J. Laverock, T. D. Haynes, S. B. Dugdale, J. A. Duffy, M. W. Butchers, J. W. Taylor, S. R. Giblin, J. G. Analytis, J.-H. Chu, I. R. Fisher, M. Itou, and Y. Sakurai

We report high-resolution, bulk Compton scattering measurements unveiling the Fermi surface of an optimally doped iron-arsenide superconductor,  $\text{Ba}(\text{Fe}_{0.93}\text{Co}_{0.07})_2\text{As}_2$ . Our measurements are in agreement with first-principles calculations of the electronic structure, revealing both the X-centered electron pockets and the  $\Gamma$ -centered hole pockets. Moreover, our data are consistent with the strong three dimensionality of one of these sheets that has been predicted by electronic structure calculations at the local-density-approximation-minimum As position. Complementary calculations of the noninteracting susceptibility,  $\chi_0(\mathbf{q}, \omega)$ , suggest that the broad peak that develops due to interband Fermi-surface nesting, and which has motivated several theories of superconductivity in this class of material, survives the measured three dimensionality of the Fermi surface in this family.



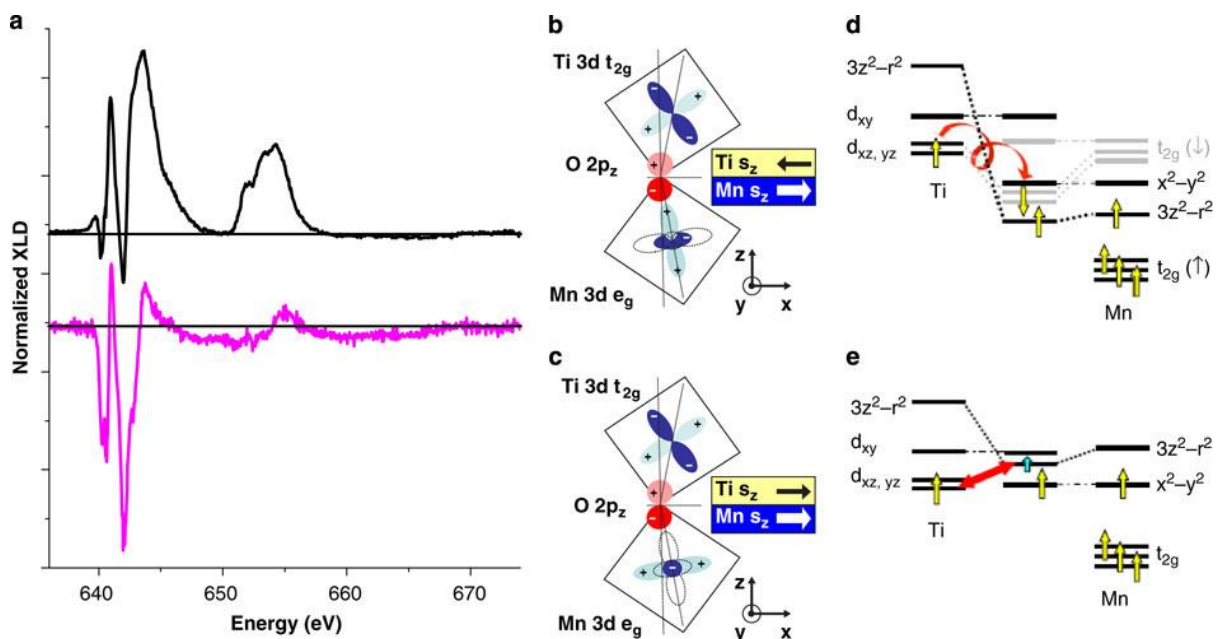
(a) The LDA FS of  $\text{Ba}(\text{Fe}_{0.93}\text{Co}_{0.07})_2\text{As}_2$  (top) and its relation to the occupation density projected down the  $c^*$  axis (bottom). Note that the occupation density has been convoluted with the experimental resolution function. (b) The overlaid FS contours (black and white lines, top) are identified via the maxima in (the absolute value of) the first derivative of the occupation density shown at the bottom along a projected, high-symmetry path.

## Spin and orbital Ti magnetism at LaMnO<sub>3</sub>/SrTiO<sub>3</sub> interfaces

*Nature Communications* 1, 82 (2010) [10.1038/ncomms1080](https://doi.org/10.1038/ncomms1080)

J. Garcia-Barriocanal, J.C. Cezar, F.Y. Bruno, P. Thakur, N.B. Brookes, C. Utfeld, A. Rivera-Calzada, S.R. Giblin, J.W. Taylor, J.A. Duffy, S.B. Dugdale, T. Nakamura, K. Kodama, C. Leon, S. Okamoto, and J. Santamaria

In systems with strong electron-lattice coupling, such as manganites, orbital degeneracy is lifted, causing a null expectation value of the orbital magnetic moment. Magnetic structure is thus determined by spin–spin superexchange. In titanates, however, with much smaller Jahn–Teller distortions, orbital degeneracy might allow non-zero values of the orbital magnetic moment, and novel forms of ferromagnetic superexchange interaction unique to  $t_{2g}$  electron systems have been theoretically predicted, although their experimental observation has remained elusive. In this paper, we report a new kind of Ti<sup>3+</sup> ferromagnetism at LaMnO<sub>3</sub>/SrTiO<sub>3</sub> epitaxial interfaces. It results from charge transfer to the empty conduction band of the titanate and has spin and orbital contributions evidencing the role of orbital degeneracy. The possibility of tuning magnetic alignment (ferromagnetic or antiferromagnetic) of Ti and Mn moments by structural parameters is demonstrated. This result will provide important clues for understanding the effects of orbital degeneracy in superexchange coupling.

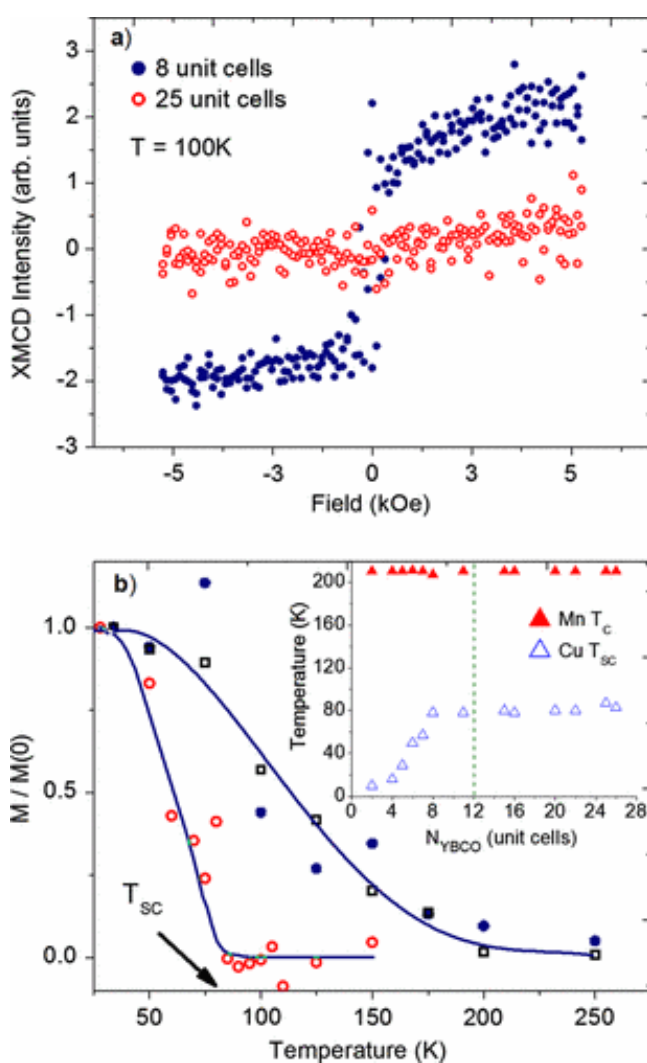


## Measurement of Magnetic Exchange in Ferromagnet-Superconductor $\text{La}_{2/3}\text{Ca}_{1/3}\text{MnO}_3/\text{YBa}_2\text{Cu}_3\text{O}_7$ Bilayers

*Phys. Rev. Lett.* 109, 137005 (2012) [10.1103/PhysRevLett.109.137005](https://doi.org/10.1103/PhysRevLett.109.137005)

S. R. Giblin, J. W. Taylor, J. A. Duffy, M. W. Butchers, C. Uffeld, S. B. Dugdale, T. Nakamura, C. Visani, and J. Santamaria

The existence of coherent magnetic correlations in the normal phase of cuprate high-temperature superconductors has proven difficult to measure directly. Here we report on a study of ferromagnetic-superconductor bilayers of  $\text{La}_{2/3}\text{Ca}_{1/3}\text{MnO}_3/\text{YBa}_2\text{Cu}_3\text{O}_7$  (LCMO/YBCO) with varying YBCO layer thicknesses. Using x-ray magnetic circular dichroism, we demonstrate that the ferromagnetic layer induces a Cu magnetic moment in the adjacent high-temperature superconductor. For thin samples, this moment exists at all temperatures below the Curie temperature of the LCMO layer. However, for a YBCO layer thicker than 12 unit cells, the Cu moment is suppressed for temperatures above the superconducting transition, suggesting this to be a direct measurement of magnetic coherence in the normal state of a superconducting oxide.



(a) Field-dependent hysteresis for samples with an YBCO thickness of 8 u.c. (solid blue circles) and 25 u.c. (open red circles) measured at 100 K. Only samples of thickness greater than 12 unit cells of YBCO show a Cu moment above  $T_{SC}$ .

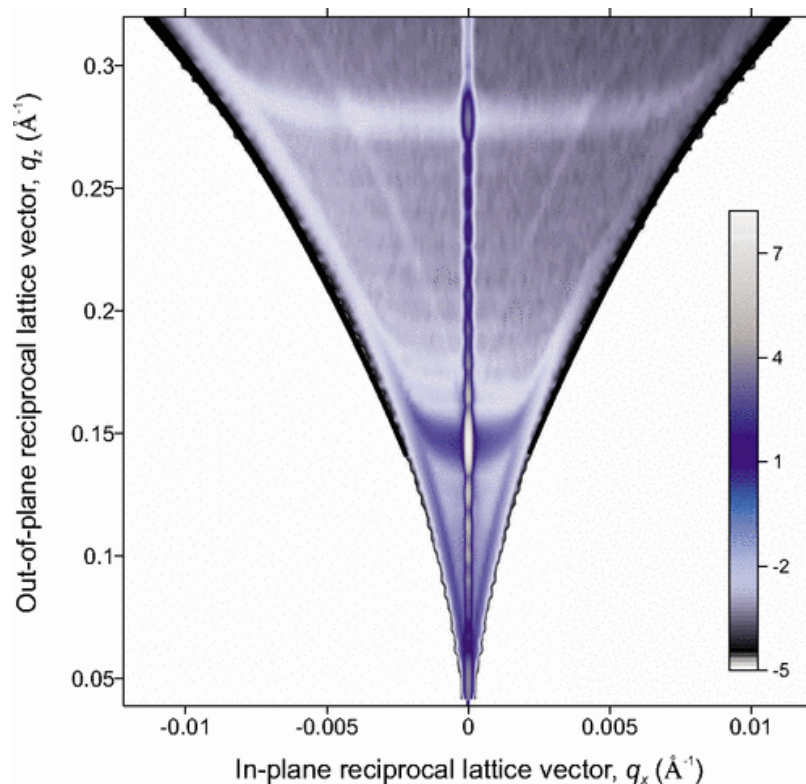
(b) Temperature dependence of the XMCD signals for samples with a YBCO thickness of 8 u.c and 25 u.c. For 8 u.c, both the Cu (solid blue circles) and Mn (open squares) moments for the normalized spectra are shown. For the 25 u.c. sample, only the Cu (open red circles) moment is shown. The arrow represents the superconducting transition, and the lines are guides to the eye. The inset shows the Mn ordering at  $T_c$  and  $T_{SC}$  for each sample obtained from magnetization measurements.

## Spin and orbital moment in amorphous $\text{Co}_{68}\text{Fe}_{24}\text{Zr}_8$ layers

Phys. Rev. B 80, 134402 (2009) [10.1103/PhysRevB.80.134402](https://doi.org/10.1103/PhysRevB.80.134402)

T. Hase, H. Raanaei, H. Lidbaum, C. Sánchez-Hanke, S. Wilkins, K. Leifer, and B. Hjörvarsson

The ratio of the orbital to the spin magnetic moment was determined for both Fe and Co in amorphous  $\text{Co}_{68}\text{Fe}_{24}\text{Zr}_8$  layers using x-ray circular dichroism. The investigations were performed on both thick  $\text{Co}_{68}\text{Fe}_{24}\text{Zr}_8$  layers as well as on amorphous  $\text{Co}_{68}\text{Fe}_{24}\text{Zr}_8/\text{Al}_7\text{OZr}_3\text{O}$  multilayers grown by dc sputtering. Structural characterization was performed using x-ray reflectometry, x-ray diffraction, and transmission electron microscopy. X-ray circular dichroism, x-ray magnetic scattering as well as the magneto-optic Kerr effect were used to characterize the magnetic properties of the amorphous materials. The ratio of the orbital to spin moments in the single CoFeZr-layer sample was  $0.012 \pm 0.005$  for Fe and  $0.078 \pm 0.005$  for Co. Substantial reduction in the the ratio of the orbital to spin moments was observed with decreasing CoFeZr-layer thickness.



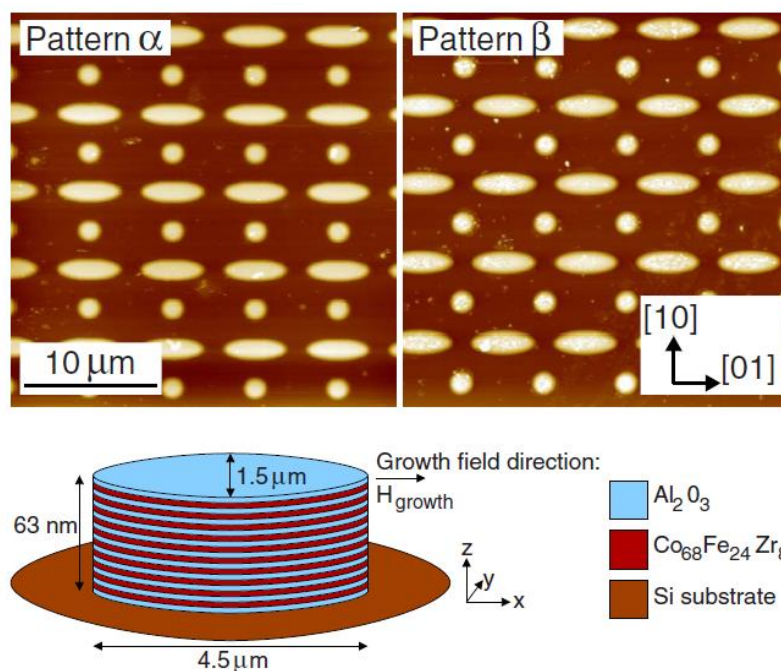
Full reciprocal space map of the diffuse scattering data from sample 20/30. Data is presented on a logarithmic scale. The diffuse scattering is predominantly found in streaks at the out-of-plane scattering vectors of the multilayer peaks seen in the specular scans shown in Fig. 3. The slight curvature of the Bragg sheets at high  $q_x$  is caused by refraction effects when either the incident or exit beams are at the critical angle.

## Magnetic structure and diffracted magneto-optics of patterned amorphous multilayers

Phys. Rev. B 82, 144434 (2010) [10.1103/PhysRevB.82.144434](https://doi.org/10.1103/PhysRevB.82.144434)

Arnalds, UB; Papaioannou, ET; Hase, TPA; Raanaei, H; Andersson, G; Charlton, TR; Langridge, S; Hjorv

We present magneto-optical Kerr effect measurements of patterned arrays of  $\text{Co}_{68}\text{Fe}_{24}\text{Zr}_8/\text{Al}_2\text{O}_3$  amorphous multilayers. The multilayers were patterned in two dimensions into two different arrangements of circular and ellipsoidal islands. Magnetization loops were recorded in a longitudinal geometry using both the specularly reflected beam as well as diffracted beams scattered off the patterned films. The magnetization of the patterned structures is significantly different from the magnetization of a continuous multilayer owing to the lateral confinement of the pattern and the introduction of additional dipolar coupling between the layers at the edges of the islands. By investigating the magnetic response at the different diffraction orders from the two different configurations of islands we are able to observe the magnetization at different length scales and determine the magnetic response of the circular and ellipsoidal islands individually.



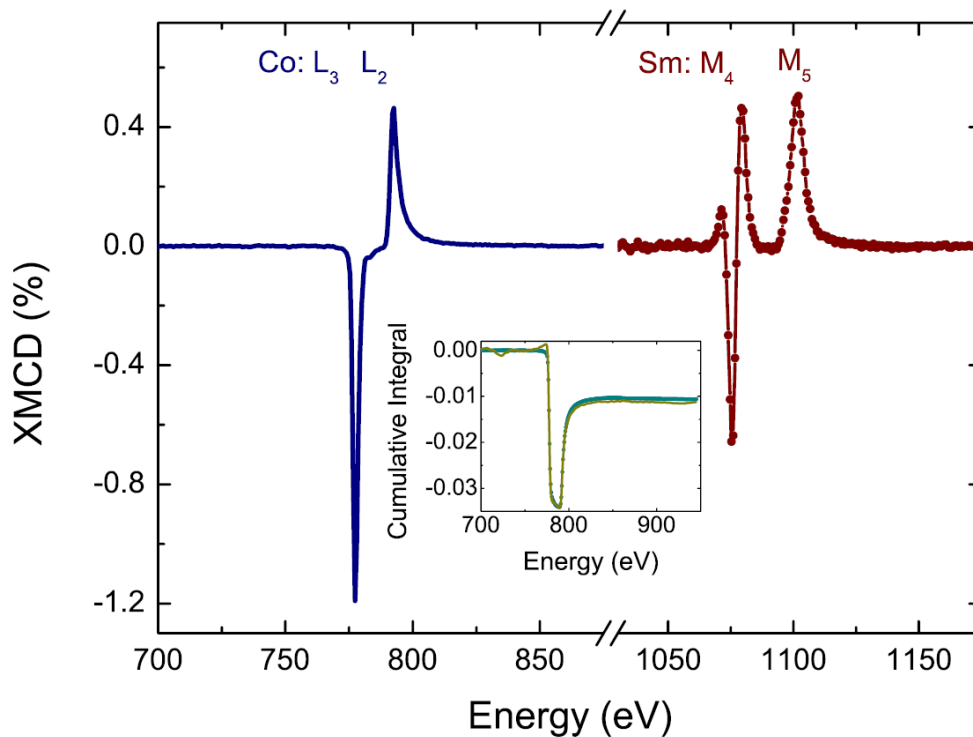
Atomic force microscopy images showing the patterns used in this investigation. The circular islands have a diameter of  $1.5 \mu\text{m}$  and the ellipsoidal islands a  $1.5 \mu\text{m}$  minor axis and a  $4.5 \mu\text{m}$  major axis. The shortest distance between the edges of the islands is  $1.5 \mu\text{m}$  resulting in a periodicity of  $6 \mu\text{m}$  for both patterns along both the  $[01]$  and  $[10]$  lattice directions, defined in the inset.

## Tunable giant magnetic anisotropy in amorphous SmCo thin films

*Applied Physics Letters*, 102, 162402 (2013) [10.1063/1.4802908](https://doi.org/10.1063/1.4802908)

F. Magnus, R. Moubah, A. H. Roos, A. Kruk, V. Kapaklis, T. Hase, B. Hjorvarsson and G. Andersson

SmCo thin films have been grown by magnetron sputtering at room temperature with a composition of 2–35 at.% Sm. Films with 5 at.% or higher Sm are amorphous and smooth. A giant tunable uniaxial in-plane magnetic anisotropy is induced in the films which peaks in the composition range 11–22 at.% Sm. This cross-over behavior is not due to changes in the atomic moments but rather the local configuration changes. The excellent layer perfection combined with highly tunable magnetic properties make these films important for spintronics applications.



## Heteroepitaxial Growth of Ferromagnetic MnSb(0001) Films on Ge/ Si(111) Virtual Substrates

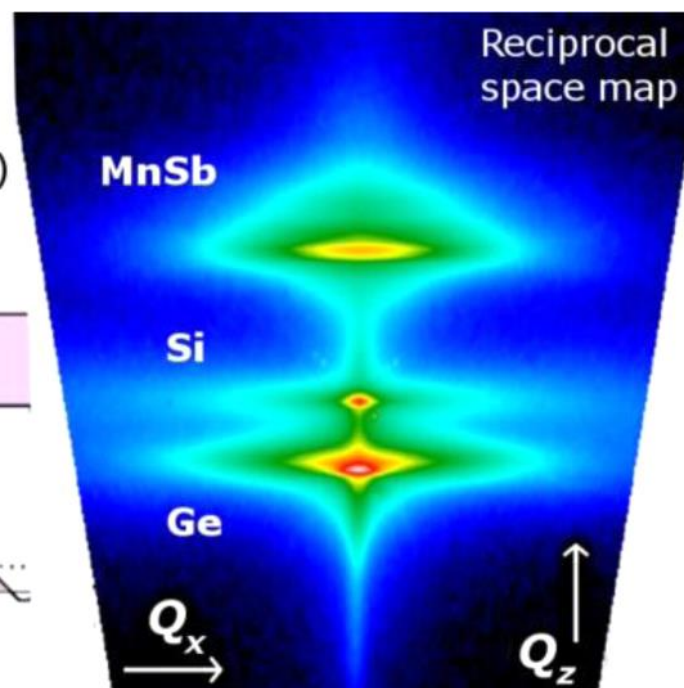
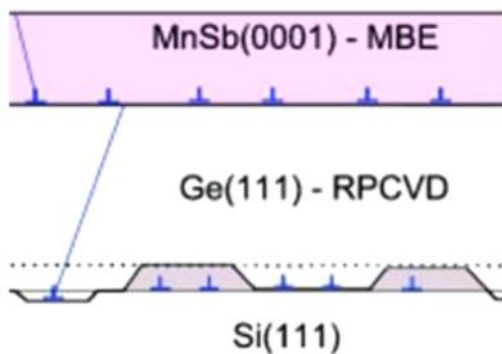
*Crystal Growth & Design*, 13, 4923 (2013)

[10.1021/cg4011136](https://doi.org/10.1021/cg4011136)

C. W. Burrows, A. Dobbie, M. Myronov, T. P. A. Hase, S.B. Wilkins, M. Walker, J.J. Mudd, I. Maskery, M.R. Lees, C.F. McConville, D.R. Leadley, and G.R. Bell

Molecular beam epitaxial growth of ferromagnetic MnSb(0001) has been achieved on high quality, fully relaxed Ge(111)/Si(111) virtual substrates grown by reduced pressure chemical vapor deposition. The epilayers were characterized using reflection high energy electron diffraction, synchrotron hard X-ray diffraction, X-ray photoemission spectroscopy, and magnetometry. The surface reconstructions, magnetic properties, crystalline quality, and strain relaxation behavior of the MnSb films are similar to those of MnSb grown on GaAs(111). In contrast to GaAs substrates, segregation of substrate atoms through the MnSb film does not occur, and alternative polymorphs of MnSb are absent.

Ferromagnetic MnSb (0001) is grown epitaxially on Ge/Si(111) virtual substrates.

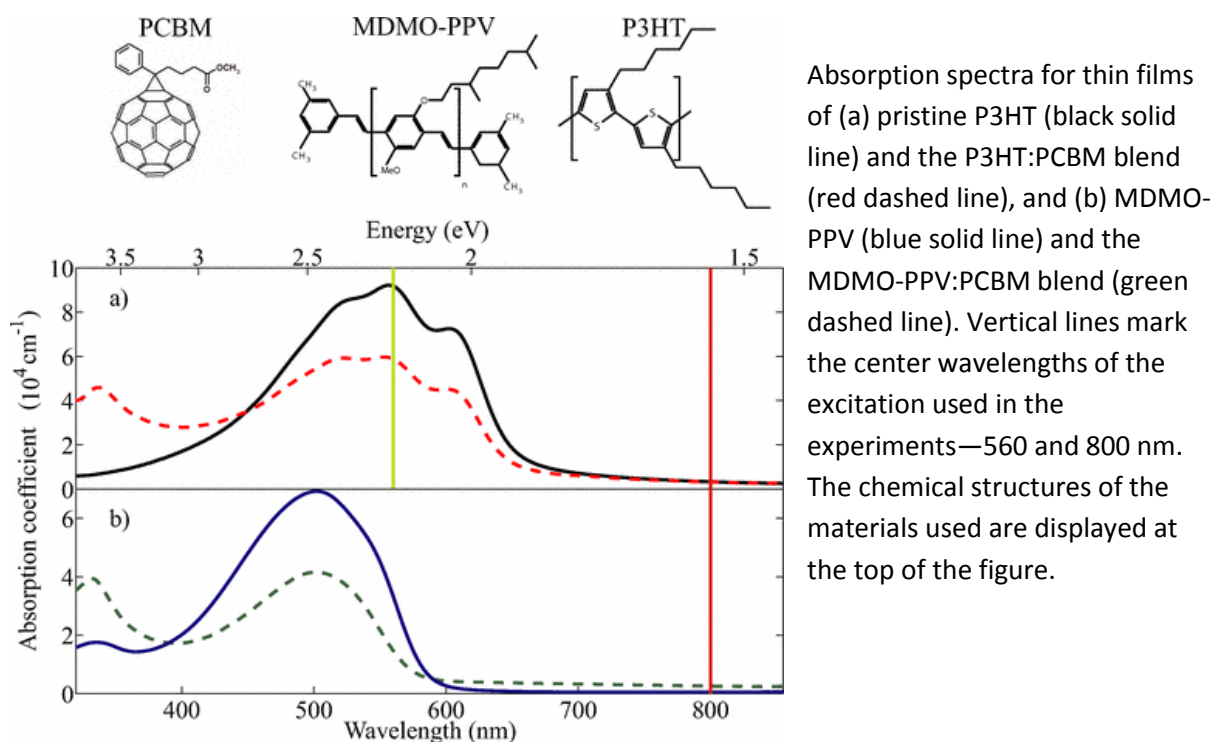


## Efficient generation of charges via below-gap photoexcitation of polymer-fullerene blend films investigated by terahertz spectroscopy

*Phys. Rev. B* 78, 115321 (2008) [10.1103/PhysRevB.78.115321](https://doi.org/10.1103/PhysRevB.78.115321)

P. Parkinson, J. Lloyd-Hughes, M. B. Johnston, and L. M. Herz

Using optical-pump terahertz-probe spectroscopy, we have investigated the time-resolved conductivity dynamics of photoexcited polymer-fullerene bulk heterojunction blends for two model polymers: poly[3-hexylthiophene] (P3HT) and poly[2-methoxy-5-(3,7-dimethyloctyloxy)-1,4-phenylenevinylene] (MDMO-PPV) blended with [6,6]-phenyl-C61 butyric acid methyl ester (PCBM). The observed terahertz-frequency conductivity is characteristic of dispersive charge transport for photoexcitation both at the  $\pi$ - $\pi^*$  absorption peak (560 nm for P3HT) and significantly below it (800 nm). The photoconductivity at 800 nm is unexpectedly high, which we attribute to the presence of a charge-transfer complex. We report the excitation-fluence dependence of the photoconductivity over more than four orders of magnitude, obtained by utilizing a terahertz spectrometer based upon on either a laser oscillator or an amplifier source. The time-averaged photoconductivity of the P3HT:PCBM blend is over 20 times larger than that of P3HT, indicating that long-lived hole polarons are responsible for the high photovoltaic efficiency of polymer:fullerene blends. At early times ( $\sim$ ps) the linear dependence of photoconductivity upon fluence indicates that interfacial charge transfer dominates as an exciton decay pathway, generating charges with mobility of at least  $\sim 0.1$   $\text{cm}^2 \text{V}^{-1} \text{s}^{-1}$ . At later times, a sublinear relationship shows that carrier-carrier recombination effects influence the conductivity on a longer time scale ( $>1$   $\mu\text{s}$ ) with a bimolecular charge annihilation constant for the blends that is approximately two to three orders of magnitude smaller than that typical for neat polymer films.



Absorption spectra for thin films of (a) pristine P3HT (black solid line) and the P3HT:PCBM blend (red dashed line), and (b) MDMO-PPV (blue solid line) and the MDMO-PPV:PCBM blend (green dashed line). Vertical lines mark the center wavelengths of the excitation used in the experiments—560 and 800 nm. The chemical structures of the materials used are displayed at the top of the figure.

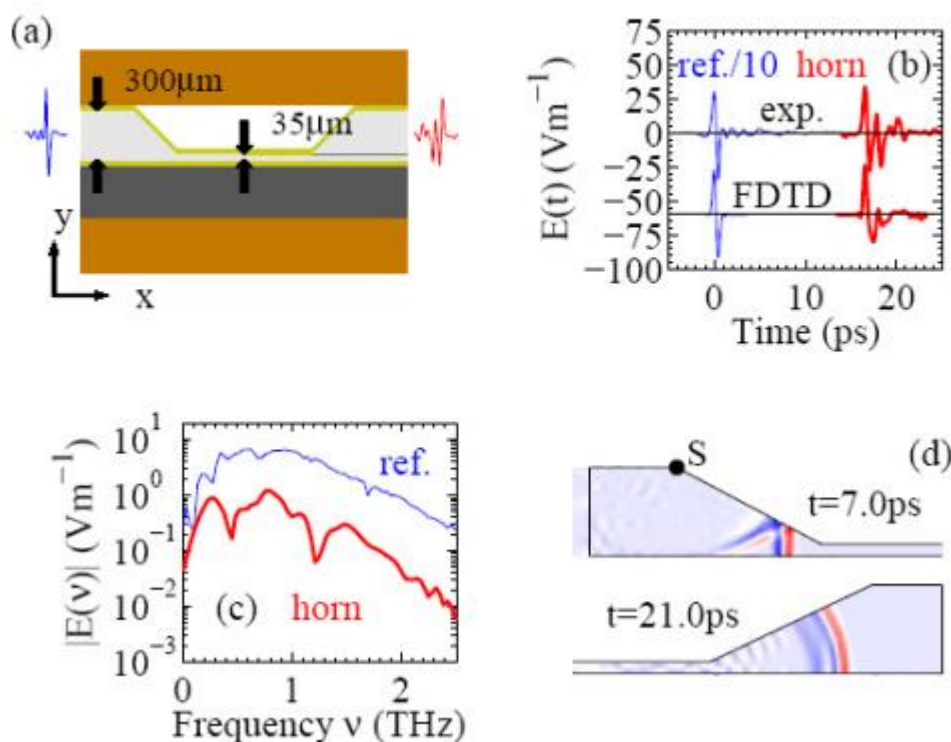
## Coupling terahertz radiation between sub-wavelength metal-metal waveguides and free space using monolithically integrated horn antennae

*Optics Express*, 17, 18387 (2009)

[10.1364/OE.17.018387](https://doi.org/10.1364/OE.17.018387)

J. Lloyd-Hughes, G. Scalari, A. van Kolck, M. Fischer, M. Beck, and J. Faist

Broadband horn antennae are presented that efficiently couple terahertz radiation between sub-wavelength metal-metal waveguides and free space. Sub-picosecond terahertz pulses were coupled into and out from sub-wavelength parallel-plate waveguides by using the horn antennae in a terahertz time-domain spectrometer. Monolithic antennae were fabricated at the facets of metal-metal terahertz quantum cascade lasers, and laser action was observed for devices emitting at 1.4 THz, 2.3 THz and 3.2 THz. A good far-field laser radiation pattern (FWHM less than 11 °) is obtained as a result of the significant expansion of the optical mode by the antenna.



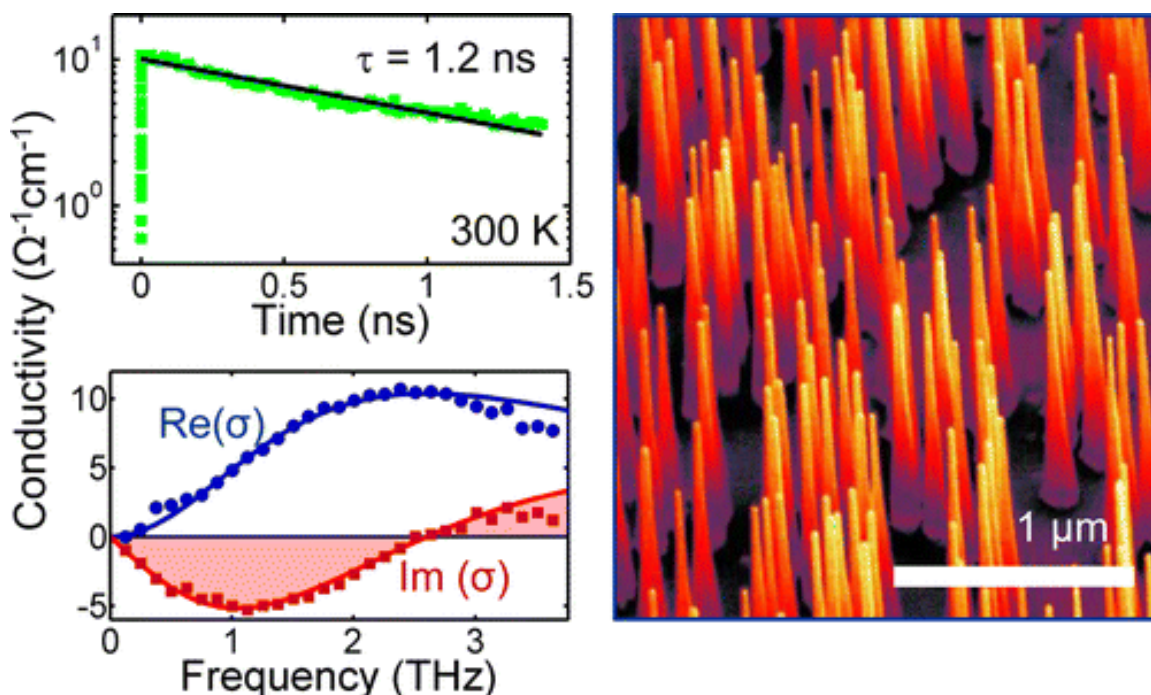
(a) In the transmission measurements terahertz pulses propagated in the x-direction, and were linearly polarized in the y-direction. The layers are (from bottom to top) copper,  $n^+$  GaAs substrate, gold, semi-insulating GaAs, gold, copper. (b) Measured electric field  $E_y$  transmitted through the reference waveguide (divided by 10) and through the horn antenna sample (top two lines). Below are FDTD simulations of  $E_y$ . (c) Electric field amplitude spectra of the pulses through the reference and horn antenna. (d) Finite-difference time-domain simulations of  $E_y$  at times of 7.0 ps and 21.0 ps after the injection of a single-cycle pulse into the waveguide at the left facet (regions with positive  $E_y$  are red, and negative are blue). Point S is the source of a secondary wavefront.

## Ultralow Surface Recombination Velocity in InP Nanowires Probed by Terahertz Spectroscopy

*Nano Letters* 12, 5325 (2012) [10.1021/nl3026828](https://doi.org/10.1021/nl3026828)

Joyce, H.J., Wong-Leung, J., Yong, C.-K., Docherty, C.J., Paiman, S., Gao, Q., Tan, H.H., Jagadish, C., Lloyd-Hughes, J., Herz, L.M., Johnston, M.B.

Using transient terahertz photoconductivity measurements, we have made noncontact, room temperature measurements of the ultrafast charge carrier dynamics in InP nanowires. InP nanowires exhibited a very long photoconductivity lifetime of over 1 ns, and carrier lifetimes were remarkably insensitive to surface states despite the large nanowire surface area-to-volume ratio. An exceptionally low surface recombination velocity (170 cm/s) was recorded at room temperature. These results suggest that InP nanowires are prime candidates for optoelectronic devices, particularly photovoltaic devices, without the need for surface passivation. We found that the carrier mobility is not limited by nanowire diameter but is strongly limited by the presence of planar crystallographic defects such as stacking faults in these predominantly wurtzite nanowires. These findings show the great potential of very narrow InP nanowires for electronic devices but indicate that improvements in the crystallographic uniformity of InP nanowires will be critical for future nanowire device engineering.

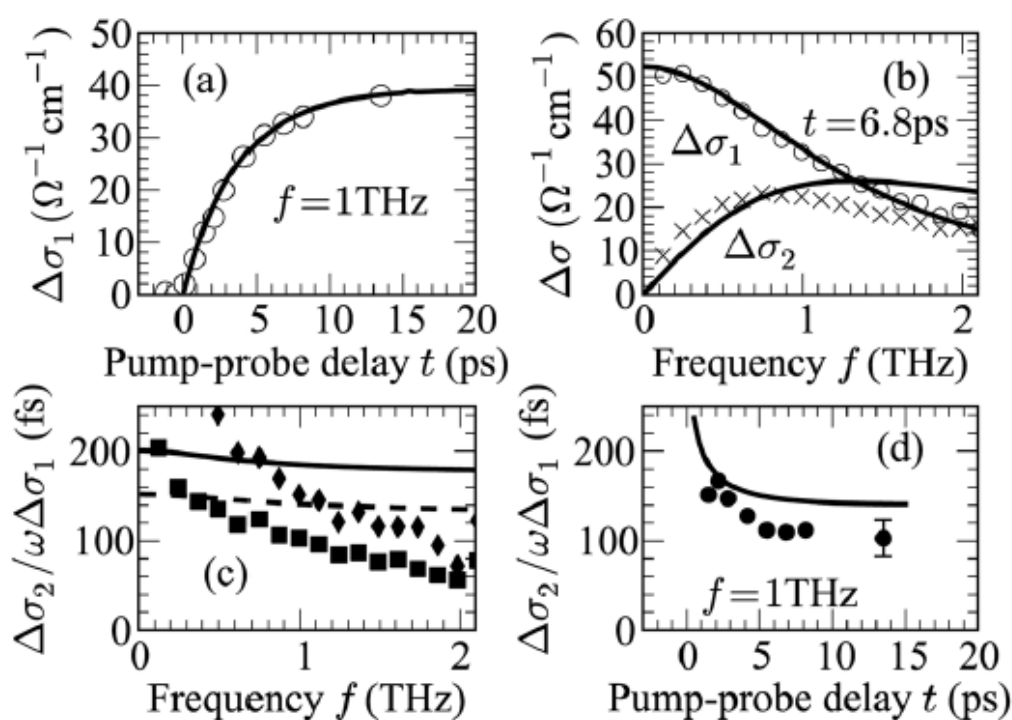


## Generalized conductivity model for polar semiconductors at terahertz frequencies

*Appl. Phys. Lett.* 100, 122103 (2012) [10.1063/1.3695161](https://doi.org/10.1063/1.3695161)

J. Lloyd-Hughes

A theoretical framework is presented that calculates the conductivity of polar semiconductors at terahertz frequencies without resorting to phenomenological fit parameters, using an expression derived from the Boltzmann transport equation. The time-dependent photoconductivity of InAs and the temperature dependent conductivity of n-doped GaAs are found experimentally by terahertz time-domain spectroscopy. The observed deviation from the Drude-Lorentz conductivity in these model systems is accounted for by this approach, which calculates the energy-dependent electron scattering time.



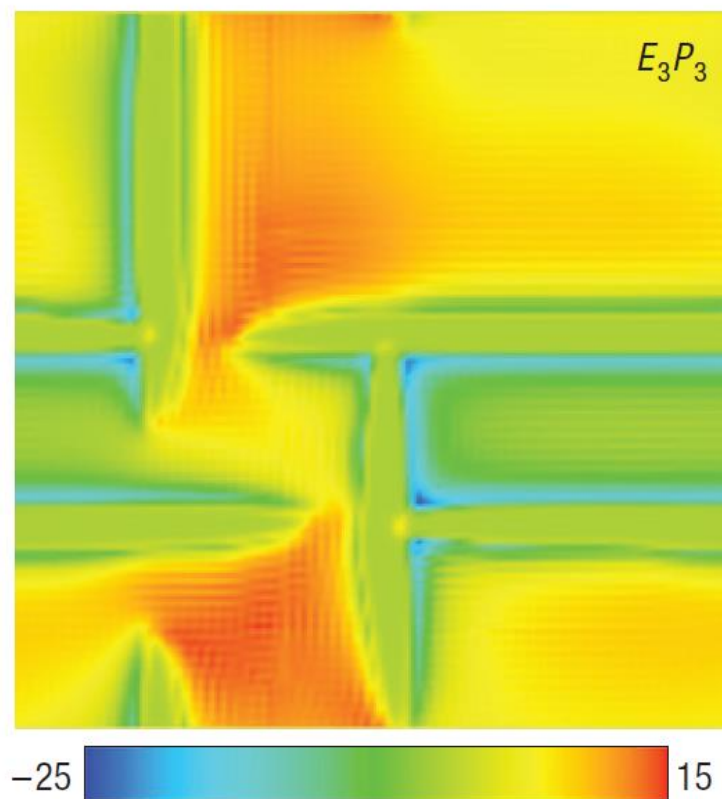
(a) Real part of photoconductivity of InAs  $\Delta\sigma_1$  (at a frequency  $f=1.0 \text{ THz}$ ) at different pump-probe delay times  $t$  from experiment (circles) and calculation (solid line). (b)  $\Delta\sigma_1$  (circles) and  $\Delta\sigma_2$  at  $t=6.8 \text{ ps}$  (crosses), and fit using the Drude-Lorentz model (solid lines). (c)  $\sigma_2/\omega\sigma_1$  at  $t=1.5 \text{ ps}$  (diamonds) and  $t=13.5 \text{ ps}$  (squares) from experiment. The solid and dashed lines show the calculated values at the same delay times. (d)  $\sigma_2/\omega\sigma_1$  at  $f=1 \text{ THz}$  from experiment (circles) and model (solid line) as a function of  $t$ .

## Direct imaging of the spatial and energy distribution of nucleation centres in ferroelectric materials

*Nature Materials* 7, 209 - 215 (2008) [10.1038/nmat2114](https://doi.org/10.1038/nmat2114)

Jesse, S., Rodriguez, B.J., Choudhury, S., Baddorf, A.P., Vrejoiu, I., Hesse, D., Alexe, M., Eliseev, E.A., Morozovska, A.N., Zhang, J., Chen, L.-Q., Kalinin, S.V.

Macroscopic ferroelectric polarization switching, similar to other first-order phase transitions, is controlled by nucleation centres. Despite 50 years of extensive theoretical and experimental effort, the microstructural origins of the Landauer paradox, that is, the experimentally observed low values of coercive fields in ferroelectrics corresponding to implausibly large nucleation activation energies, are still a mystery. Here, we develop an approach to visualize the nucleation centres controlling polarization switching processes with nanometre resolution, determine their spatial and energy distribution and correlate them to local microstructure. The random-bond and random-field components of the disorder potential are extracted from positive and negative nucleation biases. Observation of enhanced nucleation activity at the 90° domain wall boundaries and intersections combined with phase-field modelling identifies them as a class of nucleation centres that control switching in structural-defect-free materials.

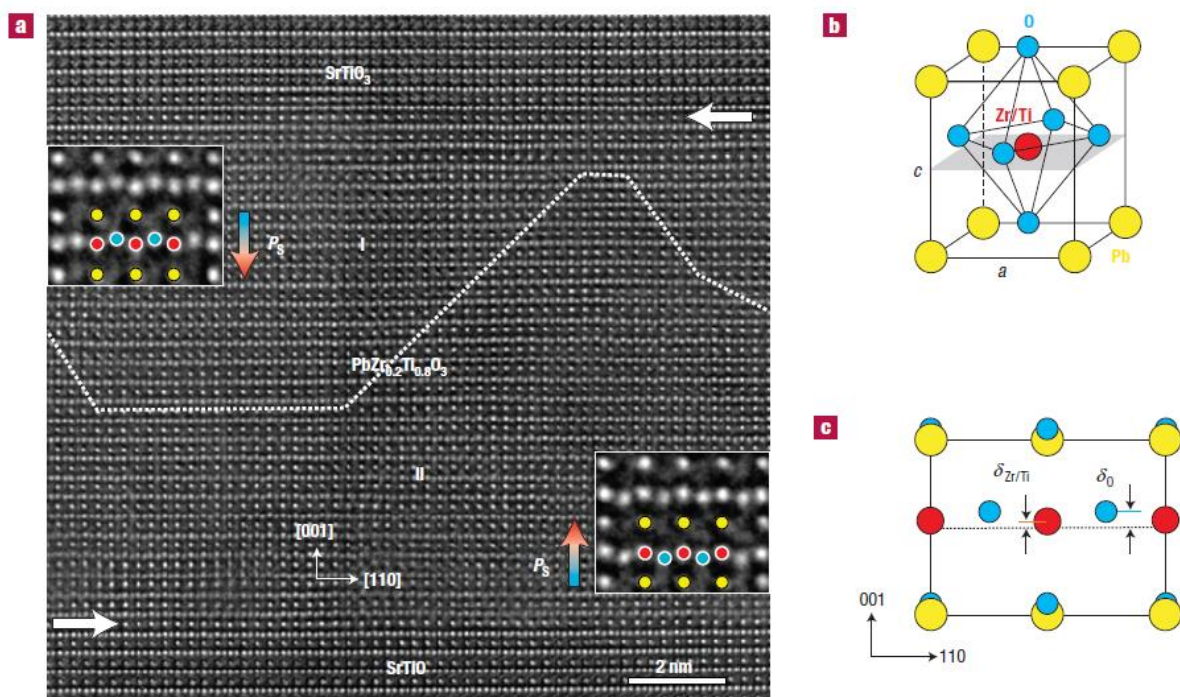


## Atomic-scale study of electric dipoles near charged and uncharged domain walls in ferroelectric films

*Nature Materials* 7, 57 - 61 (2008) [10.1038/nmat2080](https://doi.org/10.1038/nmat2080)

Jia, C.-L., Mi, S.-B., Urban, K., Vrejoiu, I., Alexe, M., Hesse, D.

Ferroelectrics are materials exhibiting spontaneous electric polarization due to dipoles formed by displacements of charged ions inside the crystal unit cell. Their exceptional properties are exploited in a variety of microelectronic applications. As ferroelectricity is strongly influenced by surfaces, interfaces and domain boundaries, there is great interest in exploring how the local atomic structure affects the electric properties. Here, using the negative spherical-aberration imaging technique in an aberration-corrected transmission electron microscope, we investigate the cation–oxygen dipoles near  $180^\circ$  domain walls in epitaxial  $\text{PbZr}_{0.2}\text{Ti}_{0.8}\text{O}_3$  thin films on the atomic scale. The width and dipole distortion across a transversal wall and a longitudinal wall are measured, and on this basis the local polarization is calculated. For the first time, a large difference in atomic details between charged and uncharged domain walls is reported.



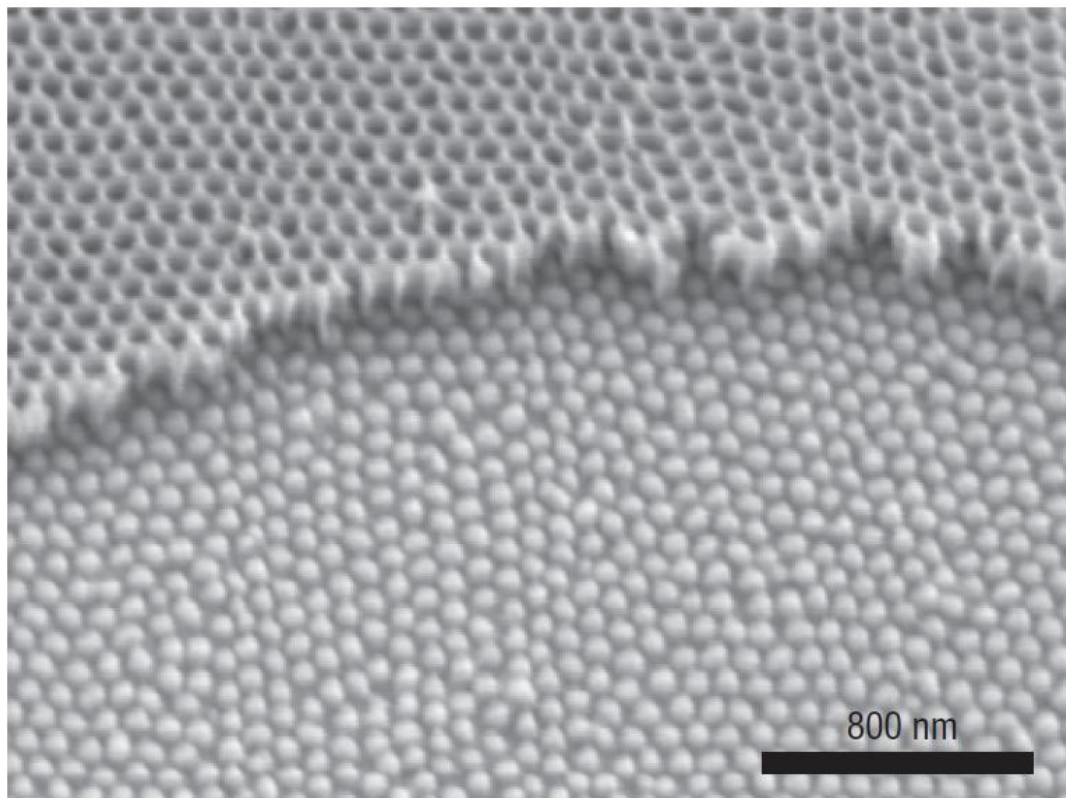
**Atomic-scale imaging of the electric dipoles formed by the relative displacements of the Zr/Ti cation columns and the O anion columns.** **a**, Image of a  $\text{SrTiO}_3/\text{PbZr}_{0.2}\text{Ti}_{0.8}\text{O}_3/\text{SrTiO}_3$  thin-film heterostructure. The horizontal arrows denote the horizontal interfaces between the  $\text{PbZr}_{0.2}\text{Ti}_{0.8}\text{O}_3$  and the top and the bottom  $\text{SrTiO}_3$  film layers. The dotted line traces the  $180^\circ$  domain wall. The insets show magnifications of the dipoles formed by the displacements of ions in the unit cells (yellow: PbO, red: Zr/Ti, blue: O). **b**, Schematic perspective view of the unit cell of ferroelectric  $\text{PbZr}_{0.2}\text{Ti}_{0.8}\text{O}_3$ . **c**, Projection of the unit cell along the  $[\bar{1}10]$  direction.  $\delta_{\text{Zr/Ti}}$  and  $\delta_{\text{O}}$  denote the shifts of the Zr/Ti atoms and the oxygen atoms, respectively, from the centrosymmetric positions.

## Individually addressable epitaxial ferroelectric nanocapacitor arrays with near $1\text{Tb inch}^{-2}$ density

*Nature Nanotechnology* 3, 402 - 407 (2008) [10.1038/nnano.2008.161](https://doi.org/10.1038/nnano.2008.161)

Lee, W., Han, H., Lotnyk, A., Schubert, M.A., Senz, S., Alexe, M., Hesse, D., Baik, S., Gösele, U.

Ferroelectric materials have emerged in recent years as an alternative to magnetic and dielectric materials for nonvolatile data-storage applications. Lithography is widely used to reduce the size of data-storage elements in ultrahigh-density memory devices. However, ferroelectric materials tend to be oxides with complex structures that are easily damaged by existing lithographic techniques, so an alternative approach is needed to fabricate ultrahigh-density ferroelectric memories. Here we report a high-temperature deposition process that can fabricate arrays of individually addressable metal/ferroelectric/metal nanocapacitors with a density of  $176\text{ Gb inch}^{-2}$ . The use of an ultrathin anodic alumina membrane as a lift-off mask makes it possible to deposit the memory elements at temperatures as high as  $650\text{ }^\circ\text{C}$ , which results in excellent ferroelectric properties.



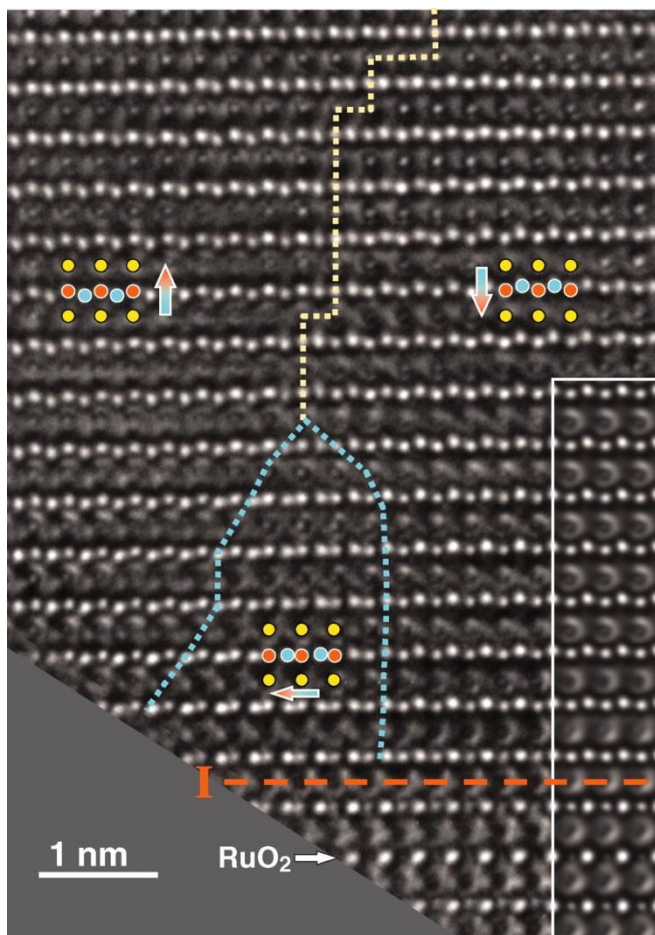
As-prepared PZT nano-island array with the AAO mask visible at the top of the image. The nano-island density can be estimated as  $176\text{ Gb inch}^{-2}$

## Direct Observation of Continuous Electric Dipole Rotation in Flux-Closure Domains in Ferroelectric $\text{Pb}(\text{Zr},\text{Ti})\text{O}_3$

*Science* 331, 1420 (2011) [10.1126/science.1200605](https://doi.org/10.1126/science.1200605)

Jia, C.-L., Urban, K.W., Alexe, M., Hesse, D., Vrejoiu, I.

Low-dimensional ferroelectric structures are a promising basis for the next generation of ultrahigh-density nonvolatile memory devices. Depolarization fields, created by incompletely compensated charges at the surfaces and interfaces, depress the polarization of such structures. Theory suggests that under conditions of uncompensated surface charges, local dipoles can organize in flux-closure structures in thin films and vortex structures in nano-sized ferroelectrics, reducing depolarization fields. However, the continuous rotation of the dipoles required in vortex structures and the behavior of unit cell dipoles in flux-closure structures have never been experimentally established. By aberration-corrected transmission electron microscopy, we obtained experimental evidence for continuous rotation of the dipoles closing the flux of  $180^\circ$  domains in a ferroelectric perovskite thin film.



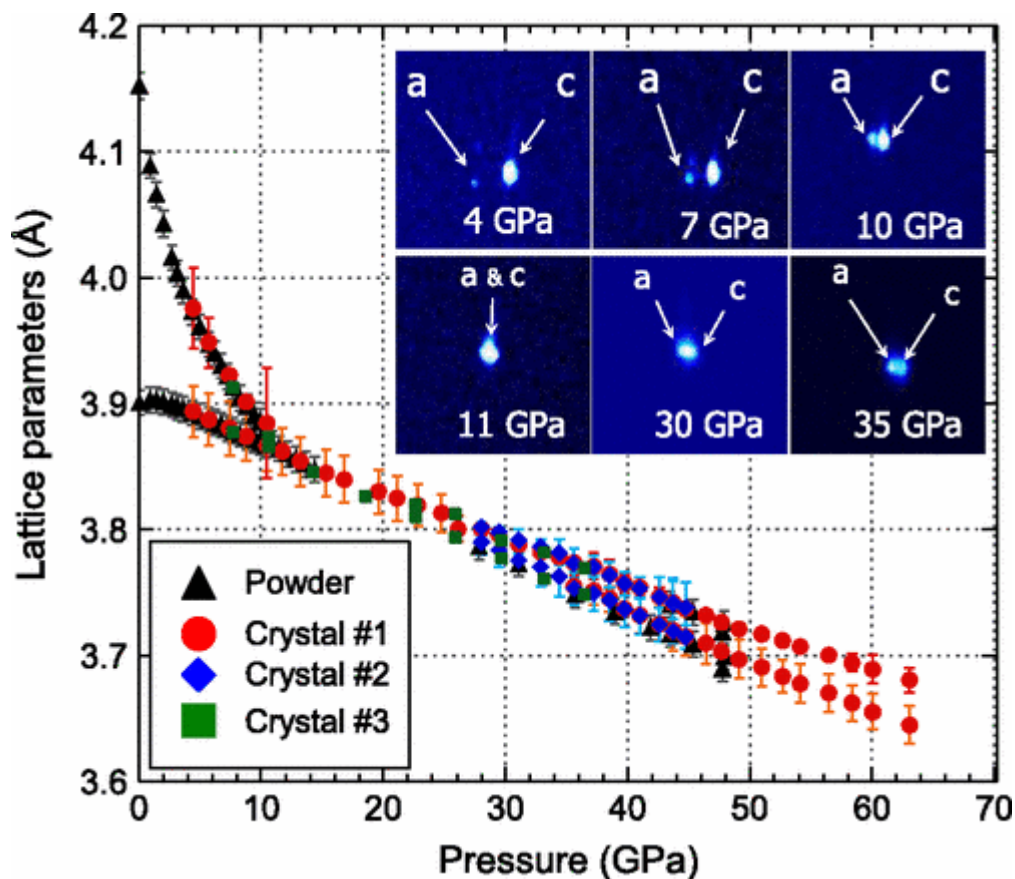
Atomic-resolution image of a flux-closure structure with continuous dipole rotation in  $\text{PbZr}_{0.2}\text{Ti}_{0.8}\text{O}_3$  (PZT) close to the interface to the  $\text{SrTiO}_3$  (STO) substrate.

## High-Pressure Effect on $\text{PbTiO}_3$ : An Investigation by Raman and X-Ray Scattering up to 63 GPa

*Phys. Rev. Lett.* 101, 237601 (2008) [10.1103/PhysRevLett.101.237601](https://doi.org/10.1103/PhysRevLett.101.237601)

P.-E. Janolin, P. Bouvier, J. Kreisel, P. A. Thomas, I. A. Kornev, L. Bellaiche, W. Crichton, M. Hanfland, and B. Dkhil

We report a room-temperature high-pressure x-ray and Raman scattering investigation of lead titanate ( $\text{PbTiO}_3$ ) up to 63 GPa. Three continuous phase transitions at 13, 20, and 45 GPa between tetragonal-like phases occur. As a result, no evidence is found for a pressure-induced morphotropic phase boundary. Our study provides experimental evidence that  $\text{PbTiO}_3$  presents a complex sequence of phases accommodating pressure through mechanisms involving oxygen octahedra tilting and re-entrance of ferroelectricity.



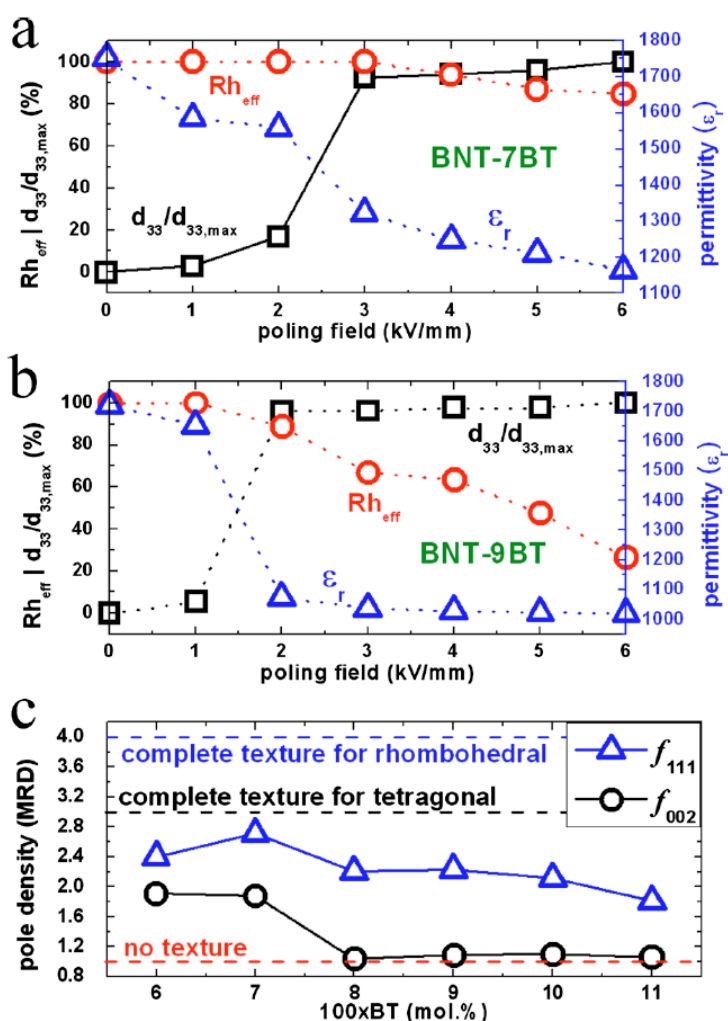
Pressure evolution of the lattice parameters of  $\text{PbTiO}_3$  from 0.1 to 63 GPa and of the  $\langle 004 \rangle$  Bragg spot (inset).

## Evolving morphotropic phase boundary in lead-free $(\text{Bi}_{1/2}\text{Na}_{1/2})\text{TiO}_3$ - $\text{BaTiO}_3$ piezoceramics

*J. Appl. Phys.* 109, 014110 (2011) [10.1063/1.3530737](https://doi.org/10.1063/1.3530737)

Jo, W, Daniels, J E., Jones, J L., Tan, X, Thomas, P A., Damjanovic, D and Rödel, J.

The correlation between structure and electrical properties of lead-free  $(1-x)(\text{Bi}_{1/2}\text{Na}_{1/2})\text{TiO}_3$ - $x\text{BaTiO}_3$  (BNT-100xBT) polycrystalline piezoceramics was investigated systematically by *in situ* synchrotron diffraction technique, combined with electrical property characterization. It was found that the morphotropic phase boundary (MPB) between a rhombohedral and a tetragonal phase evolved into a morphotropic phase region with electric field. In the unpoled material, the MPB was positioned at the transition from space group  $R3m$  to  $P4mm$  (BNT-11BT) with optimized permittivity throughout a broad single-phase  $R3m$  composition regime. Upon poling, a range of compositions from BNT-6BT to BNT-11BT became two-phase mixture, and maximum piezoelectric coefficient was observed in BNT-7BT. It was shown that optimized electrical properties are related primarily to the capacity for domain texturing and not to phase coexistence.



Evolution of piezoelectric coefficient ( $d_{33}$ ), relative permittivity ( $\epsilon_r$ ), and an effective rhombohedral volume fraction ( $Rh_{eff}$ ) of (a) BNT-7BT and (b) BNT-9BT during poling.

(c) Calculated pole densities that represent the degree of domain reorientation during poling of each composition. In the case of BNT-6BT and BNT-7BT, not only the rhombohedral but also the induced tetragonal phases develop a high degree of texture, while practically no texture develops in the induced tetragonal phases in other compositions.

The dotted lines in (a) and (b) trace the evolution of  $\epsilon_r$  and  $d_{33}$  during loading and unloading of electric fields.

## Evidence for a non-rhombohedral average structure in the lead-free piezoelectric material $\text{Na}_{0.5}\text{Bi}_{0.5}\text{TiO}_3$

*Journal of Applied Crystallography* 43, 1409 (2010). [10.1107/S002188981003342X](https://doi.org/10.1107/S002188981003342X)

S. Gorfman and P. A. Thomas

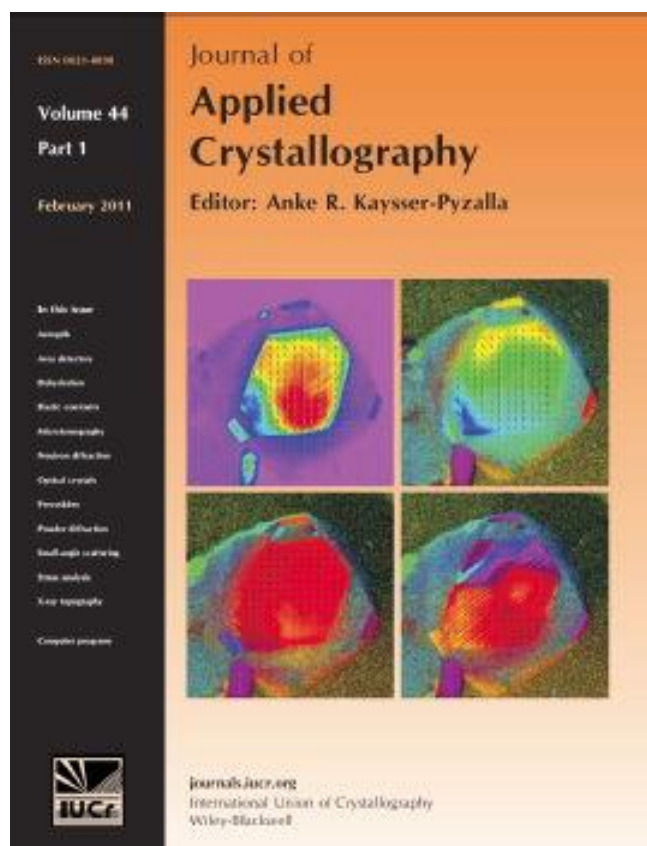
The potential lead-free piezoelectric material sodium bismuth titanate,  $\text{Na}_{0.5}\text{Bi}_{0.5}\text{TiO}_3$ , was investigated by means of high-resolution single-crystal X-ray diffractometry. The splitting of Bragg peaks observed in the high-resolution reciprocal-space maps suggests that the average structure of  $\text{Na}_{0.5}\text{Bi}_{0.5}\text{TiO}_3$  has lower than rhombohedral symmetry. This observation is contrary to the commonly adopted model, which has followed from many previous analyses of neutron and X-ray powder diffraction data.

## An investigation of the properties of large crystals of the zeolites dodecasil-3C and ferrierite by high-temperature birefringence microscopy and X-ray diffraction

*Journal of Applied Crystallography* 43, 168 (2010). [10.1107/S0021889809052753](https://doi.org/10.1107/S0021889809052753)

Z. A. D. Lethbridge, D. S. Keeble, D. Walker, P. A. Thomas and R. I. Walton

Optical birefringence has been measured as a function of temperature for two types of siliceous zeolite crystals that contain organic template molecules. The specimens were prepared using modified solvothermal synthesis to produce large ( $\sim 1$  mm dimension) crystals. In the case of the clathrasil dodecasil-3C the material undergoes a first-order phase transition at  $\sim 433$  K that is reversible after heating to 873 K and cooling to room temperature. Comparison with powder X-ray diffraction data from a bulk sample shows that this is a ferroelastic tetragonal ( $I\bar{4}2d$ ) to cubic ( $Fd\bar{3}m$ ) transition, which is supported by the functional form of temperature variation of the birefringence. There is apparently no loss of the organic template involved in this transition. For the zeolite ferrierite, the plate-like crystals show a pronounced domain-like structure, which, although not due to twinning, shows a distinctive optical birefringence change on heating, suggesting that variable concentrations of organic template might be present in different domain-like regions. In this material there is no evidence for a change in crystal symmetry up to 873 K ( $Pnmm$ ), despite apparent loss of some organic template from the material which, in turn, gives rise to strain birefringence at the edges parallel to the [010] direction.

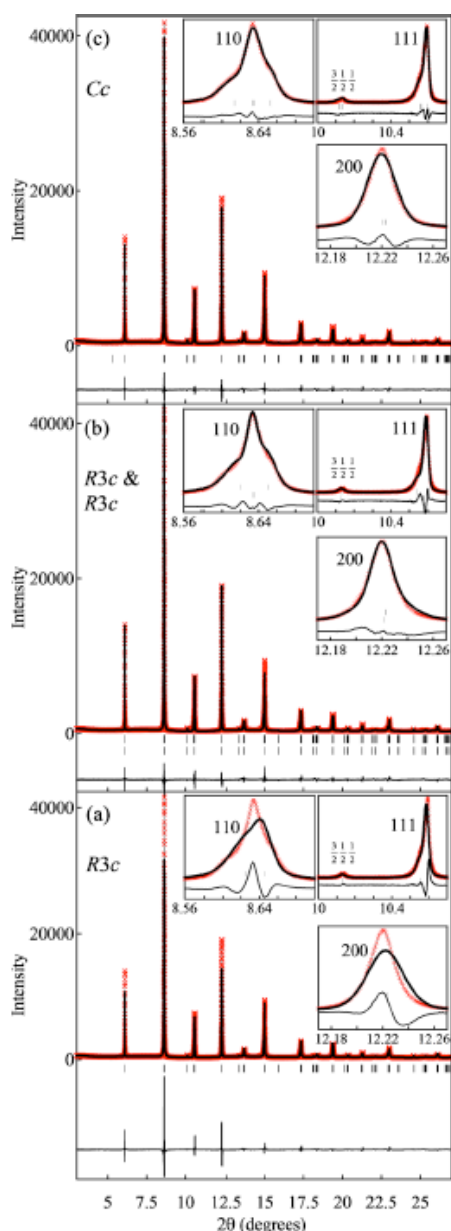


## Monoclinic crystal structure of polycrystalline $\text{Na}_{0.5}\text{Bi}_{0.5}\text{TiO}_3$

*Applied Physics Letters*, 98, 152901 (2011) [10.1063/1.3573826](https://doi.org/10.1063/1.3573826)

Aksel, E, Forrester, J S., Jones, J L., Thomas, P A., Page, K and Suchomel, M R.

Bismuth-based ferroelectric ceramics are currently under intense investigation for their potential as Pb-free alternatives to lead zirconate titanate-based piezoelectrics.  $\text{Na}_{0.5}\text{Bi}_{0.5}\text{TiO}_3$  (NBT), one of the widely studied compositions, has been assumed thus far to exhibit the rhombohedral space group  $R3c$  at room temperature. High-resolution powder x-ray diffraction patterns, however, reveal peak splitting in the room temperature phase that evidence the true structure as monoclinic with space group  $Cc$ . This peak splitting and  $Cc$  space group is only revealed in sintered powders; calcined powders are equally fit to an  $R3c$  model because microstructural contributions to peak broadening obscure the peak splitting.



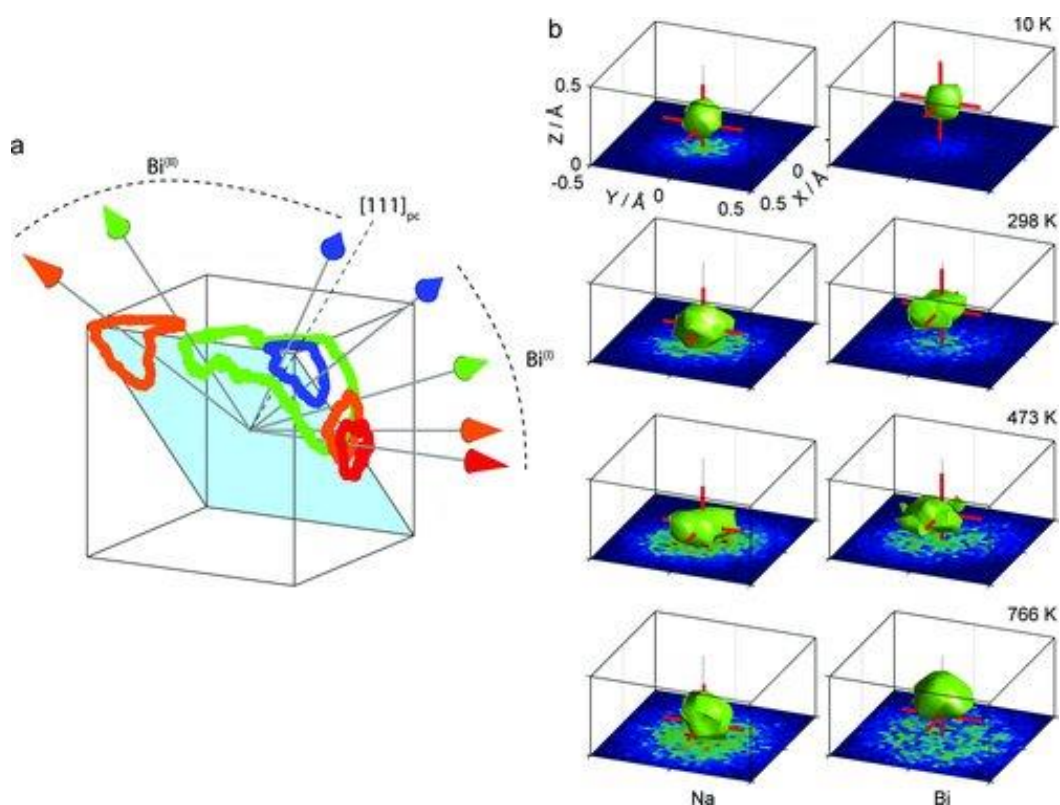
Powder diffraction pattern of sintered NBT powder and results of crystallographic refinement using an  $R3c$  space group (a), a mixture of two  $R3c$  phases (b), and a  $Cc$  space group (c). The labeled peak indices are relative to the pseudocubic perovskite unit cell.

## Bifurcated Polarization Rotation in Bismuth-Based Piezoelectrics

*Advanced Functional Materials* 23, 185, (2013) [10.1002/adfm.201201564](https://doi.org/10.1002/adfm.201201564)

D. S. Keeble , E R. Barney , D A. Keen , M G. Tucker , J Kreisel , and P. A. Thomas

$ABO_3$  perovskite-type solid solutions display a large variety of structural and physical properties, which can be tuned by chemical composition or external parameters such as temperature, pressure, strain, electric, or magnetic fields. Some solid solutions show remarkably enhanced physical properties including colossal magnetoresistance or giant piezoelectricity. It has been recognized that structural distortions, competing on the local level, are key to understanding and tuning these remarkable properties, yet, it remains a challenge to experimentally observe such local structural details. Here, from neutron pair-distribution analysis, a temperature-dependent 3D atomic-level model of the lead-free piezoelectric perovskite  $Na_{0.5}Bi_{0.5}TiO_3$  (NBT) is reported. The statistical analysis of this model shows how local distortions compete, how this competition develops with temperature, and, in particular, how different polar displacements of  $Bi^{3+}$  cations coexist as a bifurcated polarization, highlighting the interest of Bi-based materials in the search for new lead-free piezoelectrics.



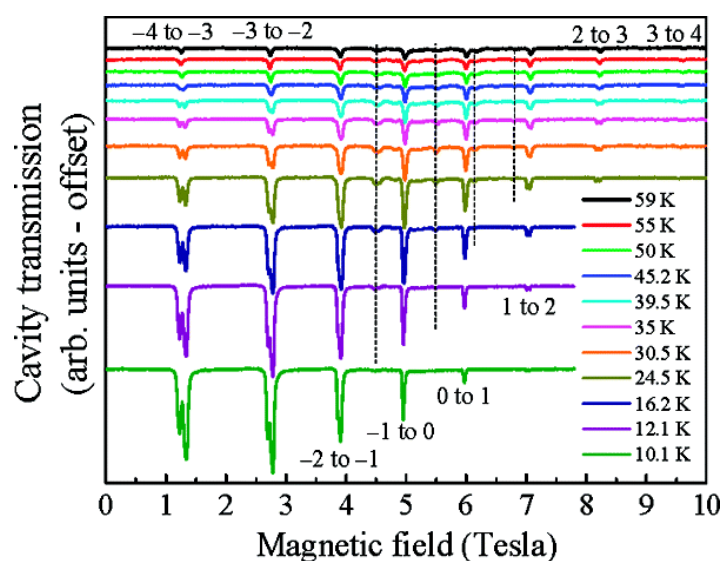
Temperature evolution of the A-site local environment. a) Schematic of the two polarization rotations within the perovskite structure seen as a function of temperature, from 10 K (blue) to 766 K (red). The arrows denote predominant displacement directions. b) Density plots of displacement vectors for  $Na^+$  and  $Bi^{3+}$  at various temperatures, with isosurfaces showing contours at 75% of normalised density.

## Disorder and intermolecular interactions in a family of tetranuclear Ni(II) complexes probed by high-frequency electron paramagnetic resonance

*Inorganic Chemistry* 47, 1965 (2008) [10.1021/ic701416w](https://doi.org/10.1021/ic701416w)

J Lawrence, EC Yang, R Edwards, MM Olmstead, C Ramsey C, NS Dalal, PK Gantzel, S Hill and DN Hendrickson

High-frequency electron paramagnetic resonance (HF-EPR) data are presented for four closely related tetranuclear Ni(II) complexes, [Ni(hmp)(MeOH)Cl]4·H2O (1a), [Ni(hmp)(MeOH)Br]4·H2O (1b), [Ni(hmp)(EtOH)Cl]4·H2O (2), and [Ni(hmp)(dmb)Cl]4 (3) (where hmp(-) is the anion of 2-hydroxymethylpyridine and dmb is 3,3'-dimethyl-1-butanol), which exhibit magnetic bistability (hysteresis) and fast magnetization tunneling at low temperatures, properties which suggest they are single-molecule magnets (SMMs). The HF-EPR spectra confirm spin  $S = 4$  ground states and dominant uniaxial anisotropy ( $DS_z(2)$ ,  $D < 0$ ) for all four complexes, which are the essential ingredients for a SMM. The individual fine structure peaks (due to zero-field splitting) for complexes 1a, 1b, and 2 are rather broad. They also exhibit further (significant) splitting, which can be explained by the fact that there exists two crystallographically distinct Ni 4 sites in the lattices for these complexes, with associated differences in metal-ligand bond lengths and different zero-field splitting (ZFS) parameters. The broad EPR lines, meanwhile, may be attributed to ligand and solvent disorder, which results in additional distributions of microenvironments. In the case of complex 3, there are no solvate molecules in the structure, and only one distinct Ni 4 molecule in the lattice. Consequently, the HF-EPR data for complex 3 are extremely sharp. As the temperature of a crystal of complex 3 is decreased, the HF-EPR spectrum splits abruptly at approximately 46 K into two patterns with very slightly different ZFS parameters. Heat capacity data suggest that this is caused by a structural transition at 46.6 K. A single-crystal X-ray structure at 12(2) K indicates large thermal parameters on the terminal methyl groups of the dmb (3,3-dimethyl-1-butanol) ligand. Most likely there exists dynamic disorder of parts of the dmb ligand above 46.6 K; an order-disorder structural phase transition at 46.6 K then removes some of the motion. A further decrease in temperature (<6 K) leads to further fine structure splittings for complex 3. This behavior is thought to be due to the onset of short-range magnetic correlations/coherences between molecules caused by weak intermolecular magnetic exchange interactions.

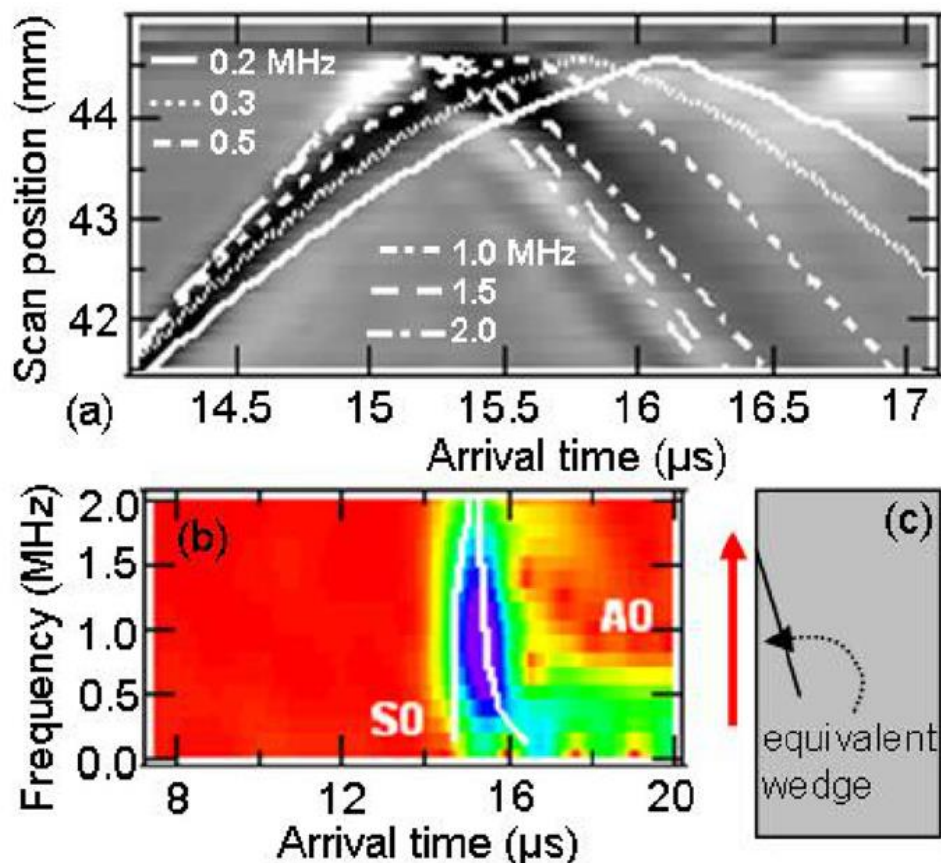


## Enhancement of ultrasonic surface waves at wedge tips and angled defects

*Applied Physics Letters* 99, 094104 (2011) [10.1063/1.3629772](https://doi.org/10.1063/1.3629772)

RS Edwards, B Dutton, AR Clough and MH Rosli

The behaviour of sound waves interacting with wedges has attracted interest from researchers in geophysics and non-destructive testing. We consider here the near-field behaviour of Rayleigh waves incident on wedges and surface-breaking defects which propagate at an angle to the surface, such as rolling contact fatigue on rails. It has been shown that, for a detection point on the edge of the crack tip, a very large signal enhancement is observed for shallow angles. We explain this behaviour through considering the effect of the defect geometry, with changes in the frequency-thickness product leading to mode-conversion of the incident Rayleigh wave.



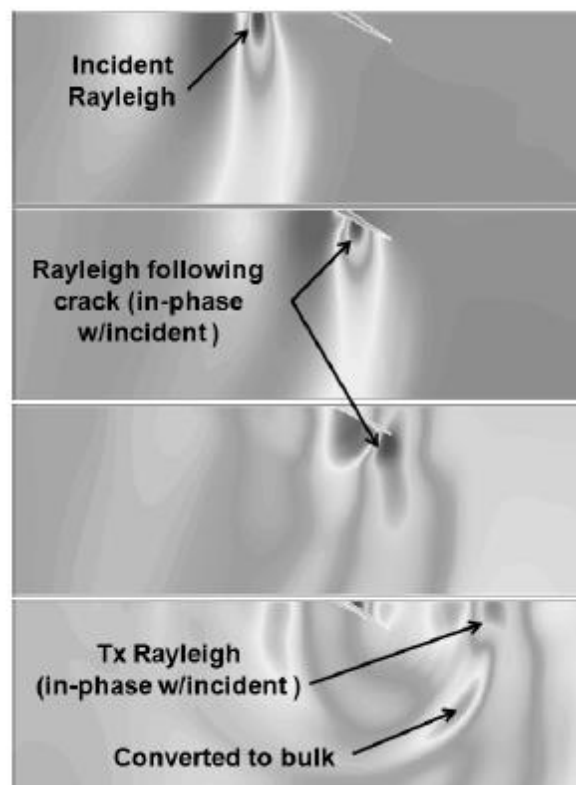
Experimental results for a 2 mm long defect inclined at  $20^\circ$  to the sample surface. (a) B-Scan, (b) STFT of the enhanced wave at the tip, (c) schematic of sample.

## Non-contact ultrasonic detection of angled surface defects.

*NDT & E International*, 44, 353 (2011) [10.1016/j.ndteint.2011.02.001](https://doi.org/10.1016/j.ndteint.2011.02.001)

Dutton, B. , Clough, A. R., Rosli, M. H. and Edwards, R. S.

Non-destructive testing is an important technique, and improvements are constantly needed. Surface defects in metals are not necessarily confined to orientations normal to the sample surface; however, much of the previous work investigating the interaction of ultrasonic surface waves with surface-breaking defects has assumed cracks inclined at  $90^\circ$  to the surface. This paper explores the interaction of Rayleigh waves with cracks which have a wide range of angles and depths relative to the surface, using a non-contact laser generation and detection system. Additional insight is acquired using a 3D model generated using finite element method software. A clear variation of the reflection and transmission coefficients with both crack angle and length is found, in both the out-of-plane and in-plane components. The 3D model is further used to understand the contributions of different wavemodes to B-Scans produced when scanning a sample, to enable understanding of the reflection and transmission behaviour, and help identify angled defects. Knowledge of these effects is essential to correctly gauge the severity of surface cracking.



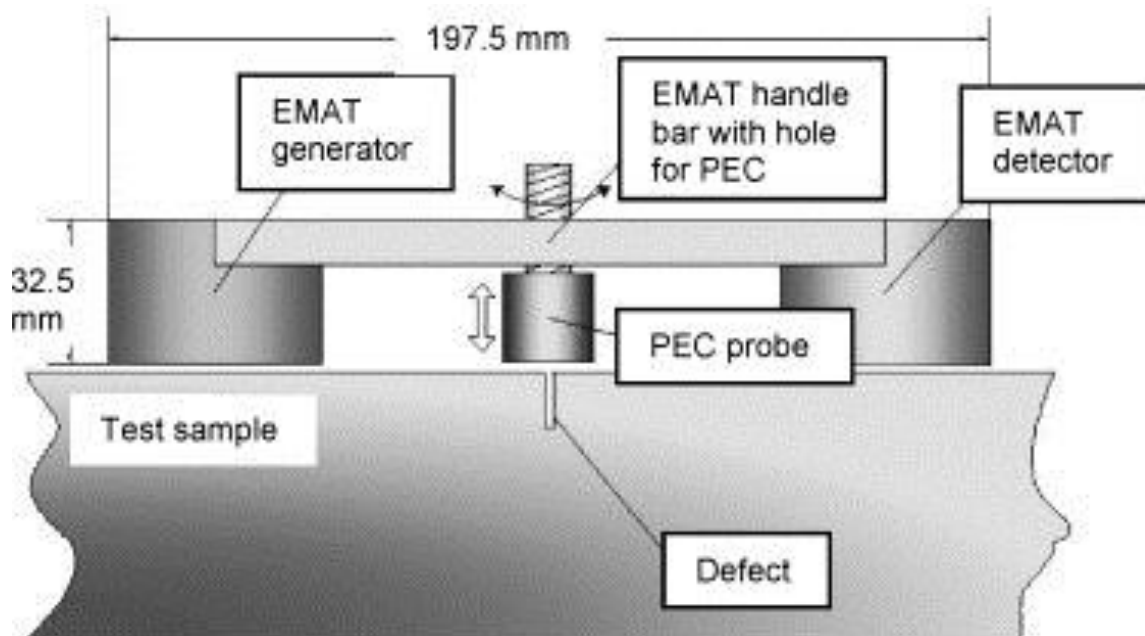
3D model output for a  $150^\circ$  crack with  $d/\lambda = 0.55$ , showing the OP component. This shows the propagation of the Rayleigh wave along the crack and mode conversion at the crack bottom.

## Data fusion for defect characterisation using a dual probe system

*Sensors and Actuators A-Physical* 144 (1) 222-228 (2008) [10.1016/j.sna.2007.12.020](https://doi.org/10.1016/j.sna.2007.12.020)

RS Edwards, A Sophian, S Dixon and GY Tian

We present recent work on a dual probe system containing electromagnetic acoustic transducers (EMATs) generating and detecting surface ultrasonic waves, and a pulsed eddy current (PEC) probe. This system is able to detect and size surface and near-surface defects in electrically conducting samples by looking at changes in the detected signal for each probe. By combining the information from each probe using a weighted logic function for data fusion, it is possible to both classify and size defects, with increased reliability. By combining the data in this way one obtains information about the defects which is not available when using either probe in isolation. Typical results on steel and aluminium samples are presented, along with information about the data fusion function. The dual probe and data fusion routine has been demonstrated to work at manual-scanning speeds, with higher speeds possible following some simple improvements to the system.

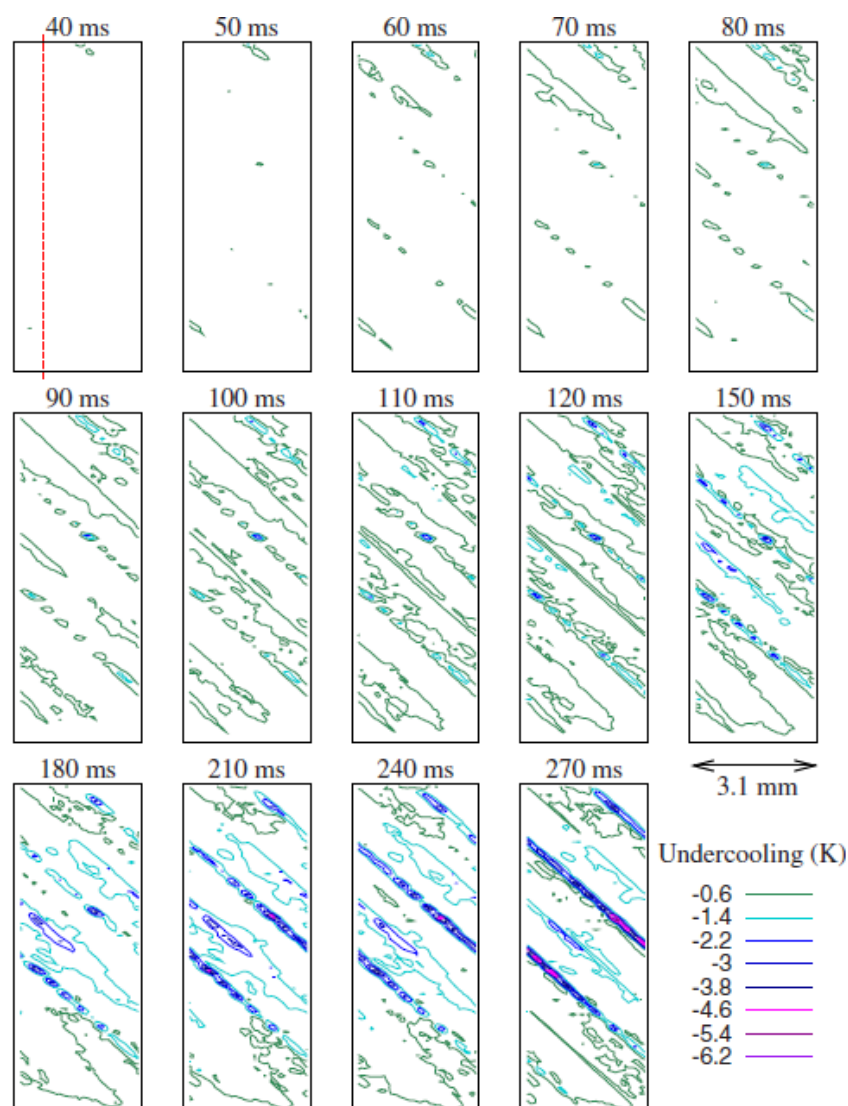


## Temperature contour maps at the strain-induced martensitic transition of a Cu-Zn-Al shape memory single crystal

*Applied Physics Letters* 98(1) 011902 (2011) [10.1063/1.3533403](https://doi.org/10.1063/1.3533403)

E Vives, S Burrows, RS Edwards, S Dixon, L Mañosa, A Planes and R Romero

We study temperature changes at the reverse strain-induced martensitic transformation in a Cu-Zn-Al single crystal. Infrared thermal imaging reveals a markedly inhomogeneous temperature distribution. The evolution of the contour temperature maps enables information to be extracted on the kinetics of the interface motion.



IR contour temperature maps at selected times during the unloading process.

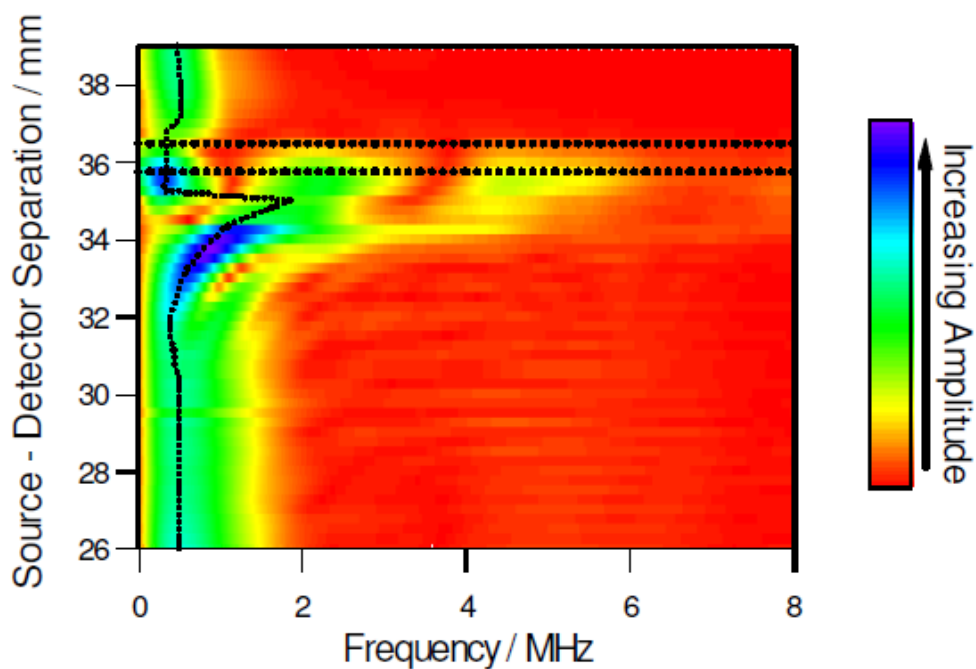
## Non-linear enhancement of laser generated ultrasonic Rayleigh waves by cracks

*Nondestructive Testing and Evaluation* 23, 25-34 (2008)

[10.1080/10589750701550640](https://doi.org/10.1080/10589750701550640)

Dixon, S., Cann, B., Carroll, Donna L., Fan, Y. and Edwards, R. S.

Laser generated ultrasound has been widely used for detecting cracks, surface and sub-surface defects in many different materials. It provides a non-contact wideband excitation source which can be focused into different geometries. Previous workers have reported enhancement of the laser generated Rayleigh wave when a crack is illuminated by pulsed laser beam irradiation. We demonstrate that the enhancement observed is due to a combination of source truncation, the free boundary condition at the edge of the crack and interference effects. Generating a Rayleigh wave over a crack can lead to enhancement of the amplitude of the Rayleigh wave signal, a shift in the dominant frequency of the wideband Rayleigh wave and strong enhancement of the high frequency components of the Rayleigh wave.



Fourier transform image B-scan plot for the Rayleigh waves detected by the interferometer for the generation pulsed laser beam approaching a simulated crack in an aluminium sample. The dotted line that runs in a vertical sense shows the position in frequency space of the peak amplitude in the magnitude FFT. The horizontal lines shown at around 36mm indicate the position of the edges of the machined slot.

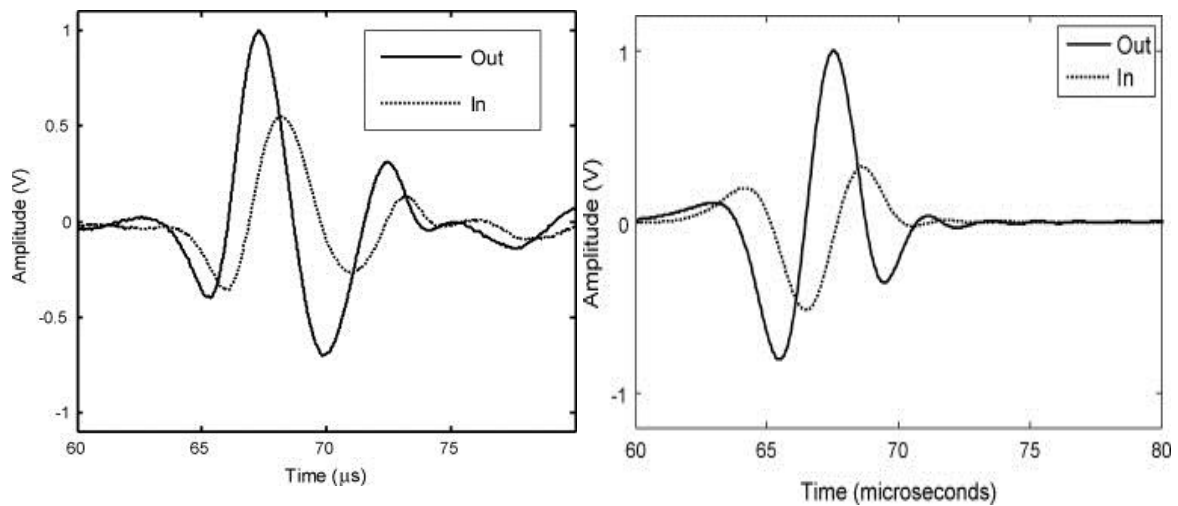
## Electromagnetic acoustic transducers for in- and out-of plane ultrasonic wave detection

*Sensors and Actuators, A: Physical* 148 , 51 (2008)

[10.1016/j.sna.2008.07.004](https://doi.org/10.1016/j.sna.2008.07.004)

Jian, X; Dixon, S; Quirk, K; Grattan, KTV

A model has been developed for the detection of ultrasonic waves using electromagnetic acoustic transducers (EMATs). EMATs are particle velocity sensors, which can be designed to have sensitivity to in-plane and, or out-of- plane ultrasonic displacements, by suitably arranging the magnetic field in the receiving EMATs relative to the orientation of the coil. Good agreement between the results from modeling and experimental measurements has been demonstrated.



Measured (left) and calculated (right) in-plane and out-of-plane particle velocity of Rayleigh waves. The out-of-plane particle velocity is of  $\pi/2$  phase ahead of the in-plane particle velocity.

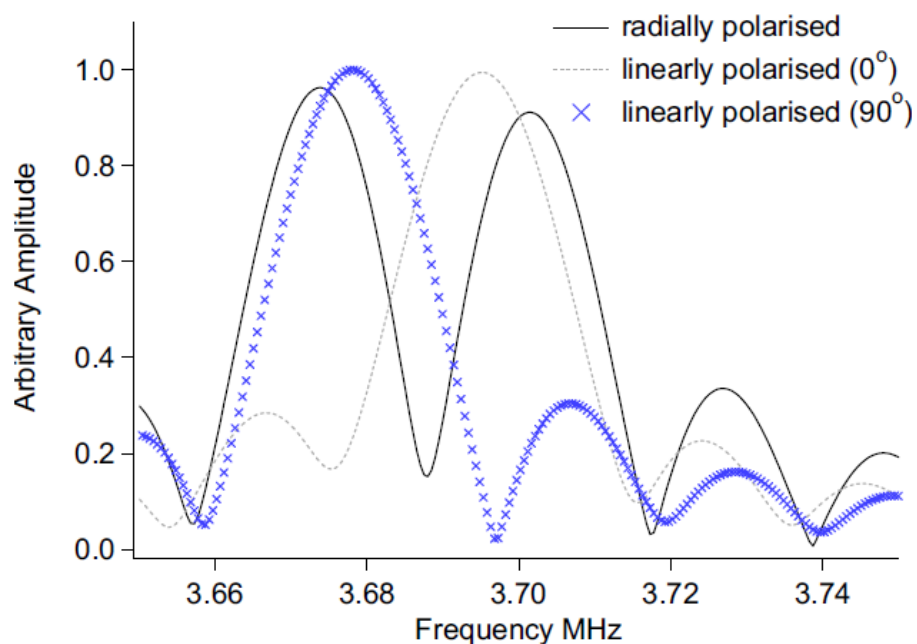
## The accuracy of acoustic birefringence shear wave measurements in sheet metal

*Journal of Applied Physics* 104 (11) , art. no. 114901 (2008)

[10.1063/1.3033395](https://doi.org/10.1063/1.3033395)

Dixon, S; Fletcher, MP; Rowlands, G

In rolled metal sheet the through thickness shear wave energy is steered into two orthogonal polarizations, parallel and perpendicular to the sheet's rolling direction. Ultrasonic velocity measurements used to determine the orientation distribution coefficients in thin sheets can be obtained from the fast Fourier transform of the time domain signal. It is observed that the data obtained using a linearly polarized electromagnetic acoustic transducer (EMAT) do not correspond with that obtained using a radially polarized EMAT. An analytical model has been developed, which explains the source of this effect from the using the fast Fourier transform.



Zoom in of peaks in the magnitude FFT spectra without a Hanning function applied in the time domain data on a 2.99 mm thick aluminum sample. The results from the radially polarized are shown as a solid line and the results from the linearly polarized EMAT orientated at  $0^\circ$  and  $90^\circ$  to the rolling direction are shown as a dashed line and crosses, respectively